Listening to Neurons

- Development and understanding of Micro-electrode Arrays (MEA's) Systems

Rongyu Tang

Submitted to the Faculty of Engineering, Department of Electronics and Electrical Engineering, University of Glasgow in fulfillment of the requirements of the degree of Doctor of Philosophy.

Department of Electronics and Electrical Engineering
University of Glasgow

March 2009

Abstract

This thesis is about the development of microelectrodes array system (MEAs), the simulation of the neuron and the recording to the living neural network. We cultured the nerve cells of rat inside a container called ‘neural bathtub’ and guided them to form predetermined network (Jude pattern) with topographical features or protein traces. In order to record the electrical activity of these nerve cells, two types of MEA systems (FlexMEAs and pMEAs) were designed and built. These extracellular MEA systems were aimed to form one-electrode-to-one-neuron connection with neural network. To assist the design, many models were built, e. g. the impedance model of the microelectrode/electrolyte interface, the oxygen model inside the ‘neural bathtub’.

During this project many difficulties were encountered especially at the coupling of MEA to neurons. To explore these questions more models and simulations were included into this thesis. The excitable membrane of neuron and the interface of neuron to microelectrode are modelled and investigated. These simulations help to explain many questions, e.g. how to form a good coupling of neuron/electrode, how the waveform of extracellular spikes changes and how much power is dissipated when neuron generates an action potential.

The first chapter introduces this project, the history of MEA and some biology about neuron. The fabrication processes of devices (the MEAs, the ‘bathtub’, the mould of Jude pattern and the preamplifier) are described in the second chapter. Chapter 3 gives the detail of the designs of these devices and how they were evolved and optimised. Chapter 4 is about the impedance model of the microelectrode, the measurements of the impedance and the data fitting to obtain the parameters of the model. Chapter 5 models the oxygen concentration inside the ‘neural bathtub’. The simulation tells whether the diffusion provides enough oxygen to sustain the nerve cells. It helped us to modify the design of ‘neural bathtub’. Chapter 6 introduces the basic principle of different microelectrode system from a circuit perspective. The importance of the seal resistance to the coupling of neuron/electrode is investigated using a circuit model. The noise caused by the preamplifier itself is estimated also. Chapter 6 also introduces a model based on the classical model by Hodgkin and Huxley (1952). The differences between the waveforms of the extracellular potential are explored with the help

of the model in this chapter. Chapter 7 represents the signal recorded from different cells with different setups. The signal is analysed preliminarily.

Table of Contents

List of Figures and Tables

Acknowledgement

First I’d like to thank Professor Chris Wilkinson for being a great supervisor and Professor Judy Wilkinson for taking care of me in a way of grandparent. I’d also like to thank Professor Adam Curtis for his elegant language and jokes. Thank Alison Beatie and Maxim Socolov for their friendship. Thank Mathis Riehle for sharing his knowledge, Dr. Nikolaj Gadegaard for his serious help, Gregory and Andy for their warm heart to me in Cell Engineering Centre.

I would like to thank the people at Electrical and Electronics Engineering department who have helped me. Stuart Fairbairn in electrical workshop has great patience on making many PCBs for me. Margaret in Optical Clean Room copied many masks for me. Mary Robertson at Biology group trained me on many things nicely. Thank Keith Mathieson in Physics Department for his guidance on fabricating MEA and teaching me Scottish dialect. Thank my office mate Yao Xu for the fun time together.

Finally I would like to thank my family. Thank my parents, my sister, my wife Xu and my parents-in-law for being greatest family members ever. Thank my cousin Ligang for her encouragement.

Author's declaration

I declare that the work contained within this thesis has carried out by me, except where acknowledged.

Rongyu Tang

March 2009

Chapter 1. Introduction

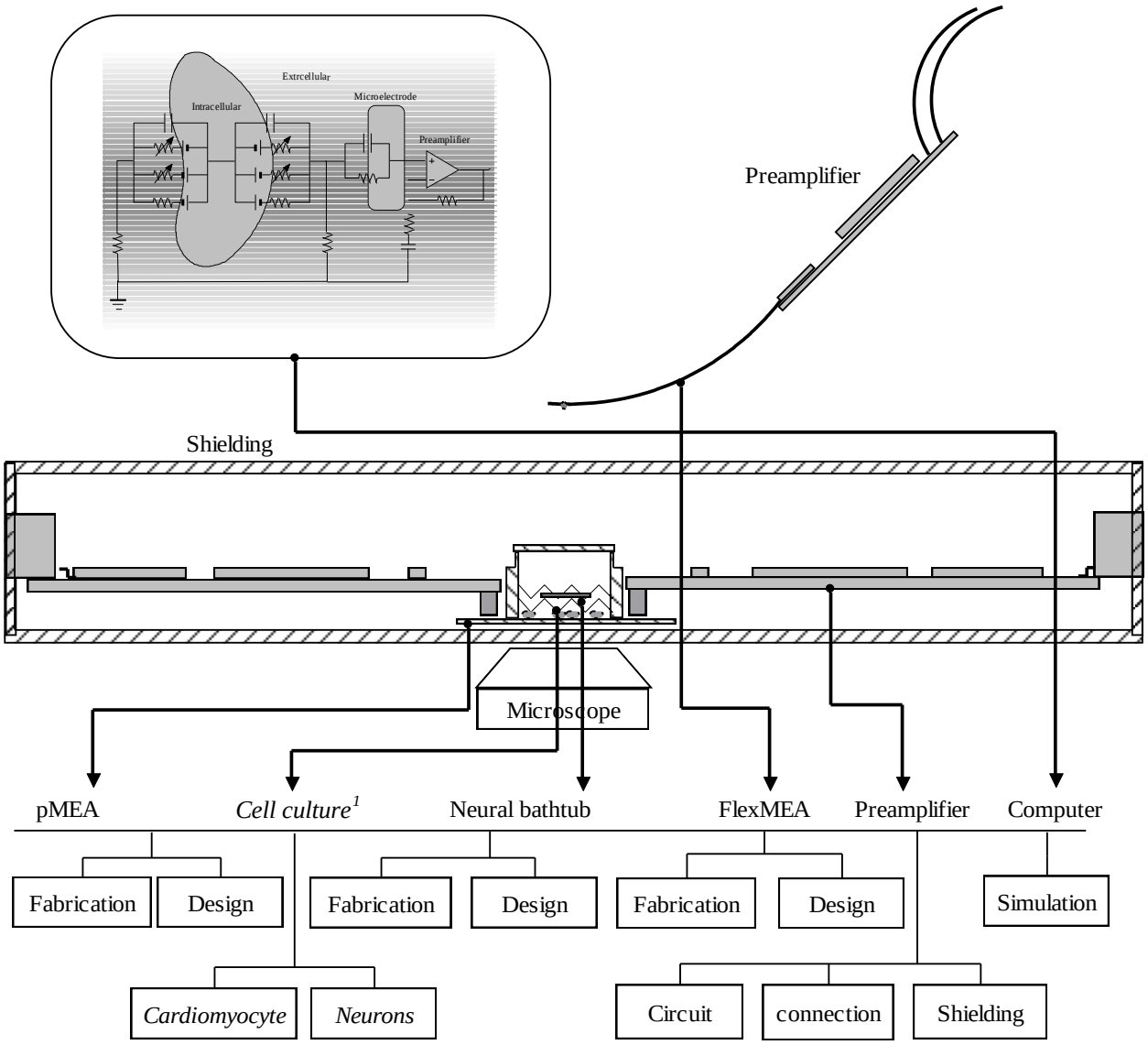

Figure 1-1: Illustration of the content of research work in this project. Cell culture was mainly done by Alison Beatie.

1.1. Introduction to this project

This project was multidisciplinary. From the biological point of view, it concerned the growth and connections of nerve cells. From the perspective of information processing, the working mechanism of the neural network, or in a more ambitious phrase, how the brain operates, is of concern. Circuits for weak signal amplification were built in this project. Different microelectrodes arrays were fabricated and optimized. Computer simulation of nerve cells and the coupling of micro-electrodes to neurons was carried out. There are many practical applications

of the interaction and connection of nerve cells with electronic equipment in, for example, drug testing and the repair of sensory nervous systems.

There are many business entities working on the microelectrode array (MEA) for the study of neurons at the present. Some of them are listed in section 1.2.2. This list does not include home-made MEA systems by research institutions. The importance of MEA's is reflected in the large number of manufacturers and researchers engaged in its development. Microelectrode arrays are basic tools to examine the electric and chemical activities of nerve cells. They are as important to neural research as the oscilloscope and signal generator to the examination of electronic devices and as logic analyzers are to the characterization of IT devices. The design of these MEA systems is optimized for and targeted to the detection of signals from and the stimulation of nerve cells. This optimization includes consideration of the shape, size, surface coating, layout of the electrodes, the detection circuitry, and the specialized software for recording the data. However, these systems are similar to the oscilloscope and signal generator in their purpose. In fact the early researchers utilized traditional electronic equipment.

There are many types of MEA systems for nerve cells. Some MEA's are sensitive to certain chemicals from neurons, some MEA detect the fluorescence resulting indirectly by neural activity, and some receive the magnetic signal from the neural activity. This thesis concerned with those MEA systems that detect the electrical activity as a current or voltage. The systems built in this project were voltage sensing systems. The theory of current detection is discussed in this thesis as it helps to understand the system.

How does the neural network process information? What is the way in which nerve cells respond to stimulus? How does the connectivity of the network influence its functionality? These problems are worth exploring. The neural network has been investigated for many years. The biological neural network inspired the mathematical neural network algorithm which has been widely used. However, many aspects of the neural networks still remain as mysteries. To a large extent, research on neural networks, has been limited and obstructed by the lack of effective tools. Stable and long-term one-to-one (one electrode to stimulate and record one neuron) coupling is difficult to establish. This one-to-one coupling is the ideal way to study of a neural network. Each neuron in the network can be stimulated by an electrode and the spikes from each neuron can be recorded by an

electrode. Most of the reports at present on one-to-one coupling are of non-vertebrate neurons which is made easier by their huge size, or about the one-to-one coupling in a small scale by several single electrodes, or about the many-to-one coupling of high-density neural culture.

This thesis describes the fabrication and modification of several MEA systems, the design and development of the so-called 'neuron bathtub', as well as the fabrication of devices that guide the growth of neurons in order to form a predetermined network (the biological aspects of this work by Alison Beatie are detailed in her thesis). These works were carried out in expectation of pushing forward neural network research. What is worth mentioning is that these works are not only basic research, but is also likely to lead to practical and profitable products.

This thesis also includes a series of theoretical study and model simulations. This theoretical work was done to increase understanding of the neural network, to clarify some doubts and to provide a basis for the improvement of MEA systems. Such modelling and analysis is presented on electrode impedance (Chapter 4), on the concentration of oxygen in the 'neural bathtub' (Chapter 5), on the model of the membrane polarity and the Hodgkin-Huxley model of the action potential (Chapter 1, 6), on the waveform of the action potential (Chapter 6) and on the extracellular potential field, the effects of the seal resistance and the noise of the system (Chapter 6).

This was cooperative project involving three groups from different universities. The group from the University of Edinburgh worked on an integrated patch-clamp array system. The group from University of Stirling was responsible for the signal identification and analysis. Our group in the University of Glasgow developed a planar microelectrode array (pMEA) system and a flexible microelectrode array (FlexMEA) system. We cultured neurons on a structure that we call a 'neuron’s bathtub' in order to improve the coupling of the neurons with the electrodes. Our group had members from the Department of Electrical and Electronics Engineering and the Centre for Cell Engineering (CCE). I worked on electronic and fabrication issues under the supervision of Professor Chris Wilkinson. We were responsible for the development of the MEA systems, manufacturing of the microelectrode array, and the development of the 'neuron's bathtub'. Professor Adam Curtis in CCE was my second supervisor. Alison Beatie and Maxim Sokolov worked at CCE and were

responsible for the cultivation of nerve cells, the guided growth of neural network.

1.1.1. Introduction to this chapter

This chapter starts with a review of the history of electrophysiology and microelectrode arrays. Then some background knowledge about neurons is provided. The characteristics of a neuron, the biological properties of neuron, the phenomenon of membrane polarization, including the Nernst and Goldman equations, the action potential generation and transmission are discussed. The concept of the resting potential and the relationship between the ion concentration and the membrane potential are introduced. The action potential is explained by H-H model. These theories are not only introduced, but also companied with some simple calculation.

Proper coupling between neuron and microelectrode is the key to successful recording and stimulation. This chapter gives an introduction to the relevant knowledge. A detailed analysis is given in chapter 6.

1.2. History and background of MEA

1.2.1. Concise history of electrophysiology

The ancient people noticed that electrical phenomenon happened in animals. There are records of people struck by electric fishes in the text remnants of the ancient Egypt. Aristotle (384 AC – 322 AC) observed the electric ray fish paralyses prey with an electric shock in water. Ancient Greeks and Romans used the shocks from Torpedo nobiliana to cure headaches.

Electrophysiology in a modern sense can be traced back to 1791 when the Italian professor Luigi Galvani discovered electrical phenomenon within the nerve fiber and the muscle of frog. Caton (1875) found brainwaves. Bernstein (1902) introduced the theory that the electric activity is generated at the cell membrane. Berger (1929) recorded the first EEG. Einthoven (1908) measured the weak current of a nerve directly with a sensitive string galvanometer. Hodgkin and Huxley (1939) measured the membrane potential difference of the squid giant axon with microelectrodes. Cole and Marmont (1952) invented the voltage clamp. Neher and Sakmann (1976) invented the patch-clamp technique. All these people, findings

and inventions form the history of electrophysiology.

1.2.2. The development of Microelectrode array (MEA)

Single microelectrode

Microelectrodes have been used to investigate the electrophysiological activity of the nervous system for more than a century. The metal stick used by Galvani can be seen as a prototype of the microelectrode albeit on a larger scale. Edes used a capillary containing platinum wire to measure the impulses in the leg muscle of a frog (Edes, 1892). In the 1920s, Craib stimulated cells with a silver needle to investigate the electric field around the heart and muscle (Craib, 1927, 1928).

An extracellular metal electrode was the first device used first to record from a single neuron (Lorente,1928; Renshaw, 1946). Afterward, a micro-pipette (invented by Marshall Barber around 1902) was used to record intracellularly (Ling and Gerard, 1949).

By the middle of last century, both intracellular and extracellular recording were made in vitro and in vivo. Graham and Gerard (1946) were the first to employ micropipette electrode to measure individual muscle fiber. In vitro studies, a platinum electrode, of diameter 175 μm, was attached to a micromanipulator to obtain external recording from rat diaphragm motor neurons (Krnjevic and Miledi, 1958; Tasaki et al., 1968). Glass micropipettes filled with 3M KCl were used for intracellular recording (Krnjevic and Miledi 1958). In situ studies steel microelectrodes was used to make extracellular recordings (Furshpan and Furukawa, 1962). Silver wire electrode was used to stimulate the cortical neurons and KCl filled glass microelectrodes to record (Pickard, 1979).

Multiple microelectrodes

The need for spatial distributed recording promotes the development of multiple electrode arrays. The earliest electrodes arrays are simply conventional microelectrodes assembled together (Verzeano, 1956).

Hanna and Johnson (1968) produced an array of 20-30 electrodes on a plastic sheet using photoetching techniques. There were some similar electrode arrays made by different groups (Prohaska et al., 1977; Jobling et al., 1981). These electrodes

array are not really microelectrodes. Some of them are designed to be used on surface potential recording. Most of them have sizes in the range of millimeters.

Chip-based MEA

There are many types of MEA. Some are merely a bundle of metal electrodes glued together. Some consist of conventional glass pipettes welded together. Some are integrated FET arrays. Some are chip-based patch clamps. Here we focus on the planar MEA made using the fabrication technology of integrated circuits. They are described variously: printed circuit MEA's, photoetched MEA's or chip-based MEA's etc. The term MEA in this thesis refers mainly to this type of MEA.

The advantages of chip-based MEA

Creating MEA using the IC fabrication techniques has many advantages. The size, distance and features of the electrodes can be precisely defined. It can be highly reproducible, if the batch-process is applied. This technique is compatible with integrated circuits. So it is easy to build a on-chip preamplifier together with the electrodes. Many advantages come with integration. It helps to minimize the size of the system and to reduce noise coupling.

The IC technology began to be used to fabricate MEA in the 1970's (Wise, K. D. and J. B. Angell, et al., 1970, 1975). This MEA had a silicon substrate, gold electrodes and silicon dioxide insulation. Thomas fabricated similar MEA and recorded from chick embryo cardiac myocytes (Thomas et al., 1972). This MEA was defined in a metal film deposited on a glass cover slip. The electrode tips were formed of platinum black to reduce the impedance. The techniques used by these pioneers are still used today.

The development of chip-based MEA

Many studies have been carried out with extracellular microelectrode arrays. The first successful recording made using extracellular microelectrode array were obtained from a confluent layer of chick embryo cardiac myocytes (Thomas 1972). A few years later, work has been extended to neural recording initially from isolated mollusk neuron (brain ganglia from the snail Helix pomatia) (Gross, 1979). and then to dissociated neural cultures. Both vertebrate (neonatal rat superior cervical ganglia) (Pine 1980) （mammalian spinal cord） (Gross, Williams & Lucas

1982) (Gross, Wen, and Lin 1985) (Oliver et al. 1986) and invertebrate (Tank, Cohan, and Kater 1986) (Regehr, Pine, and Rutledge 1988) (Aplysia abdominal ganglion) (Novak and Wheeler, 1986) neurons have been successfully cultured and monitored for periods of up to several weeks.

Stimulation by injection of current can be used in a MEA system. It was applied to embryonic chick myocytes first (Israel, et al., 1984; Israel, et al., 1990; Connolly, et al., 1990) and then to neural culture (mouse and chick dorsal root ganglion cells) (Jimbo and Kawana, 1990; Jimbo and Kawana, 1992)， （rat cortical neurons） (Jimbo, et al., 1993).

Custom MEAs and commercial MEAs

Many groups including our group (Connolly et al., 1990) build their own custom-made MEA systems. （Pochay et al., 1979; Prohaska et al., 1979; Pine,1980; Israel et al.,1984; Kuperstein and Eichenbaum, 1985; Novak and Wheeler, 1986; Connolly et al., 1990; Eggers et al.,1990; Janossy et al.,1990; Borroni et al.,1991; Jimbo and Kawana,1992; Martinoia et al.,1993; Gross and Schwalm,1994; Nisch et al., 1994; Stoppini et al, 1997;）Our group has been building and modifying our own MEA systems since our first MEA system (Connolly et al., 1990). The details of the two new custom-made MEA systems of this project are in chapters 2 and 3.

Many companies provide MEA systems including hardware for signal recording and stimulation and software for the analysis of data: in Germany, Multichannel Systems; in Japan, Alpha MED Science (Panasonic); in Switzerland, Ayanda Biosystems; and in the US, Plexon Inc., Axon Instruments and UNT Center for Network Neuroscience. These companies are listed below:

Table 1-1: An incomplete list of companies all over the world providing MEA systems.

Hardware vendors:	Products
Ayanda Biosystems SA (Switzerland)	256 channel pMEA system
Cambridge Electronic Design ltd. (UK)	pMEA system and software
DataWave Technologies (US)	pMEAs hardware and software
Multi Channel Systems (Germany)	Variety MEA systems and software
NeuroSensorix (Germany)	58 channel palladium pMEA system
Panasonic Alpha MED System (Japan)	64 channel ITO pMEA system and softeware
Plexon Inc. (US)	pMEA, penetrating MEA system and software
Tucker-Davis Technologies (US)	pMEA, penetrating MEA system and software
University of North Texas, Center for Network Neuroscience (US)	pMEA only

Software

NeuroEXplorer (NEX)	Signal analyse
Statistica	multipurpose
MatLab	multipurpose
GraphPad PRISM	multipurpose

Chip-based patch clamp array (automated patch clamp array)

Traditional patch clamp techniques utilizes glass pipette electrode. They are time consuming to make and laborious to manipulate. It is not easy to assemble these glass pipettes together when multiple recording is required. The idea of chip-based patch clamp is to fabricate the micropipettes with semiconductor and so integrate them into a chip. Chip-based patch clamp arrays are produced by many companies. Axon Inc. produces PatchXpress and SealChip; Cytocentrics has CytoPatch; Sophion Bioscience sells Qpatch.

FET array

The first field-effect transistor for neural recording was developed by Bergveld (P. Bergveld et al., 1972). The Fromherz group in Germany developed this technique and recorded from individual invertebrate neurons. (P. Fromherz, A. Offenhäusser, T. Vetter, J. Weis, 1991)

Extracellular microelectrode array

To observe the electrical activity of the cells in a neural network of specified connectivity, one needs electrodes to collect the electrical signals from many positions over a long period of time. Conventional intracellular electrodes give a signal with excellent signal to noise ratio, but they have disadvantages for observation of neural networks. Great experiment skill is required to manipulate a large number of these electrodes and the practical limit seems to be three or four electrodes. The process is inevitably traumatic to the neuron, and so observation over extended periods of time is not possible.

Extracellular electrodes are non-invasive and a number of them can be used simultaneously. Extracellular electrodes are suitable for a comprehensive recording of a neural network over a long term. These electrodes can also be used to stimulate neurons with injection of current. This allows a long-term two-way connection between a cultured neuronal network and some electric devices. The disadvantage of using an extracellular electrode is that the strength of the signal is about 100 times smaller than that observed with an intracellular electrode. Most of

the successful applications of the extracellular MEA target the nervous system in vivo, the neural tissue in vitro, dense neural culture or individual neurons of huge size. Few reports can be found on the extracellular recording of the sparse neural culture. The main reason is that the difficulty of coupling extracellular electrode with the sparse distributed neurons, in another word, the difficulty of establishing high seal resistance. However, the most suitable object for the research on the working principles of the neural network is a sparse neural culture. Small signal to noise ratio leads to the difficulty of spike (indicating the existence of action potential) detection and the analysis in terms of amplitude and waveform of the signal. However many believe that the information is not carried in the form of waveform or amplitude of impulses but in the rate that the spikes are generated. If this is correct, then the extracellular electrode is sufficient. In order to improve the signal to noise ratio, works need to be done on the design and optimization of the extracellular electrode array.

We have fabricated and investigated two different extracellular microelectrode arrays: the flexible microelectrode array and the planar microelectrode array. The former one has the flexibility of choosing which cells to record from. The later one is best for long term recording.

1.2.3. Electrode-Electrolyte Interface

The electrode serves as the transducer between the cells and the electronic systems. The electronic system is used to monitor, record, and analyze the action potential of cells. The signal is carried by ions that flow in cells. But the carrier of the signal changes to the electrons in the electrode and circuit. Neurons generate impulses (action potential) in the form of ion current. The impulses give rise to the vibration of the field potential in the extracellular electrolyte. The metal electrodes subject to the electrical field transduce the vibration to the current of electrons.

When a metal electrode is first placed in an electrolyte, there’s no potential difference across the interface. A space charge layer develops rapidly due to electrochemical reactions. Most of these reactions ionize atoms of metal and change them into positive ions. The ions leave the electrode and dissolve into the bulk electrolyte. These cause excess electron accumulate at the surface of the electrode. Thus a space charge layer builds up. The space charge inhibits the

ionization and encourages ions to deposit back to electrode. Eventually, equilibrium is reached. Chapter 4 introduces in details the model of the metal-electrolyte interface.

1.3. Guided neural network

A sparsely cultured neural network in vitro is ideal for the investigation on how the neural network process information. The pMEA and FlexMEA coupling with the neurons in one to one manner can record and stimulate the neurons.

Three ways of guiding the growth of nerve cells so that a particular pattern of network is formed have been reported in the literature. Dispersed cells are seeded onto a substrate that presents features aimed at controlling the topology of the resulting networks. Surface modifications can be classified into three broad categories: the use of surface chemistry, topography and electrophoresis. In the first two methods a particular pattern is made on the substrate in advance. This pattern will guide the growth of cells. The last method is to use electrophoresis force to maneuver cells. The forces generated by electrophoresis can attract or expel cells. The cells are placed in a given position immediately following seeding.

1.3.1. Chemical method

In this method a pattern of proteins is established on the surface of the MEA, either using lithographic techniques or using microcontact printing. Some protein encourage adhesion of cells, some discourage adhesion. In the work of James, microcontact printing was used to pattern poly-L-lysine (PLL) on the surface of pMEA's. The dissociated hippocampal pyramidal neurons formed a network and signals were recorded. (Conrad D. James et al., 2000, 2004)

1.3.2. Topographical and structure method

This method often fabricate topographical feature or build structure on the surface of MEA. Take the work by Claverol-Tinture as an example. An elastomeric structure was made by replica moulding and micro-hole punching. This three-dimensional structure was then aligned to the surface of MEA. The microporous structure is used to locate the neuron body. The micro-channels guide the nerve fibers to obtain neural network links. Snail neurons (Helix aspersa) were cultured in the structure and signal was successfully collected. (E. Claverol-Tinture, 2005)

In another example, neurons of chicken embryonic cortex and mouse embryonic cortex were used. A micro-structure made of PDMS was aligned to the surface of the MEA. Nerve cells formed a network in this structure. Signal is recorded. (Fabrice Morin, 2005)

1.3.3. Electrophoresis trap

This method utilizes the force of electrophoresis to attract cells to or repel cells from certain locations.

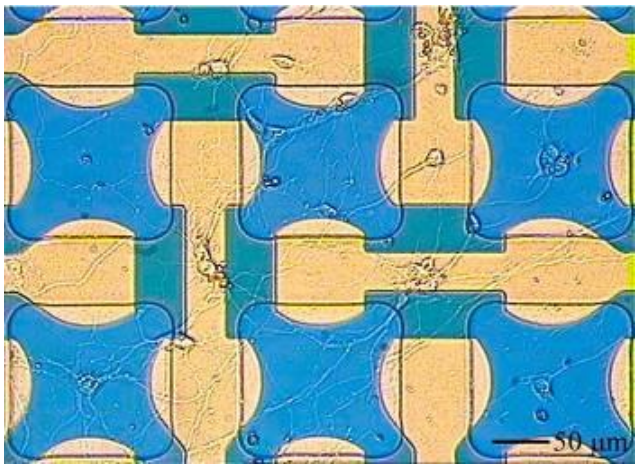

Figure 1-2: This photo is from (Zhe Yu, 2004). It shows the pattern of electrodes and the cultured neural network.

This example uses cortical neurons. The electrodes are patterned to form force traps of different scales. Some neurons were trapped in these regions and grew into a network.

1.3.4. The methods used in our project

In this project chemical and topography methods were employed. In contrast to the examples in 1.4.1 and 1.4.2, the nerve cells were not directly cultured on the MEA. Instead they were insulated in a 'neural bathtub' until a network had been established – up to ten days after seeding. Then the 'bathtub' was taken out and placed on the pMEA upside down so that the cells came into contact with the surface of the MEA. Alignment was required to move neural network over the micro-electrodes of the pMEA in a manner to be discussed later, before any recording or stimulation.

1.3.5. The types of neuron used in this project

In this work we used spinal cord and co-cultures of cortex and hippocampal tissue as these cell types show spontaneous activity in culture, which is important for recording with electrodes.

1.4. Background knowledge about neuron

This section provides a basic introduction to the mechanisms behind the generation of action potential. It is worth noting that the structure and our understanding of working mechanism of neurons is an active area of research world-wide. The present discussion is based on widely accepted ideas. It can only be regarded as a basic frame of ideas. For example, in the H-H model discussed in this section, only three types of ion channels are used to describe the action potential. Now it is know that there are many more types of ion channels.

1.4.1. The structure of a neuron

The neuron is the basic unit of the nerve system. Neurons are eukaryotic cells. They share common features with all other eukaryotic cells: a cell membrane, a nucleus and other organelles. Neurons are specialized in dealing with electrochemical signal and so possess some unique features.

A distinctive and impressive feature of neurons is the outgrowths from the cell bodies (called processes or fibres). A typical neuron is formed with three parts, soma, dendrites and the axon. The soma is the body part. It contains a nucleus and other organelles, surrounded by a cell membrane and filled with cytoplasm. The Axon and the Dendrites are fibres. Fibres contain cytoplasm which is connected to and exchanges with that of the soma. The axon is often longer and bigger than the dendrites. Most neurons have only one axon but this axon can split (as shown in Figure 1.3). The dendrites are shorter and look like branches of a tree. One neuron may have many dendrites.

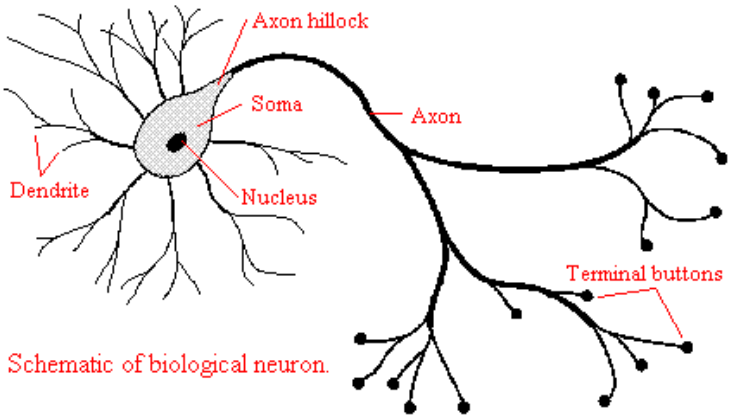

Figure 1-3: A schematic drawing of the structure of a typical neuron.

Terminal button

The axon branches at its end. The end points of these branches expand into ‘terminal buttons’.

Synapse

The terminal button is connected to other neurons. The connection spots are called ‘synapses’. An action potential is transmitted from one neuron to another through these synapses. There are about 1014 synapses in the brain of a human. One neuron in the adult human cortex on average contains about thirty thousand synapses. Some neurons may have as many as two hundred thousand synapses.

One synapse has three components: the presynaptic, the postsynaptic and the synaptic cleft. The former two are located on the membrane of the neurons. The synaptic cleft is the gap between them.

There are two types of synapses: the chemical synapse and the gap junction (electrical synapse). They are named after their different methods of transmitting the signal. Most synapses are chemical synapses. They transmit a signal by using a chemical material, known as a neurotransmitter. The electrical synapses achieve the same goal with a purely electrical method.

Electrical synapses

Electrical synapses do not use neurotransmitters. There are many gap junction channels located in the presynaptic membrane and the postsynaptic membrane. The synaptic cleft is much shallower (about 3.5 nm) than that of the chemical synapses. The cytoplasm is connected through these gap junction channels of the

two neurons and ions or small molecules diffuse or drift through these channels.

Chemical synapses

The synaptic cleft is about 20~50 nm wide. There is no cytoplasm exchange within chemical synapses. The postsynaptic membrane is unexcitable. Signal transmission occurs via the neurotransmitters. Neurotransmitters can transmit not only excitement but also inhibition to the post synaptic neuron.

Transmission of chemical synapse

The presynaptic membrane releases neurotransmitters when the incoming electrical excitation causes an influx of calcium ions. Calcium ions release the transmitter from some synaptic vesicles across the presynaptic membrane into the synaptic cleft. There are receptors in the postsynaptic membrane. The transmitter diffuses across the synaptic cleft and stimulates or inhibits the next neuron by interacting with receptors. Some receptors are called ionotropic receptors or ligand-gated ion channels. The transmitters attach to the binding site of these receptors and open the ion channels. There are also many indirect ways for transmitters to interact with the receptors and ion channels. The switching of different ion channels changes the permeability of the membrane to different ions. The change of permeability results in the change of membrane potential. The membrane become depolarized (potential magnitude decreased) or hyperpolarized (potential magnitude increased). The neuron may be stimulated to spike an impulse or be inhibited into silence on various time scales.

There are many types of neurotransmitters. Different transmitters have different effect on the postsynaptic resulting in excitement or in inhibition. One neuron may possess two or more types of neurotransmitters. Excitatory transmitters mainly raise the permeability of sodium ions through postsynaptic membrane. Sodium ions flow in and the membrane potential is reduced. These ion channels here are controlled by neurotransmitters. There are different types of potential gated ion channels involved in the propagation of excitation along an axon. These voltage-sensitive ion channels will be discussed later in the section about the H-H model.

The influence of a single synapse may not be enough to make postsynaptic neuron fire. The influence from many synapses can be added and magnified. When the membrane potential reaches threshold, an action potential is triggered. On the

contrary, the inhibitory transmitters make the postsynaptic neuron hyperpolarized and prevent the generation of the action potential. The hyperpolarization is mainly attributed to the influx of the chlorine ions or the outflow of the potassium ions.

Signal transmits through a chemical synapse within 0.5~2 ms. Electrical synapses are much faster.

One way propagation and two way

The electrochemical signal transferring from neuron to neuron generally follows certain direction. The axon carries signal away from soma. On the other hand, dendrites receive and carry incoming signals into the soma. A signal generated in the soma transfers in the following direction: soma to axon to terminal buttons to synapse on a dendrite.

Synapses are believed to play an important role in this one way propagation. Chemical synapses (electrical synapses do not) transmit signal in only one direction. The release of transmitters and the reaction to them needs specialized biological structures to complete. Only the presynaptic membrane area possesses the ability to release transmitters. Only the postsynaptic membrane can react to transmitters with its receptors and ion channels. Therefore the direction of propagation through chemical synapse is determined.

Electrical synapses transmit action potential in either direction. Similarly, the propagation along the membrane of neuron is also bidirectional. It is due to the same mechanism behind these transmissions. Neurotransmitters are not involved in these propagations. Only flow of different ions is taking place. The ion channels related with these bidirectional propagations are sensitive to membrane potential only. And any disturbance in the membrane potential spread to all sides. These factors make the propagation having no favorable direction.

Myelin Sheath

A Myelin Sheath, produced by specialized glial cells, and typically found chiefly in vertebrates is often found wrapping around the axon of a neuron. The myelin sheath insulates the axon from the outer environment. This insulation increases the transmission speed of signals. Ions cannot pass through Myelin Sheath and have to find another path. There are gaps between each myelin sheath cell along the

axon. The gaps (approximately 1 micrometer wide) are called the Nodes of Ranvier. Several factors possibly play roles in this speed up. To understand more of this increase in the velocity, space constant and time constant are needed.

Space constant and time constant

In 1850s, William Thomson (Lord Kelvin) developed a mathematical model of signal decay in submarine telegraphic cables. In the early 20th century, Hermann and Cremer developed the cable equation for neuronal fibres based on Kelvin's cable model. Space constant and time constant are the parameters associated with the signal conduction in neural fibre and can be derived from the cable equation.

A DC current is assumed to inject into a passive nerve fibres (dendrite) at a point. The membrane potential follows the exponential decay function along the nerve fiber with the distance to the inject point. From the inject point of maximum potential to attenuate to 0.37 times, the length is called the space constant.

$$\lambda = \sqrt{(r_m / (r_i + r_o))} \qquad \text{Eq. 1-1}$$

The variables and parameters represent:

r_m is the membrane resistance per unit length;
r_i is the resistance of the axoplasm per unit length;
r_o is the resistance of the extracellular medium per unit length.
λ is the space constant;
c_m is the membrane capacitance per unit length;
V is the membrane potential;

The following is a brief derivation of the space constant. It is based on the cable model of a passive nerve fiber. Assume the membrane current is injected at a point and held at constant. The nerve fiber is infinitely long.

From the cable equation:

$$\partial^2 V / ((r_i + r_o)\, \partial x^2) = c_m\, \partial V / \partial t + V / r_m \qquad \text{Eq. 1-2}$$

In the steady state, the cable equation can be simplified to:

$$\partial^2 V / ((r_i + r_o)\, \partial x^2) = V / r_m \qquad \text{Eq. 1-3}$$

The general solution to this equation is the sum of two exponential function:

$$V = A\, e^{x / \lambda} + B\, e^{-x / \lambda} \qquad \text{Eq. 1-4}$$

Given the boundary condition that:

$$V(\infty) = V(-\infty) = 0 \qquad \text{Eq. 1-5}$$

The special solution to this equation is then:

$$V = V_o\, e^{-Abs(x) / \lambda} \qquad \text{Eq. 1-6}$$

Where $\lambda = \sqrt{(r_m / (r_i + r_o))}$ is the so-called space constant.

The derivation of time constant is similar. Considering a certain point on the nerve fiber, the membrane potential changes with the passage of time. The time constant is: $\tau = r_m c_m$.

Glial cells

Glial cells form one of the two major cell groups in the nervous system. They provide physical and nutritional support to the neurons Recent researches provides evidence that showing glial cells are also involved in signal transmission and processing (Newman and Zahs, 1997). There are four types of glial cells: astrocytes, oligodendrocytes, Schwann cells and microglia. The oligodendrocytes and the Scwann cells produce myelin sheath, and the astrocytes as well provide nutrition, maintain ion concentration, digest parts of dead neurons, give mechanical support and pave the way for neural growth. The microglia are part of the reticuloendothelial system. The glial cells forming myelin sheaths are called oligodendrocytes in the central nerve system and Schwann cells in the peripheral nerve system.

Glial cells are about 10 to 50 times more numerous than neurons in human brain (E. Kandel, 2000). Many glial cells have processes as neurons do. Although they are normally smaller than neurons, experienced eyes cannot always guarantee distinguishing them from neurons.

Glial cells can interfere with the coupling of a MEA to a neuron. Measures are taken at the early stage of neural culturing to reduce the number of glial cells. However glial cells assist with neural growth. Neurons tend to attach to glial cells. Glial cells may take the place in the patterns first. Neurons like to follow and grow along the designed patterns.

1.5. Resting Potential

While at resting states, the neuron has different concentrations of negative and

positive ions on either side of the cell membrane. This difference in concentration makes the membrane similar to a charged capacitor. Some animals can generate high voltage and current from columns of charged muscle cells.

The concentration of negatively charged ions is slightly greater inside the cell membrane. The resting potential of a neuron is about -70mV. The reason to maintain the resting potential is not fully understood. It does increase the reaction speed of neuron to stimulation. And the daily energy cost on maintaining for a human is not much more than a bite of bread.

1.6. The Action Potential

Action potentials are important for animals. They can be found in the nerve system and the muscles. Action potentials set the pace of thought and action, enable activity and coordination of body. Action potentials occur also in some plants but do not propagate.

Neurons are capable of generating action potential by stimulus or spontaneously. Action potential is a sudden shift of the membrane potential away from its resting value and returns gradually in a few milliseconds. If the membrane potential migrates away from its resting value and becomes more positive, the cell is said to be depolarized. When a neuron depolarizes above a certain threshold (approximately *15 mV)*, an action potential will occur. The action potential is an all-or-nothing event that occurs only when stimulation is strong enough and the inhibition is not enough to hold it. The stimulation could be a current or a chemical material. The action potential will propagate along the cell membrane once it is generated. The transmission is called the neuronal impulse.

All-or-none law

Adrian (1912) found the all-or-none law. Stimulation either produces action potentials or not. There is no intermediate signal generated. Every spikes are similar in their waveform. This means that information is only coded in the timing of the spikes.

Domino propagation

The Action potential is not propagated like an electrical current does in a wire. It

is more like the way dominoes fall down. Neural membrane does not transmit the action potential passively. It actually provides energy for the transmission. It is just like dominoes, one falls down and releases its energy. The next domino is activated by the last one. The action potential reaches a part of membrane and makes the part active. The permeability of the active zone rises by hundreds of times abruptly. The permeability of the membrane is dependent on the membrane potential. And the change of the permeability gives rise to the change of the membrane potential. Their relationship is detailed in next section. The permeability change in fact caused by the opening and closing of different ion channels. The opening of ion channels releases currents to flow through the membrane. Currents cause rapid changes in membrane potential. The change affects neighbouring membrane and creates a new active zone. The process repeats and so the action potential is transmitted. The active zone returns to its resting state slowly after the impulse. The resting potential is rebuilt by the effort of ion pumps. The released energy is stored again and ready for the next transmission.

Why active propagation is necessary?

The action potential is propagated in an active way. In another words, energy is spend on the propagation. It is different from the passive way in which a cable propagates a signal. The reason why neurons chose the active way is that they cannot afford the signal decay over a long distance. The decay length of an axon is about several millimetres (Hodgkin and Rushton, 1946). This means that the passive way is not enough for long distance propagation within animal body. Only for short distance, such as within the retina or small animal, passive propagation works well (Robert and Bush, 1981). A graded potential instead of action potential transmits information in these situations.

The switching of the ion channels

When the action potential is initiated, the voltage-gated sodium channels opens first. The open of sodium channels results in a sudden influx of sodium ions. This is due to the unbalanced concentration gradient of sodium ions. As sodium ions flow into the cell, the membrane potential depolarizes further. This makes even greater numbers of sodium channels opening. The membrane potential approaches the equilibrium potential of sodium very fast. Then sodium channels start to close. The

closing is much slower. After a few milliseconds, all the sodium channels close.

Hodgkin and Huxley derived a series equations to describe the active membrane. Their equations are implemented here in the spreadsheet software 'Excel' to illustrate the ion current during an action potential. It simulates the response of cell membrane to a current stimulation under current clamp measurement. These parameters are from squid giant axon at *6.3 °C* (Hodgkin & Huxley, 1952). More details about the H-H model are in chapter 6.

Resting potential V_o = *-60 mV*;
Resistance of cytoplasm (radius *238 μm*) r_i = *35.4 Ω cm*; Membrane capacitance C_m = *1μF / cm*^{2}; Equilibrium potential of sodium E_{Na} = *45 mV*; Equilibrium potential of potassium E_K = *-82 mV*; Leakage potential E_{Leak} = *-59 mV*; Maximum conductance of sodium channels: $\hat{g}_{Na}$ = *120 ms / cm*^{2}; Maximum conductance of potassium channels: $\hat{g}_K$ = *36 ms / cm*^{2}; Conductance of leakage g_{Leak} = *0.3 ms / cm*^{2}; Time step in simulation δt = *0.01 ms*;

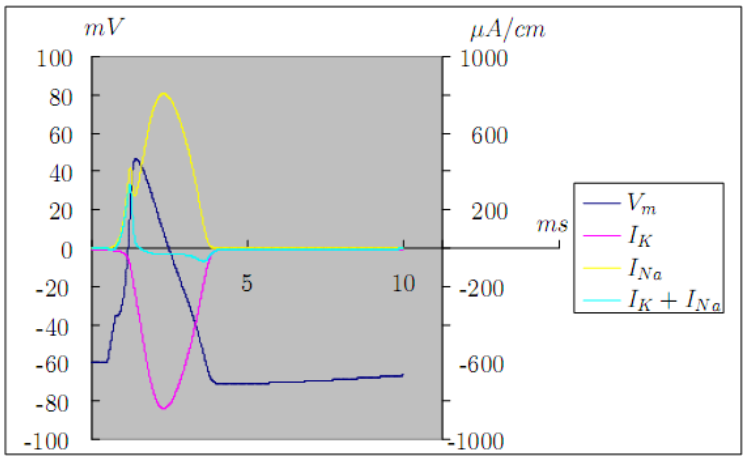

Figure 1-4: The membrane action potential (no propagation) and ion currents recorded intracellularly with the current clamp method. This is simulated with Microsoft 'Excel'. The highest curve is sodium ion current. The lowest curve is potassium ion current. The small spike is the total current. The dark curve in the middle is intracellular action potential.

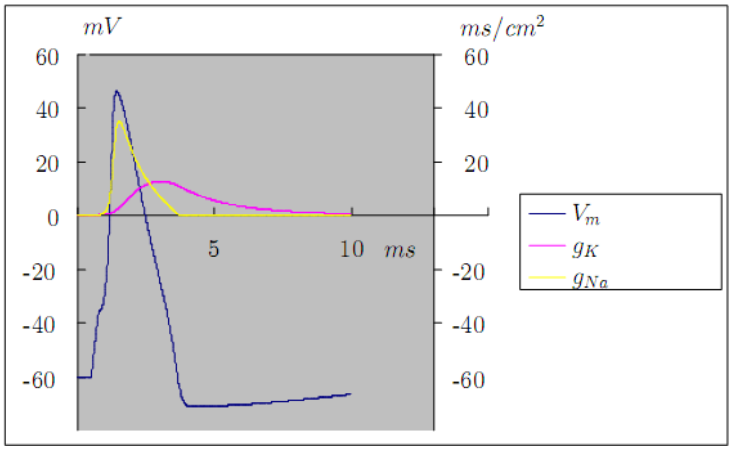

Figure 1-5: The membrane action potential (no propagation) and the membrane conductance to ions recorded intracellularly with current clamp method. This is simulated with microsoft 'Excel'. The middel curve is membrane conductance to sodium. The flat curve is membrane conductance to potassium ion current. The highest curve is intracellular action potential.

When sodium channels are working, potassium channels work too. Potassium channels start opening at the same time when sodium channels do. They do not contribute much to the depolarization phase as they open much more slowly than the sodium channels. Their force is shown at the repolarization phase after much of the sodium channels are closed and the membrane potential is far from their equilibrium potential. Potassium ions flow out of membrane and bring the membrane potential back toward the resting potential. The repolarization phase takes much longer than the short depolarization phase.

It is worth noticing that the ion concentration barely changes during the firing of the action potential. The ionic current flow generated during an action potential does not change much of the ion concentration. This is based on the fact that the membrane depolarization or polarization of tens milivolts requires only small amount of electric charges. Experiments have been done to prove this point. A few hours after the blocking of ion pumps, cells are still able to generate action potentials. This can be also proved in theory. The detail is in the section 'resting membrane potential'.

1.6.1. The action potential of the cardiac cells

In cardiac cells, the repolarization is much slower because of the action of calcium. In cardiac cells, the membrane depolarization results in the opening of voltage-gated calcium channels. Calcium channels open more slowly than the sodium channels. Therefore, following the closure of the sodium channels, calcium flows down its electrochemical gradient into the cells. Additionally, there is a temporary decrease in potassium permeability. The inward flow of calcium ions balances the outward flow of potassium ions resulting in a plateau in the cardiac action potential. Ultimately, the slow calcium channels are inactivated and the potassium permeability increases to complete the membrane repolarization.

For the cardiac cell cultures used in this work, the AP propagates through multiple cells. In cardiac tissue in vivo or a cardiac cell cultures, the cells are electrically connected via gap junctions. Gap junctions as mentioned before are regions where the cell membranes have fused in such a way to allow relatively free diffusion of

ions. Therefore an AP spreads from one cell to the neighboring cells. Typically, an AP is initiated by a single pacemaker cell and spreads throughout the entire culture. When one cell becomes excited, the AP spreads to all of the others, and the muscle contracts as a unit.

1.6.2. Action potential propagation

The H-H model provides a basic mathematical description for the excitable membrane. It forms the skeleton and can be assembled to solve more complex problems. Hodgkin and Huxley combined their model of ionic currents with core conductor theory to predict a propagating AP along a cylindrical fiber. The fiber is assumed to be unmyelinated and surrounded by homogeneous conducting medium.

In the core-conductor model, an inner conductor (intracellular medium) is separated from an outer conductor (extracellular media) by an insulator (cell membrane). This model assumes the conductor is a cylinder, and the current propagates along its axis. This model predicts a transmembrane current proportional to the second spatial derivative of the transmembrane voltage. Details of the derivation of this relationship are given in (Weiss, 1996).

Cable theory was originated from the reaserch made by Lord Kelvin on the phenomenon of the signal decay in submarine telegraphic cables. The internal metal is separated from the external seawater by a layer of insulator. This situation is very similar with the axons in medium. The intracellular fluid is separated from the extracellular fluid by the cell membrane. The following figures show the equivalent circuit of the cable and the axon. The resistors r_e , r_i represent the resistance of the extracellular fluid and the cytoplasm in a section of the axon. Between these two resistors, there is H-H model, representing the membrane capacitance and the ion channels in this section of axon. The model of the cable is similar. There are also resistors r_e , r_i representing the resistance of seawater and the internal metal. There are a capacitor and a resistor between these two resistors, representing respectively the stray capacitance and the resistance of the inductor.

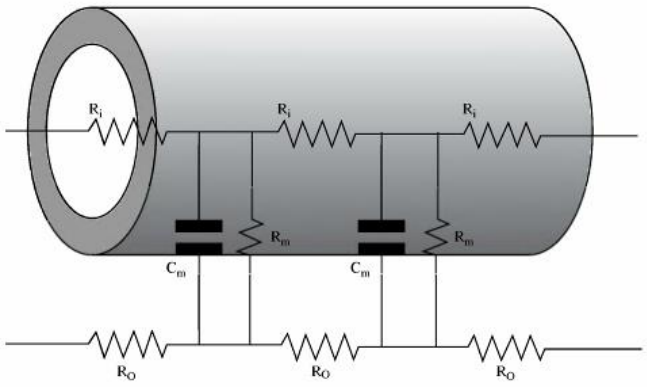

Figure 1-6: The equivalent circuit model of a cable under water. A fibre of neuron can also be described by the similar model.

A group of equations can be found from the equivalent circuit of the cable relying entirely on the Kirchhoff laws and Ohm's law. The core-conductor equation can be derived from them.

$$d^2V / dx^2 = (r_e + r_i)\, i_m \qquad \text{Eq. 1-7}$$

This equation can be used on the equivalent circuit of the axon, because this part of the circuit is exactly the same for both of them. H-H combines this core-conductor equation with the H-H model (Hodgkin and Huxley, 1952) and derives this equation.

$$d^2V / dx^2 = K\, I_m / (C_m\, \theta^2) \qquad \text{Eq. 1-8}$$

This equation shows that the membrane current is proportional to the second partial derivatives of the membrane potential. Under the circumstances of a constant propagation speed, the second temporal and partial derivatives are proportional ($\theta^2\, d^2V / dx^2 = d^2V / dt^2$). This leads to the famous equation:

$$d^2V / dt^2 = K\, I_m / C_m \qquad \text{Eq. 1-9}$$

This equation shows that the membrane current is proportional to the second temporal derivatives of the membrane potential. The proportionality factor K / C_m depends on the size of the axon the resistance of the axoplasm and the extracellular fluid.

Chapter 2.Material and Methods

2.1. Introduction

Two different recording systems were designed and manufactured in this project. One system combines planar microelectrode arrays with a novel dimethylsiloxane polymer (PDMS) neuron container ('neural bathtub'). The other system uses a flexible microelectrode array of improved design.

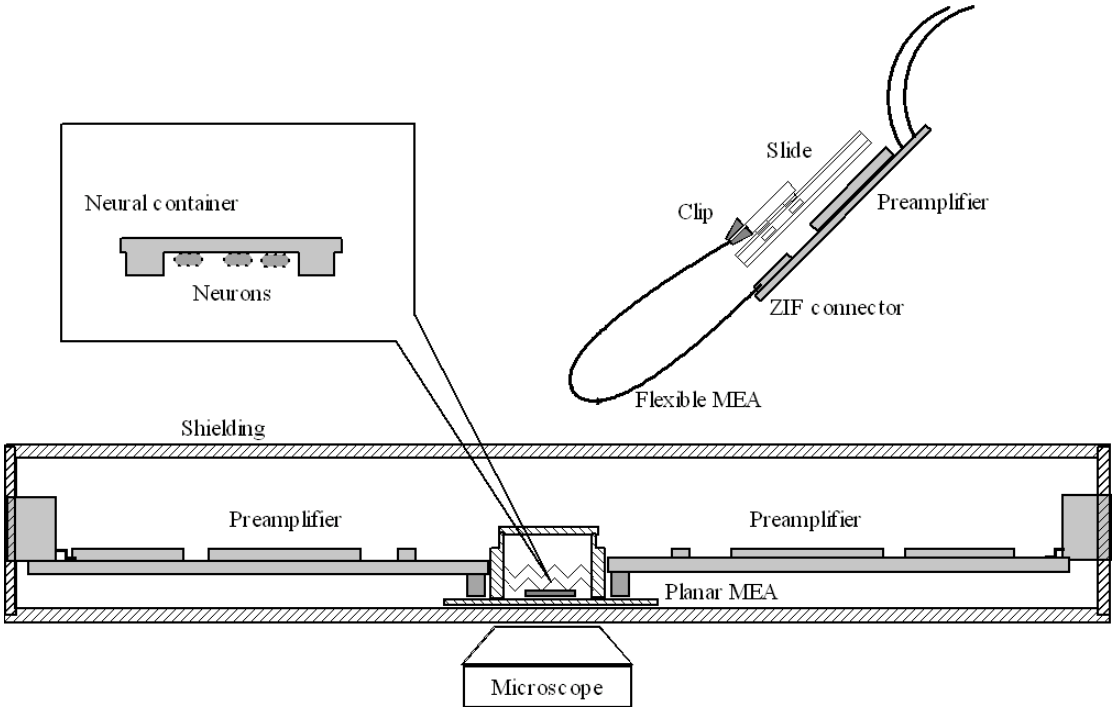

Figure 2-1: Schematic of the planar MEA and flexible MEA system. They can record from the 'neural bathtub.'

2.1.1. pMEA system and 'neural bathtub'

The fabrication of planar microelectrode arrays (pMEA) employs photolithography, metal deposition and dry etching etc. A layer of Ti/Au on a glass substrate is wet etched to define the electrodes of the pMEA. Tips of electrodes are coated with platinum black. Except the tips and connecting pads, other area of pMEA is coated with insulating layer of SU-8 resist. (The methods of the fabrication is adapted from the recipe of Keith Mathieson et. al. 2003)

The electroplating process of platinum black is called platinization. The details of the platinization process is in step 4, section 2.2. Platinum black is often electroplated on microelectrodes to reduce the impedance of electrode. Platinum

black has porous structure and in black color. This porous structure increases its actual surface and reduce the impedance at its interface to medium.

Bottom surface of the neural container is patterned either with the patterns of grooves or a pattern of protein, so that the neurons are guided. It is fabricated by casting PDMS onto a die made in Silicon and then curing the PDMS. Neurons are cultured in medium in the container in an incubator. After one week or more, the container is transferred to pMEA system (and inverted) for recording. When recording begins, the neural container and the pMEA are aligned and assembled together as shown in **Figure 2-1**. The electrodes in the pMEA are connected to a custom preamplifier. The spontaneous signal from the neurons is amplified and sent through an A/D converter to a computer. The preamplifier is made on a PCB (printed circuit board). There is a shielding enclosure around the central part of the assembly.

2.1.2. FlexMEA system

The flexible MEA system has its own custom MEA and preamplifier, but shares the same A/D converter and computer. The flexible MEA is made on a polyimide film substrate (Kapton HN® polyimide). The procedures (the procedures is modified from those of an original flexible MEA derived by M. Sandison et. al., 2002.) used for metal evaporation, pattern definition, the coating of the insulation and the platinization of the electrode are similar in principle to that used for the pMEA. Surface treating of the substrate is required to enhance the metal adhesion. Photosensitive polyimide (PI2545 HD MicroSystems) instead of SU-8 is used as insulation to achieve flexibility.

This chapter describes the fabrication procedures of the pMEA (2.2), the flexible MEA (section 2.3), the neuron container (section 2.4) and the preamplifier (section 2.5). The dissection and culture protocol of rat cardiomyocytes (section 2.6) is also included.

2.2. Fabrication process of Planar MEA

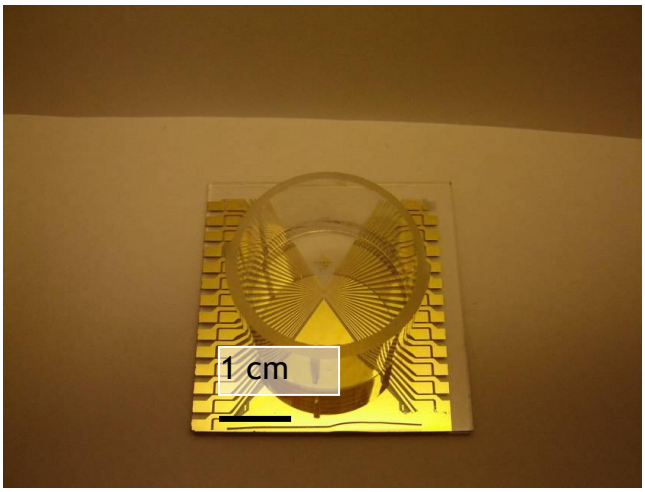

Figure 2-2: Home-made planar MEA. Glass substrate, Ti/Au conducting layer and double SU-8 2002 layer as insulation. 40mmX40mm size, 64 electrodes, integrated reference electrode (the triangular area) and 2.54mm grid double row pads.

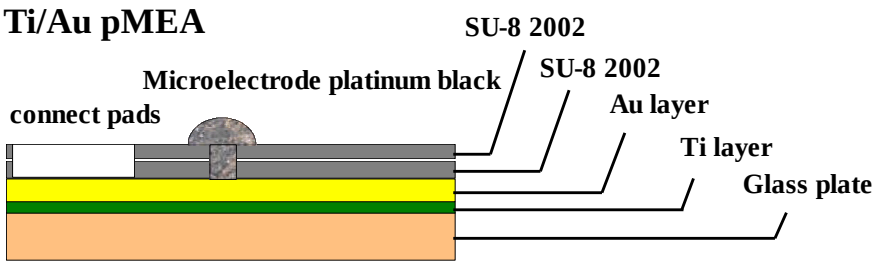

Figure 2-3: The schematic of the cross section of the Ti/Au pMEA.

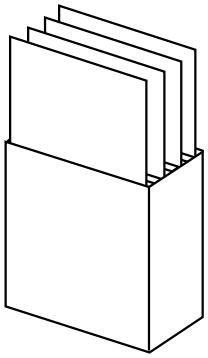

Figure 2-4: The sample shelf. It is capable of containing four glass slices. It makes batch fabrication of eight pMEAs (two pMEAs on one slice) possible and easier.

Step 1: Preparation and cleaning

- Mark one side of the glass slice with a diamond scriber. Metal deposition and the following fabrication works will be carried out on one side only. Care should be take to keep this working side clean.
- Clean the sample in an ultrasonic bath (100 Watt) for five minutes with each of the following: optoclear, acetone and methanol. After each stage rinse the sample with RO water. Finally, blow dry the sample.
- Bake the sample in oven at 100 ^{o}C for 15 minutes.

Step 2: Deposition and patterning of Ti/Au layer

- Deposit a layer of Ti/Au (30 nm Ti, 130 nm Au) in a Plassys MEB 450 Electron Beam Evaporator.
- Spin Shipley S1818 onto sample at 4000rpm for 30s. It is often found that the photoresist layer along the edge of the glass slice is thicker than it is in other area. The under-exposed photoresist will leave residues along the edges. Two measures are taken to settle this problem. First, the patterns is positioned in the middle of the glass slice and the edges of the glass slice is left empty without any pattern. Secondly, a post exposure is made to the sample, in which the central area is covered while leaving the edge uncovered. This increases the exposure dose along the edge making the photoresist there dissolvable in the subsequent developer step.
- Bake the sample in oven at 90 °C for 30 minutes. Alternatively bake them on a hotplate at 90 °C for 5 minutes. However bear in mind, according to observation, hotplate baking often yields poorer quality.
- Let the sample cool down to room temperature.
- Load the light-field mask onto the mask aligner (SUSS MicroTec MA6) and expose sample to UV light for 5 seconds (200 Watt Hg)

Figure 2-5: The photo of the Mask aligner 'SUSS MicroTec MA6'.

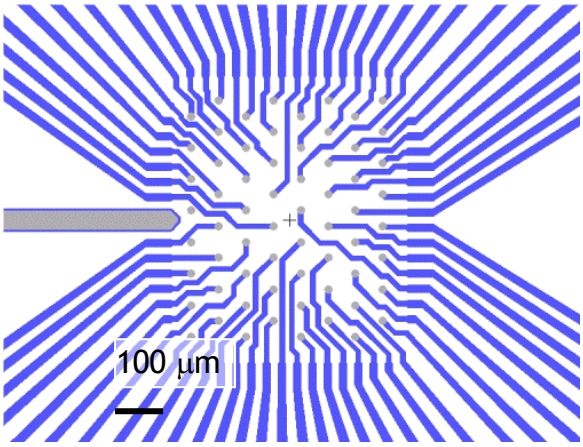

Figure 2-6: Mask pattern. The blue area defines the pattern of the Ti/Au layer. The grey parts show the electrode tips.

- Develop the sample in Microposit® concentrate(Standard ammonium hydroxide phosphate developer for positive resists): RO water (1:1) for 60 seconds.

- Wet etch the gold layer with standard gold etch solution ($KI:I_2:H_2O$ = 4 g:1 g:25 ml) for 50 seconds.
- Wet etch the Titanium layer with standard Titanium etch solution ($HF:H_2O$ = 1:20) for 10 s. The etch time of titanium is short and hence sample should be closely watched. Remove the sample out of the etching solution and rinse it in RO water soon after silver-gray color is faded totally.
- Remove the remaining photoresist by exposing the whole sample to UV light for 30 s and develop thoroughly.
- Small amount of residues may still remains. To remove them, bath the sample in Acetone at 55 ^oC for 10 mins. Then rinse it in IPA. And finally rinse it in RO water.

Step 3:Creating the insulating layer and vias

- The insulating layer is made of two layers of SU-8 2002. Each is about 2 μm thick. Double layer design is to ensure good insulation. However, one version of pMEA with single layer of SU-8 also shows good insulation and works well in the recording. Therefore choice can be made to omit the second layer SU-8. Thick insulating layer also decrease the stray capacitance between wire and medium of the neural culture. This helps to minimize the noise. Refer to Chapter 6.
- Spin on SU-8 2002 at 1000rpm, acceleration of 200 rpm/s^2, for 20 s. (slow acceleration and short spin time lead to less coating irregularities)
- Bake on hotplate from 60 ^oC–95 ^oC –60 ^oC for 20 mins
- Repeat the spinning and soft bake to coat the second layer.
- Expose for 15 s on MA6 with light field mask.
- Bake on hotplate from 60 ^oC –95 ^oC –60 ^oC for 20 mins
- Develop the sample in EC-solvent for 120 s. Keep agitating.
- Rinse in IPA. Blow dry.
- Investigate the result. Further ultrasonic bath develop may need if the vias are not clearly seen under microscope. Immerge the sample in EC-solvent in a plastic beaker and ultrasonic bath (100 Watt) them for 1 min.
- If the vias are still covered with a layer of SU-8, it is very likely that the sample did not in close contact with the mask in the exposure step. The contact problem is often caused by the raised SU-8 layer around the edges of the sample. A longer period of soft baking helps obtaining the uniform thickness over the SU-8 layer.
- Post bake, at 150^oC for 30 mins.
- Even looks clean under microscope, SU-8 often leave residues in the tips of the electrodes and the area of the connecting pads. The residue is cleaned thoroughly using an Oxford Plasmatech BP80 RIE (reactive ion etching) machine with the following recipe:
- 50% O_2 / 50% CF_4, 5 mins, 15 SCCM O_2, 15 SCCM CF_4, pressure: 20-30 mTorr, power: 50 W.

Step 4: Platinising the electrodes

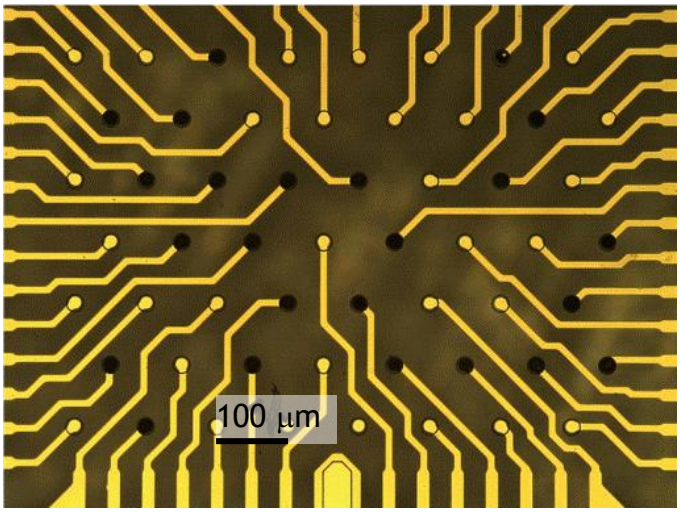

Figure 2-7: The 64 electrodes on a pMEA. The comparison of the platinized electrodes and the un-platinized ones. The square at the central bottom is the un-platinized reference electrode.

Platinization uses conventional electroplating techniques. The electrodes are connected to the negative output of a current power supply as the cathode. A platinum wire is used as the anode. The composition of the platinizing solution is 1% platinum chloride, 0.08% lead acetate and 98.92% RO water. The lead acetate improves the adherence of the platinum deposition. A drop of platinizing solution is dripped onto the sample in the region of the electrodes. A Platinum wire is placed in the droplet as the anode. The microelectrodes are connected with a connecting board (**Figure 2-8**) to the negative output of a current source as the cathode. Cathode, anode, electrolyte and the current source form a complete circuit.

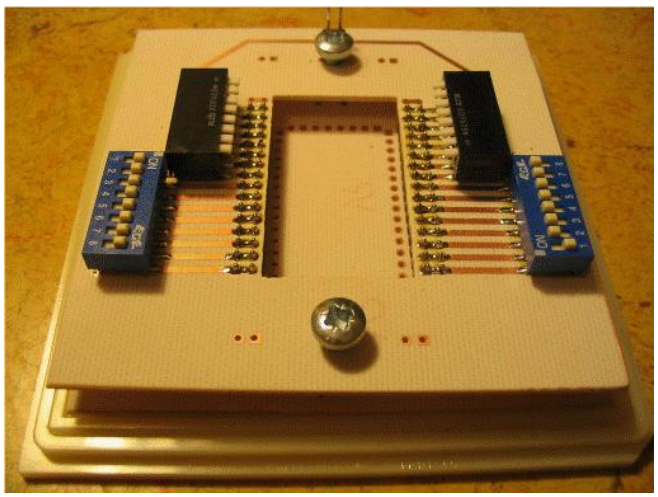

Figure 2-8: Connecting board with switch array. It connects MEA to current power supply in platinization.

The structure of the platinized surface depends strongly on the platinization conditions, particularly the concentration of the solution and the current density

used. At low current density, the formation of the platinum black deposition does not occur, whereas very high current density causes bubbles. The optimum current density may varys a little for different pMEAs. So current density need to be carefully adjusted to get a satisfactory platinization. According to experience, current density setting may vary between 4 nA/μm^2 to 15 nA/μm^2. Set the current source at 4nA/μm^2 at the beginning of the platinization. Observe the tips of the electrodes under a microscope. Their color will change from golden to gray, indicating an electroplating under low current density. Ramp up the current source slowly. When current density raised to a certain point, black color will suddenly appears around the edges of the electrodes. This is the deposition of platinum black occurring. The reason of the platinization begins at the edge may due to the higher current density there (M. Schuettler et. al., 2002). Keep ramping the current till platinum black covers the central area of the electrodes too. Count 10 seconds and switch off the current source.

2.3. The fabrication of the transparent pMEA (ITO pMEA)

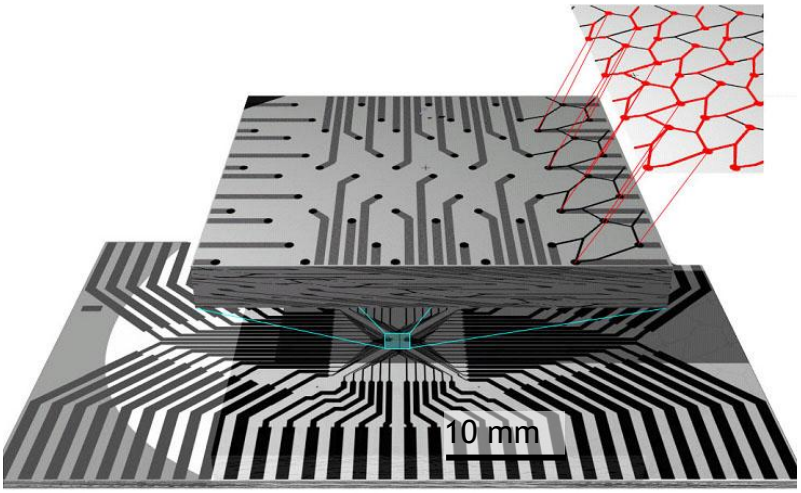

Figure 2-9: The ITO pMEA. The red lines are trying to show that the layout of electrodes corresponds to Jude pattern.

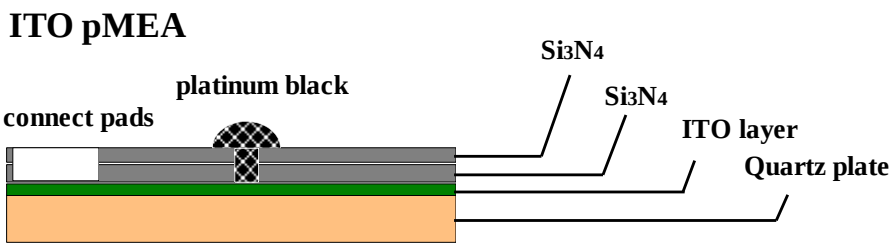

Figure 2-10: The schematic of the cross section of the ITO pMEA

This ITO (Indium tin oxide, or tin-doped indium oxide)microelectrode is patterned

on a transparent quartz plate and insulated by a layer of silicon nitride (Si_3N_4). Both of these material are transparent. This is especially designed for the convenience of the neural network study, avoid obstructing the observation during the recording. The layout of the top of the microelectrode in order to match them to the position of the neurons cultured in the guidance of the Jude pattern (a tiling pattern of the grooves in which neurons are grown). In this way, the electrical signal from each of the neurons in the network could be collected.

Fabrication of ITO pMEA

This procedure of fabrication was developed in the Physics Department for retinal cells by Keith Mathieson.

Quartz/ITO plate

Two different plates with an ITO layer of 300 μm or 150 μm thick each. The former one has a 75-85% transparency and a 13 ohms/square sheet resistance. The latter one has a 95% transparency and a 30 ohms/square sheet resistance.

Fabricating the ITO conducting wire

Photo lithography of photoresist S1818 is used as the mask for the dry etching of the ITO layer. Keith found that 5 minutes post-bake is enough to make S1818 an effective CH_4/H_2 mask and can be removed easily afterward. Longer post-bake will make S1818 difficult to be removed.

CH_4/H_2 was used in an Eletrotech ET340 with a rf power 100W, a pressure of 11 mTorr and a flow rate of 5/25 sccm CH_4/H_2. CH_4/H_2 etch rate on Eletrotech ET340 is about 25nm/min.

Insulating layer

A 500nm low stress Si_3N_4 layer is deposited to isolate and protect the ITO wires underneath. This deposition procedure is divided into two parts, 250 nm at each time. This measure is aimed to reduce the amount of the micro-pores penetrating the Si_3N_4 layer.

Silicon nitride patterning

Masking is the same photolithography method discussed already. S100 SF6 dry etch

is used for patterning Si_3N_4. The recipe is as following: 5 mins; flow rate 10 SCCM; etch pressure: open valve; power: 120W.

Cutting the electrode plate

Then the plate is cut into proper size using the Buehler Isomet 5000 saw.

Platinisation

At the final step, electrodes are coated with platinum black. This could greatly increase the actual surface of the electrode and hence minimize the electrode/medium interface impedance, which is important for collecting signal from cell.

2.4. Fabrication process of FlexMEA

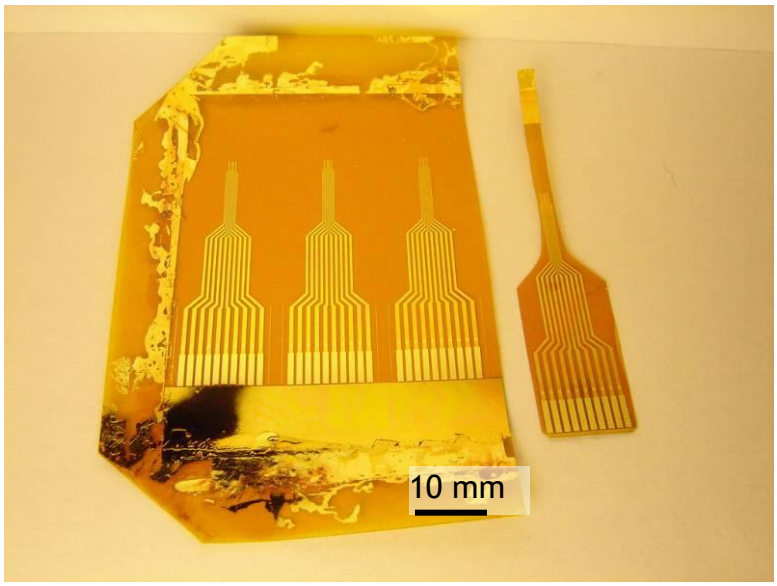

Figure 2-11: Photo of the flexible MEA. Left is three arrays on one piece of polyimide film. A finished array is on the right side. A segment of the film beyond the top of the electrodes is left without crop. This extra segement will help the array to curve like the bottom of a boat when the array is installed.

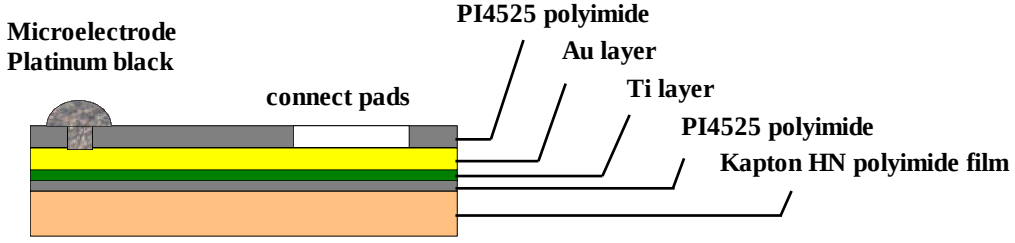

Figure 2-12: Schematic of the cross section of the FlexMEA.

The fabrication of this flexible MEA was first derived by Mary Sandison (M. Sandison

et. al., 2002.). Some modifications were made to the fabrication procedures after that. Thickness of the polyimide film is reduced from 150μm to 50μm for more flexibility and better transparency. Layout of the electrodes is changed to be compatible with the pattern of the neural network. The arrangement of the connecting pads is adapted to fit the ZIF connector.

Step 1: Cutting and Cleaning

Cut Kapton HN® polyimide film (50 μm thick) into a rectangle shape so that it fits in a chuck (**Figure 2-13**). that is approximately 5×5 cm. Snip off four of the corners. The chuck keeps the polyimide film flat through the fabrication procedures. Put the sample in the chuck and clamp with the clip.

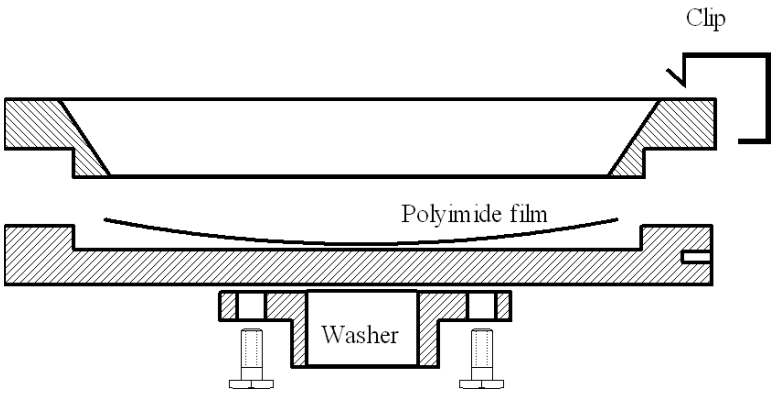

Figure 2-13: Cross section of the chuck. Washer on the bottom can be separated to avoid baking in the oven.

- Clean the sample in an ultrasonic bath for five minutes with each of the following: Optoclear; Methanol; Methanol again. After each stage rinse the sample with RO water. Finally, blow dry the sample with care taken not to crease or ruin the thin Kapton polyimide film.
- Clamp the sample in chuck and remove the washer. The washer contains plastic part which shall avoid baking. Place the sample in a oven at 100 ^{o}C for 15 minutes to dry the sample thoroughly. Take the sample out of the oven and let it cool in air. Keep the sample in the chuck for the next processes. Install washer back onto the chuck.

Step 2: Embeding polyimide layer

- Install the chuck to a photoresist spinner by insert the spindle of the spinner into the washer. Pour photosensitive polyimide PI2545 (HD MicroSystems) into a beaker and wait for it to warm to room temperature. Pour PI2545 on the sample and distribute it evenly with a plastic rod. Take care not to make air bubbles.
- Spin PI2545 as follows:
- 500 rpm for 5 seconds.
- Accelerate to 2000 rpm in10 seconds
- 2000 rpm for 30 seconds

- Decelerate in 10 seconds to stop the spinner.
- Stop the spinner with slow deceleration as the force caused by sudden stop of the steel made chuck may damage the sample.
- Leave the sample in the chuck. Unscrew and remove the washer on the bottom of the chuck. As the washer is made of plastic and should avoid heating.
- Bake the sample as follows in oven:
- 100 °C for 60 mins,
- Ramp to 200 °C in15 mins,
- 200 °C for 30 mins,
- Ramp to 300 °C in 15 mins,
- 300 °C for 60 mins.
- Ramp to 90 °C in 15 mins and take it out.
- Let the sample to cool down to room temperature and remove it from the chuck.

Step 3: Oxygen plasma and deposition of Ti/Au layer

- The adhesion between polyimide and metal can be enhanced by 'changes the chemical state of the polyimide surface' (Y. Nakamura et. al., 1996)
- This is done by Oxygen plasma etching in Oxford Plasmatech BP80 RIE (reactive ion etching) machine as follows:
- O_2 for 3 minutes in pressure of 290 mTorr and power of 50 Watt.
- The metal layer of Ti/Au (30 nm Ti, 130 nm Au) should be deposited as soon as possible by a Plassys MEB 450 Electron Beam Evaporator.

Step 4: Patterning of Ti/Au layer

- Clamp the sample into the chuck in the same position as before by following the traces left from last clamping.
- Spin Shipley S1818 on sample in 4000 rpm for 30 s and decelerate the speed down to zero in 5 s in the end.
- Bake the sample with chuck (remember to remove the washer) in oven at 90 °C for 30 minutes. Alternatively bake them on a hotplate at 90 °C for 5 minutes.
- Let the sample cool down to room temperature and remove it from the chuck.
- Load light-field mask on mask aligner (SUSS MicroTec MA6 **Figure 2-5**) and expose sample to UV light for 5 seconds (200 Watt Hg)

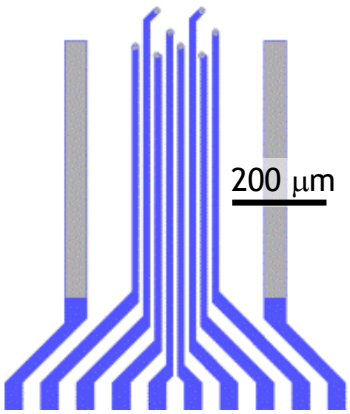

Figure 2-14: the pattern of the mask. The blue area defines the pattern of the Ti/Au layer. The grey circles are the tips of the electrodes. Two grey squares are the reference electrodes.

- Develop the sample in Microposit® concentrate(Standard ammonium hydroxide

phosphate developer for positive resists): RO water (1:1) for 60 seconds.

- Wet etch Gold layer with standard gold etch solution (KI : I_2 : H_2O = 4 g : 1 g : 25 ml) for 50 seconds.
- Wet etch the Titanium layer with standard Titanium etch solution (HF : H_2O = 1 : 20) for 10 s. The etch time of titanium is short and so the sample should be closely watched and removed from etching solution soon after silver-gray color is faded totally. Rinse the sample with RO water.
- Remove the remaining photoresist by exposing the whole sample in UV light for 30 s and develop thoroughly.

Step 5: Creating the insulating layer

- Clamp, oven dry and coat the sample with a layer of Photosensitive polyimide PI4525 as described in setp 2. The spinning procedure has some minor difference as follows, 500 rpm for 5 seconds; Accelerate to 6000 rpm in 10 seconds; 6000 rpm for 30 seconds;
- Decelerate to stop the spinner in 5 s.
- Bake the sample in oven at 100 ^oC for 60 minutes
- Spin photoresist Shipley S1818 and bake them in the routine same as described in step 4. It is better here to bake in an oven instead of on hotplate.
- Expose the sample with a dark-field mask for 5 seconds. Notice there are four arrays on sample, whereas only one set of via on mask. Each need one exposure and hence four times exposure totally. This extra labor is necessary to minimize the mismatch due to the distortion of Kapton film caused by strain forces.
- Develop the sample in Microposit® concentrate: RO water (1:1) for 75 seconds. The photoresist and the Photosensitive polyimide will both be developed.
- Complete the polyimide bake, as described in step 2, starting from the second stage.
- Remove remaining photoresist and polyimide with an oxygen-tetra fluoromethane plasma (90% O_2 ,10% CF_4) using Oxford Plasmatech BP80 RIE (reactive ion etching) machine under the following condition:
- 20 minutes, 50 Watt, 20-30 mTorr, 27 SCCM O_2, 3 SCCM CF_4

Step 6: Platinising the electrodes

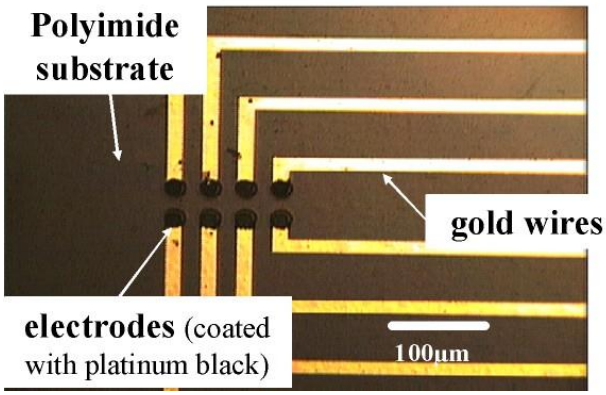

Figure 2-15: The platinized Flexible MEA under optical microscope.

The procedure is similar with that of the planar MEA (section 2.1, step 4). The only difference is that different connecting board is used here.

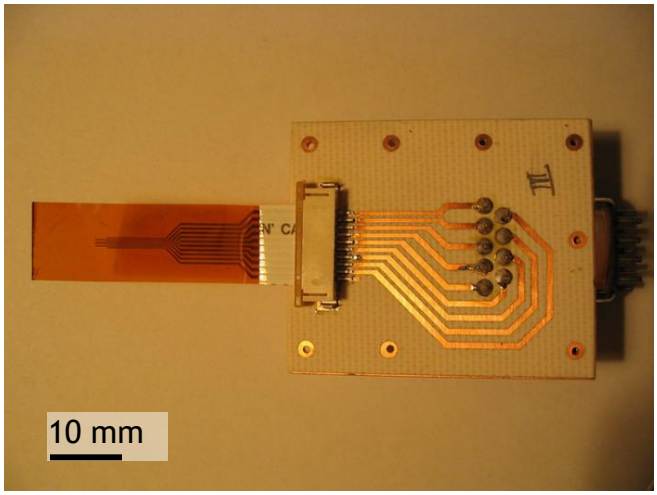

Figure 2-16: One FlexMEA was assembled with the ZIF connector.

2.5. Fabrication of the neuron container ('neural bathtub')

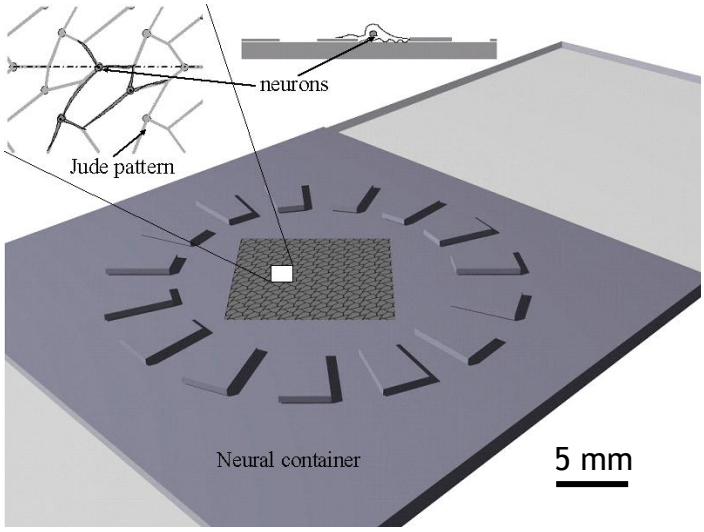

Figure 2-17: Schematic pictures of the neural container (neural bathtub). The pattern is grooves here in this graph. Actually it can be either topographic or chemical, i.e. protein traces.

Neural container (neural bathtub) is an important part of the neural chip recording system. Its purpose is to provide neurons a substrate to grow in a guided way (**Figure 2-18**). And the neural container makes it possible for the cultured neural network to be assembled to the pMEA for recording.

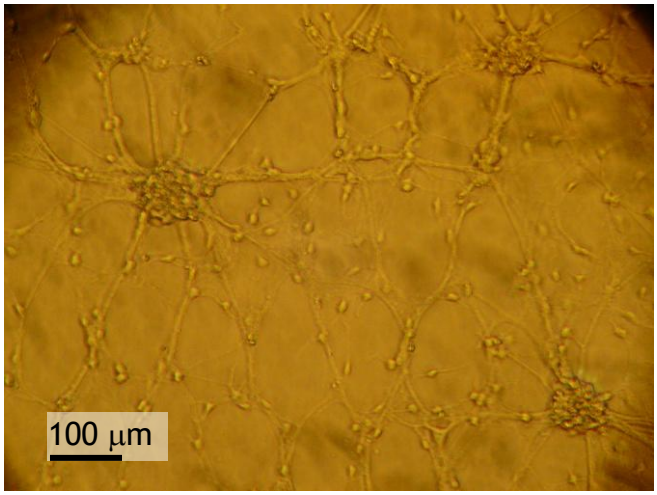

Figure 2-18: The microscope photo of the neural network cultured in 'bathtub' by Alison Beatie. The nerve cells are guided by the protein patterned on the 'bathtub'. The similarity of the neural network with Jude pattern shows that the connection of cells are well guided.

The neural container is a 3D structure made of PDMS. Radial arranged bumps will give the neural container support and prevent neurons from being squeezed when it assembles to the pMEA. . The height of these bumps (15 μm) also ensures the neurons close enough to electrodes making the signal detection possible. The central part of the neural container is patterned either with the patterns of grooves or a pattern of protein, so that the neurons are guided. These tiling patterns is called Jude pattern. Another similar pattern is called Judith pattern. The difference between these two pattern is in the angle of the grooves. Judith pattern has symmetric hexagons. Ideally neurons will grow along the pattern to form a specific network.

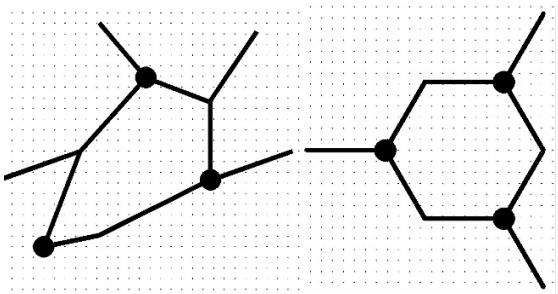

Figure 2-19: The Jude pattern and Judith pattern on the mask used in photolithography.

Different methods to fabricate the neural container were investigated. Embossing using a mould was considered in the first place as it has many advantages, e.g. mass production. Silicon was the material first tried to make the mold. Silicon mold can be fabricated with photolithography and dry etching techniques. Embossing to PMMA plate with Silicon mold under different temperature and pressure were tested. Difficulties were met during the embossing and release steps

and the efforts to solve them failed. (the detail is in setion 3.5)

After the Silicon/PMMA combination, Nickel/PMMA was investigated and gave better results. The Nickel mold is not fabricated in our lab but in a CD (compact disk) factory using the techniques of CD fabrication.

Due to the inconveniences of fabricating mold out of our lab, we investigated Silicon/PDMS combination alternatively. This method is the one we are using at present. As well as fulfilling all the functions needed for neural container, PDMS turns out to have another advantage -- oxygen diffusion control. PDMS is oxygen permeable. By vary the thickness of the bottom of the PDMS container, the oxygen concentration inside the container can be controlled more or less. (the oxygen control is described in detail at chapter 5)

2.5.1. Fabrication process of Silicon mold

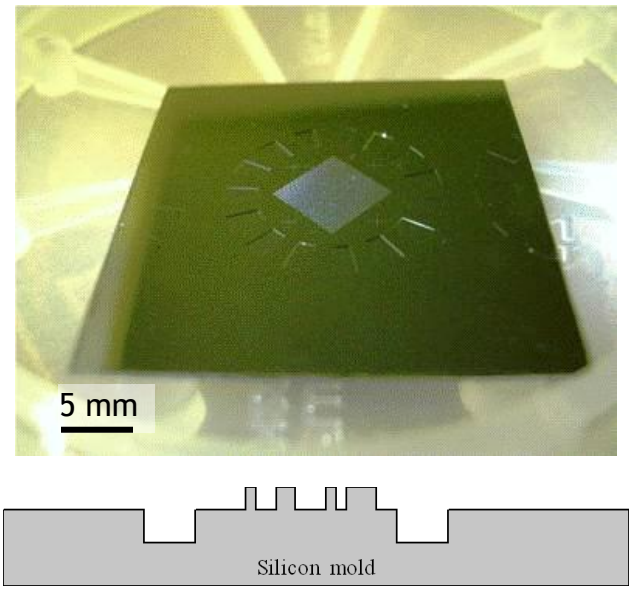

Figure 2-20: The photo and the schematics of the silicon mold for embossing of neural container.

The Silicon mold has inverse structure of the cell container. It is made by a two step dry etching process.

Step 1:Cleaning and photolithography

- Clean four inch silicon wafer in standard procedure. Ultrasonic bath wafer in optoclear, acetone and methanol for five minutes. After each stage, rinse wafer with RO water and blow dry in the end.
- Bake the wafer in oven at 100 ^{o}C for 15 minutes.
- Spin Shipley S1818 on sample in 4000 rpm for 30 s.
- Bake the sample in oven at 90 ^{o}C for 30 minutes. Alternatively bake them on a

hotplate at 90 ^{o}C for 5 minutes.
- Let the sample to cool down to room temperature.
- Load Jude pattern mask on mask aligner (SUSS MicroTec MA6) and expose sample to UV light for 5 seconds (200 Watt Hg)
- Develop the sample in Microposit® concentrate(Standard ammonium hydroxide phosphate developer for positive resists): RO water (1:1) for 60 seconds.

Step 2:Dry etching

Dry etch wafer with recipe RYT1 in ICP (Inductively Coupled Plasma) for seven minutes. This obtains five micron height Jude pattern in form of ridges.

Recipe specifics of RYT1:

Flow rate: C_4F_8/SF_6 = 50 sccm/40 sccm
Chamber pressure: 10 mTorr
Table temperature: 20 ^{o}C
Coil Power/platen power: 600 W/10 W
Process time: 5 µm/7 mins
DC self bias: 610 V

Step 3:Cleaning and photolithography II

- Clean wafer with Ultrasonic bath in acetone for five minutes. Rinse with Ro water.
- Piranha clean wafer to remove remains of the photoresist. Sulfuric acid and hydrogen peroxide in 7:1. Rinse in RO water and blow dry in the end.
- Bake the wafer in oven at 100 ^{o}C for 15 minutes.
- Spin Shipley AZ4562 on sample in 4000 rpm for 30 s.
- Bake the sample in oven at 90 ^{o}C for 30 minutes. Alternatively bake them on a hotplate at 90 ^{o}C for 5 minutes.
- Let the sample to cool down to room temperature.
- Load bathtub pattern mask on mask aligner (SUSS MicroTec MA6) and expose sample to UV light for 5 seconds (200W Hg)
- Develop the sample in Microposit® concentrate(Standard ammonium hydroxide phosphate developer for positive resists): RO water (1:1) for 60 seconds.

Step 4:Dry etching II

- Dry etch wafer with recipe RYT1 in ICP for seven minutes. This gives five micron deep bathtub pattern (the radial arranged bumps).

Step 5:Final cleaning

- Clean wafer with Ultrasonic bath in acetone for five minutes. Rinse with Ro water. Piranha clean wafer to remove remains the photoresist. Sulfuric acid and hydrogen peroxide in 7:1. Rinse in RO water and blow dry in the end.

Imprint from silicon mold to PDMS

- Mix up Sylgard 184 PDMS in a universal bottle with curing agent to base ratio of 1:9. Increasing the percentage of curing agent creates more crosslinking and makes PDMS more rigid.
- Place the universal bottle under low pressure created by flowing water (this homemade tool is located in our lab) for half hour to degas the PDMS.
- Put the washer surrounding the feature site. The washer is used to support the glass slice later. The thickness of the PDMS can be changed by varying the height of the washer.
- Pour the PDMS on the feature site of the silicon mold. Cover the PDMS with glass slice. (**Figure 2-21**)
- Place the assembly on an hotplate at 120° C to cure the PDMS for one hour.
- Remove the assembly and allow it to cool to room temperature.
- Peal off the cured PDMS from the Silicon mold carefully with a plastic tweezers.
- Get rid of the excess PDMS with a apple puncher. The apple puncher is a brass tube with sharp edge. The sharp edge cut off the PDMS outside of the tube and gives us a circular neural container.

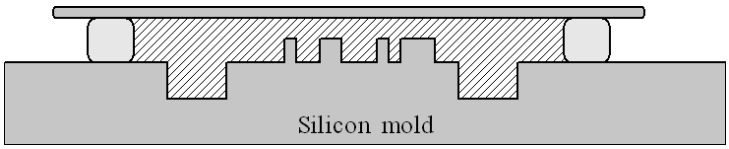

Figure 2-21: Silicon mold is on the bottom. The washer supports the glass slice on the top. PDMS is between the Silicon mold and the glass slice. The pattern on the silicon mold is transferred to the PDMS structure.

2.6. The fabrication procedure of the PCB

First step：Produce the mask with the help of Cadence® OrCAD®.

Input the designed schematic circuit diagram into OrCAD. The symbol protocols of OrCAD is slightly different with the hand drawing. OrCAD produces the layout mask from the circuit. The automatically generated layout of parts and routes need manual adjustment. The drawing of the finished mask is followed. The details of using OrCAD can be easily found elsewhere and not listed here.

The PCB factories usually need photo plot and drilling files. These files take control of photo copying and hole drilling. The formats of these files are: aperture file (*.APT), Gerber file (*.G) and drilling file (*.DRR). The PCBs in this project are made by the electrical workshop in own department. The photo plot files are not required. A printed mask (**Figure 2-22**) takes place these files.

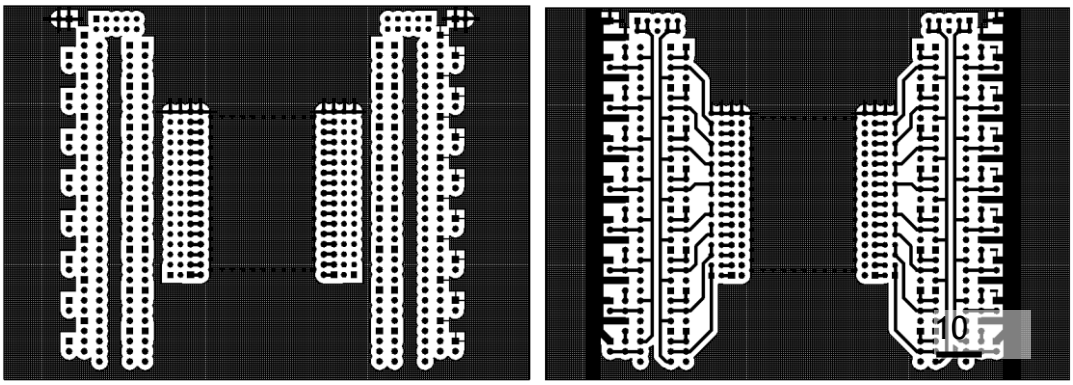

Figure 2-22: The mask of the PCB layout. Left: top side of PCB; Right: bottom side.

The above is the mask of the PCB designed for pMEA system. This is a double-sided PCB. The white area is transparent to UV light and the copper covered on the corresponding area will be etched away. The photoresist corresponding to the black areas will be exposed and the copper be remained. The remaining copper forms the routes, pads and ground plane of large area.

In order to build with the limited resources, the PCB compromises in its design. The fine and compact layout is avoid to prevent from the possible errors during the fabrication procedure, e.g., broken and misalignment. Manual operation or working with low precision equipment, e.g. the drilling machine or the manual alignment of the two masks, may cause errors. There are also troubles with printing the masks using office laser printer on papery substrate. The paper may distort under the heat from the laser printer. In considering of these limits, the design chooses thicker wires and sparse wiring distribution. The separated circuit parts are chosen instead of smaller SMD (surface mounting devices) parts. These measures also reduce cross talk and make the soldering easier.

The layout design needs taking a lot of factors into consideration, e.g., connecting the MEA, reducing the noise, shielding and grounding. The details will be described in chapter three.

Second step：Printing of the PCB mask with laser printer

The resolution needs at least 600 dpi. Switch off the toner saving option and set the toner to dense. Tracing paper proves to be the best substrate. The thickness is 90 gsm and the thicker the better due to the heat distortion problem. The superposition test is critical. Superimpose the two mask and check under a transmit lighting. Make sure every soldering pads overlaps. If there is a small

misalignment, sandwich them into a book and press with weight for a while. If there is no improvement, another printer or a thicker tracing paper may be required.

Inkjet printer and clear acetate have been tried and render poor results. The UV(ultra-violet) light seems penetrates the ink and the acetate blurs the profiles of the image.

Third step：location hole and drilling file

There are two holes designed at the top and left of the mask. They are used to locate the PCB before drilling. The drilling is done with a programmed drill machine. The operator fixes the PCB on the machine with the guidance of these location holes. The rest is finished by the machine with the data provided by the drilling file. The drilling files are in text format. They are basically the coordinates and the sizes of the holes. The unit of the data is mil (thou).

Fourth step：Works by the electrical workshop

The mask and the drilling files are taking over by the stuff in the electrical workshop. Thanks to Stuard. He did all the works of exposing, developing, etching, cleaning, drilling and polishing. The brief description of these processes is followed:

The material of the PCB is a pre-coated positive photoresist fiberglass board (FR4). The whole procedure needs no dark room. Just avoid direct sunlight and develop immediately after the exposure.

Exposure

A UV(ultra-violet) exposure box is used. Sandwich the PCB inside the two masks with the toner sides facing each other. Align them up carefully.

Developing

Dip the exposed board into a tank filled with developer. The developer is the sodium metasilicate pentahydrate (Na_2SiO_3).

Etching

Clean the expose PCB and remove the remaining photoresist. Dip the board into a

tank to etch. The medium is kept at a temperature and agitated.

Clean

Remove the rest of the photoresist and polish the board.

Drilling

Mount the drilling file and fix the board to the drill machine for drilling.

Last step：Assemble the parts

The PCB of the pMEA needs cutting a rectangular hole in the center. The PCB of the FlexMEA needs cutting also. Install all parts, e.g., plugs, connectors, op amplifiers, resistors and capacitors. The parts are designed to be plug and removed easily in order to modulate or reuse. The function can be adjusted by changing the parts, e.g., varying the bandwidth by replacing a capacitor. This design compromises with the performance. A solid and compact PCB is better. Plugging may bring undesired problems, e.g., unpredictable interface resistance or bigger stray capacitance.

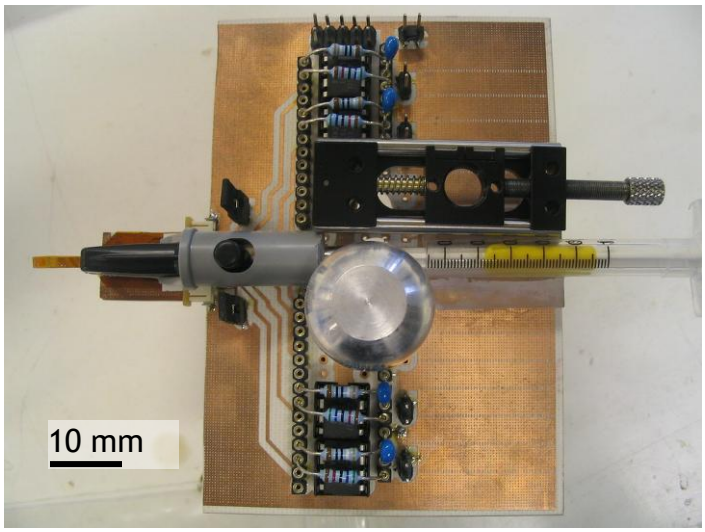

Figure 2-23: The photo of the pre-amplifier of FlexMEA. Electric parts have been assembled on the PCB.

2.7. Dissection and culture of the rat cardiomyocytes

Thanks Alison Beatie for teaching me the procedures.

Culture medium(Ham F10 or DMEM):

DMEM medium 194ml supplemented with FBS (or FCS) 20 ml, Antibiotics 5ml, ITS 2 ml and 7.5% bicabonate 3 ml.

Hams F10 medium can replace DMEM.

Hams F10 174 ml supplemented with RO water 20 ml, FBS (or FCS) 20 ml, Antibiotics 5 ml, ITS 2 ml and 7.5% bicabonate 3 ml.

Digestion medium (Papain or Trypsin):

Add 0.4 ml Papain or 0.4 ml Trypsin to 5 ml HEPES saline.

Dissection medium:

Calcium and magnesium-free PBS.

Steps:

1. Culture medium and digestion medium are pre-warmed to 37°C in hot bath. Dissection medium is stored in a glass plate on a ice block (a iron block kept cool in refrigerator) to keep ice-cold.

2. Sacrifice 1-3 day old neonatal rats and isolate hearts from them. Store the

excised hearts in the calcium and magnesium-free PBS on the ice block.

3. Squeeze the heart gently with a forceps to expel the blood from the lumen of the heart. Remove the atria and the vascular of the heart. Transfer the ventricle of the heart into a dry dissection plate.

4. Chop the ventricle of the heart into small pieces with a scalpel blade.

5. Collect tissue fragments with a 10ml pipette and transfer them into warm digestion medium in a universal tube. Shake it gently with a stirrer in the hot room (temperature kept at 37°C).

6. Truturate the tissue gently to break down the big pieces. Add in 5ml 20% FBS with hepes saline to stop digestion.

7. Centrifuge the cell suspension for 5 minutes in 1500 rpm, Discard supernatant and collect the separated cells with a 10 ml pipette. Re-suspend cells in 2 ml warm culture medium and plate cells in high density to culture wells or PDMS cell container.

8. Incubate cells in hot room (37 °C / 5% CO_2).

9. Add in more fresh culture medium after one hour.

10. Incubate cells in hot room (37 °C / 5% CO_2).

Chapter 3.Design and Optimization

3.1. Introduction

The project has a lot of home-made device, for example, the MEA systems. The fabrication methods have been described in previous chapter. This chapter is about why these methods were used, as well as the purpose of the design and the process of modification. Many manufacturing methods drew experiences from other researchers (Keith Mathesion, Mary Sandison) and were improved in account of the specific requirements of this project.

It starts at the FlexMEA. The ways of bending and the gradually improved design are descrided. The design of pMEA is followed, then to the design of the 'neural bathtub' (section 3.5). How different approaches were tried to overcome the thermal expansion and separation difficulties in the process of imprint. Different formulas of dry etching of the silicon mold are described. We tried different Jude patterns to compare the growth of neurons on them in order to find the best pattern for culturing neural network. Finally it is the design of the preamplifier (section 3.8) including the circuit design, the power design, the grounding and shielding and the interface of MEA to PCB.

3.2. Ways to bend FlexMEA

Boiling water

From the initial design to the final realisation, the FlexMEA has experienced many changes. As all of the microelectrodes at the front of the MEA need to come into contact with the surface plane of the cell culture, the MEA has to be bent in some way (see fig 2.1). The first method used to insert the MEA into a custom made bending block while bent, immerse the lot in hot water (nearly boiling) for some time. In this way, the MEA is permanently bent.

This approach has shortcomings. The deformation is not stable. As time goes by, the MEA returns towards its original shape. Considerable initial over bending is needed to compensate for that. This increases the possibility of damaging the electrodes. Bending in this way is a delicate job needing precise adjustment. It is

very difficult to bend the MEA at just the right place and into the right angle with only one shot and no adjustment afterwards. The biggest problem is that the bending is destructive of the electrodes to some extent. Measurements before and after bending show a significant rise in the impedance of the electrodes. Not all the blame should go on the bending as experience shows that the impedance will continue to rise with the increasing time and use.

Much effort has been spent in trying to improve the bending process. It is better to platinise the electrodes after bending as so avoiding damage to the platinum black, but the bending can still damage the metal layer. Optimization on the design of the bending block was also tried. The following picture shows one of these improved designs.

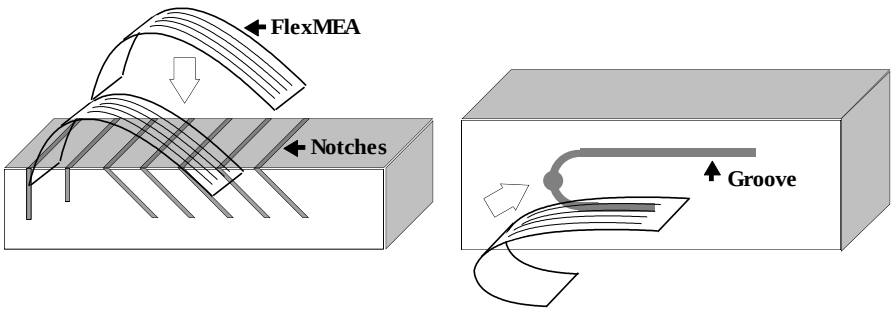

Figure 3-1: The one at left is the old design of the bending block. The one at right is the improved design. There are notches in the bending block in which FlexMEA is slotted and kept bended when it was in hot water

Given sufficient numbers of electrodes sacrificed on experiments (very wasteful behavior), the angle and position of the grooves in the bending block could be adjusted and optimized but before this optimization work was finished, a completely different bending method was devised.

Clip into position

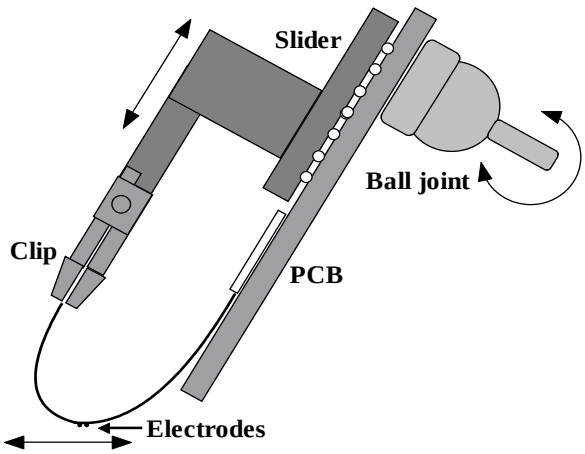

Figure 3-2: Schematic of the FlexMEA in its working position. The clip helps to bend the FlexMEA. The slider and ball joint can adjust its angle and position.

As shown Figure 3.2, the film is extended considerably before the site of the electrodes. It is clamped by a clip as shown. The middle part, where the electrodes are, is bent downwards. and get closer to the cells. The clip is fixed on a slide stage and can go forward and backward with precision. The PCB is connected to a micromanipulator with a ball joint and can rotate easily. The electrodes can be watched closely under the microscope to adjust the plane of the electrodes to be parallel to the plane of the cell container using the slider and ball joint. This approach proved very easy to adjust to get the ideal angle and position.

3.2.1. Reduce the thickness of FlexMEA

Although the original FlexMEA was reasonably flexible, cells were often injured after contact with the FlexMEA and many cells were scratched off the substrate. A softer FlexMEA was needed to reduce the damage. Therefore, a thinner substrate Kapton film was used. The thickness was reduced from the 150 μm to 50 μm. The modified FlexMEA is no thicker than common paper. However, although the new FlexMEA reduces the injury significantly, there is still some damage every now and then. Perhaps a thinner FlexMEA would better, but it would be very difficult to fabricate. Therefore, we decided to be satisfied with the improvements already made and not to push it any further. In fact, the cells are now very likely to survive from contact with the FlexMEA, if care is taken during the operation.

3.3. Other improvements made to FlexMEA

1. The head size of the electrodes of the FlexMEA is reduced to minimize the contact area with cells. The contact with FlexMEA is likely to cause death of cells. Less contact means fewer cells damage.

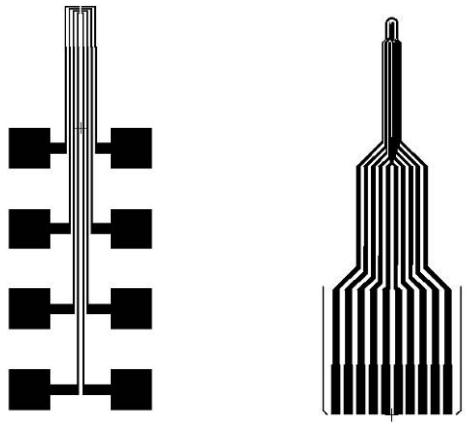

Figure 3-3: The mask of FlexMEA. The black region represents the pattern of metal layers. The one at left is the original design of FlexMEA [M. Sandison et. al., 2002]. The one at right is the improved design. Photos of the original FlexMEAs can be found in chapter 2 and chapter 4.

2. The length from the electrodes to the soldering pads was increased. The original FlexMEA requires two rows of huge soldering pads. The improved design needs only one row of small pads for the ZIF connector. This improved connecting method freed up valueable area and length for the bending.

3. The electrode layout was changed to be compatible with the layout of Jude pattern.

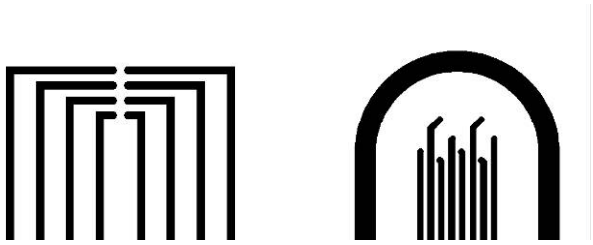

Figure 3-4: The close up view of the microelectrodes on the FlexMEAs of two different versions.

In figure 3.5 the drawing on left is the original design. The eight microelectrodes are put in two tidy rows. The one at right is the improved design. The eight microelectrodes are distributed corresponding to the layout of the nodes in Jude pattern. The arch structure is the integrated grounding electrode.

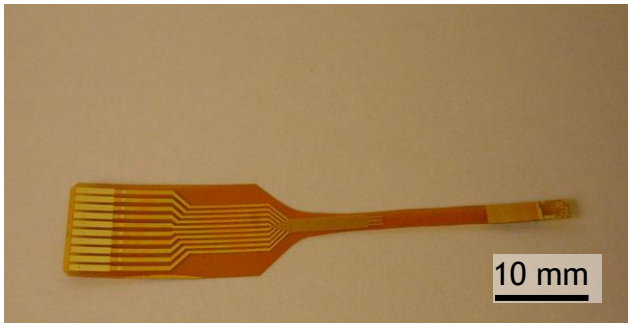

Figure 3-5: Photo of a FlexMEA.

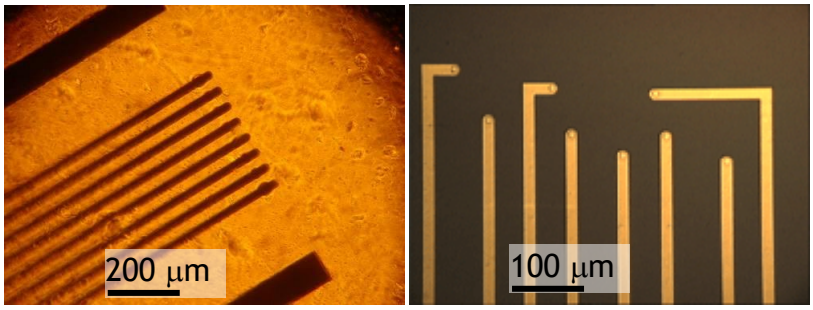

Figure 3-6: The FlexMEA under microscope. These are two different versions of FlexMEA. The one at left has the electrodes arranged in one row. The two thick lines are the integrated reference electrodes. The one at right side has its electrodes arranged according to the layout of the nodes in Jude pattern. The electrodes were not be platinised yet.

3.4. pMEA design change

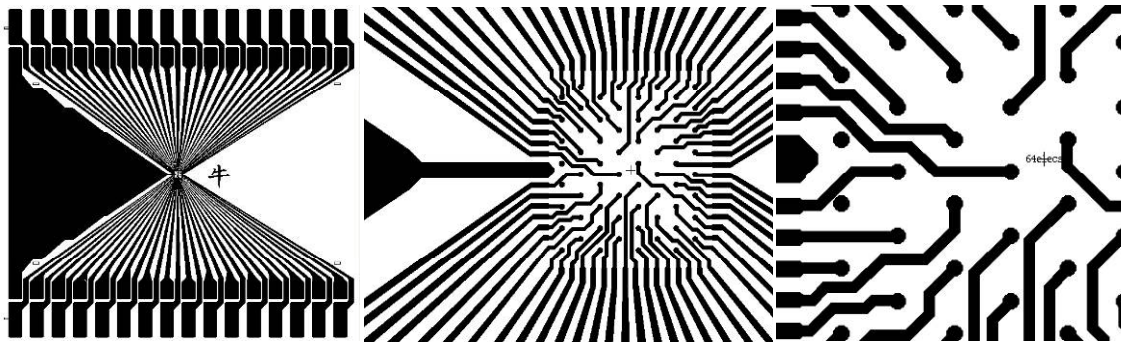

Figure 3-7: The mask of 40×35 mm pMEA. The width is adequate for the installation of glass ring of 20 mm diameter (culture well). The two rows of connecting pads are compatible with the 2.54 mm spacing of the spring-loaded pin connector.

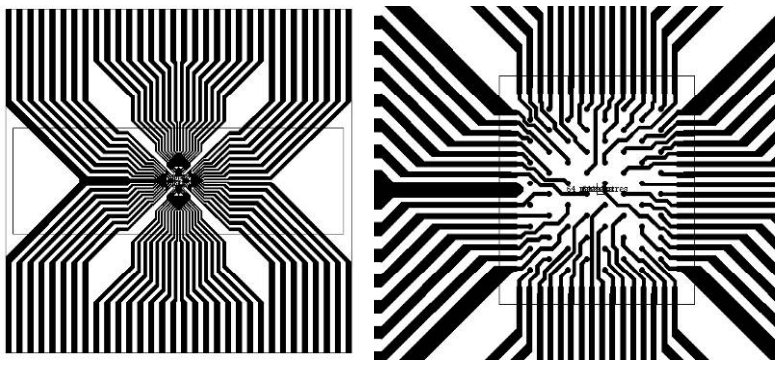

Figure 3-8: The mask of 40×40 mm pMEA. The width is adequate for the installation of glass ring of 20 mm diameter. The pads are compatible with both Z-axis connector and 1.25 mm pitch connector.

The planar MEAs used in this project are mainly based on two types of design. The materials used are entirely different. These two types of MEA are called here ITO pMEA and Ti / Au pMEA. The former one uses the quartz plate as its substrate, the ITO as the conductive layer and the Si_3N_4 as the insulating layer. All of these materials are transparent. One of its design goals is transparency. The ITO pMEAs are good from this point of view but have a long fabrication cycle, requiring two dry etching processes and two depositions of Si_3N_4. It is quite common that the fabrication of one batch of ITO pMEA takes weeks.

The Ti / Au pMEA is designed to cover the deficiencies of the former. Its design goal is mass production and to be transparent as possible in the meantime. The number of the MEAs consumed in the experiments is large. For example, the project used more than 100 pMEAs in year 2005. If all of these had been ITO pMEAs, it would have taken one full man-year on this fabrication work.

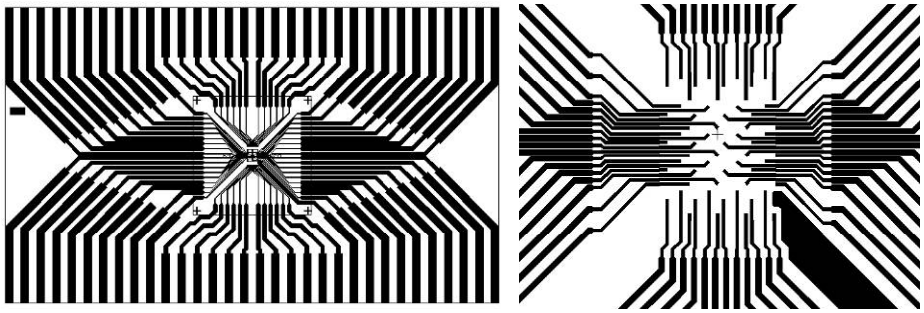

Figure 3-9: The mask of 40×23 mm pMEA. The original design was by Keith Mathieson. Both the plate size and pads spacing are compatible with the ITO pMEA by Keith. The width was not sufficient for the installment of glass ring. Therefore this newer version has an increased plate size. It uses a Z-axis connector.

The method of connecting the pMEA to the circuit has already been introduced in chapter 2. One method uses z-axis connector. The other method uses spring-loaded pin connector. The preamplifier made by Keith Mathieson team uses z-axis connector. Their preamplifier takes 40×23 mm pMEA. Our preamplifer integrates spring-loaded pin connector. Different versions of our preamplifiers take 40×40 mm, 40×35 mm and 40×23 mm pMEA.

The 40×35 mm pMEA in figure 3-9 has two rows of connecting pads. It is designed to connect with the spring-loaded connector. Multiple rows of pads support denser connecting and compact design. This is very important for the array integrating hundreds of electrodes, such as the 519 electrode arrays [Keith Mathieson, 2003]. Usually this type of MEA utilizes the so-called wire-bonding technology commonly used in IC package. But the wire-bonding is a permanent connection. It is not made to load or unload the MEA easily. If this needs to be improved, the spring-loaded connector is a good candidate. The Z-axis connector is insufficient for high-density MEA.

3.4.1. Biocompatibility of SU-8

The SU-8 is a negative, epoxy-type, near-UV photoresist based on EPON SU-8 epoxy resin. This photoresist can be as thick as 2 mm and have an aspect ratio >20 with standard contact lithography equipment. [Liu, J., 2004]

According to the publications of the neuroscientists working in electrophysiology, it seems that the biocompatibility of this material is good. They are widely used as the substrate for cell culture. The SU-8 here is used as insulating and protecting layer for our pMEA.

3.5. Design and optimization of the 'neural bathtub'

The container for the cells is an important part of the neural chip recording and stimulating system. A good way of making the neural chip is embossing. The details of fabrication can be found in chapter 2. A Silicon die, that has a structure that is reverse of that of the cell holder, is made first by dry etching. The PMMA cell holder is then made by embossing with this Silicon die.

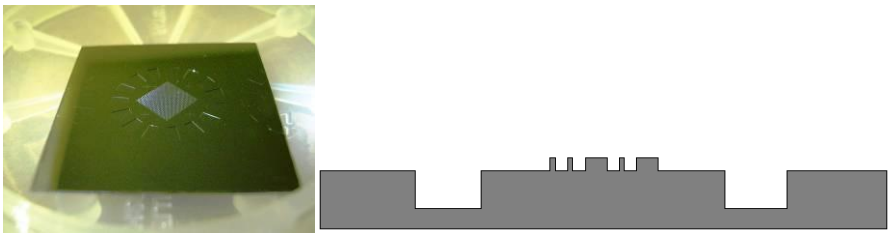

Figure 3-10: The Silicon die for embossing of 'neural bathtub'.

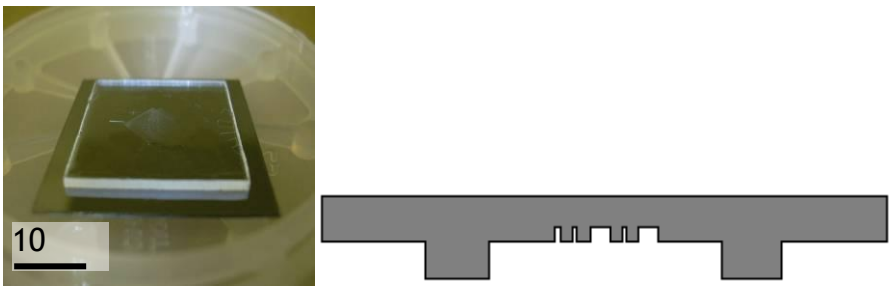

Figure 3-11: The 'neural bathtub' is a PMMA plate with Jude pattern and bathtub pattern embossed on.

This Silicon/PMMA technology has many problems in practice. An account of the efforts to solve these problems is given in the next section. In the end we decided to move to Nickel/PMMA embossing.

3.5.1. Different thermal expansion between Silicon and PMMA

The Silicon die is embossed into the PMMA plate at a relative high temperature around 170 ^{o}C. Then on cooling, both the Silicon die and the PMMA plate shrink towards their centers. Due to different coefficients of thermal expansion, PMMA shrinks more than Silicon. The PMMA in front of the Silicon sidewall is pushed, but the PMMA behind the Silicon sidewall stays put. It tries to push the Silicon sidewall

in front of it but since Silicon is solid and can not be pushed easily, the PMMA has no choice and has to follow the Silicon sidewall. All these make the radial features of the pattern on the PMMA wider.

The different thermal expansion rate between the Silicon die and PMMA makes the features of the pattern on the PMMA plate shift a certain distance towards its geometrical center.

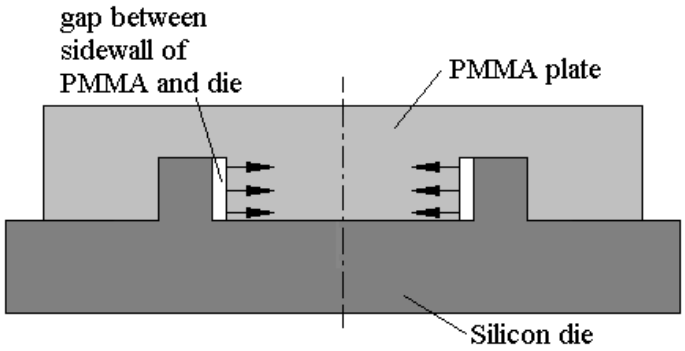

Figure 3-12: The thermal expansion of the Silicon wafer and the PMMA sample (will be 'neural bathtub').

The problem of differential thermal expansion may be solved by separating the die and PMMA at a relatively high temperature. Alternatively, Nickel instead of Silicon can be used as the material of the die. Nickel has a thermal expansion rate closer to that of PMMA.

3.5.2. Separation difficulty after embossing

For Jude pattern, there is difficulty in the separation of the Silicon die and PMMA plate. Small pieces of silicon are broken off and left in the PMMA due to the excess mechanical force that had to be applied during the separation.

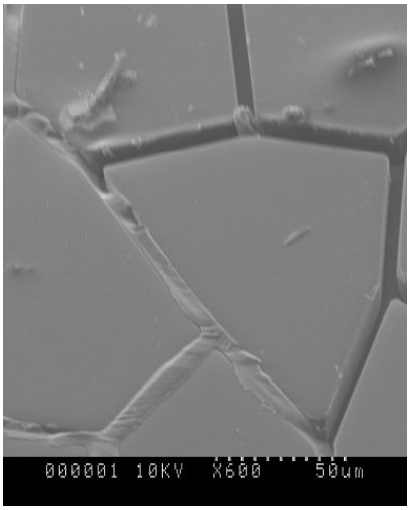

Figure 3-13: SEM picture shows silicon pieces in the grooves of 'neural bathtub' made of PMMA.

In order to solve this problem, a Teflon coating was applied to the surface of the silicon die. After that separation become much easier, but there are still some silicon pieces remaining in the PMMA plate.

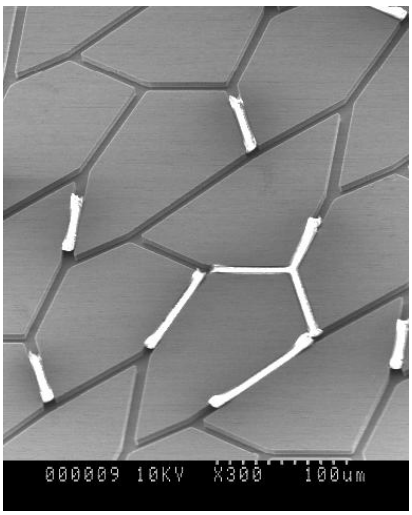

Figure 3-14: SEM picture shows small amount of PMMA pieces in the grooves of silicon mold.

We tried Nickel coating instead of Teflon coating then. A 200 nm thick layer of Nickel is sputtered on the surface of the silicon die. The result is good.

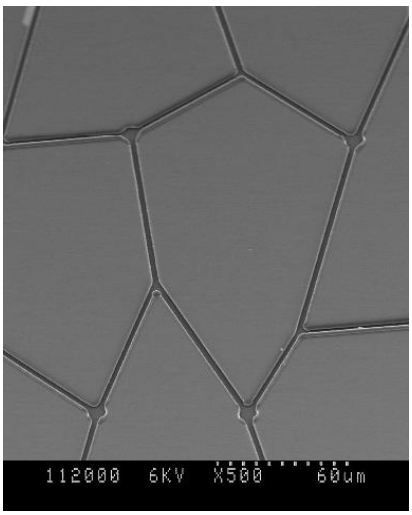

Figure 3-15: SEM picture shows clean and smooth surface of the PMMA 'neural bathtub' embossed from nickel mold.

3.5.3. How much is the expansion?

The linear expansion coefficient is defined by $a = (1 / l)(dl / dT)$

The coefficient of Silicon: $a = 2.8\times10^{-6}\ T^{-1}$;
Of PMMA: $a = 9.7\times10^{-6}\ T^{-1}$;
Nickel: $a = 13.4\times10^{-6}\ T^{-1}$
[Handbook.of.Chemistry.and.Physics, 2003]

The expansion of a material, having a coefficient of linear thermal expansion *a*,

when the temperature changes by ΔT is.$\Delta L = L_o\, a\, \Delta T$

where,
ΔL is the change of the length;
L_o is the length at the original temperature.

For the features at the edge (where the distortion is the biggest) of the Jude pattern on the PMMA plate, the distortion for feature 5 mm from the middle when the temperature decreases from $160\ ^oC$ to $90\ ^oC$ is $1.3\ \mu m$ as a for Si is $2.8 \times 10^{-6}\ T^{-1}$, while for PMMA ($a = 9.7 \times 10^{-6}$) the corresponding distortion is $4.4\ \mu m$, for Nickel ($a = 13.4 \times 10^{-6}$) the corresponding distortion is $6\ \mu m$.

Hence, the expansion difference between Si and PMMA is $4.365 - 1.26 = 3.105\ (\mu m)$ at the edge of the Jude pattern.

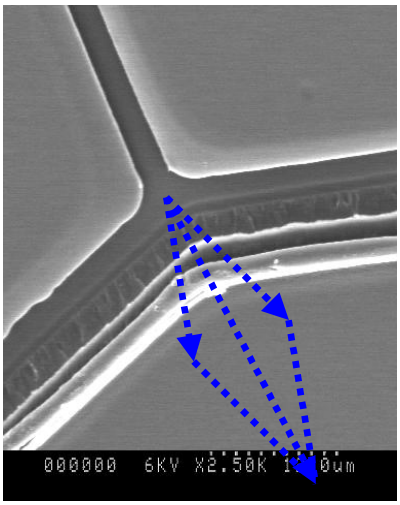

Figure 3-16: An SEM picture of Jude pattern in PMMA plate. The track-like structure is the trace left by sidewall movement caused by thermal shrinkage.

The direction of the sidewall movement can be measured at the SEM picture of the embossed Jude pattern on the PMMA plate. In theory the direction should point to the geometric center of the PMMA plate. Measured from photos the magnitude of the movement is $\Delta L \approx 5.0\ (\mu m)$. The value obtained from measurement is in the same range as the calculated value.

3.5.4. Nickel instead of silicon

As stated, embossing with silicon die met many difficulties. Nickel is a better material. It is not fragile, not sticky to PMMA and thermal expansion coefficient is closer to PMMA. The expansion difference between Nickel and PMMA (at 5 cm edge) is therefore smaller, which is $6.030 - 4.365 = 1.665\ (\mu m)$.

3.6. Different recipes of silicon dry etching

3.6.1. Switched gas (Bosch recipe)

The dry etch machine is called as Inductively Coupled Plasma (ICP). In order to optimize the process for silicon mold, different recipes are tested. The old recipe of dry etching is called Bosch process. It is based on a cycle of two steps.

Deposition step

A passivating layer is deposited on the surface. The passivation layer is only built by the nCF_2 film (in contrast to other side wall passivation techniques generating reacted films like SiO_2).

Etch step

The SF_6 dissociates. Then the fluorine radicals have to remove the surface passivation layer, before the silicon etching can proceed.

The etch deposition process leads to scallops to the sidewall (**Figure 3-17**). These scallops will make embossing more difficult and hence is not desirable.

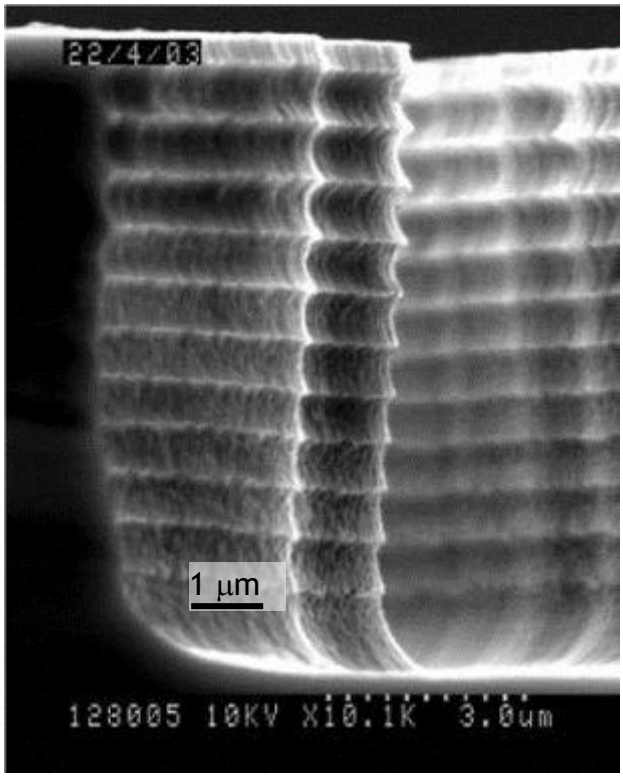

Figure 3-17: Picture taken by a Hitachi S800 scanning electron microscope (SEM) shows scallops on the sidewall of the silicon etched by switching gases.

In the new recipe, rather than switching the two gases we use them at the same time. It is like to do the deposition step and the etch step at the same time. This recipe makes the sidewall of the etched profile smoother (**Figure 3-18**) than before. This un-switching gas recipe is detailed in the next section.

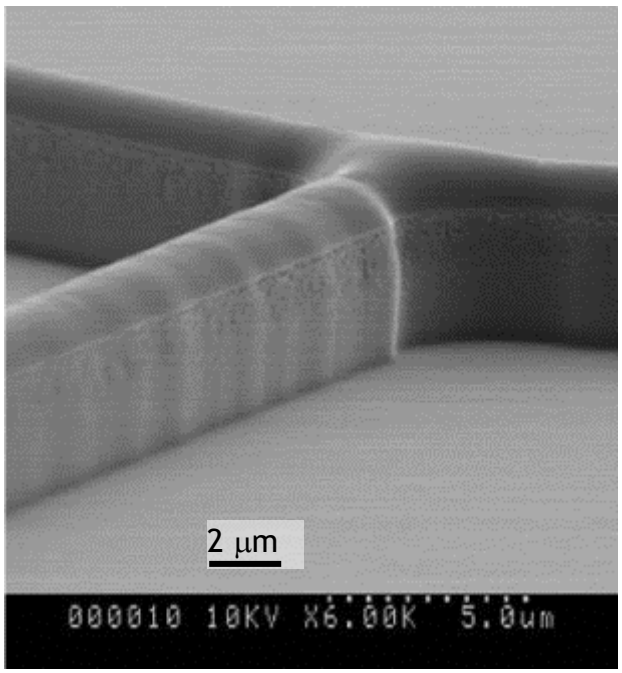

Figure 3-18: The SEM picture shows no scallops on the sidewall of the sample etched by un-switched gases.

The formula based on Bosch process is not fully abandoned. For embossing of pattern with large feature size, the scallops on the sidewall cause less trouble. This formula can be used to etch such pattern and take its advantage of fast etching. Therefore, after minor optimization (oxygen, etching rate, lateral gradient), the formula is used. The formulas are called UDO1A and UDO1B. (**Table 3-1**)

The optimization to Bosch formula

Two different Bosch recipes were used to dry etch the silicon die. They are called UDO1A and UDO1B.The difference between these two recipe are: The first, they have different Etch/Deposition time. The second, oxygen is not used in UDO1B.

Table 3-1: The difference between two recipes, both of which are Bosch processes.

	UDO1A	UDO1B
Time of Etch/Deposition	12 s / 9 s	9 s / 6.5 s
Use of Oxygen	Yes	No

The samples etched using these recipes all show ripples on the etched sidewall. They can be used when the sample do not require smooth sidewall. Their advantage is the high etch speed. UDO1A etches faster than UDO1B due to the oxygen.

Aspect ratio effect etch speed

The aspect ratio effects the Bosch etch speed. There is a reduction in etch rate as the aspect ratio increases. The following photo shows fact.

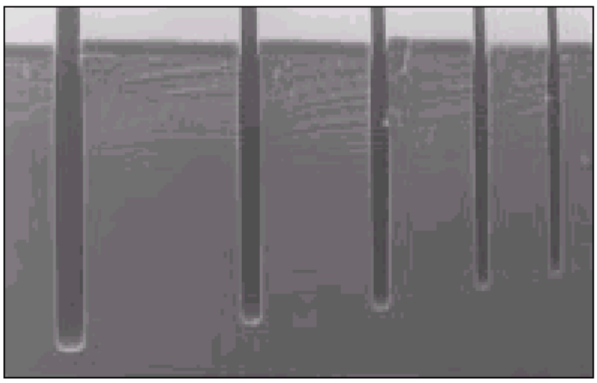

Figure 3-19: This SEM picture is from www. chestech.co.uk. The trenches with different width from 4 to 10 μm (different aspect ratio). These trenchesare etched at the same condition but show different depth.

3.6.2. Un-switched gases

As explained in the last section, un-switched gases were used in a STS ICP (Inductive Coupled Plasma) etching machine to etch the Silicon dies. The parameters in the recipe affect the etching the sidewall profile and the etch rate. Different combinations of parameters were tested. The recipes and the corresponding SEM picture of the cross section are shown below.

Table 3-2: The parameters of the different recipes of dry etching.

	RYT03	RYT04	RYT06	RYT07	RYT08	RYT09	RYT1
Flow rate C_4F_8/SF_6	40 /60 sccm	40 /40 sccm	40 /40 sccm	40 /40 sccm	40 /40 sccm	80 /80 sccm	50 /40 sccm
Chamber pressure	30 mTorr	30 mTorr	10 mTorr	10 mTorr	10 mTorr	12 mTorr	10 mTorr
Table temperature	20 °C	20 °C	20 °C	20 °C	20 °C	20 °C	20 °C
Coil/platen power	300/12 W	300/10 W	300/15 W	600/12 W	600/12 W	600/12 W	600/10 W
Etch speed	N/A	N/A	N/A	N/A	N/A	N/A	5 /7 μm/mins
DC self bias	610 V	610 V	610 V	610 V	610 V	610 V	610 V

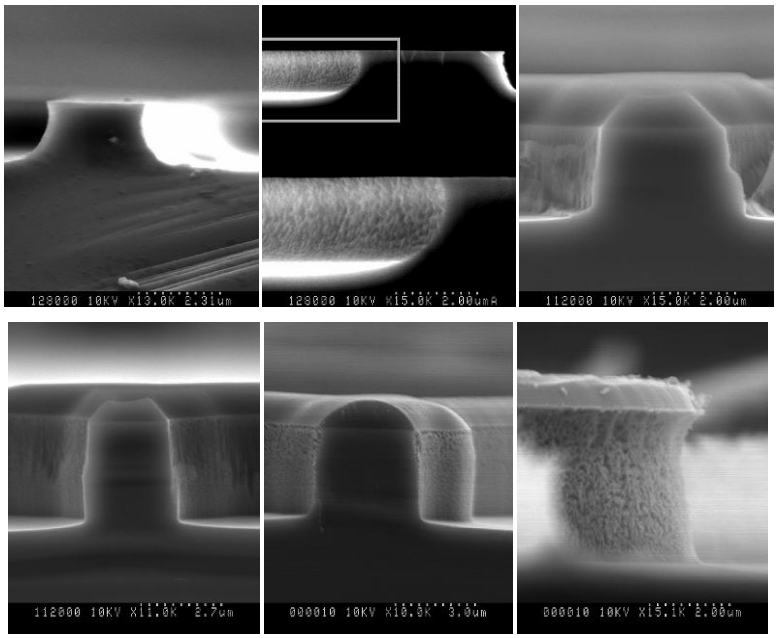

Figure 3-20: SEM pictures of the side-wall profile of silicon ridges etched by different recipes. From left to right, from top to bottom, they are etched respectively by recipes RYT03, RYT04, RYT06, RYT07, RYT08, RYT09.

Finally, RYT1 was chosen as the default recipe for etching Jude patterns in a silicon substrate.

The specifics of RYT1 are:

Flow rate: C_4F_8/SF_6 = 50 sccm/40 sccm
Chamber pressure: 10 mTorr
Table temperature: 20 ^oC
Coil Power/platen power: 600 W/10 W
Etch speed: 5 μm/7 mins
DC self bias: 610 V

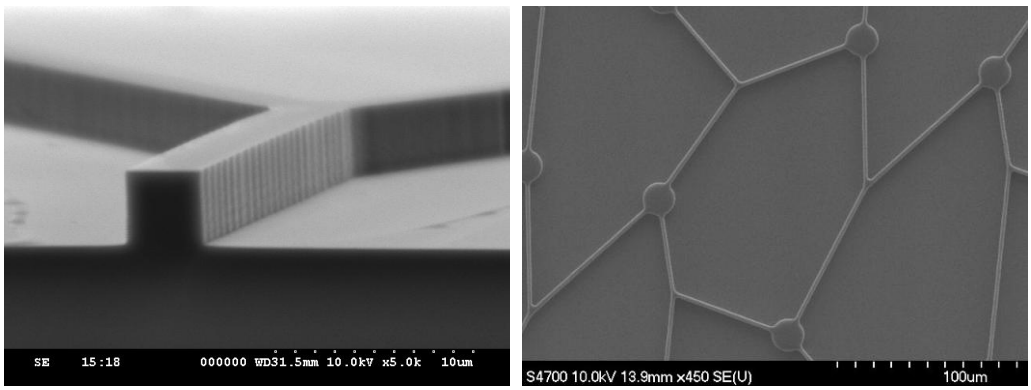

Figure 3-21: A positive (ridge-like) Jude pattern etched by RYT1. The micrographs show the Jude pattern at the central part of the silicon mold for making the 'neural bathtub'.

3.7. Modification to Jude pattern

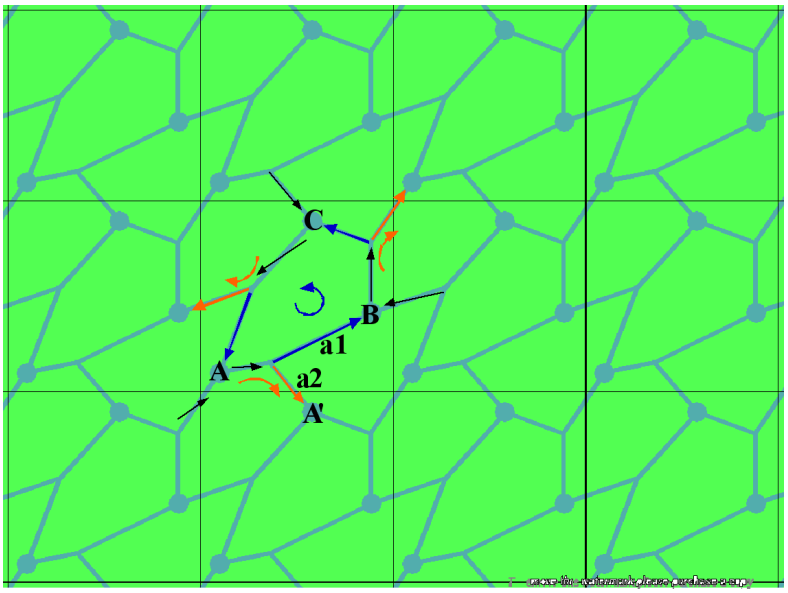

Figure 3-22: Jude pattern. Arrows indicate the direction in which the signal transferred.

We want to make nerve cells grow along artificial topographic or chemical patterns to form living neural network. With such a neural network it may be possible to determine the effects of the pattern on the behaviour of the network.

A simple pattern (called the Jude pattern) was designed by Dr. J A H Wilkinson and is a simple pattern that could be tiled. Each tile has space for three nerve bodies.. The dots and lines in the tile correspond to cell bodies and axons respectively. Each cell body has three axon connections. One of these axons is supposed to be the output and the other two to be inputs from other neurons. Each output axon splits into two go off in different directions. One is connect to a cell in the tile and the other one goes to the cell out in neighbouring tile.

Assume cell body *A* generated an action potential. The signal sent out through the axon *a* in direction *a1* or *a2*. *a1* goes to the next cell body *A*' in the same tile and *a2* goes to cell body *B* in the neighbouring tile. The same thing happens on the next cell *A*' or *B*. In this way the signal could be transferred from one tile to the next (*A* to *A*') or just circulate within one same tile (*A* to *B* to *C* to *A*).

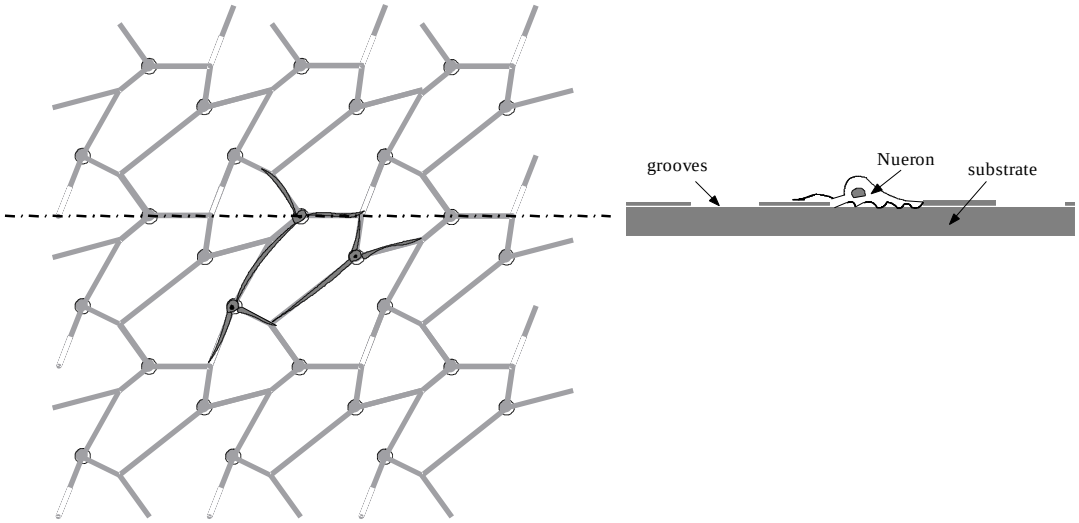

Figure 3-23: Top view (left) and side view (right) of the Jude pattern in which neurons are cultured.

The topographical Jude pattern is made up of pits for the cell bodies and grooves for the axons. The size of the pits and grooves is compatible to the size of neuron's body and processes respectively. Ideally neurons will grow inside these pits and grooves as the picture shown to form a specific network. Besides the topographical Jude pattern, we also imprint the Jude pattern with adhesive protein as another way to grow neuron networks. The following picture shows the result of this chemical method.

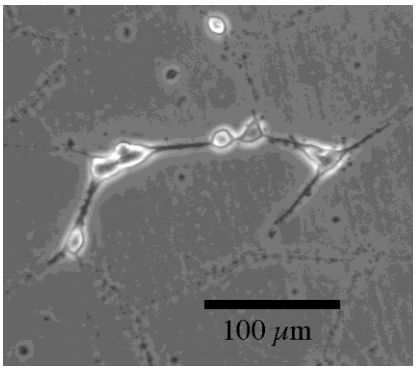

Figure 3-24: Nerve cells grown along the laminin trace (Jude pattern) on polycarbonate substrate. The picture was taken by Alison Beatie.

Our experiments shown some good results but many cells still did not conform to the pattern. The cells show some tendency to grow along the pattern and some of them do connect to network but not always. In figure 3.29, the cells are fully stretched out and and stick to the substrate. They do if there is a good surface adhesion. The circular shape of cells in this photo suggests that they are not fully settled on the substrate.

We are looking for ways to improve the cell adhesion. Some of them go back to the

design of Jude pattern. Many different versions of Jude patterns are derived. Their efficiency was tested with neural culture. These different patterns will be introdced in the following sections 3.7.1-3.7.4. These patterns are first etched into silicon mold. PDMS (sylgard 184) or microset (microset product Ltd) stamps are made from these molds. Sticky protein pattern (poly-l-lysine) is then imprinted (physiorption microcontact printing) on Petri dishes for test with nerve cell culture. The imprinting work, culture tests and results analysis were carried out by Allison Beatie in the Centre for Cell Engineering. The results and discussions on the efficiency of these different patterns are detailed in chapter 4 of her thesis.

Allison stamped these different versions of Jude patterns and cultured the embryonic rat spinal cord cells on them. After two weeks incubation, these cultures were observed using antibody staining and SEM. Allison gathered statistic from these observation, e.g. the percentage of the cells following the pattern, the cell body on the node and on the tracks. The statistics show that cell compliance is significantly increased on the hexagonal Jude (70% cells follow the pattern) in comparison to the original Jude pattern (20% cells follow the pattern).

The decorated node design (sun, oak and lattice) were expected to encourage the development of neural fibers. Most of the individual cells shown no significant affection by these decorations. However Allison showed a SEM picture of one neuron on a lattice pattern. The finer processes of this neuron were clearly guided by the pattern. Despite the little effect on individual cells, the decorations showed significant improvement to the overall network formation. More cells were encouraged to follow the pattern than that of the initial Jude pattern.

The increase on the node size show an effect on the cell compliance and connection.

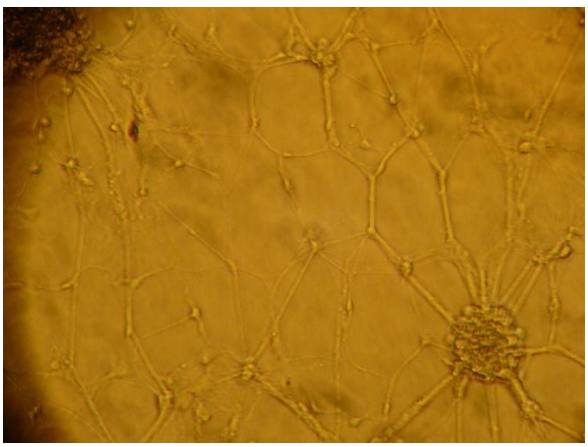

Figure 3-25: One sample of the experiment under microscope. Jude pattern of poly-l-lysine was stamped on a glass coverslip. Not all but some of the nerve cells followed the protein traces and connected into Jude pattern clearly.

3.7.1. The size of the dots

The diameter of the dots in original design is *10 μm* which turned out to be small for the cell type we were using and so we increased it to *20 μm*. The new design worked better and so we also tried other sizes.

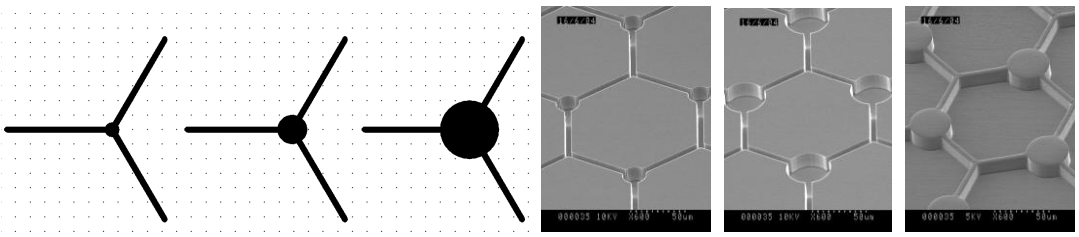

Figure 3-26: Different sizes of the dots in Jude pattern (10 μm, 20 μm, 40 μm). The sunken patterns are in silicon molds. The raised patterns are on PDMS or Microset stamps. This is so for all SEM pictures in figure 3-26 to 3-29.

3.7.2. Space for dendrites

The dendrites play an important role on cell extension and adhesion. In the former design of Jude pattern there was no special consideration given to making space for dendrites.

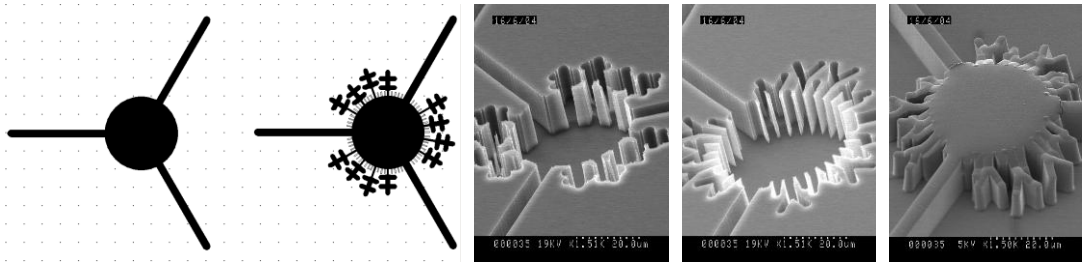

Figure 3-27: Original design of the dot in Jude pattern and the decorated dot of newly designed. The SEM pictures from left to right are the 'oak', 'sun' and 'sun' in PDMS.

3.7.3. Stress balance

In the original design, the pattern is not symmetrical. Lines go from dots radially and the angles are different. This selection of angle was based on the observation that the processes of rat nodose ganglia cells tend to split in an angle of about sixty degree.

This asymmetry may cause asymmetrical stress. There is often a problem in that a process between two cell bodies tightens and one cell is pulled off the surface.

This observation of 'tight-roping' suggested that possibly the forces could be balanced by a more symmetric layout. In the new design, the angle between two radial lines is 120 degrees so balancing the stress.

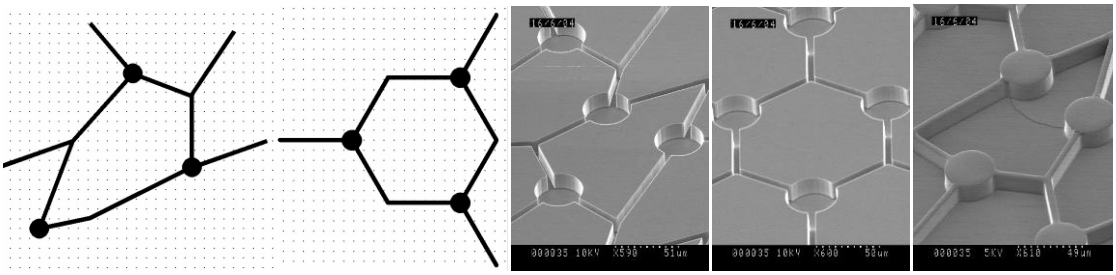

Figure 3-28: Different angles of lines in Jude pattern and equal angles in Judith pattern.

3.7.4. Direction of guidance

As stated at the beginning of this chapter, it is desired that each cell body has one axon growing out and two coming in. In order to guide the direction of the axon's growth, gaps were introduced on two of the paths away from the cell body in the hope that this will discourage the axon to cross and encourage axon to grow only down the third path (Offenhauser et al.). Some output paths were made wider to encourage axonal growth.

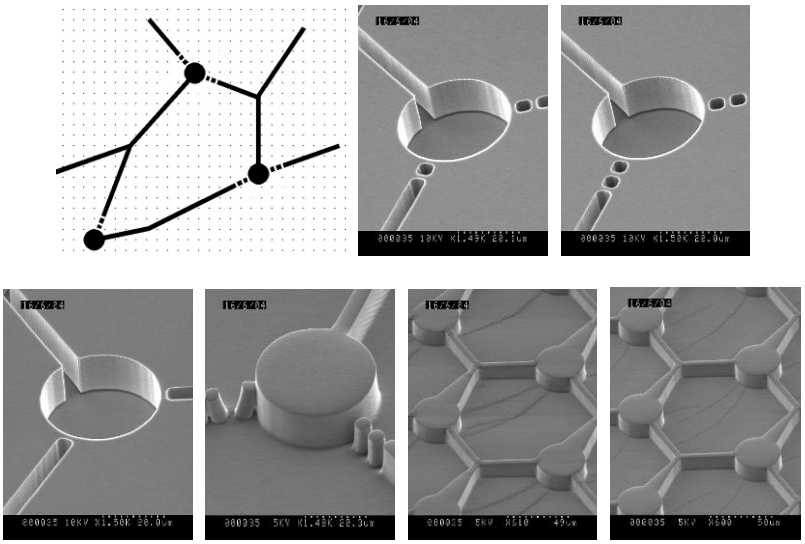

Figure 3-29: Gaps are introduced at the joint of each input line to the dot. Some output lines were made wider.

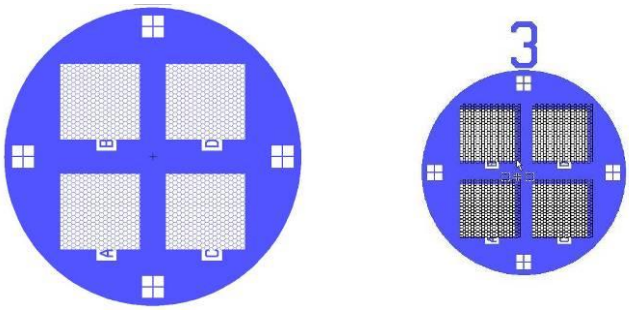

Figure 3-30: Different patterns were included on one stamp. It helped with the comparison of different cell cultures. Each stamp and each pattern are labeled with a number and character. This makes statistical work easier.

3.8. The design of the preamplifier

This section describes the design and manufacture of the preamplifier, including the details of the circuit, the shielding, and the mechanical and electrical connections.

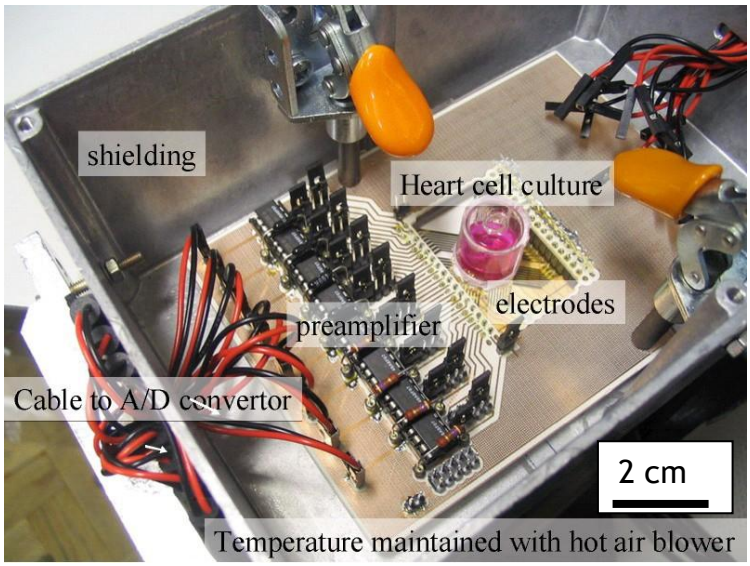

Figure 3-31: The preamplifier of the pMEA system in a shielding enclosure. A pMEA is clamped to the preamplifier.

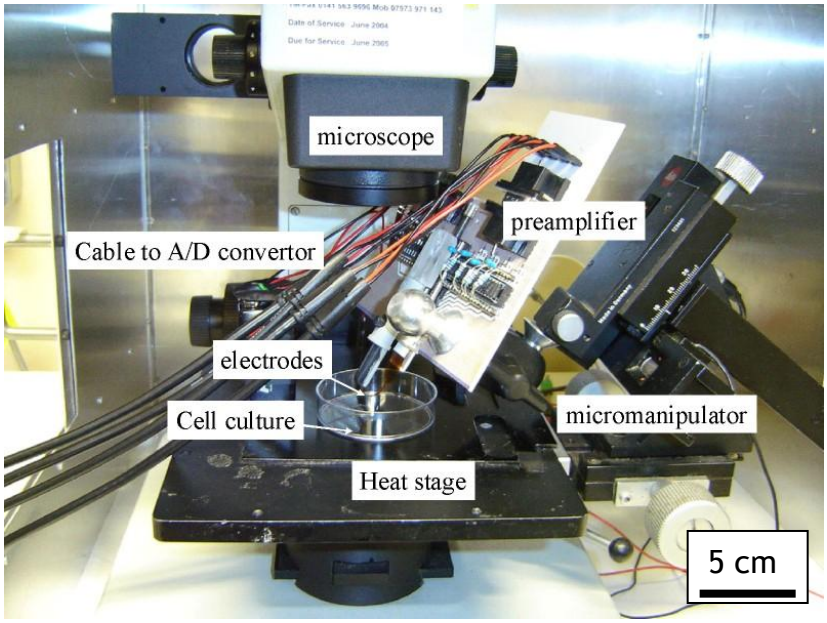

Figure 3-32: The preamplifier of the flexible MEA system. As shown in the photo, the whole setup is inside a Farady cage. The circuit will be shielded by grounded aluminium foil when recording starts.

3.8.1. Circuit design

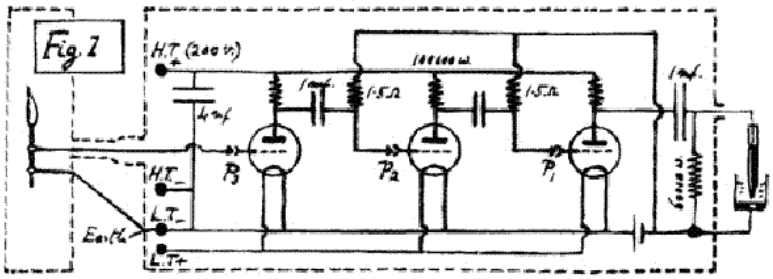

Figure 3-33: Pre-amplifier built by Lucas [1917]. Two electrodes are on a nerve fibre at the left. The voltage vibration between the electrodes is amplified by a series of vacuum tubes. Mercury column is used to record. [Fred Rieke, 1997]

Differential amplification

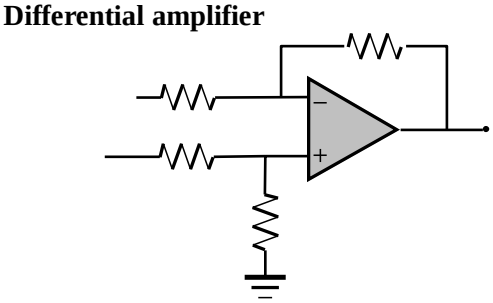

Figure 3-34: The circuit of a standard differential amplifier.

The advantage of the differential amplifier is that the common-mode noise can be

cancelled. If buffer amplifiers are added to its inputs, it becomes an instrumentation amplifier.

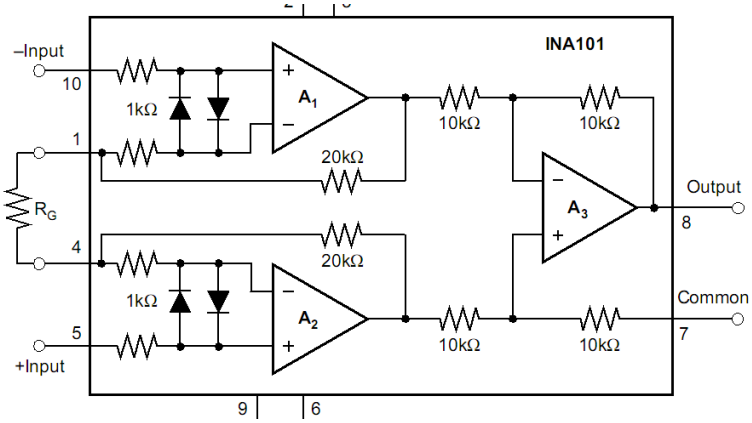

Figure 3-35: The circuit of a high accuracy instrumentation amplifier Burr-Brown INA101.

The input impedance of instrumentation amplifier is high, which is suitable to detect a signal of high internal resistance. An Instrument amplifier is a type of differential amplifier so it is suitable for amplification of the a weak differential mode signal immersed in the common mode noise.

A differential pre-amplifier was built using an INA101 instrumentation amplifier. The two inputs of the INA101 are connected to two microelectrodes spacing about tens of micrometers and the common to the reference electrode in the bath. The differential signal between two microelectrodes can be amplified. But no useable signal was recorded in experiments using this circuit type with both the FlexMEA and the pMEA systems.

By observing the spikes recorded with the non-differential amplifiers (see chapter 8), little difference can be found between the signal in different channels. The differential mode signal is weak. This may be the reason why differential amplifier did not work well.

Non-differential amplification

For recording extracellular signals from one side of the neuron body opposite to the substrate, the cell container is placed upside down on top of the pMEA. The cell container stands on bumps patterned on its outer ring. The bumps give neurons a few micrometer deep space between the container and the electrode plane, so they will not be crushed when their membrane is in contact with the electrode plane.

In order to amplify the weak voltage signal from these sources of relatively large equivalent resistance, a voltage preamplifier needs to have a very high input impedance. The bias current must be kept low, (< *1 nA* to avoid injecting current into the polarising the electrode. The expected signal is the tens to hundreds of micro-volts so a peak-to-peak noise of less than 10 microvolts referred to he input is needed over a 10 KHz bandwidth.

Our custom preamplifier is a classic non-inverting amplifier with FET op amp LT1793 with low noise and low bias current is chosen as the front end. The op amps are arranged as close to the MEA as possible. The distance is 3 cm or 1 cm for pMEA system (there are two versions) and 5 cm or 4 cm for FlexMEA system (two versions). Metal film (low 1/f noise) precision resistors (0.25 W, 0.1%) were used. The resistors set the gain of voltage at 500 times, which is sufficient that the noise in later stages is negligible.

The input stage of the preamplifier must be AC coupled to the electrodes in order to avoid amplification of the offset potential (half-cell potential) that appears at the electrode-electrolyte interface. AC coupling is realized by making the front end op-amp a high pass filter. The lower cut-off frequency of the high pass filter is about 10 Hz. So overall the frequency range of the amplifier is from 10 HZ to 10 kHz.

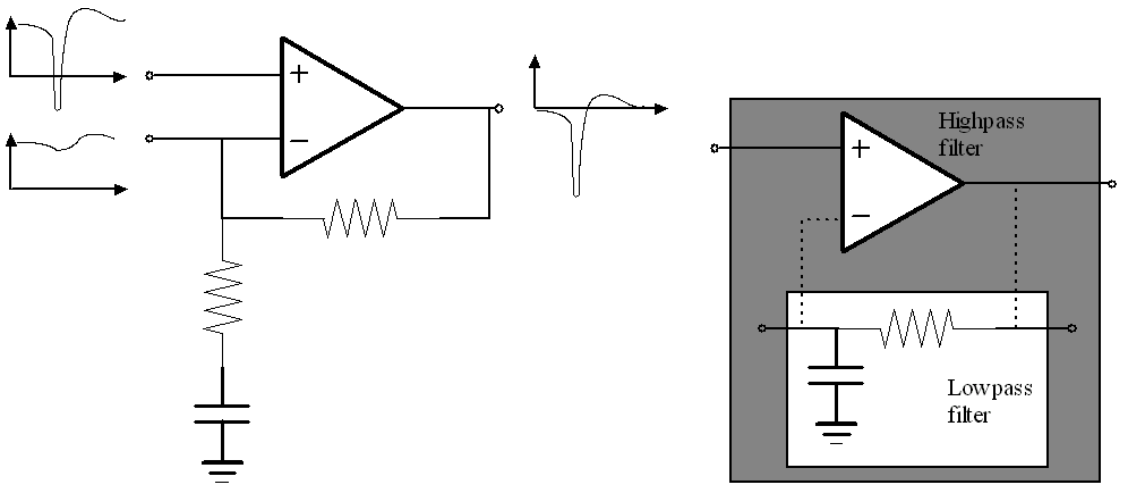

Figure 3-36: Preamplifier is both an inverting amplifier and a highpass filter. Right side of the graph shows that a lowpass filter is placed between the output and the negative input of the op-amp.

The output of the preamplifier feedbacks to the negative input through a low-pass filter. The low frequency signal arrived at the negative input and offsets its

equivalent at the positive input. The overall result is that the high frequency part of the raw signal is amplified.

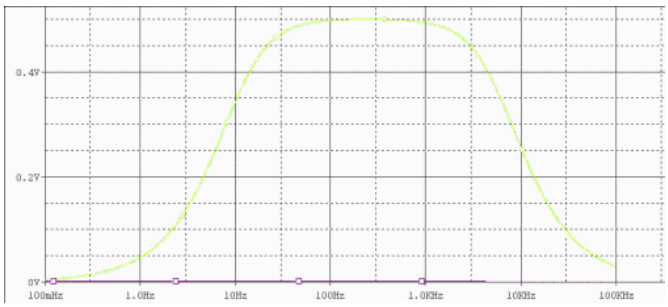

Figure 3-37: Passband 10 Hz-10 KHz (AC sweep 0.1 Hz-100 KHz) as simulated in SPICE.

3.8.2. Power supply

The preamplifier is powered by two 9 V Alkaline batteries to give + and – V. to avoid any noise from an AC/DC power supply. Inevitably the voltage of the batteries will not be precisely equal and this difference will cause a DC offset at the input of the op amp. This DC offset may drive current through the electrodes so causing damage to neuron or electrode.

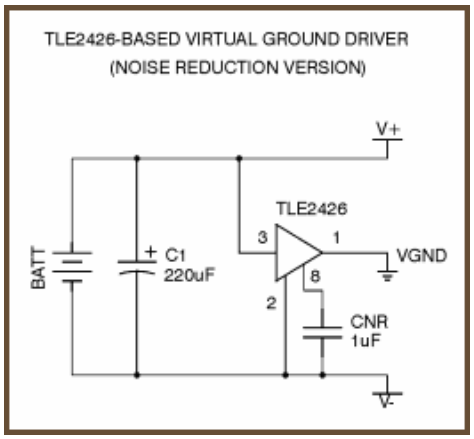

Figure 3-38: The circuit of the buffered virtual ground.

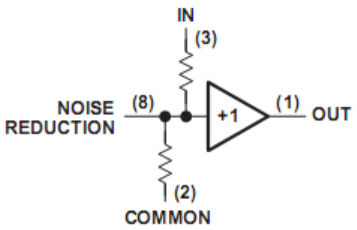

Figure 3-39: The internal circuit of the chip 'TLE2426'.

A buffered virtual ground circuit was used to eliminate this problem. This circuit is a buffered voltage divider. It utilizes a "rail splitter", Texas Instruments TLE2426. Two series connected resistors inside the chip split the input voltage into one half

precisely. The internal op amp buffer keeps the voltage stable even if its loading changes.

Overall the specification of the preamplifier was:

(1) Gain of 500 times, sufficient to amplify spikes from neuron of typical uV range into mV range;

(2) Passband from 10 Hz to 10 kHz, matching the main frequency component of spikes from neurons;

(3) 10 nV/Hz noise when input shorted;

(4) 10^{12} Ω high input impedance;

(5)10 pA bias current. To minimize the disturbance to the cell and noise arising from the bias current passing through source impedance;

(6) Dual nine volt battery power source.

3.8.3. Grounding and shielding

Differential amplifiers have strong immunity to environmental noise as they have a symmetrical circuit that avoids common-mode noise. Non-differential amplifiers are more vulnerable to external interference and noise reduction relies on grounding and shielding.

The shielding of the preamplifier is based on single-point ground system. All signal ground and shield enclosure are connected to earth at one central point. The idea is to keep signal ground, earth and shield enclosure at one zero-signal-reference potential (Ralph Morrison, 1967). It insures that no ground loops are created. This shielding method works well in low frequency circuits, like the preamplifier here.

In the preamplifier, the central point is located on the reference electrode, which is immersed in cell culture medium. In practice it is difficult to wire up all these ground at one single point. The connection is applied by extending a single point into a ground plane. A ground plane is a large copper area on PCB (print circuit board). This copper ground plane provides a low resistance connection to reference electrode and hence maintain zero-signal-reference potential all over the plane. The chassis ground and cable shielding are connected to this ground

plane.

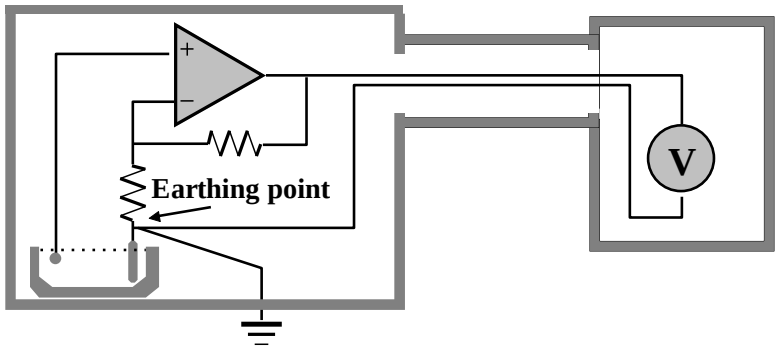

Figure 3-40: The schematic of the single-point grounding.

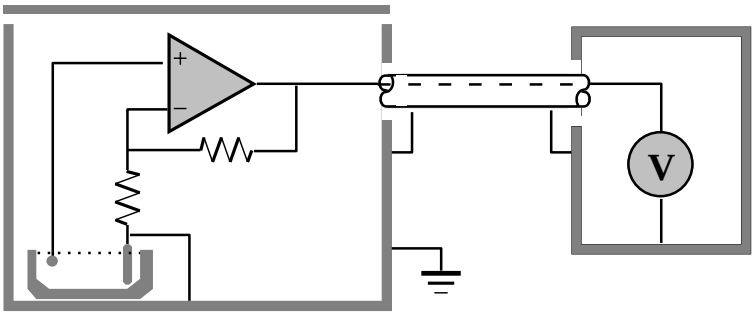

Figure 3-41: Extend the single-point into a ground plane.

Connection of the MEA to the preamplifiers

Each the 64 electrodes in the MEA is connected to a preamplifier. The Connections need to be reliable ensuring low resistance coupling. The electrodes in the MEA need platinization. The electroplating is usually performed in a separate set-up. Therefore the connection between the electrodes and the electronics cannot be permanent. A plug-in arrangement is also helpful in that it makes the replacement of a used MEA easier.

Different connecting techniques were investigated. A z-axis connector was tried first. As the name implies, the z-axis connector builds vertical connection between the objects in parallel, e.g. PCB boards. The interconnecting element is a block of elastomer filled with conductive material. Electric connection is made by ‘sandwiching’ the elastomeric block between two contacts. Such a connecting technique needs relatively precise alignment and clamping. The manufacturer of z-axis connector of can provide custom services to fabricate specific connectors for the required geometry and clamping forces.

Figure 3-42: An elastomeric block with silicone rubber core and gold coating.

We ordered connectors from 'Z-Axis Connector Company' and tried to fabricate accessories ourselves. The homemade connector works but is not very reliable. Hence this connecting method was abandoned.

Another connecting technique, the 'spring loaded pin connection', offers a better solution.

The connector has a series of spring loaded pins mounted in a frame. The Bottom of each pin is soldered to the PCB. A convenient and reliable connection is formed by pressing these pins onto the pads of the MEA.

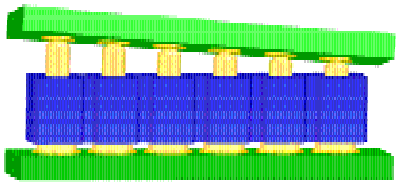

Figure 3-43: Schematic of the sring loaded pin connection.

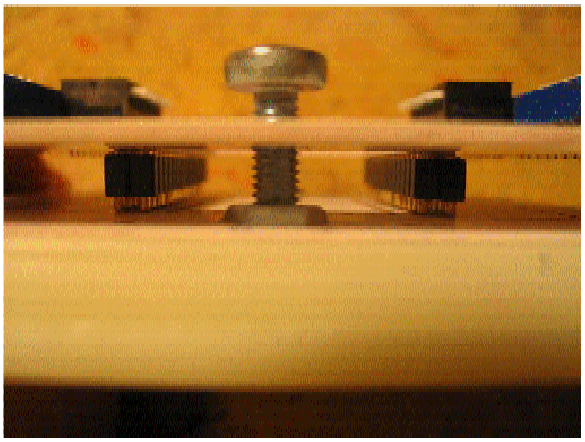

Figure 3-44: The MEA is connected to preamplifier with 4×16 spring loaded pin connector.

Figure 3-45: A toggle clamp.

The two toggle clamps provide force for clamping. They also earth the shielding enclosure to the ground plane.

3.8.4. Connection of the FlexMEA

In the original design, the FlexMEA is soldered to the preamplifier circuits. This proved difficult to perfect for MEA's on 150 micron thick Kapton and impossible on the 50 micron material. The need for insulation to avoid contact to the medium was a further complication.

The final solution was to use a ribbon cables connector, the so-called ZIF (zero insertion force) connector. The contact resistance is only a few ohms and the success rate reaches almost one hundred percent. The connection is stable and reliable. It is convenient to assemble and unassembled. Because the connection region is compact, the distance between the electrode tip and the contact pads is easily redesigned to be over 3 cm. Therefore the insulation layer is no longer required. The standard connector is designed to take 0.25 mm FPC (flexible printed circuit) cables. As our FlexMEA is no thicker than 70 μm, a gasket is employed to make a tight connection.

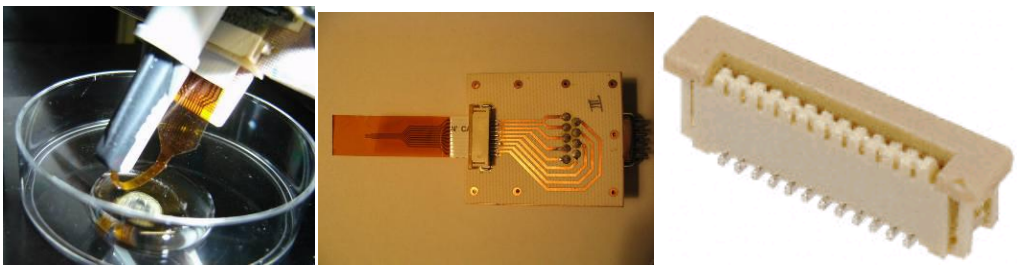

Figure 3-46: The FlexMEA and the ZIF connector.

The ZIF connector can be conveniently soldered at the front end of the PCB. With the FlexMEA inserted in the connector, the pre-amplifier and the MEA becomes a single unit. They are fixed on a micromanipulator with a ball joint. The angle and the position can be adjusted conveniently. The ZIF connector has ten pins in total. Eight of them are connected to the microelectrodes. The left two are connected to the integrated reference electrodes on the MEA.

3.8.5. System installation

Figure 3-47: The pre-amplifier of pMEA in working condition. It is on an inverted microscope stage. The cables at the right are connected to A/D converter and computer. All circuits are in the shielding box. There are holes on the box. The one top is for observation. The one at left is the tunnel for the hot air that controls the temperature to 37 ^{o}C as required for cells.

3.9. conclusions

This chapter describes the design and evolution of each component in the home-made MEA system. These components include different versions of the FlexMEA, pMEA, neural bathtub, Jude pattern and pre-amplifier. These MEA systems operate in many experiments and collected large quantity of signal from neural network (details in chapter 7). In addition to the common features of MEA systems, our systems have some advanced and unique characteristics, e.g. thin FlexMEA (50 μm thick), bottom of boat shaped FlexMEA, neural bathtub, Jude pattern, low-noise pre-amplifier of battery powered.

There are some possible improvements that could be considered making in the future. At present the function of stimulating cells rely on the external signal generator. The module of stimulation could be integrated into the circuit in the future.

The neural bathtub needs manipulation with precision over the pMEA during the experiment. The manipulation at present is done manually or with a micro-manipulator. The object stage on the mask aligner or the microscope has the ability to move precisely. Similar devices may be included into our system.

Chapter 4.Model and Measurement of Microelectrode Impedance

4.1. Introduction

One of the aims of this thesis is to produce a model that allows simulation of the observed signal (recorded with a MEA system) taking into account the inter-cellular action potential, the corresponding extra-cellular potential and the effects of the micro-electrode and amplifying circuitry. The characteristics of the micro-electrode are discussed in this chapter and the model obtained will be used in chapter 6.

The conventional circuit model is tried. This model contains four elements, i.e. the interfacial capacitor (C_i), the charge transfer resistor (R_t), the Warburg impedance (Z_w) and the spreading resistance (R_s). Each of these elements is introduced, including their physical meaning and the formulas. This content is basically a summary of existing theories [Gregory T. A. Kovacs, 1994]. Based on the theory, the value of each element is predicted. The predicted values are adjusted by fitting the model with the experimental data. The instalments and method of the measurement are detailed. The data fitting is carried out in Mathematica. Three slightly different fitting algorithms are used.

This conventional model is not entirely consistent with the data. Another empirical model by MacAdam [1995] is investigated and show good consistency.

Some of the work presented in the chapter was done during my M.Sc project at Glasgow University. I present here a summary of the theory and some earlier measurements. However section 4.11 and section 4.13 are wholly new.

4.2. Double Layer

There may be no potential difference across the electrode/electrolyte interface when an electrode is first put into an electrolyte. But a space charge layer will rapidly build up due to electrochemical reactions. Some reactions have a tendency to form positive metal ions, which may dissolve into the bulk electrolyte. The excess electrons left behind will accumulate at the surface of the electrode. Thus

a space charge layer builds up at the electrode/electrolyte interface. This redox reaction eventually reaches equilibrium.

A layer of oriented water molecules is attached to the surface of the electrode attracted by the charges there. It is called the Hydration Sheath or Inner Helmholtz Plane. Outward from this layer there is an Outer Helmholtz Plane. It is made up of hydrated metal ions attracted by the negative charge. The Inner Helmholtz Plane together with Outer Helmholtz Plane is referred to as the Electrical Double Layer.

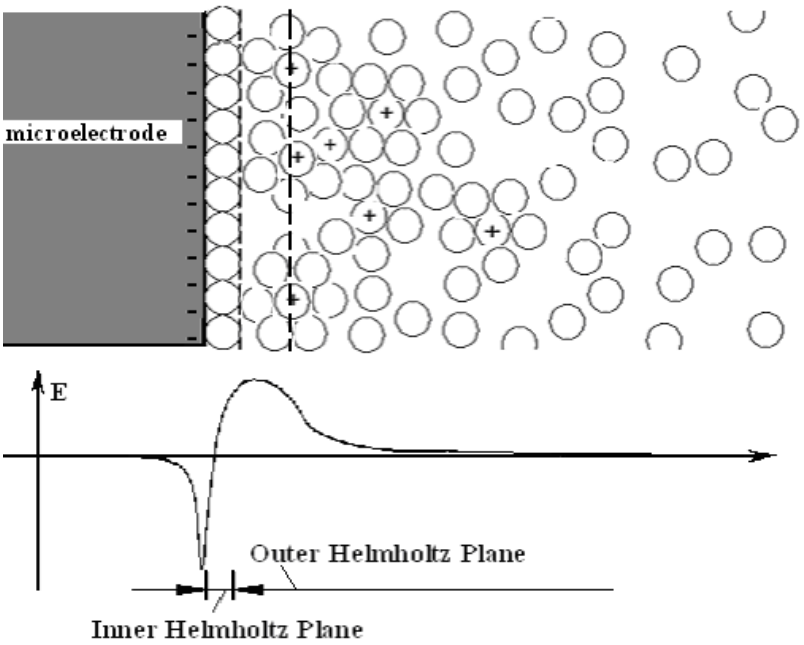

Figure 4-1: Schematic diagram of a metal electrode immersed in electrolyte. The reaction between metal and electrolyte result in an electrical double-layer structure at their interface. The hollow circles represent water molecules. Those circles with a plus in the centre are metal ions. The metal ions surrounded by water molecules are hydrated ions. A diagrammatic sketch of the distribution of the electric potential field at the interface is also shown.

All metal electrodes in the solution have a double layer around them, including the reference electrode (grounding electrode). However, as the size of the reference electrode is by far bigger than the working microelectrode, the capacitance of the double layer of the reference electrode will be much greater than that of the microelectrode and so effectively shorts the reference electrode to the electrolyte. Therefore, the double layer of the reference electrode is generally ignored in the modelling. The modelling of the double layer in this chapter is aimed at the microelectrode of MEAs. The diameter of these microelectrodes is around 30 μm. They are thin film electrodes made of different metals, e.g. Au/Ti, ITO etc. Some of them are electroplated with platinum black.

4.3. The Interfacial Capacitance

The Interfacial Capacitance is the capacitance between the electrode and the region of hydrated ions (including the Outer Helmholtz Plane and the Diffusion Region). Three models for the interfacial capacitance will be discussed.

4.3.1. The Helmholtz-Perrin model

The Helmholtz-Perrin model, which is the simplest one, assumes that there is only a layer of hydrated ions in the space charge region. This layer forms a parallel-plate capacitor with the electrode.

$$C_H = \varepsilon_o \, \varepsilon_r \, A \, / \, d \qquad \text{Eq. 4-1}$$

Where,

ε_o is the dielectric permittivity of free space,
ε_r is the relative dielectric permittivity of the medium in the double layer, A is the surface area of the electrode, d is the distance between electrode and Outer Helmholtz Plane.

4.3.2. The Gouy-Chapman model

The Gouy-Chapman model goes beyond the Helmholtz-Perrin allowing for diffusion of the ions and assumes that there is a more complex and voltage dependent potential profile in the space charge region (outward from the Outer Helmholtz Plane). When the voltage applied to the electrode increases the Outer Helmholtz Plane becomes more compact and vice versa.

$$C_D = (\varepsilon_o \, \varepsilon_r \, A \, / \, L_D) \cosh (z \, V_o \, / \, 2 \, V_t) \qquad \text{Eq. 4-2}$$

Where,

L_D is the Debye Length (the distance at which the potential decreases “e” times),
V_o is the voltage applied to the electrode/electrolyte interface, V_t is thermal voltage ($V_t = k \, T \, / \, q$).

4.3.3. The Stern model

The Stern model, which fits experiment well, combines the above two models. This model assumes that there is a parallel-plate capacitor (Helmholtz-Perrin model) between electrode and Outer Helmholtz Plane and in the space charge region outward from Outer Helmholtz Plane, there is a Gouy-Chapman capacitor. This assumption leads to a capacitor which is the sum of two series connected capacitors.

$$C_i = 1 / (1 / C_H + 1 / C_D) = 1 / (d / \varepsilon_o \varepsilon_r A + L_D / \varepsilon_o \varepsilon_r A \, Cosh(z V_o / 2V_t))$$ Eq. 4-3

Where,

$$A = \pi r^2$$ Eq. 4-4

$$L_D = \sqrt{(\varepsilon_o \varepsilon_r V_t / 2 n^o z^2 q)}$$ Eq. 4-5

$$V_t = k T / q$$ Eq. 4-6

Where,

ε_o is the dielectric permittivity of free space ($\varepsilon_o = 8.85419 \times 10^{-12}$ *F / m*).

ε_r is the relative dielectric permittivity of the medium, which is water here, in the capacitor ($\varepsilon_r = 78.54$ at $25\ ^oC$).
A is the surface area of the electrode.
d is the distance between electrode and Outer Helmholtz Plane ($d = 5.0 \times 10^{-10}$ *m* [Gregory T. A. Kovacs, 1994]).
L_D is the Debye Length.
z is the charge of the ion in question.
V_o is the voltage applied to the electrode/electrolyte interface ($V_o = 0.2$ *V*).
V_t is the thermal voltage.
r is the radius of the microelectrode.
n^o is the bulk number concentration of the ion in question (n^o = *Avogadro's number* × C).
C is bulk concentration of the ion in question ($C = 0.1$ *mole / Liter*)
q is the charge of the electron ($q = 1.60219 \times 10^{-19}$ *C*).
k is Boltzmann's constant ($k = 1.38066 \times 10^{-23}$ *J / K*).
T is the temperature in *K* (here $T = 25\ ^oC = 298$ *K*).

For example with a 25 μm radius micro-electrode in saline of ion concentration C = 0.1 M, the Debye length is about 0.96 nm, the thermal voltage at room temperature is about 25.6 mV and the interface capacitance of the electrode according to the Stern model is about 2.53 nF.

4.4. Charge Transfer Resistance

The charge transfer resistance is a nonlinear resistive element in the model. When a small external current (comparing with exchange current density J_o) is applied to the electrode, the electrode shows high resistance. When the current increases and becomes big enough compare with J_o the charge transfer resistance exhibits an exponential decrease with applied potential.

The charge transfer resistance is defined (of the Guoy-Chapman model) as,

$$R_t = V_t / A J_o \, Cosh (V_o / (2V_t))$$ Eq. 4-7

Where,

V_t is thermal voltage ($V_t = 0.02568$ *V*).

A is surface area of the electrode (1.9635×10^{-9} m^2).
V_o is the voltage applied to the electrode/electrolyte interface ($V_o = 0.2$ *V*)
J_o is the exchange current density ($J_o = 3.98 \times 10^{-5}$ A/cm^2 at Au/saline interface, hydrogen reaction of Au)

It is not easy to predict the value of J_o for a certain system theoretically. The value

of J_o used here in the calculation is only provisional. It will be decided later from the experimental data. Before calculating the charge transfer resistance the understanding the exchange current density is necessary.

4.4.1. The Exchange Current Density

The exchange current density, J_o, is a fundamental characteristic of electrode behaviour related to the rate of reaction happening at the electrode/electrolyte interface, which proceeds at "equal rates" both in the forward and in the reverse direction. At this dynamic equilibrium there is no net current flowing through the electrode. The absolute value of this current for a given surface area is referred to as the exchange current density. A large exchange current density indicates a fast reaction.

It is difficult to predict accurately the exchange current density of an electrode/electrolyte interface. One reason is that the actual electrochemical reaction dominating is not often known. The exchange current density can be determined experimentally.

The magnitude of exchange current density related to the composition of the electrode and the solution, the concentration of both the reactants and products involved in the specific reaction, the impurities adsorbed on the surface of the electrode and the surface roughness of the electrode.

The most interesting parameter here is the surface roughness of the electrode. A bigger actual surface area can support a higher exchange current density.

For example [Various, the exchange current density]

For H^+ / H_2 equilibrium system on a platinized platinum electrode,

$J_o = 10^{-2}\ A / cm^2$

For H^+ / H_2 equilibrium system on a bright platinum,

$J_o = 10^{-3}\ A / cm^2$

This explains why platinisation is used to reduce the impedance of the microelectrode.

If we assume that the dominant reaction happening at the Au electrode / saline solution interface is a hydrogen reaction of Au, which has an exchange current density of $3.98\times10^{-6}\ A\ /\ cm^2$, then the charge transfer resistance is:

$$R_t = V_t\ /\ A\ J_o\ Cosh\ (V_o\ /\ (2V_t)) = 1.33769 \times 10^7\ \Omega$$

This value proved later to be around ten times the experiment value, which is not a surprising result considering the extremely broad range of J_o and the difficulty in predicting a correct number for it.

4.5. Warburg Impedance

There is a concentration gradient of ions outward from the electrode into the bulk solution. When the frequency of the applied sinusoidal potential increases, the concentration gradient increases. These lead to faster diffusion of ions and so smaller impedance. This frequency associated impedance is called Warburg impedance or polarization resistance.

The Warburg impedance is a frequency-dependent impedance modelled as a parallel R-C network with a constant phase angle of 45°.

The Warburg impedance is often called a constant phase element as its real part and imaginary parts are equal. Drawn on a Nyquist diagram, Warburg impedance is a straight line at an angle of 45°. Warburg impedance is often shown schematically as a parallel RC circuit. While the resistance of a real resistor is frequency independent, the real part of the Warburg impedance is frequency dependent. In another word, Warburg impedance cannot be represented by real electric elements. This complicates the simulation in as much as no procedure can be found in PSPICE to simulate Warburg impedance. Therefore, Mathematica was used to do most of the simulations.

The Warburg Impedance defined as,

$$Z_w = (1\ /\ R_w + j\ 2\pi\ C_w)^{-1} \qquad \text{Eq. 4-8}$$

It is different with the formula of the impedance of a real parallel R-C network, which is,

$$Z_{RC} = (1 / R + j\, 2\pi f C)^{-1} \quad \text{Eq. 4-9}$$

$$R_w = V_t / z^2 q n^o S \sqrt{(\pi f D)} \quad \text{Eq. 4-10}$$

$$C_w = 1 / 2\pi R_w \quad \text{Eq. 4-11}$$

Hence,
$Z_w = (1 / R_w + j\, 2\pi C_w)^{-1} = V_t (1 - j) / 2z^2 q n^o S \sqrt{(\pi f D)}$

Where,

V_t is the thermal voltage ($V_t = 0.02568\ V$),
z is the charge of the diffusion ion,
q is the charge of the electron ($q = 1.60219 \times 10^{-19}\ C$),
n^o is the bulk number concentration of the ion in question (n^o = Avogadro's number × C = $6.02205 \times 10^{25}\ m^{-3}$)
C is bulk concentration of the ion in question ($C = 0.1\ mol/L$),
S is the surface area of the electrode ($1.9635 \times 10^{-9}\ m^2$),
f is frequency of the applied sinusoidal potential,
D is the diffusion coefficient of the diffusion ion ($D = 1.483 \times 10^{-9}\ m^2 / s$ [Handbook of Physics and Chemistry, 2003])

$R_w = V_t / z^2 q n^o S \sqrt{(\pi f D)} = 198.59 / \sqrt{f}\ (\Omega)$

$C_w = 1 / 2\pi R_w = 8.0142 \times 10^{-4} \sqrt{f}\ (F)$

$Z_w = 0.5 R_w (1 - j) = 99.295 \times (1 - j) / \sqrt{f}\ (\Omega)$

4.6. Spreading Resistance

An ionic current meets resistance when it spreads out from electrode into the bulk solution. This resistance depends on the surface area of the electrode, the concentration of the bulk solution and the geometric layout of the electrode as this determines the route by which ions spread. Spreading resistance is also called solution resistance. Before calculating the spreading resistance, let us see the relation between resistance and capacitance in a steady current situation.

4.6.1. Static electric field and steady electric current density

From Ohm's law at a point [Kraus, John D. Electromagnetics]:

$$\mathbf{E} = \mathbf{J} / \sigma \quad \text{Eq. 4-12}$$

The static electric field and steady electric current at a point are at the same direction and the magnitude of field is linear to current density. A solution to the current flow can be found from Laplace's equation. Formally the solution for the capacitance between the two conductors has the same analytic form so if one has an expression for the capacitance the resistance can be calculated.

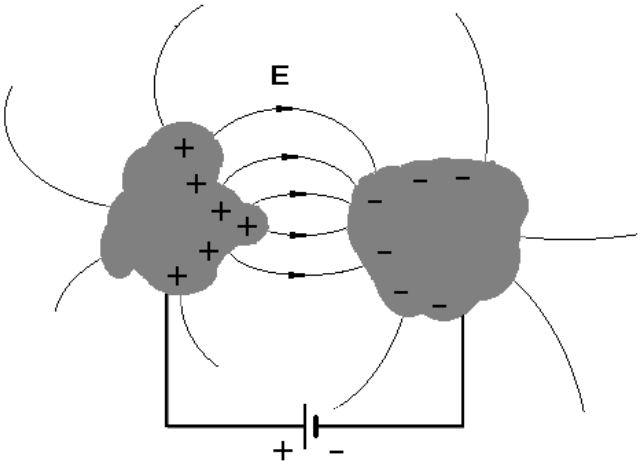

Figure 4-2: The schematic map of electric field between two conductors in space.

$$R = \frac{V}{I} = \frac{\int \frac{J}{\sigma} \cdot dl}{\oint \bar{J} \cdot d\bar{S}} = \frac{\int E \cdot dl}{\oint \sigma \bar{E} \cdot d\bar{S}} \qquad \text{Eq. 4-13}$$

$$C_g = \frac{Q}{V} = \frac{\oint \varepsilon \bar{E} \cdot d\bar{S}}{\int E \cdot dl} \qquad \text{Eq. 4-14}$$

Where C_g is the geometric capacitance between the conductors.

So,

$R = \varepsilon \,/\, (\sigma\, C_g)$ Eq. 4-15

If we can obtain the geometric capacitance of our microelectrode, the spreading resistance can be obtained easily using the above equation.

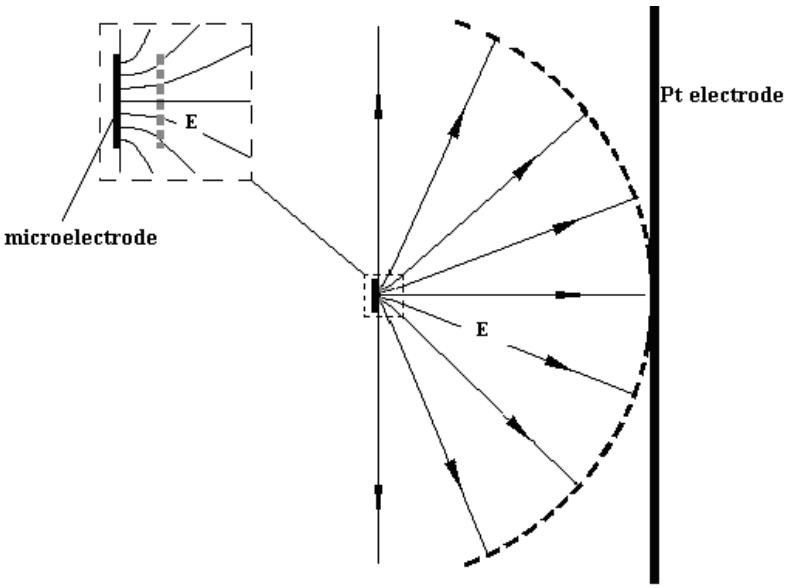

Figure 4-3: The schematic electrical field map between a microelectrode and a platinum wire.

The electric field between the microelectrode and the reference electrode (Pt

wire) is shown in the above figure. To simplify the calculation, several assumptions were made. First, the Pt wire is assumed to be half a sphere. Second, the electric field is believed as the same as the field which between two concentric spherical shells, except in the part near the microelectrode. Third, the field near the microelectrode is assumed as the same kind of field between the parallel-plate capacitor.

The whole capacitance is the combination of two series connected capacitors, the concentric sphere part C_s and the parallel-plate part C_p.

The capacitance is then $\varepsilon A / l + 2\pi\varepsilon r R / (R - r)$. Where r is the radius of the microelectrode and R is the radius of outer sphere. Assuming that the reference electrode is a long way from the microelectrode (so $1/R$ can be regarded as zero). Then by Eq 4-15, the spreading resistance is found to be $l / (\sigma A)+1 / (\sigma\ 2\ \pi\ r)$. For physiological saline (*0.9 % NaCl*) of conductivity *1.6 S* m^{-1} [Handbook of Physics and Chemistry, 2003] and 25 μm radius microelectrode, the spreading resistance is about *12 kΩ*.

4.7. The circuit model of a un-platinized electrode

The circuit elements in the previous chapter can be combined into a circuit model for the electrode/electrolyte interface.

The completed circuit model, as shown in the **Figure 4-4**, includes the interfacial capacitance of the double layer C_i, the resistance to charge across it R_t, the impedance of the diffusion into bulk solution Z_w the spreading resistance across the bulk solution.

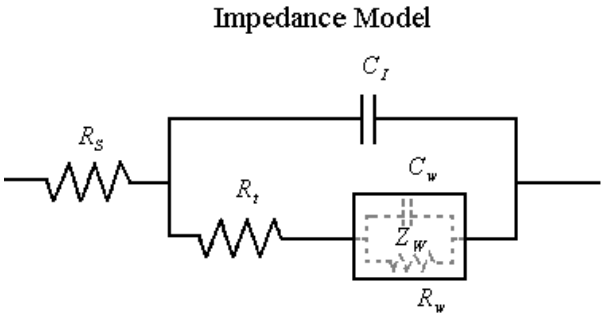

Figure 4-4: The impedance model of an un-platinized microelectrode.

4.8. The circuit model of a platinized electrode

4.8.1. Pore impedance

One would like the impedance of the micro-electrode to be as small as possible. Increasing the actual surface area is an effective way to obtain a lower impedance while not increasing the electrode size. Platinisation as described in Chapter 2 effectively does this by making the surface become rougher thus increasing the surface area.

The effect of this porous surface to the electrode can be thought as adding in a pore impedance Zp parallel with other circuit elements [Gregory T. A. Kovacs, 1994], as shown in the **Figure 4-5**.

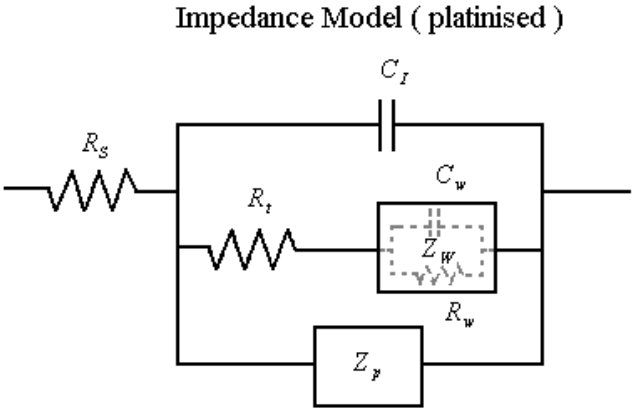

Figure 4-5: The impedance model of a platinized microelectrode.

But in practice, it is hard to measure the pore size, depth and number. Hence, it is difficult to derive and calculate the pore impedance. Usually experimental data is used to obtain a value of pore impedance rather than to predict it using a theoretical model.

In the expression for pore impedance, there is a variable scaling factor k, which is used to fit the experiment value. It should be noted that this has the same functional form as the Warburg impedance.

$$Z_p = k\,(1 - j) / \sqrt{f}$$

4.9. Measurement

The impedance meter I used (HP 4192) can sweep the frequency range from 5 Hz to 13 MHz. In most cases in this chapter, the measurements ranged from 5 Hz to

100 KHz. Outside this range, impedance value were either too low or too high for this instrument to display. The voltage was kept at 0.2 V or lower to ensure that no extra chemical reactions will interfere with the measurement. The concentration of the NaCl solution is 0.1 mol / L which is close to the 0.9% NaCl solution. DMEM (Dulbeccos Modification of Eagles Medium) was also used in some occasions. It is one of the media used in this project for cell culture and for recording.

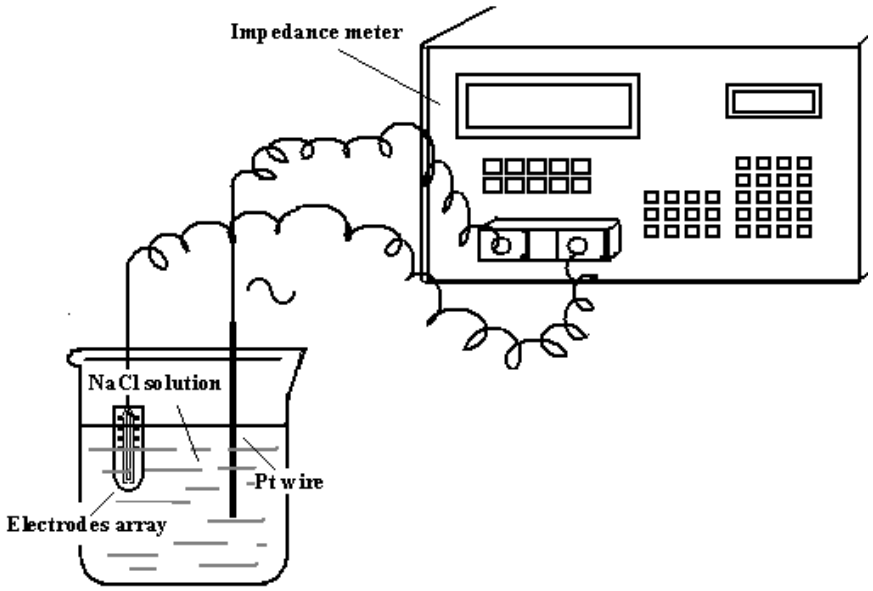

Figure 4-6: The set up for measuring the impedance between the FlexMEA and the reference electrode immersed in the electrolyte.

The microelectrodes measured were mainly platinized FlexMEA of 25 *μm* diameter. There were some un-platinized FlexMEA also, as well as some platinized pMEA of 5 to 100 *μm* diameter. The FlexMEA is on a substrate of Kapton HN ® polyimide film. As mentioned in Chapter two, most of the electrode array including the connecting wires is insulated with a polyimide layer (PI2545) except for the vias at the tip of microelectrodes.

Figure 4-7: The schematic of an insulated FlexMEA.

The reference electrode is a platinum wire. Its diameter is about *0.5 mm*. The reference electrode together with the FlexMEA were immersed in the electrolyte. They are the only solid conductors in the solution. The impedance at the interface of FlexMEA/electrolyte dominates the measured impedance.

During the measurement it was found that the value of the impedance at low frequency has a tendency to decrease over time. The decreasing was up to 20% of the total impedance. The impedance of the platinized electrode appears to be more stable than the un-platinized electrode in the measurement.

4.10. Data fitting

4.10.1. Nyquist plot of parallel R-C

A Nyquist plot can present on a 2D coordinates the impedance data *Z(ω)* that is dependent to the frequency. The impedance of microelectrodes here was measured by driving the AC current of different frequency through them. In a Nyquist plot the real part of *Z(ω)* is plotted on the *X* axis and the imaginary part on the Y axis. Each point on the plot is corresponding to an impedance value at a certain frequency. These point together form a curve.

A capacitor *C* and a resistor *R* in parallel have a Nyquist plot that is a half-circle.

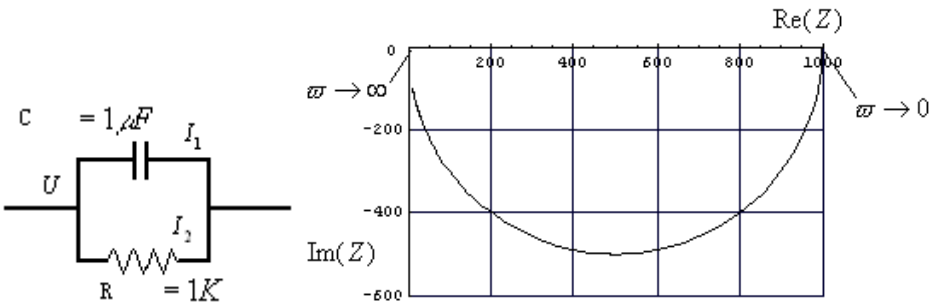

Figure 4-8: A capacitor in parallel with a resistor. The Nyquist plot of their impedance is a half circle of radius R/2 centred at (R/2,0).

4.10.2. Ideal impedance plot of microelectrode

From the theoretical model of un-platinised microelectrode (section 4.7) and that of the platinised one (section 4.8), the ideal Nyquist plot of their impedance *Z(ω)* is shown in the following figure. The parameters of the un-platinised microelectrode in the figure are:

Frequency range	1 Hz ~ 10 KHz
Charge transfer resistance	$R_t = 1\times10^6\ \Omega$
Interfacial capacitance	$C_i = 1\times10^{-9}$ F
Spreading resistance	$R_s = 1\times10^5\ \Omega$
Warburg impedance (real part)	$Real[Z_w] = 5\times10^5 / \sqrt{\omega}$

The parameters of the platinised microelectrode have the same value except its

pore impedance:

$$Real[Z_p] = 1\times10^7 / \sqrt{\omega}$$

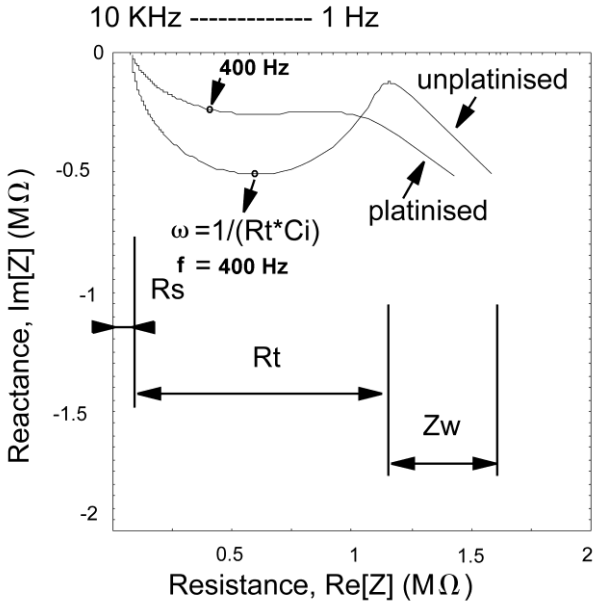

Figure 4-9: The ideal and typical Nyquist plot of the impedance of microelectrode. The plot of the un-platinised microelectrode is the combination of a half circle and a straight line. The platinised one is like a distorted version of the un-platinised one. Points on the left hand side of the plot have higher frequency than those on the right hand side. The frequency of 400 Hz was marked on the plot.

The little gap at the top left part is caused by the spreading resistance. The diameter of the half circle is equal to the charge transfer resistance R_t. The straight line part suggests the existence of a Warburg impedance. This line has a slope of 0.5. That is why the Warburg impedance is called a constant phase element also. The interfacial capacitance C_i affects the plot in a way that cannot be easily seen. It does not change the shape of the curve. The following diagrams show how the interfacial capacitance changes the Nyquist plot.

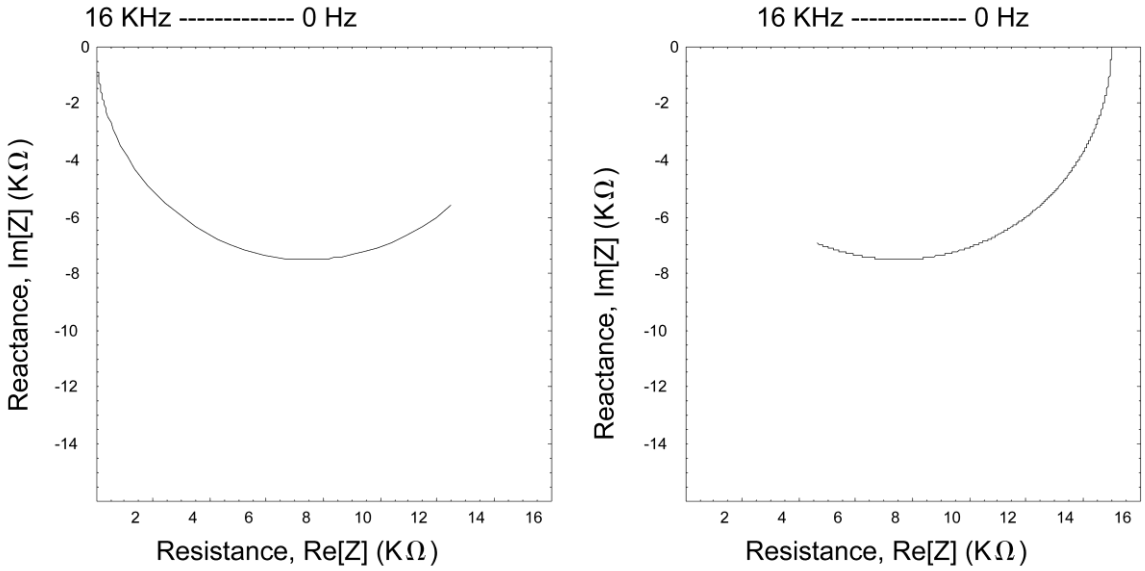

Figure 4-10: The Nyquist plot of impedance model with different parameters. The parameters are: The charge transfer resistance is R_t = 15 KΩ. The spreading resistance is R_s = 0. The Warburg impedance basically does not affect this plot. The interfacial capacitance in the first plot is bigger C_i = 30 μF. It is smaller in the second plot C_i = 0.3 μF. Both diagram are in the frequency range 0 ~ 16 KHz.

As shown in the plot, with the decrease of the interfacial capacitance, the arc shifts to the region of lower frequency.

For a CR circuit the point in the centre of the arc (shown in **Figure 4-9**) corresponds to the frequency $\omega = 1 / (R_t C_i)$. This is roughly true for the impedance model of the un-platinised microelectrode. It is not followed at all by the model of the platinised microelectrode. So in principle we can use the Nyquist Plot to obtain values for the spreading resistance, charge transfer resistance, interfacial capacitance of the un-platinized electrode. However many microelectrodes do not have a Nyquist plot that is a clear arc followed by a line of slope 45°.

4.10.3. Data fitting

As described above, the value of R_s , R_t *and* C_i can be estimated by reading the Nyquist plot of experimental data. But this is not enough. Not only because that accurate values cannot be obtained from picture reading, but also because of Nyquist plot obtained from the experiment data is not an ideal Nyquist plot. The experimental data covers only part of the whole frequency range. And the data from experiment simply does not behave well as what the model predicted.

The following chart is the measured impedance of both a platinised and an un-platinised microelectrode. By comparing them with the ideal Nyquist plot in **Figure**

4-9, it is difficult to decide which part they belong to. The data could be part of the circle or be part of the declining line. These alternative interpretations lead to different values. The former results in small Warburg impedance. The latter leads to huge Warburg impedance. Later in the data fitting, both were obtained. For some electrodes small Z_w gave the LMSR and for some else big Z_w fitted better. The details are in section 4.11.1.

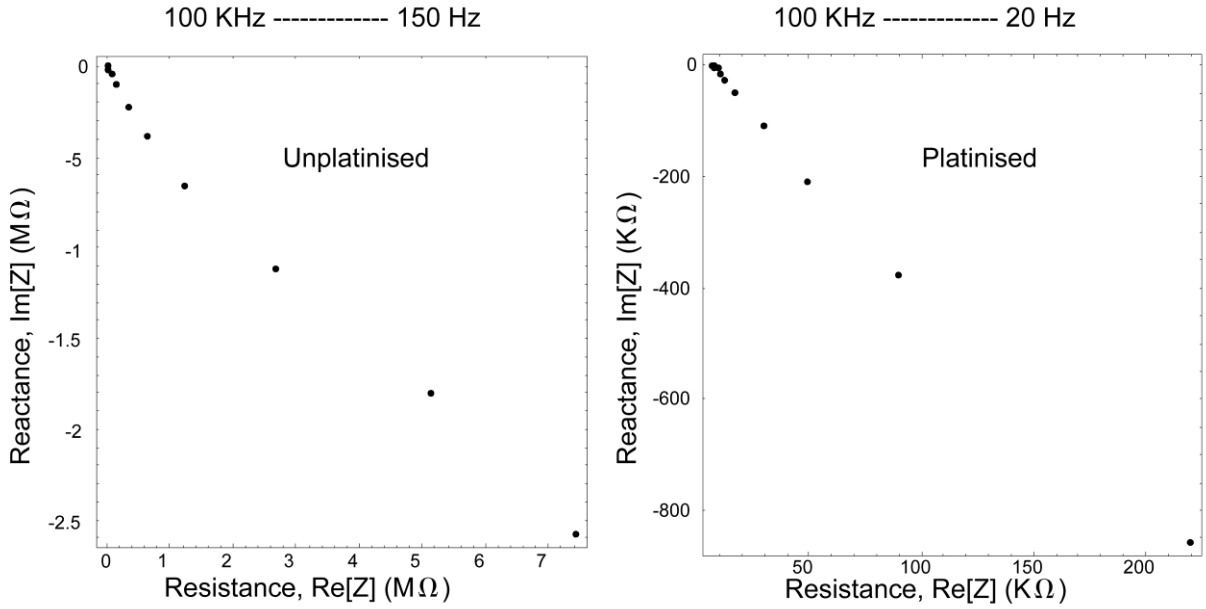

Figure 4-11: The Nyquist plot of the experimental data of two electrodes. One is platinised and the other is not. Each point represents a measured impedance at a certain frequency. One plot shows the impedance of one microelectrode. A MEA needs many Nyquist plots to show the impedance of every electrodes.

If the model with estimated value of parameters and the experiment data are compared, differences will be found between each pair of data. Therefore, an algorithm is required to fit the model to the experimental data. An algorithm using the least root mean square is employed.

Root mean square = $\sqrt{(d_1^2 + d_2^2 + \cdots + d_k^2) / k}$

Two types Mathematica programs (details in section 4.11.3) were programmed. One program utilizes the exhaust algorithm to search for the LMSR. The other program uses the built-in function of Mathematica (NonLinearFit). This function also looks for a least-squares fit. The algorithm used by this function are LevenbergMarquardt and FindMinimum.[NonLinearFit notes, wolfram research]

4.11. Fit the conventional circuit model

In the previous sections we introduced two circuit models. One is for the un-

platinised electrode and the other for the platinised electrode. They are called as the conventional circuit model or the complete circuit model. This is to distinguish them from the simplified circuit model that will appear in the next section. In this section the complete circuit model is used to fit with the experiment data. The value of parameters obtained are presented and compared with those predicted in the previous sections.

4.11.1. Fit the un-platinised

The ideal Nyquist plot of the conventional circuit model of a un-platinised electrode is a combination of a semicircle and an oblique line. That of the platinised electrode varies a little but these features can be recognized still. However, the vast majority of our data does not show these features. It was appeared only in a few platinsed electrodes (the semi-circle at the top right of the **Figure 4-24**). The impedance of them is distinctively larger than other microelectrodes in the same array, which suggests failed platinisation or fabrication.

Although the conventional circuit model was not well consistent with the experimental data, we still tried to fit them. Each electrode was fitted and generated one set of parameters. The results are shown here.

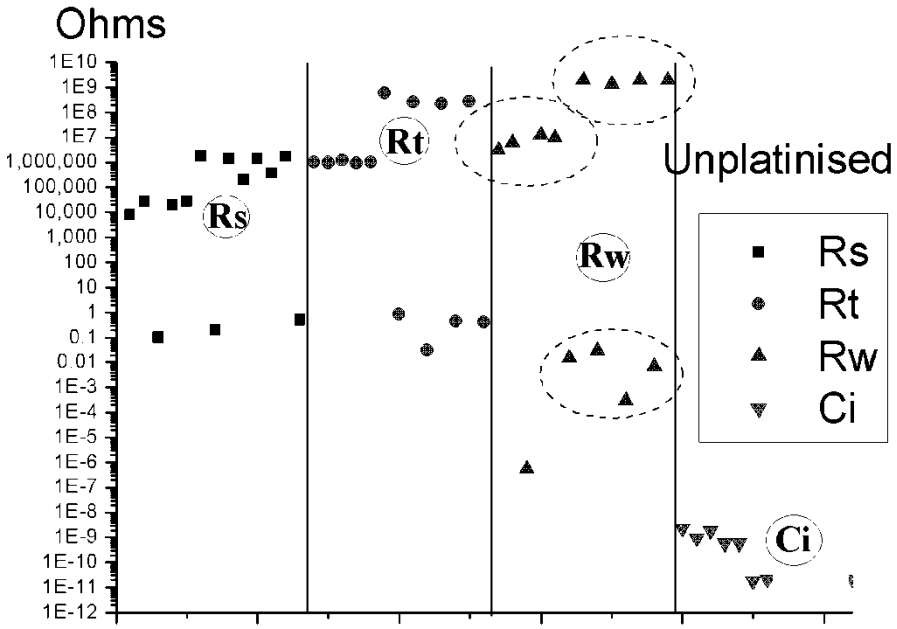

Figure 4-12: The data fitted parameters of each unplatinised electrode. The x axis is the sample number of the electrode. Each point reprents a fitted parameter value. The circled parameters (e.g. circled Rs) is the average value which will be used in the final model.

Although some of these electrodes are from one same array, the estimators of Rt

and Rw in different electrode show significant difference. These electrodes can be distinguished into many groups according to the value range of their parameters. Some groups features bigger Rt and other groups has bigger Rw.

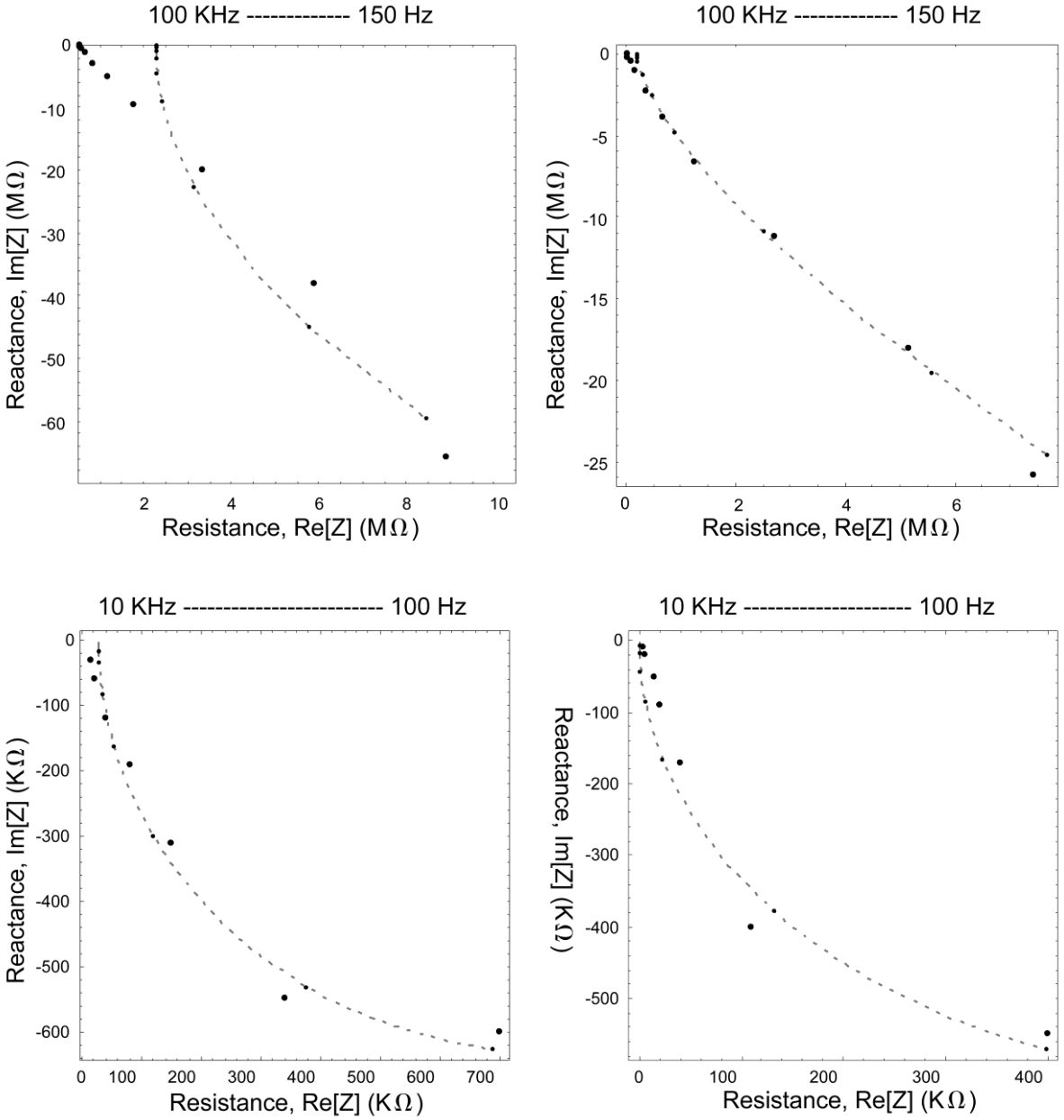

Figure 4-13: Four examples of data fitting. These electrodes were from two unplatinised FlexMEAs. The bigger dots are the experiment data. The smaller dots on the dashed line are fitted.

The fitted parameters of these four electrodes are:

	R_s	R_t	C_i (Farad)	Z_w	mean squared error
UL	$1.78*10^6$	$5.81*10^8$	$1.76*10^{-11}$	$0.035(1-j)/\sqrt{\omega}$	$1.9*10^{13}$
UR	$1.98*10^5$	0.27	$2.74*10^{-11}$	$1.35*10^9(1-j)/\sqrt{\omega}$	$1.5*10^{12}$
BL	$2.8*10^4$	$9.6*10^5$	$9.4*10^{-10}$	$6.3*10^6(1-j)/\sqrt{\omega}$	$1.1*10^9$
BR	0.1	$1.2*10^6$	$1.9*10^{-9}$	$5.6*10^{-7}(1-j)/\sqrt{\omega}$	$4.3*10^8$

The data fitting interprets the data in two different ways. In the first, R_t dominates and Z_w can be ignored. In the second way, Warburg impedance plays the

major role.

For my personal view, I tend to trust the interpretation with negligible Zw. Even the other has smaller MSE (mean squared error). Because it has been predicted in previous sections that the Warburg impedance is not significant (*99.3 × (1 - j) / √f (Ω)*) in the whole impedance of the microelectrode. However, this brings subjective judgment to the data fitting. The judgment is not necessarily correct.

If Warburg impedance is chosen to be neglected in the model, the impedance model will be simplified and makes its simulation in PSPICE possible, because implementing Warburg impedance in PSPICE is not easy. In the next section a simplified model, in which the Warburg impedance is removed, is used to fit the data.

4.11.2. The difference between the value predicted and the value from experiment (un-platinised electrode)

The following are the values obtained from data fitting of un-platinised electrodes. The results were divided into four groups as stated at last section and were averaged separately.

Table 4-1: The comparison of parameters predicted and that from fitting the measured.

	R_s	R_t	C_i (Farad)	Z_w
Value predicted	4~12 kΩ	13.4 MΩ	2.5 nF	99.3 (1-j) /√f Ω
Fitted (average of all)	535 kΩ	104 MΩ	0.5 nF	551(1-j) /√ω MΩ
Fitted (average of group 2, 4)	750 kΩ	128 MΩ	1.1 nF	0.005(1-j) /√ω Ω
Fitted (average of group 1)	21 kΩ	0.97 MΩ	1.1 nF	**7.9 (1-j) /√ω MΩ**
Fitted (average of group 2)	0.01 kΩ	1.2 MΩ	1.9 nF	$5*10^{-7}$ (1-j) /√ω Ω
Fitted (average of group 3)	*141 kΩ*	*0.4 Ω*	*0.2 nF*	***1.8 (1-j) /√ω GΩ***
Fitted (average of group 4)	*1.5 MΩ*	*254 MΩ*	*0.3 nF*	*0.01 (1-j) /√ω Ω*

The value of Z_w in group 1 and 3 is far too larger than that predicted. The value of Z_w in group 2 and 4 is small. The predicted value of the Warburg impedance is far smaller (around *1Ω* at *10 KHz*) than the charge transfer resistance. Due to this reason, Warburg impedance is sometimes neglected with little change to the accuracy of the model.

The value of the C_i from data fitting is consistent with the theoretically predicted value. While the value of the R_s and R_t are not.

4.11.3. Fit the platinised

For the circuit model of un-platinised electrode, three of its four parameters can be predicted (R_s , C_i , R_w) and one parameter(R_t) with a rough value range. A prediction narrows the range of searching in data fitting. For that of a platinised electrode, only two of its five parameters can be predicted (R_s , R_w). The effect of platinum black coating is hard to predict without measurements. Therefore, the parameters of platinised electrode (C_i , R_t , Z_p) are not predicted in this chapter. More unknown parameter and wider value range reduce the reliability of the results from data fitting.

Although lacking reliability, data fitting to the platinised electrodes was conducted and the results are presented here.

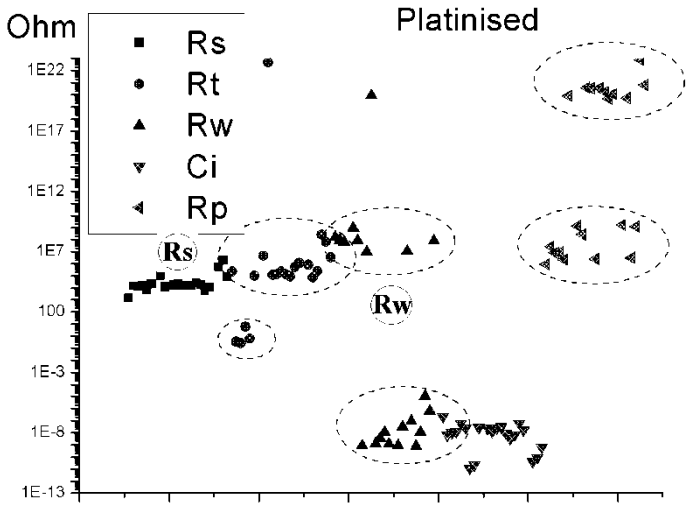

Figure 4-14: The estimated parameters of platinised electrodes obtained by data fitting. The x axis is the sample number of the electrode. These electrodes were from several different arrays. The predicted value of Rs and Rt are marked in the graph.

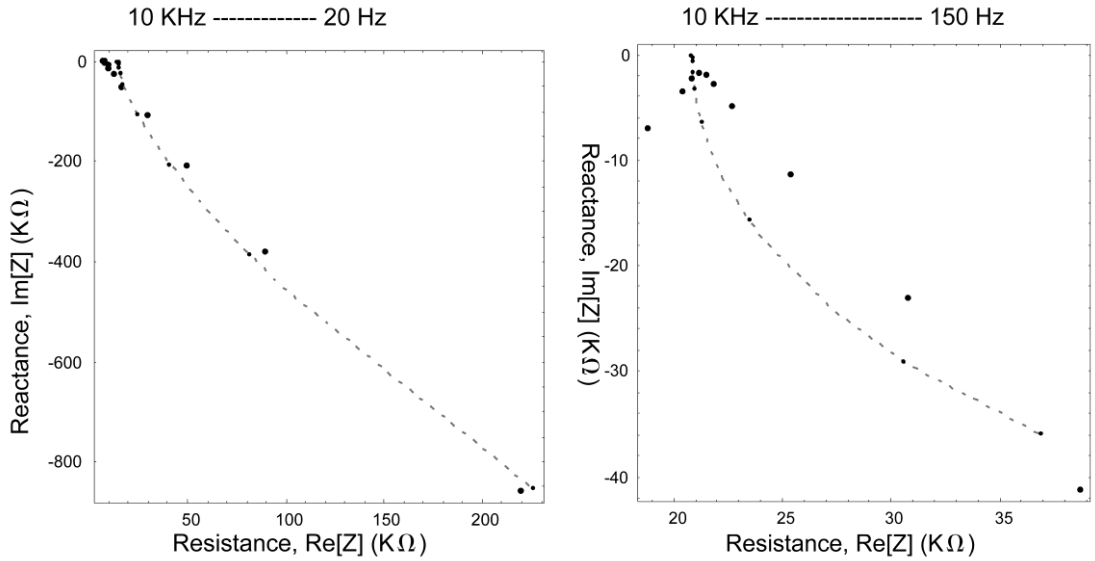

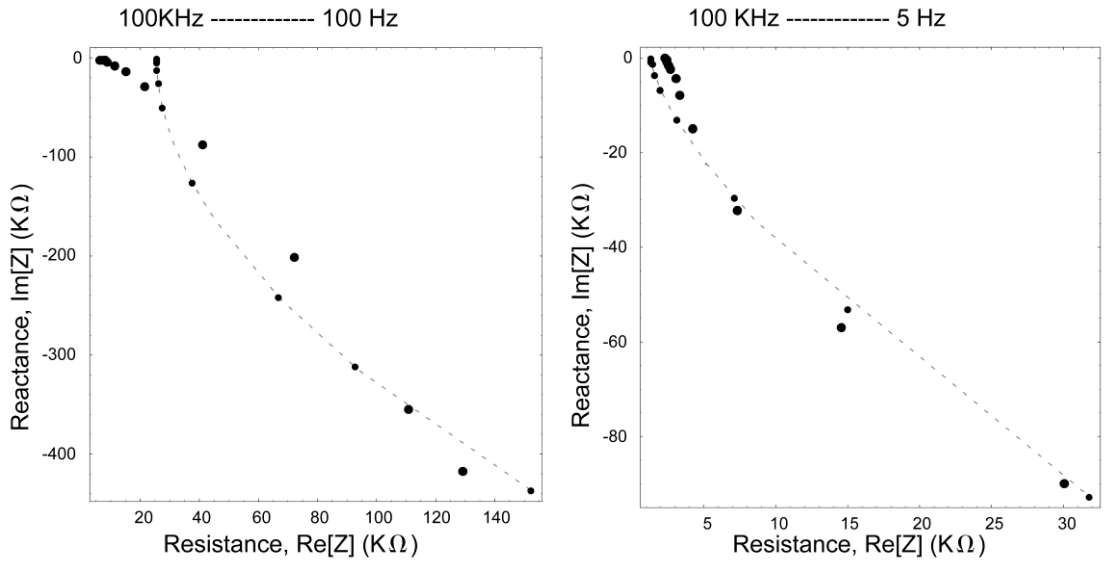

Figure 4-15: Four electrodes are shown as some examples. These platinised electrodes were from four different arrays. The bigger dots are experiment data. The smaller dots and the dashed line are fitted.

The parameters of these electrodes estimated are:

	R_s	R_t	C_i (Farad)	Z_w	Z_p	MSE
UL	$1.46*10^4$	0.34	$6.6*10^{-9}$	$9.3*10^7$ (1-j)/ $\sqrt{\omega}$	$2.63*10^7$ (1-j)/ $\sqrt{\omega}$	$6.1*10^7$
UR	$2.1*10^4$	$9.7*10^4$	$2.46*10^{-8}$	$8.46*10^{-10}$ (1-j)/ $\sqrt{\omega}$	$7.83*10^{19}$ (1-j)/ $\sqrt{\omega}$	$2.4*10^7$
BL	$2.6*10^4$	$1.1*10^6$	$3.1*10^{-9}$	$1.05*10^7$(1-j)/ $\sqrt{\omega}$	$1.1*10^{20}$(1-j)/ $\sqrt{\omega}$	$1.0*10^9$
BR	$1.3*10^3$	$2.23*10^5$	$2.08*10^{-7}$	$1.7*10^8$(1-j)/ $\sqrt{\omega}$	$8.8*10^5$(1-j)/ $\sqrt{\omega}$	$5.5*10^6$

Take the average value of all electrodes, the results are:

	R_s	R_t	C_i (Farad)	Z_w	Z_p
Value predicted	4~12 kΩ	?	?	248 (1-j) /$\sqrt{\omega}$ Ω	?
Fitted (average)	110 kΩ	12.5 MΩ	58.1 nF	68(1-j) /$\sqrt{\omega}$ MΩ	$3.2*10^{21}$(1-j)/$\sqrt{\omega}$ Ω

4.11.4. Some guidance for analyzing data

The spreading resistance is the most accurately predicted element in the model, because its mechanism is clear. Those parameters to define it, like the geometry of microelectrode and the conductivity of electrolyte, are well known. They are not uncertain unlike the actual surface area and the exchange current density, whose values are never know for sure. Therefore, the theoretical predicted value of spreading resistance is believable. Moreover, the spreading resistance in the Nyquist plot is also easy to recognize. It is the intersection point of the arc with the *X*-axis.

For the microelectrode of thirty microns diameter, the spreading resistance is in the ten thousand ohms range. When analyzing data, it is recommended first to look for the spreading resistance (Rs). If the intersection point is at about ten thousands of ohms on the *X* axis, it could be Rs. If it is much larger than that, it could be the

charge transfer resistance (Rt). Or it may suggests an accidentally increased spreading resistance, which may caused by electrode damage.

In the Nyquist plot of an ideal microelectrode (Figure 4-9), what follows R_s has to be an arc and what follows R_t is a straight line.

4.12. The circuit model of simplified

The model in this section is a simplified version of the model used in previous sections. The Warburg impedance and the pore impedance are removed. Both the platinised and un-platinised electrodes share the same model as shown below. This is to obtain a model that could be used in PSPICE. This simplified model is compared to the complete circuit model and the MacAdam's model (figure 4-18). In sense of MSE to the data this model is not significantly worse than the other two.

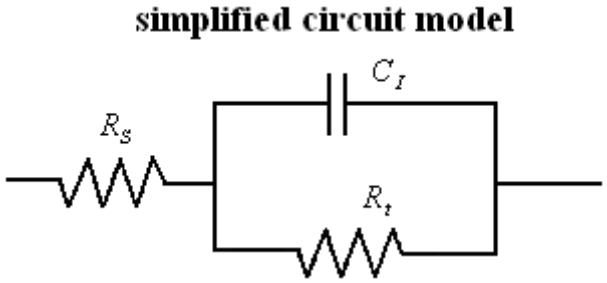

Figure 4-16: The simplified circuit model. It is used to fit both platinised and un-platinised electrodes.

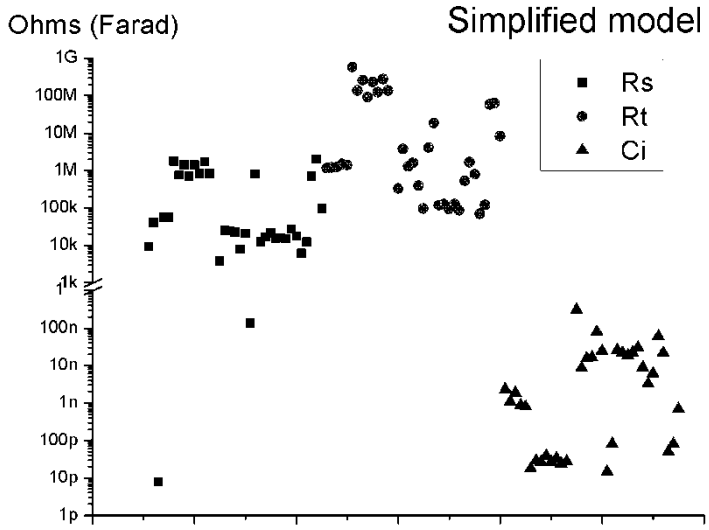

Figure 4-17: The values of the parameters obtained by fitting the simplified model to the data. The x axis is the sample number of the electrode. Both platinised and un-platinised microelectrodes are shown in this graph since they share the same model.

The results are compared to that predictied.

	R_s	R_t	C_i
Value predicted (unplatinised)	4~12 kΩ	13.4 MΩ	2.5 nF

Mean value of fitted (unplatinised)	736 kΩ	141 MΩ	0.5 nF
Value predicted (platinised)	4~12 kΩ	?	?
Mean value of fitted (platinised)	183 kΩ	7.7 MΩ	32 nF

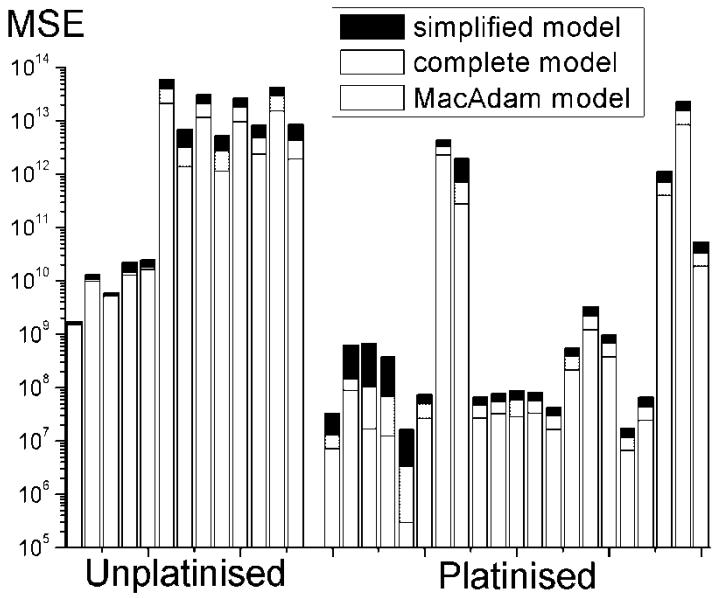

Figure 4-18: The mean square error of data fitting. That is a measure of the difference of the model to the data. Three models were compared. Despite only a few, most of the electrodes fit bestly with MacAdams model. The complete circuit model and the simplified circuit model followed.

4.13. MacAdam's empirical model

4.13.1. MacAdam's empirical model

Most of our microelectrodes show an impedance over the frequency range that can be approximated by an oblique line on the Nyquist plot. MacAdam found the same tendency in his measurements of metal electrodes. He proposed an empirical equation to describe the data [MacAdam, 1985].

$$Z = R_{total} + K\,(j\omega)^{-\beta}$$

Where,
Z is the impedance of the electrode;
R_{total} is the sum of the spreading resistance and the resistance of conductor;
ω is the radian frequency;
$\Phi = \beta\pi/2$ is the phase angle in radian.

The equation can be transformed into:

$$Z = R_{total} + K\cdot\omega^{-\beta}\cos(\beta\cdot\pi/2) - j\cdot K\cdot\omega^{-\beta}\sin(\beta\cdot\pi/2)$$

The variables corresponding to experimental data are the impedance (Z) and the radian frequency (ω). The parameters need to be determined are R_{total}, K, β.

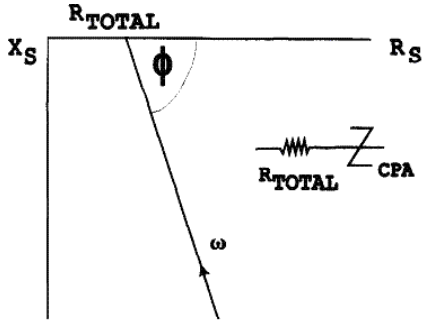

Figure 4-19: Redrawn from MacAdam [1995] with inverted Y axis. Typical Nyquist plot of a metal electrode.

4.13.2. Fit the data with MacAdam's mode

The MacAdam's empirical equation is used to fit our data. They fit well. The figure is one example of these data fittings.

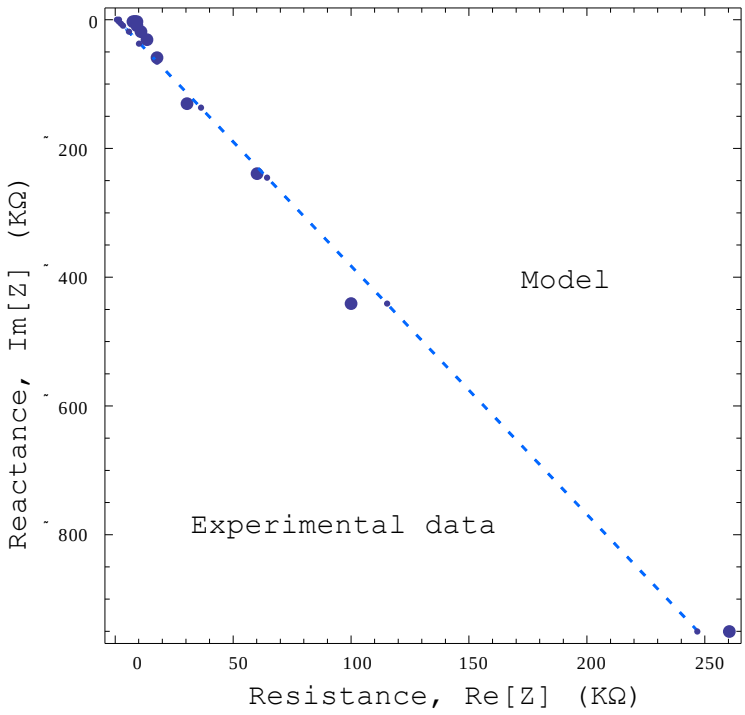

Figure 4-20: The figure shows one example of the data fitting. This electrode is a platinised FlexMEA. The thick dots are the experimental data. The sample frequency range was from 20 Hz to 100 KHz. The dashed line and thin dots are estimated with MacAdam's empirical equation. The estimators are: r = 860; K = $5.6*10^7$; ß = 0.84.

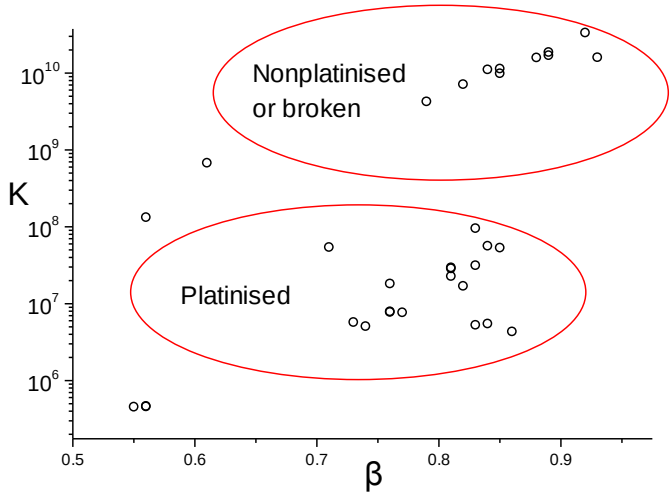

Figure 4-21: The parameters (K, ß) obtained from data fitting of FlexMEAs using MacAdam's empirical equation.

As seen in the figure, the *K* and *ß* of the platinised electrodes are smaller than the un-platinised in average. Also, the phase angle of both platinised and unplatinised are bigger than 45 degrees ($ß > 0.5$).

4.13.3. The value obtained for MacAdam's model

Table 4-2: The mean value of the parameters obtained by fitting MacAdam's model to the data.

	Un-platinised electrode	Platinised electrode
K	1×10^{10}	2×10^{7}
ß	0.85	0.80

4.13.4. The methods used in data fitting

Construct a new function

Two methods are used for data fitting. The first is programming in Mathematica looking for the least mean square. The second uses the integrated function (*NonLinearFit*) in Mathematica.

There are commercial software for data fitting. For example, MatLab, Origin Pro. However, according to the preliminary understanding, these software do not support complex functions. Two ways are tried here to avoid dealing directly with complex function. In the first way, the complex function is divided into the real part and the imaginary part: $R_{total} + K\cdot\omega^{-ß} cos(ß\cdot\pi/2)$ *and* $- j\cdot K\cdot\omega^{-ß} sin(ß\cdot\pi/2)$. They are fitted respectively and result in two sets of optimized parameters. The problem of this method is that two sets of parameters do not necessarily match.

The other method constructs a new function:

$$Zero = [R_{total} + K\cdot\omega^{-\beta}\cos(\beta\cdot\pi/2) - Z_x]^2 + [-K\cdot\omega^{-\beta}\sin(\beta\cdot\pi/2) - Z_y]^2$$

This function is the square difference of the data to the model.

Exhaustive search for the least mean square

The most primitive method is used in our program. The exhaustive search in other words is that calculates all possible and find the smallest. All parameters are valued in their value range in a certain density. Each set of parameters gives a set of impedance values, which are compared with the data. The least mean square difference is found in this way. The shortcoming of this approach is the huge amount of calculation. The higher precision of the parameters, the more calculations are required. Therefore it is important to narrow the value range of the parameters, to avoid unnecessary calculations. Here we define $r>0$, $K>0$, $0<\beta<1$.

Integrated NonLinearFit function in Mathematica

The built-in function NonLinearFit finds a least-squares fit to a list of data for a model. The algorithm used by the NonlinearFit function are LevenbergMarquardt and FindMinimum. [NonLinearFit notes, wolfram research]

4.14. Plot of experimental data

The examination of electrode impedance between uses is important to know which electrodes are working. The failure includes both very high resistance (may caused by loosing connection or metal film broken) and very low resistance (by failed insulation).

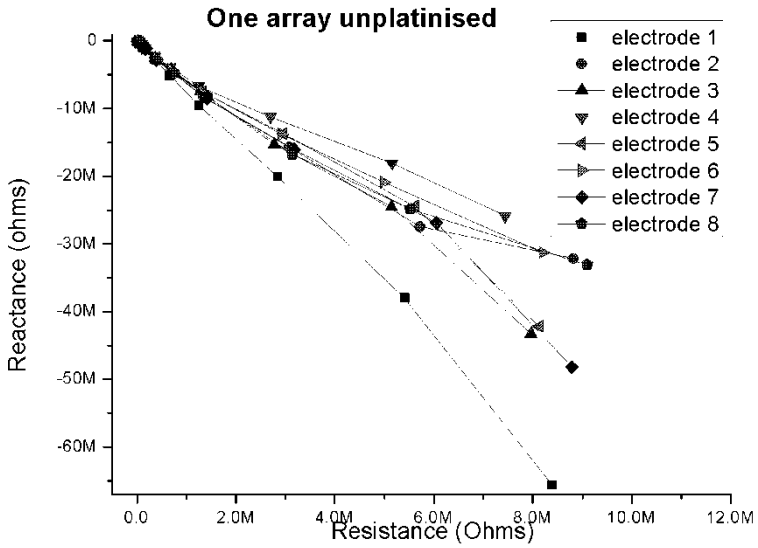

Figure 4-22: The Nyquist plot of eight un-platinized microelectrodes of one same array.

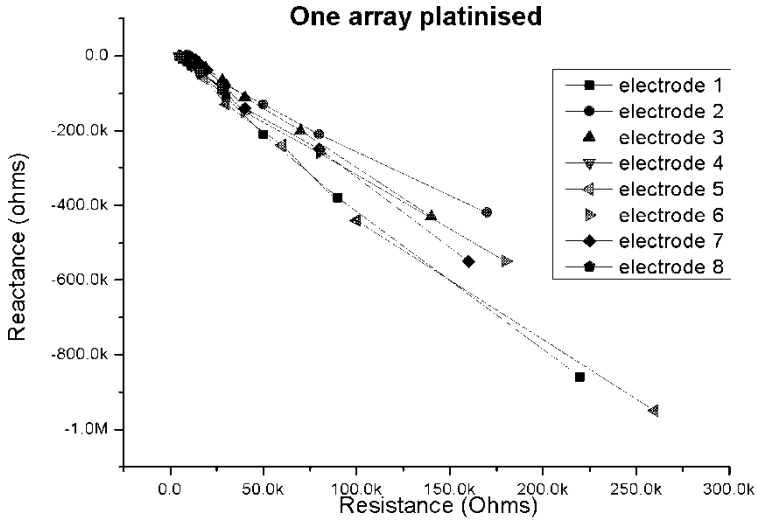

Figure 4-23: The Nyquist plot of eight platinized microelectrodes on one same array.

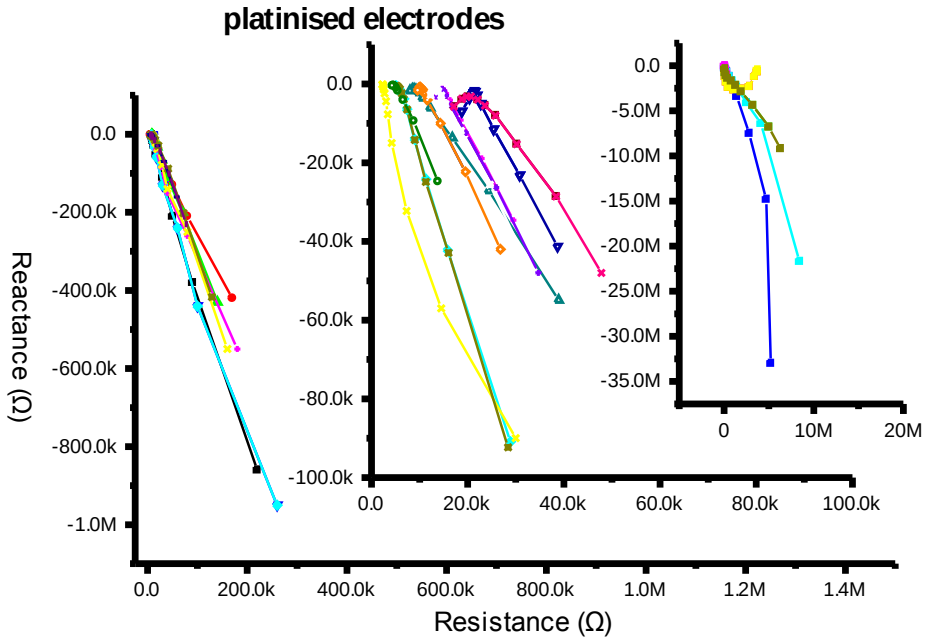

Figure 4-24: The Nyquist plot of a series of data of platinized microelectrodes. Different colors represent different microelectrodes. Data is put in three groups according to their range of magnitude. Those electrodes at right side with very high resistance can be identified as failed.

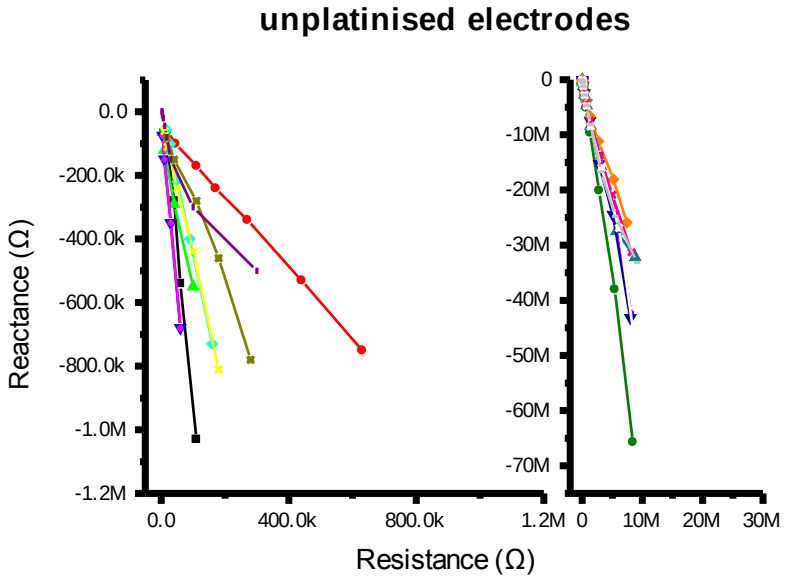

Figure 4-25: The Nyquist plot of a group of un-platinized microelectrodes. Different colors represent different microelectrodes. Data is divided into two groups according to their range of magnitude.

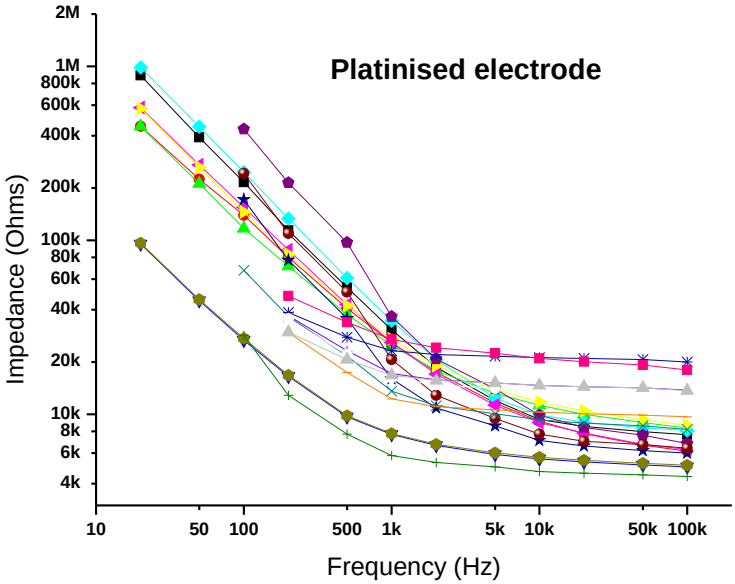

Figure 4-26: The impedance magnitude of a group of platinized microelectrodes against frequency. Different colors represent different microelectrodes.

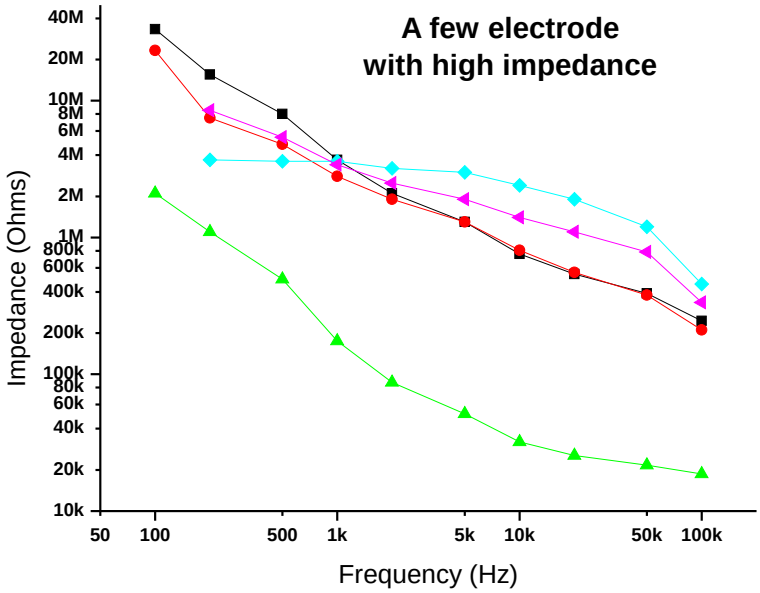

Figure 4-27: The impedance magnitude of a group of unsuccessfully platinized or broken microelectrodes against frequency. Different colours represent different microelectrodes.

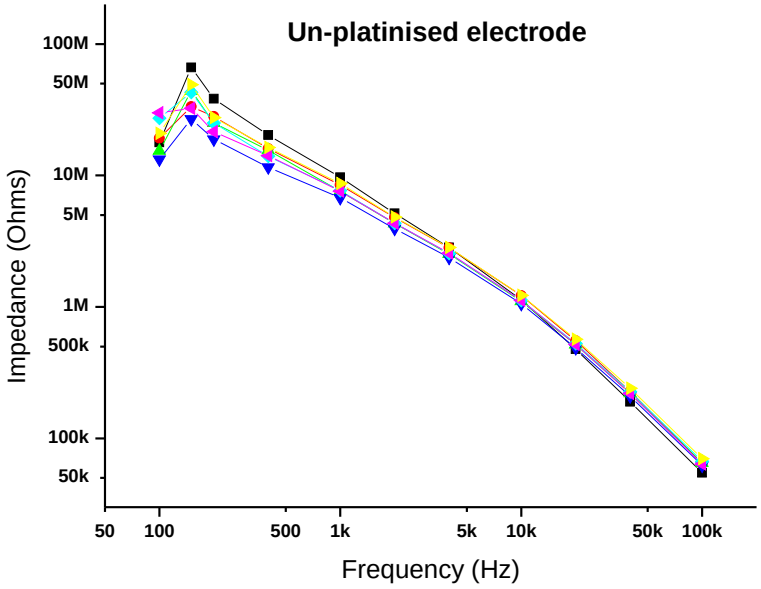

Figure 4-28: The impedance magnitude of a group of un-platinized microelectrodes against frequency. Different colors represent different microelectrodes.

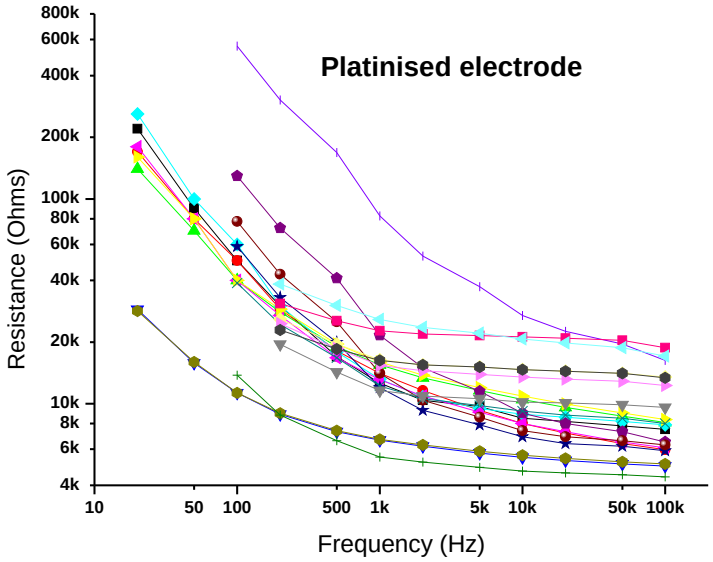

Figure 4-29: The resistance (real part of the impedance) of a group of platinized microelectrodes against frequency. Different colors represent different microelectrodes.

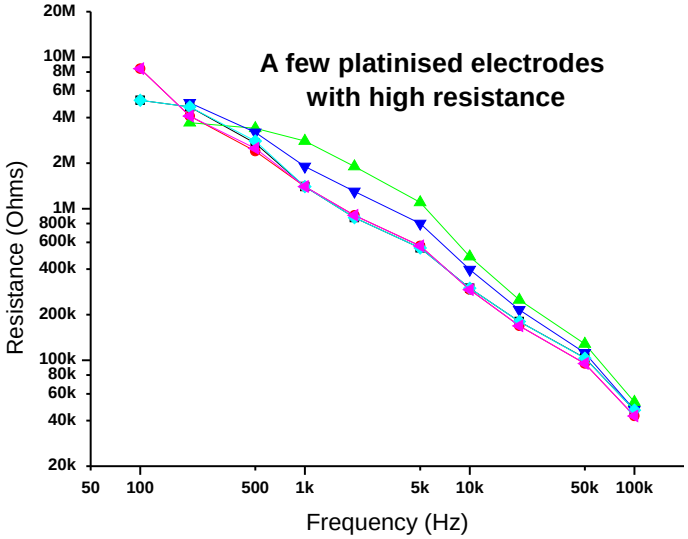

Figure 4-30: The resistance (real part of the impedance) of a group of unsuccessfully platinised or

broken microelectrodes against frequency. Different colors represent different microelectrodes.

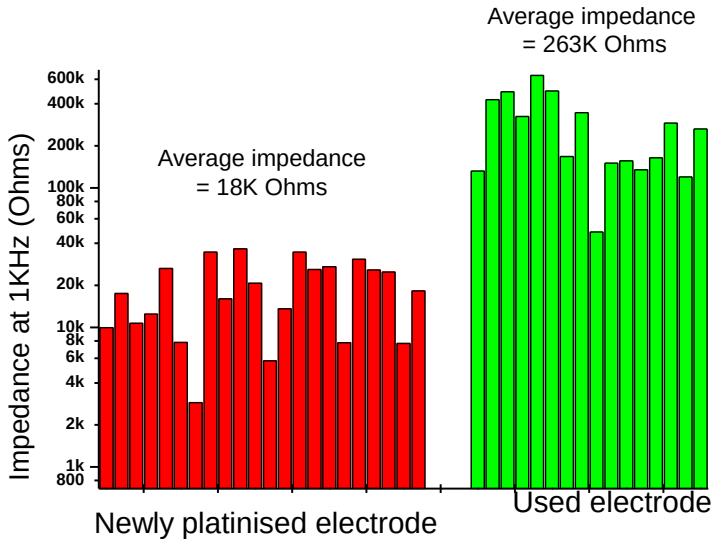

Figure 4-31: The comparison of the impedance magnitude between a group of new and used microelectrodes at 1 KHz. Each pillar represents one microelectrode.

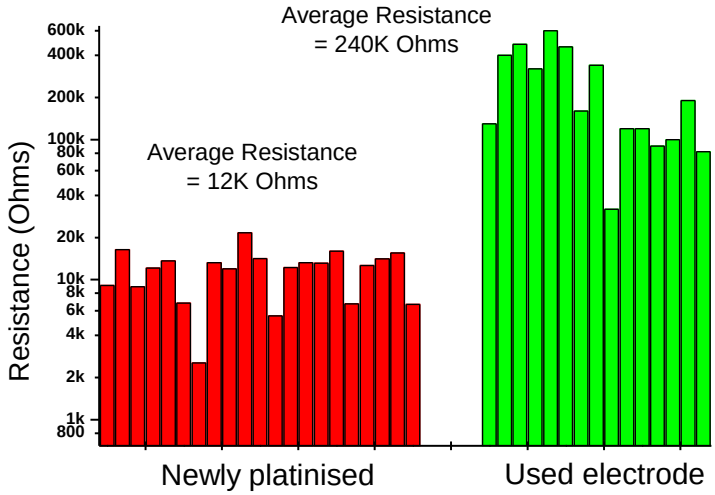

Figure 4-32: The comparison of the resistance (real part of the impedance) between a group of new and used microelectrodes at 1 KHz. Each pillar represents one microelectrode

These FlexMEAs in **Figure 4-31** and **Figure 4-32** are on substrate of Kapton HN ® polyimide film (150 µm) with electrodes of 25µm diameter. These used FlexMEAs have been emerged in medium (DMEM supplemented with FBS) for recording from the culture of cortex or hippocampal cells. Each recording will last for 1 to 8 hours. They were taken out of medium and left in air at room temperature between the experiments. The time that they have been used were from 1 to 2 months. Before this measurement they were rinsed in flowing water to clean. Harsh ways of cleaning was not used to avoid damage the microelectrodes.

The reason why the resistance rises in these used FlexMEA needs further investigation. The damage of the platinum black coating may raise the resistance.

The debris of cells or other materials may also block the coating and raise the resistance. The clean procedure before the measurement cannot take away all these materials.

4.15. Summary

The conventional circuit model does not fit well with the experimental data. An ideal fit would have the estimators of similar electrodes distributed around one certain value. Because these electrodes are supposed to have similar impedance with a few exceptions. However, the fitted values distributed widely in several groups (Fig4.12, Fig4.14). Therefore taking the average value as the result is not convincing. It is worse when the conventional circuit model is used to fit the platinised electrodes.

The simplified circuit model does not fit well with the data too. This can be concluded from the mean square error of the data fitting (Fig 4.18). This model has the highest MSE in comparison to that of the conventional circuit model and MacAdam's model. The good aspect of this model is that its estimators for the similar electrodes have a converged distribution (Fig 4.17).

The empirical model of MacAdam's is more suitable to fit the data than the other two models. The experiment data conform to the model by the MSE of the fitting (Fig 4.18). The distribution of the estimators of similar electrodes also converges(Fig 4.21).

The value predicted and the value estimated from fitting are listed here. Note that the conformity of the two circuit models with data is low. And MacAdam's model does not have predicted values.

Table 4-3: The parameters obtained for the three models, including the value predicted and the value estimated.

Conventional circuit model	*Rs*	*Rt*	*Ci*	*Zw*	*Zp*
Predicted(unplatinised)	*4~12 kΩ*	*13.4 MΩ*	*2.5 nF*	*99.3 (1-j) /√f Ω*	
Fitted(unplatinised)	*535 kΩ*	*104 MΩ*	*0.5 nF*	*551(1-j) /√ω MΩ*	
Predicted(platinised)	*4~12 kΩ*	*?*	*?*	*248 (1-j) /√ω Ω*	*?*
Fitted (platinised)	*110 kΩ*	*12.5 MΩ*	*58.1 nF*	*68(1-j) /√ω MΩ*	$3.2\times10^{21}(1-j)/\sqrt{\omega}\ \Omega$

Simplified circuit model	R_s	R_t	C_i
Value predicted (unplatinised)	*4~12 kΩ*	*13.4 MΩ*	*2.5 nF*
Mean value of fitted (unplatinised)	*736 kΩ*	*141 MΩ*	*0.5 nF*

Value predicted (platinised)	*4~12 kΩ*	*?*	*?*
Mean value of fitted (platinised)	*183 kΩ*	*7.7 MΩ*	*32 nF*

MacAdam's model	Unplatinised electrode	Platinised electrode
K	1×10^{10}	2×10^{7}
B	*0.85*	*0.80*

Many factors in the measurement of impedance may affect the reliability of the data obtained. The voltage applied on the electrode by the impedance meter is one of these factors. The transfer function of the electrode in medium is not linear. The current driven through the electrode/electrolyte interface is only semi-linear to the voltage applied. It means that by varying the voltage the impedance will change as well. The voltage used in the measurement was 0.2 mV.

The stray capacitance is another factor that may effect the reliability of the measurement. There is stray capacitance between the wires that connect to the microelectrode and to the reference electrode. To minimize it, short wire was used (about 20 cm) and the distance between two wires were kept at about 20 cm.

Chapter 5.Oxygen diffusion model

5.1. Introduction

Cells die without oxygen. Normally *in vitro* they take up oxygen from the medium and the oxygen level in the medium is maintained by atmospheric pressure. However in this work we wished to culture the cells in a small volume – the space between the neural bathtub and the MEA. This cylindrical chamber is *15 μm* high and has a diameter of *13 mm*. In such a chamber, molecular diffusion is the main mechanism by which oxygen is transported to cells as convective flow of the medium is deliberately avoided so that the network is preserved intact.

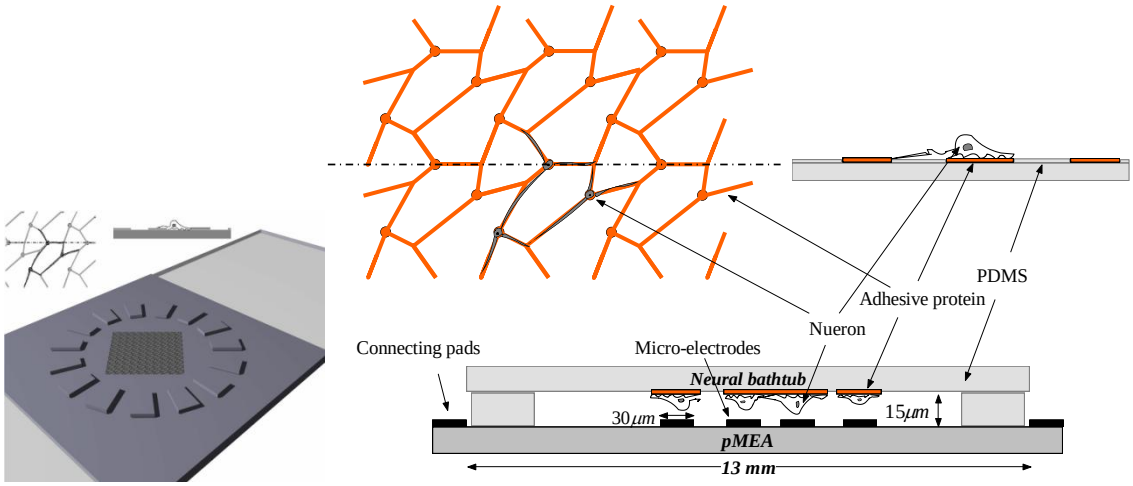

Figure 5-1: The figure at left is a 3D represent of the 'neural bathtub'. The one at right is a schematic drawing of the 'neural bathtub' at its working position sitting on a pMEA. The oxygen concentration inside the shallow space (cylindrical chamber) between them is what we are going to model.

However, oxygen diffusion is only efficient over relatively short distances. Krogh (1941) said, 'diffusion alone can provide sufficient oxygen only to organisms of 1mm diameter or less'. The oxygen diffuses in water for 1 hour gives a value of $\sqrt{Dt}$ of *3.64 mm* [Han, P., and D. M. Bartels, 1996]. The possibility of anoxia in the tiny chamber exists. To gain a quantitative insight, the distribution of oxygen in the chamber was modelled in this chapter.

5.2. Brief description of the model

This model assumes no medium flow in the 'bathtub', so the supply of oxygen to the cells in the chamber relies only on molecular diffusion.

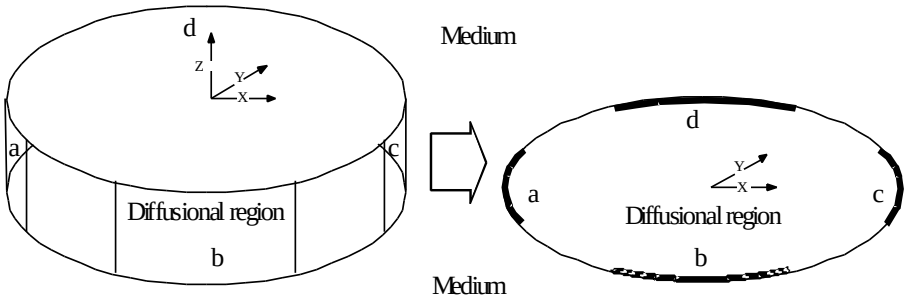

Figure 5-2: Cell chamber (or diffusion region) in 3D and its mathematic representation in 2D surrounded by medium. The roof and floor together with a, b, c, d are impermeable boundary.

Since the 'bathtub' is uniform in the vertical direction, a 2-D representation can be used to simplify the calculation. The circular region represents the chamber. The curved regions a, b, c, d are impermeable to oxygen and represent the pillars surrounding the 'bathtub'. We can assume the oxygen concentration outside the chamber is maintained at its saturation concentration in medium. The oxygen concentration inside this region will change with time as it diffuses out of the chamber and is consumed by the cells. The oxygen consumption of cells is also included into consideration. The consumption rate of cell is not a constant but depends on the oxygen concentration surrounding the cells.

The cell culture is incubated in a box with 18% O_2, 5% CO_2. The partial pressure of oxygen in the medium is so around 140 mmHg (c_m). The initial concentration ($c_{initial}$) of oxygen inside the region is the same with that in bulk medium. The oxygen then starts to decrease as being consumed by cells and a concentration gradient is formed. Oxygen will then diffuse into the circular region following the gradient. The former process decreases the oxygen concentration in the region and the latter one increases it. Whether or how long will hypoxia appear depends on this balance.

As shown later by the simulation, oxygen supply to the bathtub by only lateral diffusion is not enough. We modified the design of the 'bathtub' and utilize the high oxygen permeability of PDMS. The oxygen now comes from both the lateral diffusion and the permeation through PDMS substrate. The permeation of oxygen can be adjusted by altering the thickness of PDMS substrate. The simulation result gives a reference to choose the thickness of PDMS substrate.

5.3. Consumption rate of oxygen

Oxygen will be consumed inside the chamber by living cells. The consumption rate will not be constant but depend on the activity of cells and on the local oxygen concentration (J. L. W. GIELEN, Oxygen Balance for Small Organisms, 2001). Nerve cells consume more oxygen than normal when they are generating an action potential.

The oxygen consumption rate is assumed to be linear to concentration till reaching a maximum value ($k\ c_c$). Cells breathe comfortable under this oxygen concentration and the oxygen consumption rate is saturated.

$$\frac{\partial a}{\partial t} = \begin{cases} k \cdot c & if\ c \le c_c \\ k \cdot c_c & if\ c \ge c_c \end{cases} \qquad \text{Eq. 5-1}$$

Where,

a is the concentration of oxygen consumed by cells. It is a function $a(t,x,y)$ of time and position.
$\partial a / \partial t$ is the consumption rate. k is the rate constant. c is the concentration of oxygen in bathtub. It is a function $c(t,x,y)$ of time and position. c_c is the critical concentration at which the consumption rate is saturated.

The values to these parameters need to be resolved.

Critical concentration (c_c):

The partial pressure of oxygen in the atmosphere is 159.5 mmHg and about 40 mmHg in the venous blood of human body. The oxygen concentration of *40 mmHg* would be a reasonable estimate to the value of the critical concentration. Therefore, c_c = *40 mmHg*[1] is assumed.

Rate constant (k):

The value range of the consumption rate of neurons and glial cells ($0.1 \sim 101 \times 10^{-5}$ $\mu l.hour^{-1}cell^{-1}$) from the literature [L. Dittmann et. Al., 1973] is surprisingly wide. We will take the mean value here. Perhaps the value range of oxygen consumption rate is in its nature wide. The oxygen consumption by animals in hibernating is surely different with that in activity. The total consumption rate constant (k) of all cells in the 'bathtub' is calculated in the following.

[1] Partial pressure is used to measure all the oxygen concentrations here in this chapter.

The volume of 'bathtub': about *2 μl*.
The amount of oxygen in 'bathtub': 0.06 *μl* (STP) (140 mmHg), 0.02 *μl* (STP) (40 mmHg).
The consumption rate of single cell: $0.1\sim101\times10^{-5}$ $\mu l \cdot hour^{-1} cell^{-1}$.
The mean consumption rate of single cell: 3×10^{-5} $\mu l \cdot hour^{-1} cell^{-1}$.
The number of cells in the 'bathtub': 1×10^{4}.
The maxim consumption rate of all cells: 0.3 $\mu l \cdot hour^{-1}$
The critical concentration: $c_c = 40\ mmHg$, that is about *0.02 μl* (STP) oxygen in 'bathtub'.

$k = 0.3 / (0.02\times3600) = 4 \times 10^{-3}\ (s^{-1})$

5.3.1. For how long can it stand without oxygen supply

Assume the initial concentration of oxygen $c_{initial} = 140\ mmHg$, hypoxia concentration is 20mmHg. How long it takes that oxygen is consumed to reach hypoxia without oxygen supply to the 'bathtub'?

In the first stage, oxygen level decreases to 40 mmHg. The oxygen consumption stays at $k \cdot c_c$.

$$d(c_c - c) = k \cdot c_c \cdot dt$$
$$\Rightarrow -\int_{140}^{40} dc = \int_0^{T_1} k \cdot c_c \cdot dt$$
$$\Rightarrow T_1 = 625(s)$$

In the second stage, oxygen level decreases to 20 mmHg. The oxygen consumption is $k\ c$.

$$d(c_c - c) = k \cdot c \cdot dt$$
$$-\int_{40}^{20} \frac{1}{c} dc = \int_0^{T} k\, dt$$
$$\Rightarrow T_2 = 173(s)$$

Two stages together take about 13 minutes. In another words, without oxygen supply, the cells in the 'bathtub' become hypoxia after 13 minutes. As the data of consumption rate ranges from *0.1* to 101×10^{-5} $\mu l \cdot hour^{-1} cell^{-1}$, this result is for reference only.

5.4. Fick's Second Law

Fick's Second Law states that the rate of change of concentration in a volume element, is proportional to the partial derivative of concentration gradient at that point, thus:

$$\partial c / \partial t = D\, \partial^2 c / \partial x^2 \qquad \text{Eq. 5-2}$$

D is the diffusion coefficient of oxygen in medium.

This equation can be modified to include the consumption rate and adapt it for two dimensions as:

$$\partial c / \partial t = D\, (\partial^2 c / \partial x^2 + \partial^2 c / \partial y^2) - \partial a / \partial t \qquad \text{Eq. 5-3}$$

5.5. Finite-difference method

Numerical solution to the Fick's second law can be obtained by replacing the derivatives by finite-difference approximations. [Crank, Mathematic of diffusion, 1975]

Let the range in *x* and *y* be divided into a *m* equal intervals of Δx and *n* equal intervals of Δy, and the time into *i* time steps of Δt. We denote by $c_{m,n}$ the concentration at the point *(x,y)* at the time $t = i\,\Delta t$. Similarly we denote by $c^{+}_{m,n}$, $c^{-}_{m,n}$ the concentration at the point ($m\Delta x$, $n\Delta y$) at time $t = (i + 1)\,\Delta t$ and $t = (i - 1)\,\Delta t$ respectively.

The simplest finite difference approximation to $\partial^2 c / \partial x^2 + \partial^2 c / \partial y^2$ at the point ($m\Delta x$, $n\Delta y$) and time $i\Delta t$ is:

$$\left(\frac{\partial^2 c}{\partial x^2} + \frac{\partial^2 c}{\partial y^2}\right)_{(i,m,n)} = \frac{c_{m+1,n} - 2c_{m,n} + c_{m-1,n}}{(\delta x)^2} + \frac{c_{m,n+1} - 2c_{m,n} + c_{m,n-1}}{(\delta y)^2}$$

Similarly,

$$\left(\frac{\partial c}{\partial t}\right)_{(i,m,n)} = \frac{c^{+}_{m,n} - c_{m,n}}{\delta t}$$

$$\left(\frac{\Delta a}{\Delta t}\right)_{(i,m,n)} = \begin{cases} k \cdot c_{m,n} & \text{if } c_{m,n} \le c_c \\ a_c & \text{if } c_{m,n} \ge c_c \end{cases}$$

And we know $\Delta x = \Delta y$

Put in these approximations:

$$c^{+}_{m,n} = \begin{cases} \frac{2 \cdot D \cdot \delta t}{(\delta x)^2}(c_{m+1,n} - 4c_{m,n} + c_{m-1,n} + c_{m,n+1} + c_{m,n-1}) + c_{m,n} - k \cdot c_{m,n} \cdot \delta t & if\ c_{m,n} \le c_c \\ \frac{2 \cdot D \cdot \delta t}{(\delta x)^2}(c_{m+1,n} - 4c_{m,n} + c_{m-1,n} + c_{m,n+1} + c_{m,n-1}) + c_{m,n} - k \cdot c_c \cdot \delta t & if\ c_{m,n} > c_c \end{cases}$$

The stability restriction need to be $D(1/\partial x^2 + 1/\partial y^2)\ \Delta t \le 1/2$. This has to be followed, otherwise the numerical solution will lost its stability and result in values with error. [Crank, 1975, p151] It is set to 2/5 in the first simulation and to 2/15 in the second simulation.

5.6. Permeable substrate

The 'bathtub' can be fabricated on top of many materials, like glass slips (non-oxygen-permeable), or PDMS (oxygen permeable). If the simulation proves 'bathtub' in hypoxia, a solution is to use an oxygen permeable substrate. The method to model a permeable substrate is described in this section.

Assume PDMS is a membrane. The rate of transfer through unit area of this membrane is F_p. It is defined as: [Crank, 1975, p45]

$$F_p = P_e\ (\Delta p\ /\ \Delta z) \qquad \text{Eq. 5-4}$$

Where,

F_p is the rate of transfer through unit area of PDMS;

Δp is the difference of intensity of pressure;

Δz is the thickness of the permeable substrate;

P_e is the permeability of the PDMS substrate. The unit is ($cm^3(STP)cm\ cm^{-2}s^{-1}mmHg^{-1}$).

The data of P_e found in references often uses volume (STP) to measure the amount of gas permeated through PDMS. In the equation above, gas is measured with its concentration in the element. Therefore a conversion is needed.

$$F_p = P_e\ (\Delta p\ /\ \Delta z)\ (6 \times 760\ mmHg\ /\ h\ \Delta x\ \Delta y) \qquad \text{Eq. 5-5}$$

Where,

$(6 \times 760\ mmHg\ /\ h\ \Delta x\ \Delta y)$ convert the volume into concentration;

$760\ mmHg$ is the pressure of atmosphere;
h is the height of the element (bathtub);
The constant 6 comes from the solubility of oxygen in medium. The concentration of oxygen (measured by volume ratio) in atmosphere is about six times of it is in medium.

Consider an element of volume on the inner surface of the substrate. Oxygen

penetrates the substrate into the element and there is no flux at the top of the element. The increase in the rate of concentration in the element is:

$$\frac{\partial c}{\partial t} = F_p dxdy$$
$$\Rightarrow \frac{\partial c}{\partial t} = P_e \frac{\Delta p}{\Delta z} \frac{\delta x \delta y \cdot 6 \times 760}{h \cdot \delta x \delta y}$$
$$\Rightarrow \frac{c_{m,n}{}^{+} - c_{m,n}}{\delta t} = P_e \frac{(c_m - c_{m,n}) \times 6 \times 760}{d \cdot h}$$

Where,

d: is the thickness of the permeable substrate;
c_m: is the oxygen concentration outside 'bathtub' in medium. Here oxygen concentration is measured with its partial pressure (mmHg).

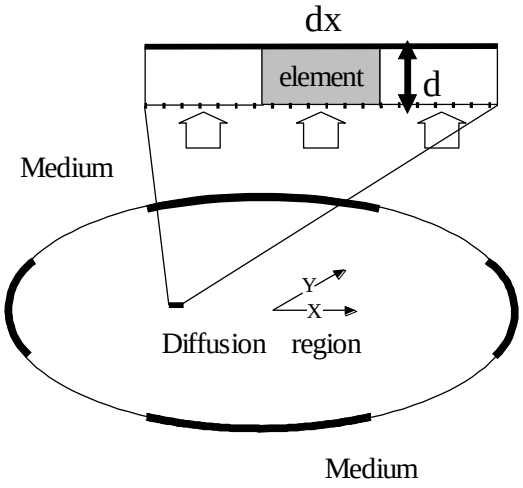

Figure 5-3: An element of volume in the 'bathtub'. Its floor is oxygen permeable and the roof is impermeable.

There is not only penetration at the floor but also diffusion at the x and y sidewall of this element. Taking them into consideration, the finite difference formula becomes:

$$c^{+}{}_{m,n} - c_{m,n} = \frac{D \cdot \delta t}{(\delta x)^2}(c_{m+1,n} - 4c_{m,n} + c_{m-1,n} + c_{m,n+1} + c_{m,n-1}) + P_e \frac{(c_m - c_{m,n}) \times 6 \times 760}{d \cdot h} \cdot \delta t$$

5.7. Simulation

Two conditions are simulated. One is a 'bathtub' on the oxygen permeable PDMS substrate; the other is a non-permeable one.

For the first situation, the 'bathtub' is on a glass slip and is not permeable by oxygen. The oxygen in bulk medium can only diffuse into the 'bathtub' through the

lateral opens. The initial oxygen concentration in 'bathtub' is the same with it in bulk medium ($c_{initial}$ = *140 mmHg*). The consumption rate constant is $k = 4\times10^{-3}\ (s^{-1})$. The critical concentration is c_c = *40 mmHg*. The hypoxia level is assumed to be c_h = 20 mmHg.

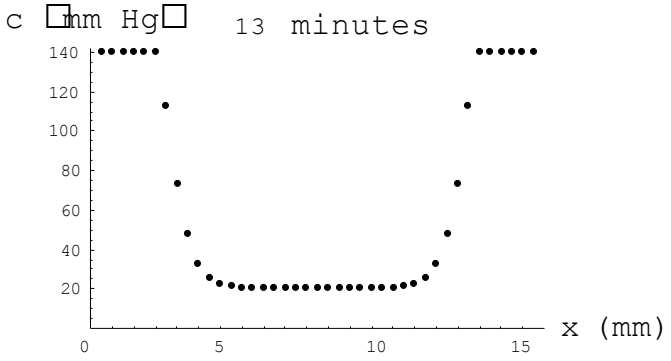

Figure 5-4: Profile of oxygen concentration across 'bathtub' on glass substrate after 13 minutes.

As shown in the figure, the lateral diffusion can only affect the oxygen level in the outer edge of the bathtub within a few millimetres. The central domain of the 'bathtub' is dominated by the consumption of cells.

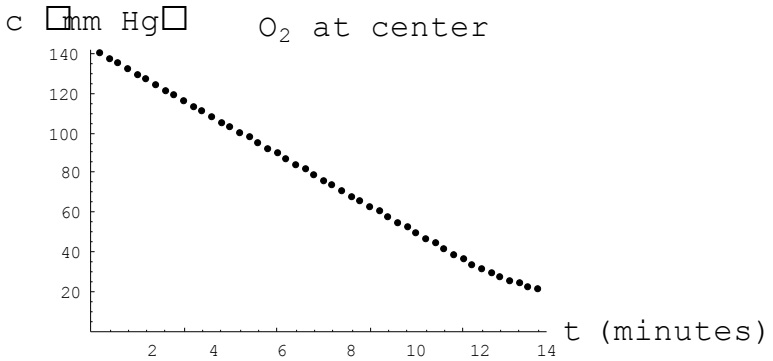

Figure 5-5: Oxygen concentration at the centre of the 'bathtub' decreases as time past.

Within 13 minutes, except for the outer edge, most of the 'bathtub' falls under hypoxia (*c = 20 mmHg*). This result agrees with the calculation in section 5.3.1. This trend continues and the oxygen concentration drops to around zero after 26 minutes.

In the second situation, the substrate is PDMS and is an oxygen permeable material. The thickness is *d* = 1 mm. The permeability constant of PDMS at *28 °C* is 6.2×10^{-9} $cm^3(STP)cm\ cm^{-2}s^{-1}mmHg^{-1}$ [James E. Mark, 1999]. The initial oxygen concentration in 'bathtub' is $c_{initial}$ = 140 mmHg. The consumption rate constant is $k = 4\times10^{-3}\ (s^{-1})$. The critical concentration is c_c = 40 mmHg. The hypoxia concentration is c_h = 20

mmHg.

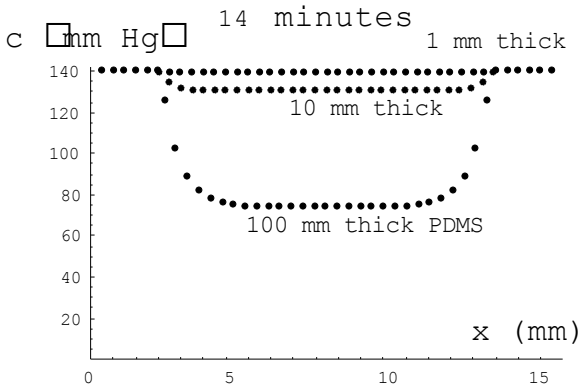

Figure 5-6: Profile of oxygen concentration across 'bathtub' on oxygen permeable PDMS substrate after 14 minutes. The plot shows three substrates with different thickness.

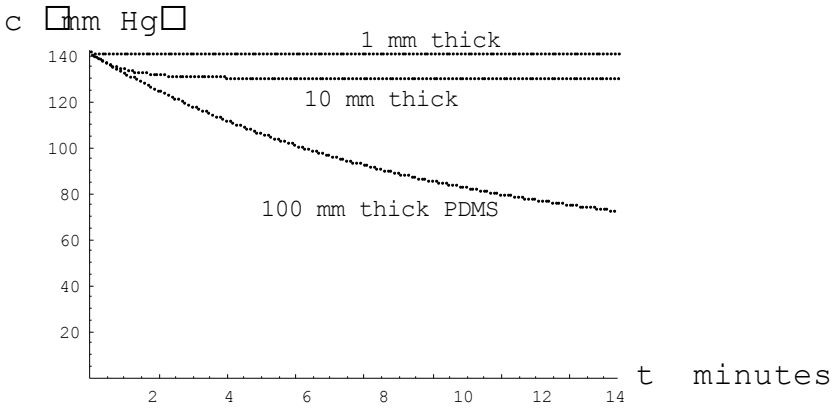

Figure 5-7: Oxygen concentration changes with time at the centre of the 'bathtub'. Substrates with different thickness are shown.

The stability restrict is set to 2/15 in this simulation. The result shows the oxygen permeability of PDMS is high. A PDMS substrate of 1 mm thick pass through oxygen in such a high rate that the oxygen inside 'bathtub' maintains at 139 mmHg after 4 minutes. This oxygen permeability is even higher than we need it to be.

As mentioned before, the different values of oxygen consumption rate from references give different result. They are listed here:

Equilibrium concentration[2] of oxygen in 'bathtub' (mmHg)	Oxygen consumption rate ($\mu l \cdot hour^{-1} cell^{-1}$)	Thickness of PDMS substrate (mm)
139	0.1×10^{-5}	1
139	0.1×10^{-5}	10
137	0.1×10^{-5}	100
139	3×10^{-5}	1

[2] Equilibrium concentration refers to the oxygen level where it is finally stabilized when the consumption and supply process reaches a balance.

131	3×10^{-5}	10
60	3×10^{-5}	100
114	101×10^{-5}	1
19	101×10^{-5}	10
2	101×10^{-5}	100

5.8. Conclusion

The first simulation shows that the oxygen level near the edge is relatively high. But most of the centre area of the chamber suffers from a hypoxia after 13 minutes. Both hypoxia and high oxygen level are not good for cell survival and can be even lethal to cells. This phenomenon happens in practice [Gregory J. Brewer, 1989]. They found a region of ring shape on many glass cover slips where cells lived. The cells elsewhere on the cover slip were dead probably because of oxygen issue.

In the second simulation, the PDMS substrate shows high oxygen permeability. It eliminated the worry about the possible hypoxia inside the 'bathtub'. High oxygen level is also not good for neural culture. However this problem can be solved by altering the composite of PDMS (permeability change) or simply by reducing oxygen level in medium. The data from the simulation provides reference to the fabrication of the 'bathtub'.

Chapter 6.The waveforms of extracellular signal

6.1. Introduction

Many people have been working on the modelling of the extracellular recording of neuron with microelectrodes. E. Lind et al. (1991) modelled the neuron as a current source in the trench bottom of a pMEA. 3D finite element method was used to simulate the distribution of the electrical potential in the medium outside the membrane. S. Martinoia (2004) built a circuit model in SPICE modelling the neuron/electrode junction. Their model features a coupling capacitance (C_{me}) in the junction. The change of the coupling capacitance and the coupling strength gives rise to different waveforms of extracellular recording. J. R. Buitenweg (2003, 2006) modelled the neural soma growing on a pMEA with 3D finite element method. The geometry of the soma and its postition were considered in the model.

The intracellularly recorded action potentials of a certain neuron are often similar in their waveforms. These signal always starts with a sharp rising to the peak from the static membrane potential and falls back quickly with a little overshot and returns slowly. Different with that, the signal recorded with extracellular MEA exhibits in various waveforms, even them actually come from the same neuron. What makes the differences between these waveforms? Finding the reasons could help us with getting more information from these waveforms. This chapter try to find the causes of the variation in the waveforms recorded in this project.

A circuit model was built to simulate the recording of extracellular action potential. This model include the microelectrode, the neural membrane, the interface between them and the pre-amplifier. This circuit model helps to gain insight to the recording and helps to improve the design of the system. However the model is a circuit interpretation and a simplification to the real situation, e.g. the H-H model to the neural membrane, the seal resistance to the neuron/electrode interface. The real situation is more complex.

This chapter starts with a introduction to different types of microelectrodes, recording methods and pre-amplifier structures. Then it gives some background knowledge on the Hodgkin and Huxley model (section 6.7.1), the membrane action potential and the propagated action potential (section section 6.8). Discussion

about whether extracellular potential can be detected starts with the static membrane potential, then with the membrane action potential and the propagated action potential.

At least three factors are found in our research having their effects on the extracellular potential waveforms. They are respectively the distribution of ion channels, the propagation of action potential and the couple of electrode. They are detailed in three sections (section 6.10.3, section 6.10.4 and section 6.10.5). There are also simulation results presented in figures.

Then some waveforms of real signal recorded in this project from neuron is presented. The details of the methods of simulation in PSPICE and Mathematica are put in appendix.

6.2. Different techniques of recording

6.2.1. Different microelectrodes

In most electrophysiological recording techniques, electrodes serves as the transducer between cells and circuits. The ion flow or potential changes through cell membrane is detected and coupled into circuit using electrode. There are different kinds of electrodes.

According to the passband of the electrode/cell interface, the electrode arrays can be roughly divided into three types: conductive high pass, conductive low pass and insulated high pass. Metal electrodes, glass micropipette electrodes and FET electrodes are the representatives of these different types. The MEAs used in this project are metal electrodes. However they are used to measure voltage signal. There is no any current flowing through them. The preamplifier circuit behind them is a FET with extremely high input resistance. The MEAs can be regarded as the extension of the metal pieces on the gate of the FET. From this point of view, the MEAs can be classified into the insulated high pass type. If the same MEAs are used to measure current signal, they can be classified into conductive high pass type.

Glass micropipette

It is a glass capillary (glass tube) with a sharp tip, typically on the order of 1-50 μm

diameter. The micropipette can be filled with various electrolyte depend on need. A silver chloride-coated silver wire inside the micropipette is immerged in the electrolyte.

The glass walls of micropipettes can attach to cell membrane to form tight seal. Traditional micropipette technique gives MΩ seal resistance. The later on appeared patch clamp technique can form so-called 'Giga-seal'. Such high seal resistance makes patch clamp capable of detecting single ion channel switching. Seal resistance is very important for weak current signal detection. Cell membrane (except ion channel opening) possesses high resistance and the glass wall of micropipette is also insulator. If the seal resistance is also high, they form a high resistance route. Most of the current from ion channel choose the low resistance route instead and flow into the detecting circuit. Good seal ensures low leakage current and rises the amplitude of signal significantly. Also, high seal resistance reduces thermal noise current greatly. These facts make single ion channel current (several *pA*) detectable by patch clamp.

Solid conductor microelectrode

Solid conductor microelectrodes are made of various conductive materials (e.g., Tungsten, carbon fibre, stainless steel, platinum, etc.) and coated with nonconductive materials (e.g., polymers, silicon nitride, etc.) except the tip.

The MEA (microelectrode array) used in this project can be classified into the solid conductor microelectrode type. MEA often utilizes integrate circuit techniques (i.e. photolithography, etching, sputtering and deposition etc.) to fabricate multiple thin-film electrodes in one chip or substrate. Two different types of MEA are fabricated in my project, so-called flexible MEA (FlexMEA) and planar MEA (pMEA).

Advantages of MEAs

Singular electrode can only record from one position and cannot provide enough information about the working principle of neural network. MEA can record from multiple positions in network and provide temporal and spatial information. MEAs are mostly extracellular electrodes. The metal electrodes of the MEAs usually cannot record high resolution signals extracellularly like the glass micropipettes do due to the seal resistance and the electrode impedance. The advantages of MEAs is not to provide detailed waveform but to provide large quantity of spikes from large

area.

Electrode coating

The microelectrodes often need coating to increase the surface area and reduce the impedance. A common coating material is platinum black. Platinum black is not very durable. The impedance of microelectrode rises with time and usage. This is reported in chapter 4 in details. Titanium nitride [Egert et al., 1998] or Iridium oxide [Blau et al.,1997] sputtering are tougher alternatives to platinum black plating.

Impedance of microelectrode

Most electrodes are designed to provide electric signal a low ohm connection to recording circuit. Zero resistance electrode would be ideal, however is impossible as long as there is demand on minimization of electrode. High resistance of electrode causes various drawbacks to small signal recording. In case of extracellular field potential recording, bigger resistance brings higher thermal noise voltage. It is a critical problem since extracellular field potential signal is in the range of 10~500μV and can easily immerge into thermal noise. High resistance of electrode also dissipates signal. Signal voltage is distributed on the electrode instead of acts on preamplifier. It is worse if the resistance of the electrode is unstable. Unstable and unknown voltage drop across the resistance of the electrode introduce errors in the recording. The impedance of electrode itself or together with stray capacitor forms filter, which limits the bandwidth of recording.

For intracellular and on-cell recording of membrane potential, resistance of electrode is less critical. Thermal noise arises mainly from seal resistance, which is often huge in the order of 1~500 MΩ. The noise contribution from electrode resistance itself can be ignored. Nevertheless, high electrode resistance still causes problem. It reduces system's bandwidth.

As for membrane current recording techniques, no matter intracellular or other, low electrode resistance means not lower thermal noise, but on the contrary, rising of thermal noise current. Low electrode resistance is desired for different reason. It reduces voltage error (in patch clamp techniques) and increases time resolution or bandwidth of signal (all current recording).

The impedance of metal electrode and glass micropipette electrode

Metal electrodes have a relatively high low-frequency impedance. In contrast the impedance of an electrolyte-filled micropipette is resistive (high capacitance) which means that it has similar impedance over the whole frequency range. The medium in contact with metal electrode will form an interface with a structure of so-called double layer. This interface can be considered generally as a capacitor in parallel with a resistor. The detail of this interface is in chapter 4, where a circuit model of this interface is built. Although micropipette electrode has a metal coil inside and therefore has also a metal/medium interface. However the capacitive reactance of the interface can be ignored. Because the metal coil has a huge surface area in comparing with metal microelectrodes. The capacitance of the double layer is proportional to the actual surface area of the electrode. The impedance of a micropipette electrode is mainly from the resistance of the medium inside the electrode. The resistance is mainly distributed at the tip of the micropipette. The thinner and longer the tip becomes, the bigger the resistance grows. Typical resistance of a micropipette to DC current is from 10 to 500 MΩ.

The impedance of a micropipette at low frequencies is usually lower than that of a metal electrode. But it is reversed at high frequencies. The real part of the impedance of the electrodes used in this project is about ten thousands ohms in frequency range of 1Hz~10KHz. The huge capacitive reactance of the metal microelectrode make it not suitable for recording low-frequency signal. The high-frequency impedance of the metal electrode is lower and so does its thermal noise voltage. The waveform of extracellular spikes is usually similar to the first or second derivative of the intracellular voltage (see chapter 6). Therefore the frequency range of the former is higher than that of the latter.

Therefore, metal electrodes are usually used for extracellular action potentials. By contrast, the micropipettes are more versatile. Variety of micropipettes can be used to record signal of low-frequency or high-frequency, of current or voltage. Although extracellular recording of voltage signal uses mostly metal electrodes, there are also micropipettes. The one of the shortcomings of the micropipettes is its complexity. The metal electrode arrays are more convenient to use and become more and more widely used.

6.2.2. Other electrodes

Carbon-fibre electrode

The impedance of high frequency is lower than glass micropipette. Its tip is often covered with a layer of silver to reduce the low-frequency noise [Millar and Williams, 1988].

Ion-sensitive resin

The resin is sensitive to the concentration of ions. The microelectrode with this resin on the tip is used to detect the potential or concentration of certain ions. The resin is so sensitive that does not allow high bias current to pass through.

FET

An EOSFET or electrolyte-oxide-semiconductor FET is a special field effect transistor. The metal at the gate junction is taken place by the electrolyte medium. This technique at present can detect the extracellular spikes from invertebrate neurons. This technique has the advantage of being easily integrated into a chip.

Others

There are many sensing elements instead of electrodes, like the magnetic sensor in magnetoencephalography, the fluorescent in calcium imaging.

6.3. Intracellular and extracellular recording

6.3.1. The conformations of patch clamp

Patch-clamp technique has four basic record modes. (1) Records of cell-attached mode (Cell-attached recording or On cell recording), (2) for the record mode (Inside-out recording), (3) outside the field record mode (Outside-out recording); (4) whole-cell recording mode (Whole-cell recording).

Cell-attached recording can be classified as extracellular recording. The whole-cell recording can be classified as intracellular recording. The inside-out recording and outside-out recording cannot be done with the extracellular MEAs. These recording modes study a patch of the cell membrane. For neural network research, single

neuron is already the smallest unit.

Take the current recording with 'on cell' mode as an example. The patch-clamp micropipette sucks up an small membrane patch of several micron square containing only a few ion channels. The tip of the glass wall sticks to the membrane and forms high seal resistance. This patch of membrane is isolated from other part of membrane extracellularly by the seal resistance. The medium inside the micropipette is connected with this patch of membrane. Part of the ion current through this piece of membrane is offset by the displacement current through the membrane capacitor. This current circulates locally and cannot be detected by the electrode. Another part of the current circulates between this membrane patch and the rest membrane. Most of this current flow through the low ohm loop it can find. This loop begins from the grounded bulk medium, goes to other parts of membrane, through the cytoplasmic membrane, crosses the membrane patch, into micropipette and the pre-amplifier circuit, arrives at the virtual ground of the circuit. This part of the current can be recorded. Only a small part of this current leakages through the seal resistor directly to the bulk medium and cannot be detected.

The 'on cell' mode described above is similar in many ways with the extracellular voltage recording implemented with MEAs in this project. There are also local current and the current circulating through different parts of the membrane. The couple rely on high seal resistance also. They both record extracellularly. The differences are the types of signal they record. The input resistance of the preamplifier of MEAs is huge, since it intent to measure the voltage signal. Therefore, the majority of current flows through the seal resistor instead of into electrode and creates the extracellular voltage to be recorded. The input resistance of the patch-clamp pre-amplifier is close to zero, since it try to measure the weak current signal.

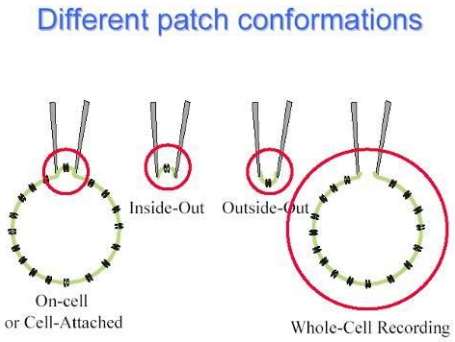

Figure 6-1: Different patch conformations.

For a neuron in integrity, the recording modes can be classified into two basic types, the intracellular recording and the extracellular recording. From an extensive understanding of their mechanism, they have many features in common. It is like measuring an electrical capacitor. There is no ‘intra-capacitor’ recording or ‘extra-capacitor’ recording. For both intracellular and extracellular recording, the signal source is the excitable membrane of neuron. Both of their microelectrode need be coupled to the cell membrane. Either inside or outside membrane, the key for a good coupling is to form a high seal resistance.

Recording of extracellular field potential, gives the timing and the low resolution profile of action potentials from neuron. This is a relatively limited view of the neuronal activity than what provided by intracellular or on cell patch clamp recording. Whereas, extracellular recording makes simultaneous measurement of many neurons possible. This makes it a good tool on the research of the electric activity of the neuronal networks.

6.4. Different pre-amplifier

Voltage across a cell membrane, current flowing through a cell membrane and extracellular field potential are targets of most electrophysiological recording. These recording employ different techniques. Despite various electrodes, different circuits are important for successful recording. Among all parts of circuit, preamplifier often set the high limit of system performance and distinguish different systems (rest of the system, e.g. post amplifier, A/D converter etc. are more or less the same).

This section try to classify the preamplifier circuit designs into three main types: Voltage clamp, current to voltage converter and potential sensing.

6.4.1. Voltage Clamp

In the voltage clamp technique, measurement is made on the current flowing through the membrane. As a straightforward thinking, its preamplifier should be a current to voltage converter. Whereas the voltage clamp measures current in a not

so straightforward way. Instead of the membrane current, the current driven into neuron by a negative feedback amplifier through electrode is measured. This current is identical but reverse to the membrane current. It is how the membrane voltage is maintained stable or clamped.

The classic voltage clamp circuit employ two electrodes. One electrode transduces the cell's membrane potential to the input of a unity-gain buffer amplifier. The output signal of a unity-gain buffer amplifier is different with the input signal. The current of the buffered signal is increased and the resistance is reduced comparing to that of the input signal, while the potential remains the same. The buffered potential is compared to a command potential with another op-amplifier. The difference between the membrane potential and the command potential drive a current to flow through another electrode into the cell. This current brings the membrane potential back to the same value of the command potential. The current flow through the second electrode is identical to the membrane current. And hence can be measure either at the output of the second op-amplifier or at the reference electrode in the bulk medium.

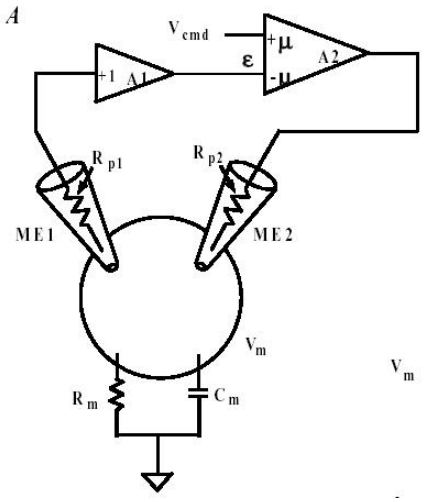

Figure 6-2: The circuit of a traditional voltage clamp pre-amplifier with two intracellular electrodes.

In voltage clamp, measuring membrane current is a way to investigate the membrane conductance. The membrane potential is held constant (i.e., 'clamped') to ensure the recorded current is linear to conductance.

6.4.2. Current to voltage converter (Transconductance amplifier)

Patch clamp is a type of voltage clamp. If an active neuron can be simplified as a current source, which is not proper to say strictly, the best device to amplify and

record the signal current is a current preamplifier, which is specified to record the current signal. In order to preserve the input current, the input resistance of the preamplifier is designed to be small. The basic circuit behind patch clamp is a current preamplifier or a current-to-voltage converter to be more precise. The potential at the far from neuron side of the electrode is maintained at the command voltage. It is virtual ground if the command voltage is zero. The core element of the current-to-voltage converter is a high value feedback resistor often in the range of hundreds of MΩ to GΩ. This current amplifier sinks input current signal directly into the virtual ground, or to the selected command voltage V_{cmd}. A feedback current of the same amplitude with the input current flow through the feedback resistor and is transferred into voltage at the output. Weak input current is converted into high voltage due to the high resistance of the feedback resistor.

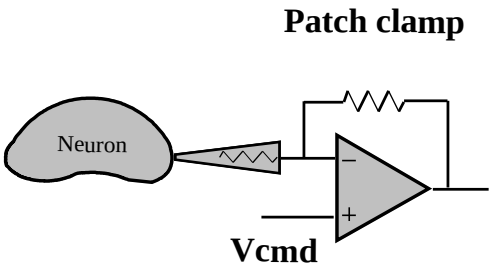

Figure 6-3: The pre-amplifier of a patch clamp.

Patch clamp is available of detecting the current of single ion channel, which is in a few pica Amps. The Giga ohms feedback resistor gives mV range output signal.

Patch clamp

The preamplifier of patch clamp is very similar with the amplifier commonly used after the photodiode. Both o them are used to amplify the weak current signal.

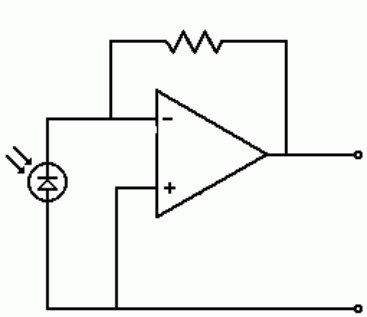

Figure 6-4: The preamplifier of a photodiode.

6.4.3. Voltage amplifier (voltage follower)

Then another way to record the signal is it can be terminated with a resistor and the resulting voltage can be recorded with a voltage preamplifier.

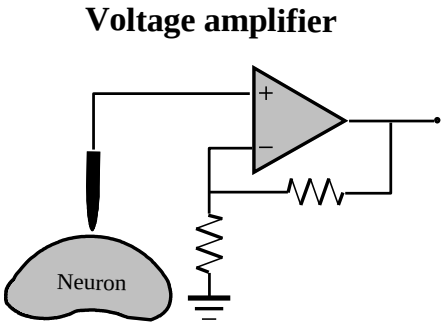

Figure 6-5: The preamplifier to measure voltage signal. Both intracellular and extracellular recording can use this type of pre-amplifier.

In order to detect the membrane potential changes, potential sensing or charge amplifier circuit is used. It can be found in all preamplifiers circuit protocol of extracellular recording. The MEA preamplifier built in my project is in no exception.

Differs from voltage clamp and patch clamp circuit, it is a passive recording technique. Very high input impedance and low bias current minimize disturbance to cells and the noise level as well.

6.5. Summary for the preamplifiers

The several pre-amplifier circuits described above can basically be divided into two categories, i.e. the current amplifier and the voltage amplifier. These diagrams include not only the circuit of pre-amplifier, but also include the signal source. The cell membrane is interpreted as a signal source capable of generating impulses. The membrane resistance is high, and so it is regarded as a current signal source. Strictly speaking, the cell membrane is not an ideal current source. The internal resistance is not entirely resistive, but has capacitive reactance.

The current loop is as following. Let the current starts inside a neuron. It will travel through the membrane patch coupled with a microelectrode. And then flows through the seal resistance to the earth and back to where it started through other part of membrane of this neuron. The internal resistance and the seal resistance is what the current met along this loop. The internal resistance of this current source is composed by the resistance of the coupled membrane patch, the intracellular

resistance and the membrane resistance of other un-coupled area.

The circuit at right side further simplifies the preamplifier leaving only the input resistance of it. The purpose is to demonstrate the principle of neural recording from a perspective of signal source resistance, seal resistance and the input resistance of pre-amplifier.

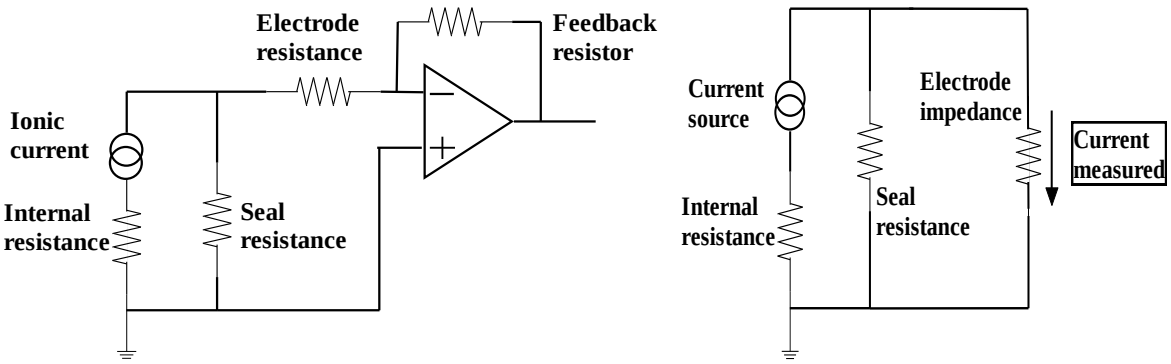

Figure 6-6: The equivalent circuit of the current recording with micropipette.

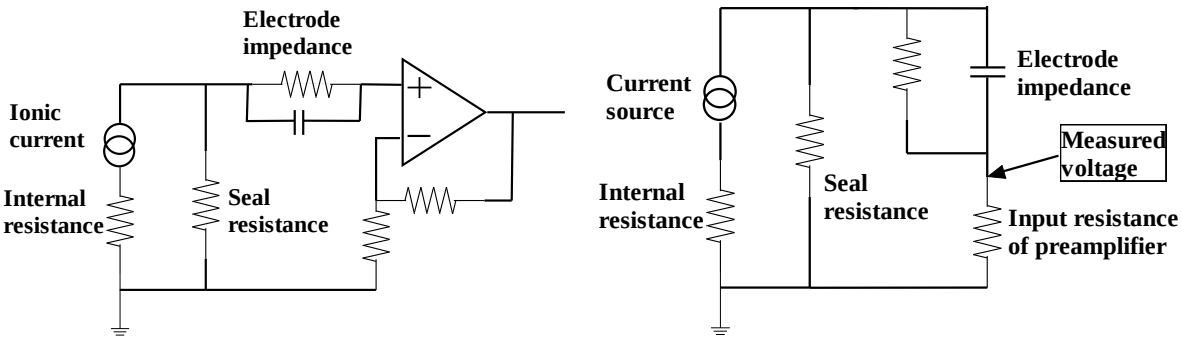

Figure 6-7: The equivalent circuit of the voltage recording with metal microelectrode. The electrode impedance is simplified as a parallel connected RC (section 4.12).

Micropipette is often used to measure the current signal. Metal microelectrodes are often used to record the voltage signal. The circuit model with more details of cell membrane can be found in chapter six. The details about the membrane resistance, the power of the signal, the magnitude of the membrane current and the extracellular voltage will be described in the following sections.

However, the neuron as the signal source is not exactly the same with ordinary signal source of electronics. The internal resistance is not fixed. The membrane resistance remains high at the state of rest. During the generation of an action potential, the membrane resistance greatly changes. The neural membrane

resistance of some animals are listed in the following table.

Table 6-1: The neural membrane resistance of some animals.

Cat motor neuron: *1000 Ω cm^2*
Cat cortex neuron: *4000 Ω cm^2*
Mammal motor neuron：*400 ~ 1000 Ω cm^2*
Crab axon: *8000Ω cm^2* [Hodgkin, 1947]
Lobster axon: 7330 *Ω cm^2* [Hodgkin and Rushton, 1946]
Squid giant axon: 5400 *Ω cm^2* [Cole, 1968]
Squid giant axon: 1000 *Ω cm^2* (resting), 25 *Ω cm^2* (excited) [Cole and Hodgkin, 1939]

The coupling of electrodes to neurons is also more complex than the wiring of the probes of oscilloscope to the output terminal of ordinary signal source. First neural recording is in medium not on the table in the air. Imagine soaking an electronic equipment water (assuming that the equipment will not short-circuit), and then used probes to measure the current and voltage. This is roughly the situation faced by neural record. In order to measure the neuron in medium, a proper electrode/membrane coupling with high sealing resistance is very important.

There are some other differences between neuron and electronic device. Take the signal source resistance again as an example. Different contact area of neuron with electrode will change the internal resistance. The whole-cell recording targets the all membrane. Its source resistance is much lower than that of the patch clamp. Because patch clamp records only from a small piece of membrane.

6.5.1. The resistance of signal source

The resistance of membrane patch

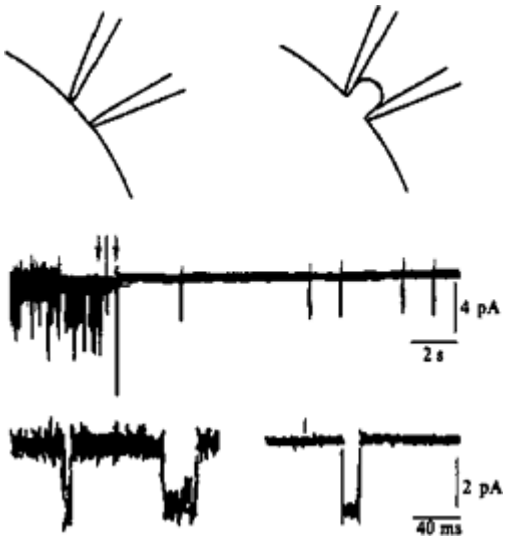

Figure 6-8: Neher and Sakmann (1976) recorded for the first time of human the current through a

single ion channel (AchR). The magnitude of current is about 2-4 pA. One spike lasts about miliseconds. [N. Zhao, Biology physics, p194]

The recording of current signal in picoamp scale is very difficult. The key making the recording possible is the resistance of the current source. According to estimation, the internal resistance of a signal source of 100 MΩ has thermal noise of picoamps. In order to record signal in the background of the thermal noise, the internal resistance must be over 100 MΩ. Take the whole cell recording as an example, the membrane resistance (the resistance from inside the cell across the whole membrane to the extracellular medium) of a 10 microns diameter cell (membrane area is about 300 micron square) is about 8 MΩ. Therefore, it is impossible for whole cell recording to detect a single ion channel currents. The success of patch clamp is that it selects a small patch of membrane as the recording target. The membrane resistance of 1 micron diameter is about 2.5 GΩ. It meets the requirement of the resistance of the signal source. In addition, a high seal patch clamp resistance is also a key to success. Otherwise, the seal resistance connected parallel to the signal source resistor will reduce the total resistance.

6.6. Estimation of pulse power

The giant squid axon is taken as an example to estimate the peak power and average energy of an impulse. Assume a section of the axon is suspended in the medium. The resistance of the medium is neglected. The parameters of this model are as follows:

Table 6-2: The parameters of the model, which used to estimate the power of an action potential in squid giant axon.

The length of axon: 1 *cm*
The radius of axon: 238 *μm*
The resistivity of cytoplasm: 35.4×10^{-3} *KΩ cm*
The cytoplasm resistance per unit length: 20 *KΩ cm*
The resistivity of extracellular medium: 0 (it is neglected)
The intracellular current: *8 μA*
Membrane resistance: *1000 Ω* cm^2 (resting), *25 Ω* cm^2 (excited)
Membrane current density: *300 μA / * cm^2 (peak) , *100 μA / * cm^2 (average)

The energy of the impulse is consumed on two resistors. The ions flow through the cell membrane and dissipate energy on the membrane resistance. The ions flow inside the axon also consumes energy against the resistance of the cytoplasm. In fact, there is also energy dissipation at the extracellular medium. It is neglected here since the resistivity is low.

By the membrane current density and the membrane resistivity, the power density dissipated on the membrane resistance can be resolved: *2.2 microwatts/cm*^{2}. The power density consumed on cytoplasm can also be derived: *1.3 microwatts/cm*.

The power consumption to transmit the action potentials for a distance can be estimated also. This area of the axon of *1 cm* is: *0.15 cm*^{2}. The power consumption on this piece of membrane is: 0.34 microwatts. The power consumption on this section of cytoplasm is: 1.3 microwatts.

The energy can be estimated from the power. The current pulse duration is about *0.5 ms*. Then the energy consumed on the membrane resistance is: 0.17 nanojoules. The energy on cytoplasm is: 0.65 nanojoules.

Different current of ions

The calculation above neglects a fact that the current is composed by two ion currents and flow in opposite direction. Because the sodium and potassium current overlap each other. Therefore the total current is smaller in magnitude than each of its components. This means that the power consumption calculated above is less than the actual value. Calculation with more accuracy should distinct two ion currents and their power consumption. The calculation on the basis of this idea is followed. However, the portion of each ion current in the intracellular current is unknown. Hence the power consumption on cytoplasm is ignored. Only the power consumption on membrane resistance is followed.

Table 6-3: The parameters of different ions. Each ion current has its own power consumption during an action potential.

The sodium current density: 800 *μA / cm*^{2} (peak), 400 *μA / cm*^{2} (average)
The potassium current density: 800 *μA / cm*^{2} (peak), 400 *μA / cm*^{2} (average)
The duration of the current: about 3 *ms*
The membrane resistance to sodium: *30 Ω cm*^{2} (peak), 70 *Ω cm*^{2} (average)
The membrane resistance to potassium: 80 *Ω cm*^{2} (peak), 200 *Ω cm*^{2} (average)

The mean values instead of the peak values are chosen here. For sodium ions the power density on membrane resistance is about: *11 microwatts/cm*^{2} (average). For potassium ions power density is: *32 microwatts/cm*^{2} (average).

Then the power consumption to transmit the action potential for 1 cm can be estimated. The membrane area of *1 cm* axon is: *0.15 cm*^{2}. For sodium current, the power consumption is: 1.6 microwatts/cm (average). For potassium current, the

power consumption is: 4.8 microwatts/cm (average).

The energy dissipation can then be estimated from the power consumption. The duration of the current pulse is about 3 milliseconds. The sodium ion current dissipates energy: 4.8 nanojoules/cm. The potassium current dissipates energy: 14.4 nanojoules/cm.

Clearly, these results are significantly larger than those obtained for total current before. Similar results can be found in published paper. [Patrick Crotty, 2006] Only the energy cost of potassium current is higher than that in the paper. This may due to the error caused by rough estimation here.

This result is valid only with the above parameters. If the parameters change, the result will be naturally different. Such as the myelin nerve fibres in the biological membrane, resulting in increased resistance, as well as nerve fibres of different radius, and so on.

Is neuron an energy saver?

From the above data, the signal propagation in squid axon seems not energy saving. Transmission of action potential for 1 cm costs microwatt power. The power of many microelectronic products can achieve microwatt range. However, the signal that the squid axon transmits are pulses. Each pulse lasts only a few milliseconds. Therefore, the energy consumption is still very low and is about nanojoules/cm range. In addition, the squid giant axon is uncommonly large. According to the simulation, the energy cost is proportional to the radius of the nerve fibres. The energy cost of the mammalian nerve fibres of microns, in according to this relationship, may be two orders smaller than that of the squid axon.

The energy picked up by electrode

The above calculations ignored the power cost of the extracellular resistance because it is relatively small. However, it is this power that matters to us. The extracellular electrodes detect this power. The other two powers dissipate inside the signal source and cannot be detected by extracellular electrode. The electrode couples with neuron and form seal resistance. The current flow through the seal resistance and causes the potential pulse which can be detected by electrode. The seal resistance needs be high to raise the potential and the power level. The raised

power cannot be neglected anymore.

The extracellular signal when ion channels are unevenly distributed

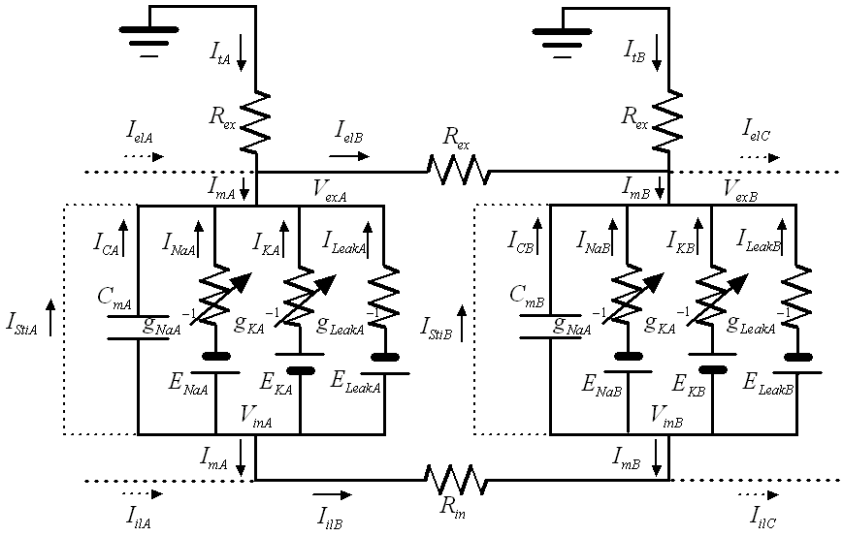

Figure 6-9: The circuits of the simulation model build in Mathematica. Here the membrane is divided into two parts of equal sizes. They represent respectively the electrode-covered membrane area and the not-covered membrane area of the opposite side. One part is distributed many ion channels. The other part is assumed to be no exist of ion channel. The electrode-covered part is assumed having seal resistance of 1 MΩ extracellularly. The extracellular resistance at the not-covered part may be small, if it is immerged in the medium, or may be high, if it attaches to substrate. In either of these situations, the simulation result in similar current density flowing extracellularly, which is about 50 μA / cm^2 (peak).

Simulations show that for same membrane parameters (e.g. ion channel density, membrane capacitance, etc.), even if other parameters (e.g. membrane area, cytoplasm resistivity) change, the current density will remain basically unchanged. Assume an electrode of 1000 micron square area (about 30 microns in diameter) forms a seal resistance of 1 MΩ. The current flowing through the seal resistance is about 0.5 nanoamps (peak). The power consumption on the seal resistor is about 0.25 Picawatts (peak). The voltage across the seal resistor is about 500 microvolts (peak).

6.7. Hodgkin and Huxley's Model

The Hodgkin and Huxley model was built for the membrane of the giant axon of the squid. It is now widely used to describe the excitable membrane of numerous types of cells, like neurons and cardiac myocytes. The spinal cord neurons and cardiac myocytes of rats are used in our project. The Hodgkin and Huxley model is utilized in this thesis to simulate the recorded signal from these cells.

A detailed description of the H-H model can be found in [Weiss, 1996] or [Hille,

1992]. Models have been developed for cardiac cells based on the principles of Hodgkin-Huxley model [Nygren, et al., 1998, Di Francesco and Noble, 1985].

The experiments by Hodgkin and Huxley

Hodgkin and Huxley (Hodgkin and Huxley, 1952) performed a series of experiments on the giant axon of the squid to study its conductance and excitability. The resting potential and the action potential were recorded using an oscilloscope. The giant axon of squid is about *500μm* in diameter. The electrode can be inserted easily.

6.7.1. The circuit model of H-H

Hodgkin and Huxley derived a group of equations describing the electrical properties of the membrane. The derivation is based on the assumption of voltage-gated ion channels. The parameters of these equations are chose carefully to fit with the recorded data. These mathematical descriptions can be expressed also as an equivalent circuit model called Hodgkin and Huxley's model.

This model remains as a standard in the simulation of excitable membranes. It is still widely used to describe the excitable membrane of various types of cells or used as a framework.

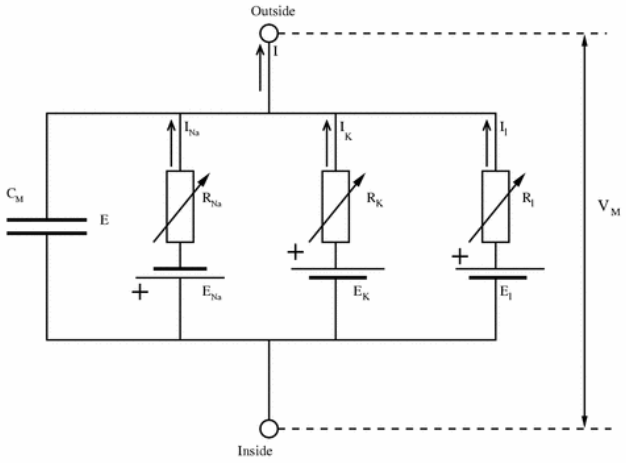

Figure-6-10: The equivalent circuit of Hodgkin and Huxley model.

The circuit is composed of one capacitor, three voltage power sources and three resistors (as shown in the figure above).

The capacitor

The capacitor represents the membrane capacitance, through which capacitive current flows. The capacitance is origin from the lipid bilayer structure of the membrane.

The variable resistors

The permeability of ions through the membrane is controlled by the gating of ion channels. The conductance of the variable resistor (H-H uses conductance instead of resistance) is proportional to the percentage or possibility of opened ion channels. The three ion channels are respectively the sodium, potassium ion channel and the leak current channel.

The leak current channel

The leak current represents the flow of some unidentified ion types. The leak current is small and also important to keep the currents balanced and the resting membrane potential in equilibrium.

The voltage power sources

The voltage power sources represent the equilibrium potential of ions across the membrane.

6.7.2. Membrane current and displacement current

The membrane current is a sum of the capacitive current, different ion currents through the ion channels and the small leak current.

$I_{mem} = I_c + I_{Na} + I_K + I_{Leak}$

Where,
$I_{Na} = (E - E_{Na})\, g_{Na}$;

$I_K = (E - E_K)\, g_K$;

$I_{Leak} = (E - E_{Leak})\, g_{Leak}$;

$I_C = - C_m\, (dE / dt)$;

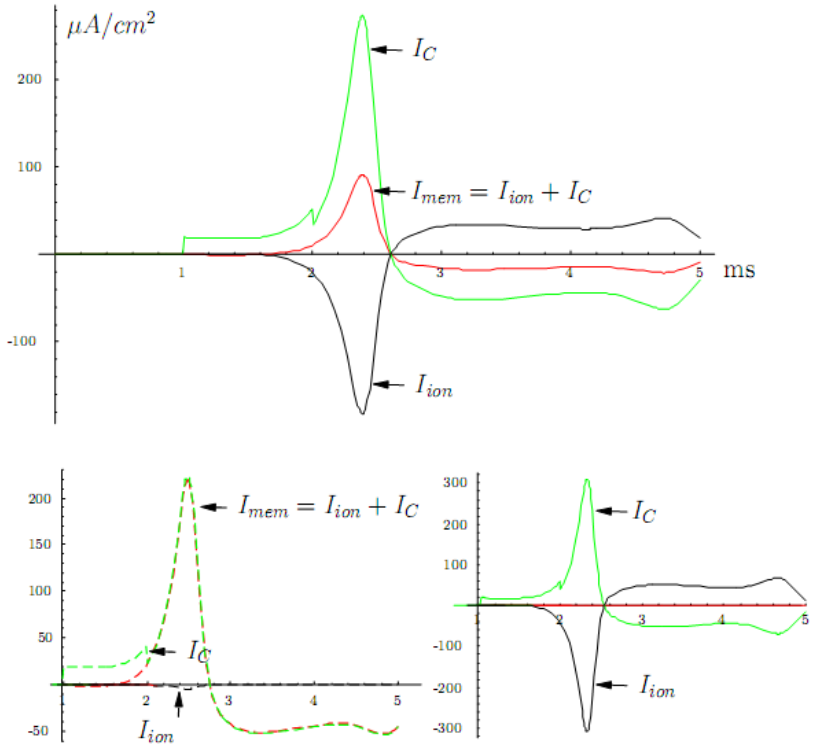

Figure-6-11: The Mathematica simulated membrane action potential of the squid giant axon. The simulation uses two compartment H-H model. The diagram shows the membrane current (I_{mem}), the capacitive current (the displace current I_C) and the ionic current (I_{ion}) of a patch of membrane(compartment A). On the top plot the compartment A has 50% ion channel density in compare to the other compartment (B). The density is set to 1% and 99% at the bottom left and bottom right plot respectively.

As shown in the figure, Ion current increases with the ion channel density. The capacitive current does not change much. The membrane current is a sum of these two currents. Therefore it increases when the ion channel density difference between two compartments increases.

Displacement current is easy to be overlooked

The membrane current includes the ion current through ion channels, but that is not all of it. There is also displacement current through the membrane capacitor. The ions current changes the membrane potential. That causes the electric field changing inside the membrane capacitor. The change in the electric field is equivalent to a current, known as the displacement current. It is also called as the capacitive current. The capacitive current is a part of the membrane current, but it is easy to be overlooked. The membrane current is often been imagined as only the ions crossing the membrane.

When displacement current offsets ion current

An action potential is always involving ions flowing through membrane. But if the

capacitive current exactly offsets the ionic current, the total membrane current will be zero. In this condition, although there is still ion current, the extracellular microelectrode can not detect any signal. This situation will be discussed in the followed sections later. It requires completely uniform distribution of ion channels and fully synchronized membrane action potential without propagation.

Current between multiple compartments

Separating the membrane into many parts (multiple compartments), will help to understand the membrane current. The membrane current circulates between different parts of the membrane. If there is no current flowing in from other parts, nor current flow out to other parts, the membrane current at this part is zero.

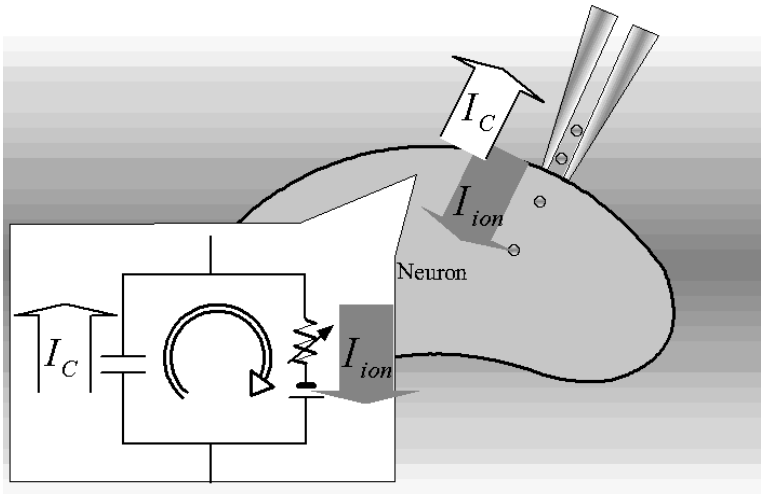

Figure-6-12: The current circulating only between membrane capacitor and ion channels does not count in the net membrane current.

6.7.3. N，m，h

Hodgkin and Huxley introduced the variables m, h, and n to describe the variable conductance of the ion channels (g_{Na} , g_K). They are named as state variables or gating parameters. The variable m, n and h each change between 0 and 1 as a function of time and membrane voltage. If the membrane potential is raised from resting potential above a threshold, m, h and n change gradually from the steady state values to other new steady state values. Different membrane potential corresponds to different state values of m, h and n. Variable m corresponds to the open of the sodium channels. Variable n corresponds to the open of the potassium channels. Variable h corresponds to the close of the sodium channels.

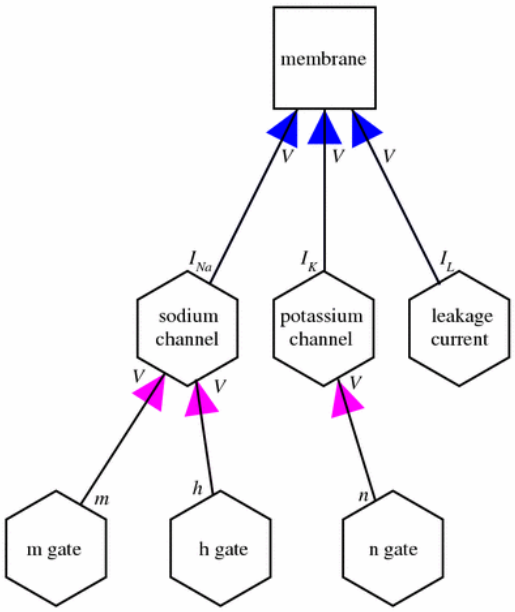

Figure-6-13: The mathematical relationship of the variables in the Hodgkin and Huxley model.

The following are the equations that define n. Those equations of m, h are similar and not listed here. a_n , β_n are called of rate constants. There are also rate constants of a_m , β_m , a_h , β_h relating to m, h. They determine the change rate of m, h, n. a_n , β_n are the function of membrane potential. Each value of potential corresponds to a value of a_n , β_n . If the membrane potential remains stable, so are the a_n , β_n . Under such circumstances, the n is an exponential function of time. However, under the actual circumstances, the membrane potential is not fixed.

$$dn / dt = \alpha_n (1 - n) - \beta_n n \qquad \text{Eq-6}$$

Where,

$$a_n = 0.01 (V_m + 10) / (Exp (1 + 0.1 V_m) - 1) \qquad \text{Eq-7}$$

$$\beta_n = 0.125 Exp (V_m / 80) \qquad \text{Eq-8}$$

The variable m, h jointly determines the conductance of the sodium channel. The m rises quickly to a maximum, and the h decreases more slowly to the minimum. Therefore the conductivity of the sodium channels rises rapidly at beginning and then declines slowly. As for the conductivity of potassium channel, it increases to a maximum value controlled by the variable n. When the membrane potential changes the variables n, m, h and the conductance also changes.

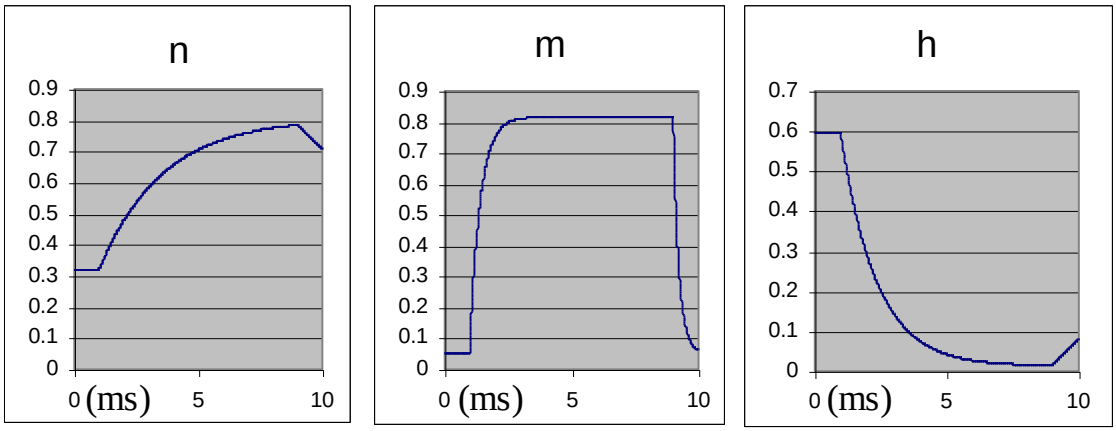

Figure-6-14: The gating parameter of squid giant axon simulated by spreadsheet software 'excel'. The membrane potential is under the control of voltage clamp and changes from 0 mV to 60 mV then return to 0mV (It is the intracellular voltage at 1952. It is equivalent to today's -60mV, 0mV, -60mV). The gating parameters are exponential functions. Variable n determines potassium channels, variable m, h determines sodium channels.

6.7.4. Conductance of ion channels gNa, gK

The variable conductance of the ion channels is defined by the gating parameters (n, m, h) in the following equations:

$$g_{Na} = \hat{g}_{Na}\, m^3\, h \qquad \text{Eq-9}$$

$$g_K = \hat{g}_K\, n^4 \qquad \text{Eq-10}$$

In this equation, $\hat{g}_{Na}$ *and* $\hat{g}_K$ are the maximum conductance of the membrane for Sodium and Potassium. They correspond to the conductance when all sodium and Potassium ion channels are open.

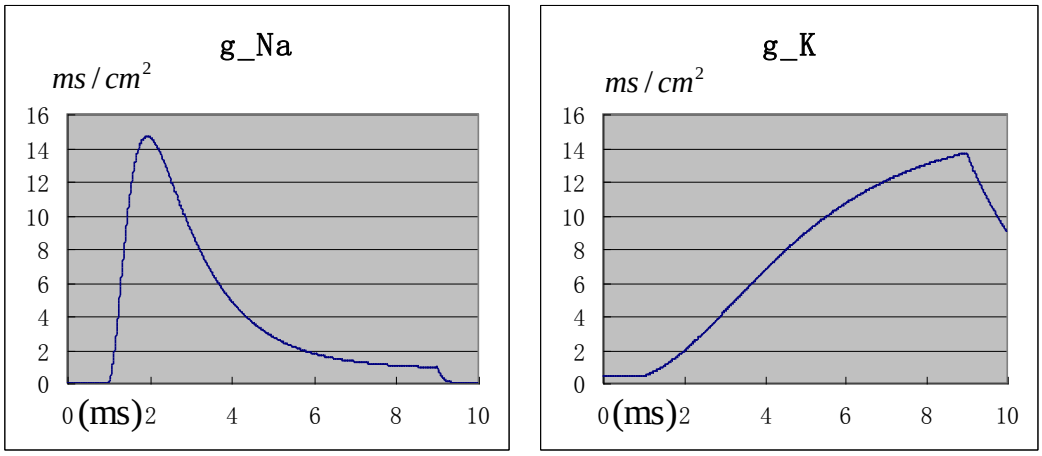

Figure-6-15: The membrane conductance of squid giant axon to sodium and potassium simulated by 'excel'. The voltage clamp control the membrane potential from 0 mV to 60 mV then return to 0mV (equivalent to today's -60mV, 0mV, -60mV).

The dynamic conductance of the ion channels gives rise to the generation of the

action potential. When membrane voltage is stimulated above the threshold, the conductance of the ion channels increases and returns following the curve defined by the equations above. The variation of the conductance of the ion channels breaks the equilibrium of the distribution of the ions. The ion currents flow through membrane and change the membrane potential. The membrane voltage changes suddenly and returns to the static value in milliseconds. This cycle of voltage variation is so called action potential.

FET instead of resistor

More recently a field effect transistor is used to take place the variable resistor in the attempt to build a real circuit simulating the function of the excitable membrane. The gating of the FET is voltage dependent just like the voltage-gated ion channels.

6.8. Membrane AP and propagated AP

This section gives some background knowledge about membrane action potential and propagated action potential.

6.8.1. Graded potential and action potential

In the nervous system, signals are not only in the form of impulses, but also in the form of slow potential fluctuation. It is the so-called graded potential [Vanderwold and Leung, 1985]. Graded potential may be caused by postsynaptic potential. If the membrane potential fluctuation does not reach the threshold, it will not trigger action potentials. If the neuron is under inhibition, action potential will not be generated even when the threshold is reached. The potential fluctuation can reach the range of mV.

6.8.2. Membrane action potential and propagated action potential

“Membrane action potential”, in opposite to “propagated action potential”, means that during the firing of an action potential the membrane potential is uniform at each instant over the whole neural membrane. In another words, the whole membrane acts with the same pace and all the ion channels are synchronized. This concept is raised for the convenience of the theoretical study [Hodgkin and Huxley,

1952]. There are circumstances that the propagation can be ignored and the theory of membrane action potential can be applied.

As the name suggested, membrane action potential does not propagate and is limited at local membrane. This is based on an assumption that the local membrane does not exchange currents with other membrane area. The current only circulates locally and the net membrane current is zero. Therefore, membrane action potential does not affect the membrane nearby. No current sink or current source is formed extracellularly. The extracellular potential does not change too. The membrane action potential is the undetectable action potential with extracellular MEAs, which has been described in previous sections. The membrane action potential in strict sense may not exist in reality. The actual action potential rouses more or less potential fluctuation extracellularly.

Propagated action potential gives rise to net membrane current. The membrane current circulates between the local membrane and other parts of the membrane. The membrane nearby will be depolarized, which initiates the generation of new action potential. Propagated action potential can be classified in the unsynchronized action potentials, which is discussed in Chapter six. Such action potentials cause current flowing and potential fluctuation extracellularly, that can be detected by extracellular MEAs.

6.8.3. The membrane potential in vivo

When muscle cells receive impulses, the impulse is ended as a membrane action potential at the joint of nerve and muscle (nerve endplate). This kind of membrane action potential is called as the end-plate potential. Photoreceptor cells in the retina also generate membrane action potentials in response to light stimulation. These types of membrane action potential affect the membrane potential in neighbouring. But the affection does not give rise to active propagation. The cells are not capable of active propagation due to the absence of ion channels or being inhibited. The passive propagation of membrane action potential is like the transmission of signal in man-made cable. The farther away from the region, the smaller is the potential. The attenuation can be described by an exponential function.

6.8.4. Propagation in soma can be neglected

The velocity of action potential travel along nerve fibre of mammal is 0.5-120 m/sec [W.F. Ganong, 2003]. The velocity of propagated action potential in squid giant axon of 238 μm radius (Hodgkin, A.L. and Huxley, A.F., A quantitative description…, 1952) is 18.8 m/s. According to my searching, there is no report on the velocity in soma. A reasonable estimation is that the velocity in soma should not be smaller than it in fibre, due to higher volume to surface area ratio of soma, which is regarded as an important factor to accelerate propagation in un-myelinated axon. Based on this estimation, the time of an action potential traverse a neural soma of *10μm* diameter should be below micro second. The upper limit of the frequency spectrum of the action potential recorded extracellularly is below 10kHz normally. In another word, the shortest time for the potential to rise from bottom to its top value is 50 μs. So the biggest difference between the action potential recorded at each end of the soma is around mV. In terms of circuit theory, the time constant of Hodgkin-Huxley model of neural membrane is much bigger than micro second. Therefore it is safe to assume that different membrane patches of soma fire synchronously. Notice that synchronous is used here in no intention to deny the propagation of action potential. It will be discussed later about what happens when action potential propagates.

6.8.5. The model of myelinated neuron

The velocity of the action potential propagated in a neural fibre is proportional to the diameter of the fibre [Hursh, 1939; Rushton, 1951]. The myelinated neural fibre can be represented by a cable model similar with the un-myelinated fibre. The difference is that there are two types of elements in the former one. The passive element represents the myelinated region and the active element represents the node of Ranvier [Frankenhaeuser and Huxley, 1964; McNeal, 1976].

6.9. Detect any extracellular signal?

The detection of extracellular potential signal is discussed in this section. It is proved first that nothing can be recorded with extracellular electrodes when neurons are at rest. Then the discussion move on to the membrane action potential and to the propagated action potential.

It is derived that not all the action potential give rise to detectable extracellular

field potential. The asymmetric distribution of ion channels (section 6.9.3) and the propagation of action potential (section 6.9.4) causes current sink or source to be formed while neuron fires. So creates various forms of extracellular field potential. The extracellular MEAs cannot detect the static membrane potential and the membrane action potential when ion channels are uniformly distributed (section 6.9.2).

This section gives deduction based on two compartment H-H model (section 6.9.1) to reach these conclusions above. Simulation results by PSPICE and Mathematica are also given to prove these conclusions.

Detect the resting potential

It is well known that static membrane potential is around -70mV. This value can be obtained by measuring the voltage between an intracellular electrode and a reference electrode emerged in the extracellular medium. Without intracellular electrode, but with only extracellular electrode, static membrane potential cannot be detected.

This can be understood with help of electrostatics. Electrostatic field cannot be built inside a volume conductor. Hence potential is in the same value all over the bulk medium outside cell body. It is obvious that no potential difference can be detected between the extracellular electrode and the reference electrode.

6.9.1. Model of two compartments

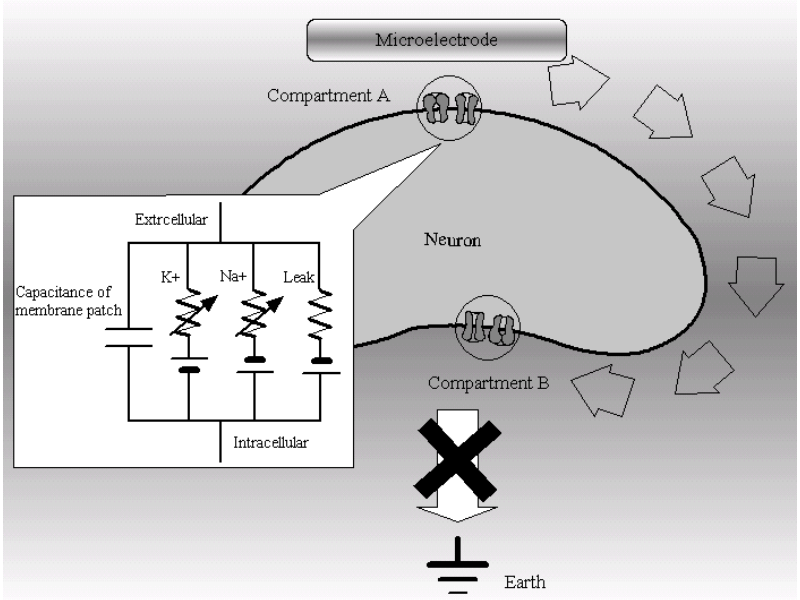

Figure-6-16: the soma of a neuron is modelled with Hodgkin-Huxley model of two compartments. The compartment A is in contact with the microelectrode and the compartment B is the other membrane area which is not coupled with the microelectrode. Arrows indicate the possible direction of ion current. Crossed arrow denotes that no net current flows between the whole neuron and earth.

Hodgkin-Huxley model can be used to describe any part of the membrane in principle as multi-compartment model did. It is applied here to describe two membrane patches of a neuron with the same measure of area. They can be any part of the membrane.

An isolated neuron (not connected to other neurons) in medium does not support net current flowing to or from earth according to Kirchhoff's current law. So the neuron as a whole does not form current sinks or sources. The current sinks or sources could only exist partially over the whole neural membrane. The following discussion will focus on whether there is current flowing from one patch to the other under certain circumstances. The existence of the extracellular current flow during the generation of membrane action potential determines the existence of current sinks and sources and further on whether the action potential can be detected by extracellular microelectrodes.

Because the area of the two membrane patches are the same, so the membrane capacitance in two circuit models are equal. The equilibrium potential for Potassium and Sodium in two circuits are the same too. The membrane resistance to ions in different patches of the membrane may be different. It depends on the partial density of ion channels around the area of the membrane. The discussion is carried out based on the density of ion channels.

6.9.2. Membrane AP with same density of ion channels

To be detectable by extracellular MEAs, the neuron has to generate current through extracellular space and so creates extracellular field potential. The following derives whether current flows through extracellular medium between the two compartments.

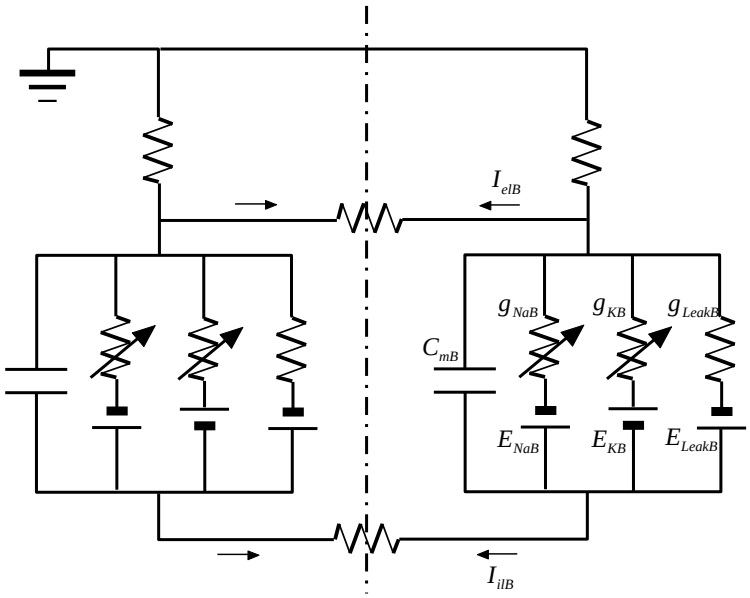

Figure-6-17: The equivalent circuit of Hodgkin-Huxley model with two compartments. The two compartments are proved to be identical to each other.

We already know that $E_{NaA} = E_{NaB}$, $E_{KA} = E_{KB}$, $E_{LeakA} = E_{LeakB}$. And since compartment A and B are in the same size, so $C_A = C_B$. And ion channels are uniformly distributed, so $\hat{g}_{NaA} = \hat{g}_{NaB}$, $\hat{g}_{KA} = \hat{g}_{KB}$, $\hat{g}_{LeakA} = \hat{g}_{LeakB}$. Stated in the definition of "membrane action potential", membrane potential keeps uniform at any instant and anywhere. The membrane resistance to ions are functions of time and membrane potential. So, the time courses of the resistance in different patches of the membrane are the same. Therefore, $g_{NaA} = g_{NaB}$, $g_{KA} = g_{KB}$, $g_{LeakA} = g_{LeakB}$.

As shown above, the two compartments are exactly the same. The two sub circuits are flipped version of each other. Each compartment drives current to the other. It is easy to find out each current is reverse to the other ($I_{elA} = I_{elB}$, $I_{ilA} = I_{ilB}$. According to Kirchhoff's current law, $I_{elA} + I_{elB} = 0$, $I_{ilA} + I_{ilB} = 0$. Therefore, the current is zero. $I_{elA} = I_{elB} = 0$, $I_{ilA} = I_{ilB} = 0$.

As shown above, two membrane patches with same density of ion channels do not drive current through the extracellular space between them. Therefore no extracellular field potential arises.

Because the compartment A and B can be any part of the neural membrane, this conclusion can be extended to the whole soma of a neuron (not to dendrite and axon. Propagation of action potential cannot be ignored there). A neuron with an uniform distribution of ion channels does not generates current through extracellular space around its soma. In another word, action potential cannot be

detected extracellularly under this circumstance.

This conclusion is conformed with the Mathematica simulation as shown in the following figure.

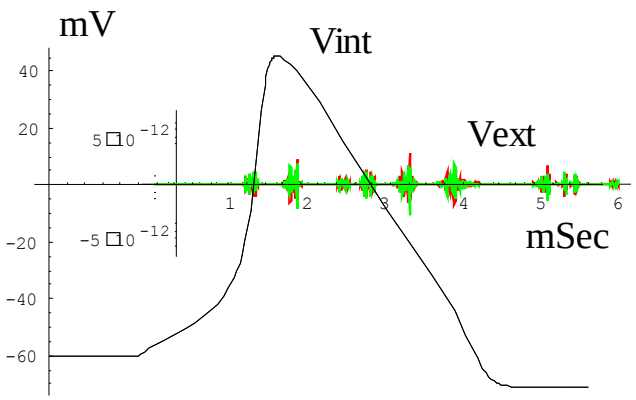

Figure 6-18: The Mathematica simulation of the two compartment model. Membrane AP with same density of ion channels distributed on compartment A and B. The Vint is the intracellular potential and Vext is the extracellular potential. The noise-like Vext is actually the residue from the calculation of Mathematica. It proves that no extracellular potential when the ion channels are evenly distributed.

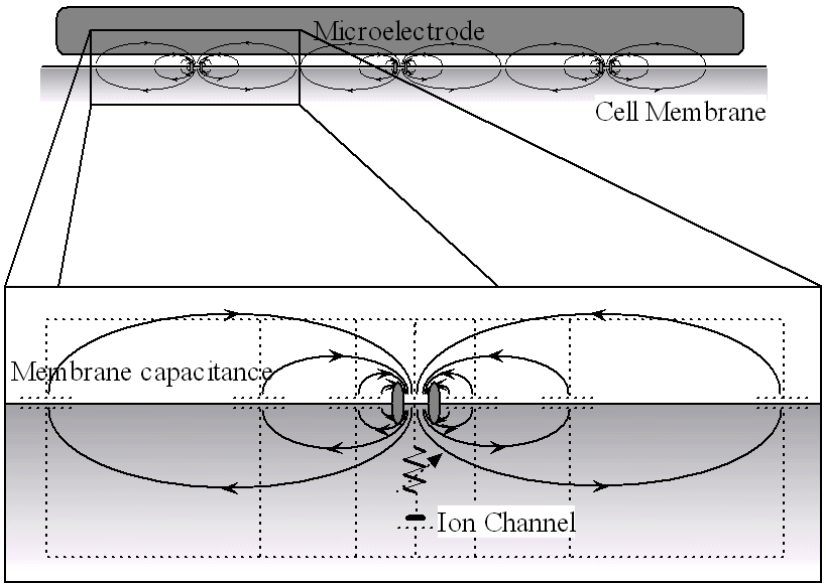

Figure-6-19: The membrane is uniformly distributed with ion channels. Extracellular microelectrode may not detect any voltage fluctuation.

6.9.3. Membrane AP with different density of ion channels

This section extends the discussion to whether current flows between two membrane patches with different density of ion channels.

High density of Sodium ion channels

Assume the extracellular resistance is small and can be neglected. Therefore $E_A = E_B$. Assume the only difference between the two membrane patches is the density

of Sodium ion channels. Patch A has a higher density and so $\hat{g}_{NaA} > \hat{g}_{NaB}$.

Together with:
$I_{NaA} = (E_A - E_{NaA})\ \hat{g}_{NaA}\ m^3\ h$
$I_{NaB} = (E_B - E_{NaB})\ \hat{g}_{NaB}\ m^3\ h$

Results in:
$I_{NaA} > I_{NaB}$

Similarly:
$I_{KA} > I_{KB}$;
$I_{LeakA} > I_{LeakB}$;
$I_{CA} > I_{CB}$;

A current $I_{NaA} - I_{NaB}$ flows from patch B to patch A through the extracellular medium. The compartment with more Sodium ion channels acts as a current sink and that with less Sodium ion channels like a current source.

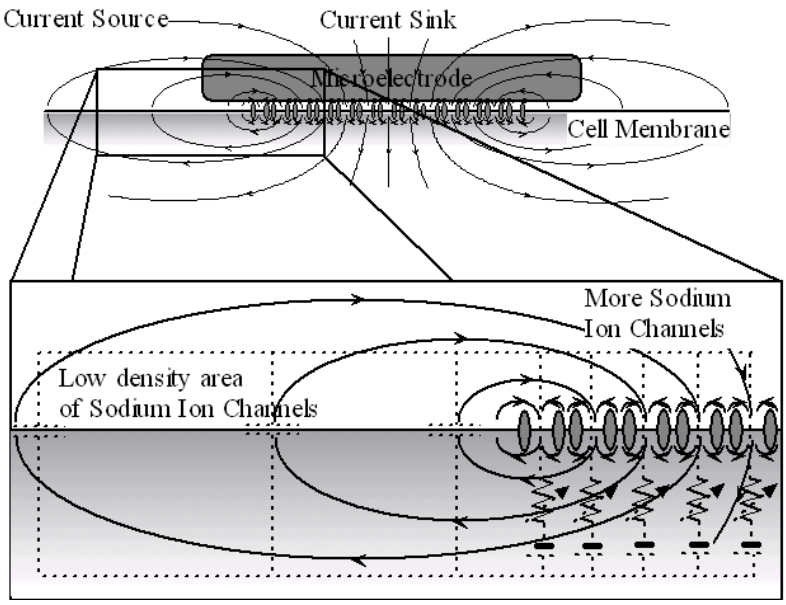

Figure-6-20: The schematic drawing of current map when the ion channels are not uniformly distributed. The ion channel density under microelectrode is higher than other places. A current sink is formed under the microelectrode.

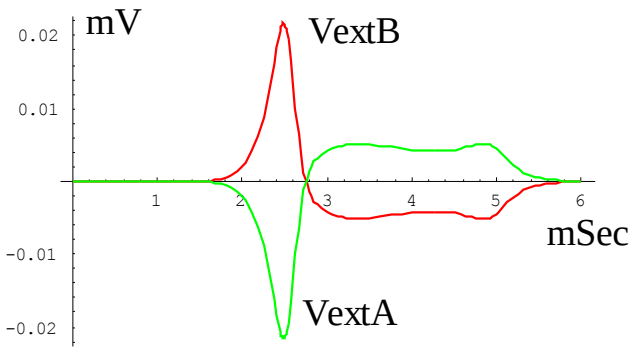

Figure 6-21: The Mathematica simulation of the two compartment model. Membrane AP with different density of ion channels. Compartment A has more ion channels ($\hat{g}_{NaA} > \hat{g}_{NaB}$ and $\hat{g}_{KA} > \hat{g}_{KB}$).

The negative spike is the extracellular potential near compartment A. It indicates the exist of a current sink caused by denser Sodium channels. The positive wave following the spike indicates the current source cause by denser Potassium channels.

High density of Potassium ion channels

Similarly the area with more Potassium ion channels tends to generate current flowing to other part of the membrane. This area acts like current source. The field potential around this area is positive.

Both current source and current sink create local field potential, which can be detected by extracellular electrodes.

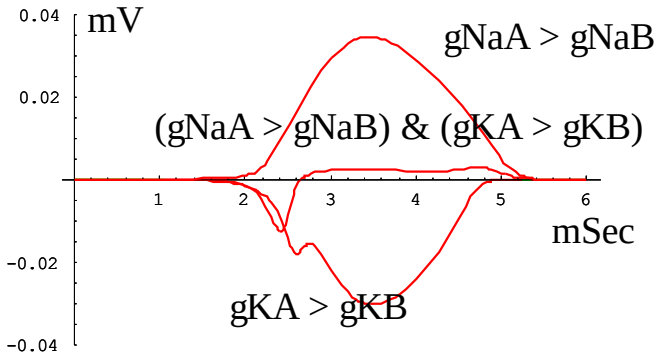

Figure 6-22: The Mathematica simulation. Membrane AP with different density of ion channels. The extracellular potential near compartment A. Different combination of ion channels density renders current source or sink.

6.9.4. Propagated action potential

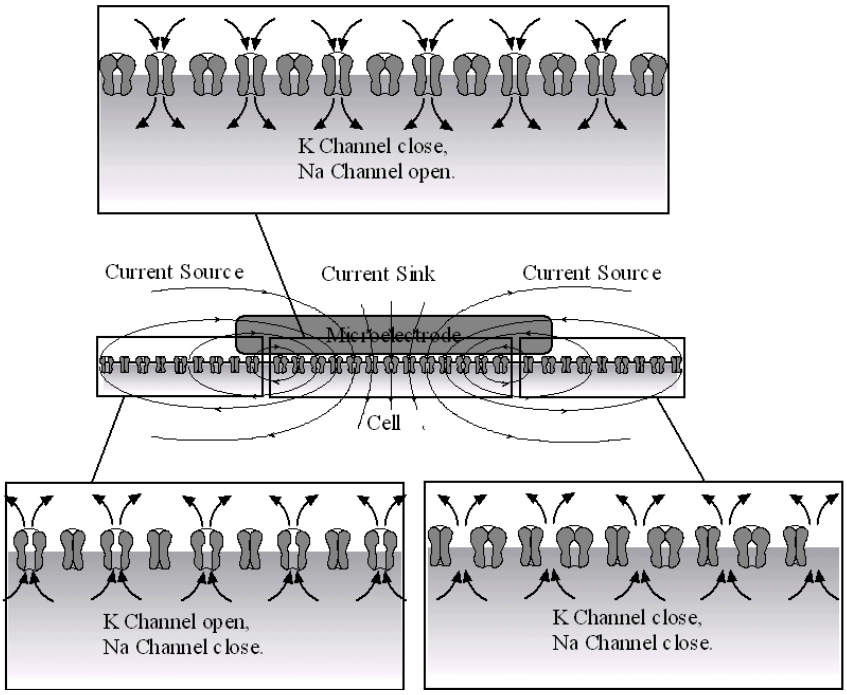

Figure-6-23: A schematic picture presenting one instant of an action potential propagating along the neural membrane. The action potential propagates from left to right. The Sodium ion channels underneath the microelectrode are just opening, while those Sodium ion channels on the left are just closed and those on the right have not opened yet. The Potassium ion channels exhibit similar asynchronous behaviours too. They together create a current sink underneath the microelectrode at this instant.

The propagation of action potential can be quantitatively explained with Hodgkin-Huxley model of neural membrane. Any patch of neural membrane can be represented with a H-H compartment.

Action potential propagates along the neural membrane in a certain velocity (*18.8 m/s* in squid giant axon) [Hodgkin and Huxley, 1952]. The Sodium and Potassium ion channels are potential sensitive. They switch on or off responding to the local potential. These ion channels in the front along the direction of the propagation have a delay in their switching comparing with those ion channels at the backside. This section discuss about how this delay or asynchronous effects the extracellular field potential.

The two patches model is still usable (**Figure-6-17**) by introducing a time delay into the time variable resistors. Assume the patch A locates in the front along the direction of propagation and the patch B at the back. So the time dependent variables in patch A have a delay (Δt) in their function ($g_{NaA} = g_{NaB}\ (t - \Delta t)$, $g_{KA} = g_{KB}\ (t - \Delta t)$, $E_A = E_B\ (t - \Delta t)$).

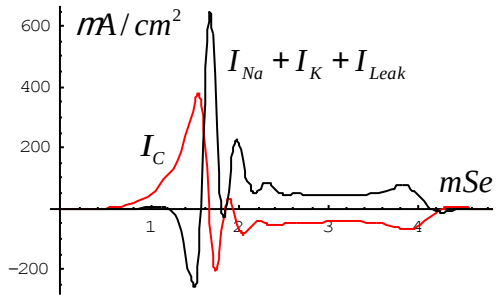

Figure-6-24: The Mathematica simulation of Propagated AP. The current through membrane capacitor (I_c) and through ion channels (I_{Na} + I_K + I_{Leak}).

The time shift (Δt) gives different values to the parameters of two compartments ($g_{NaA} \neq g_{NaB}$, $g_{KA} \neq g_{KB}$ $(t - \Delta t)$, $E_A \neq E_B$). The current through ion channels (I_{Na} , I_K , I_{Leak}) and membrane capacitor (I_c) are all the function of these parameters (g_{Na} , g_K , E). These currents add up to be the membrane current (I_{mem}), which flows through extracellular medium. The Mathematica simulation proves that it is not zero.

$I_{Na} = (E - E_{Na})\, g_{Na}$;

$I_K = (E - E_K)\, g_K$;

$I_{Leak} = (E - E_{Leak})\, g_{Leak}$;

$I_C = - C_m\, (dE / dt)$;

$I_{mem} = I_{Na} + I_K + I_{Leak} + I_C$

The propagation of action potential causes the difference of parameters along the membrane. The asynchronously activated ion channels and propagation of the membrane potential creates extracellular field potential, like the inhomogeneous distribution of ion channels did too.

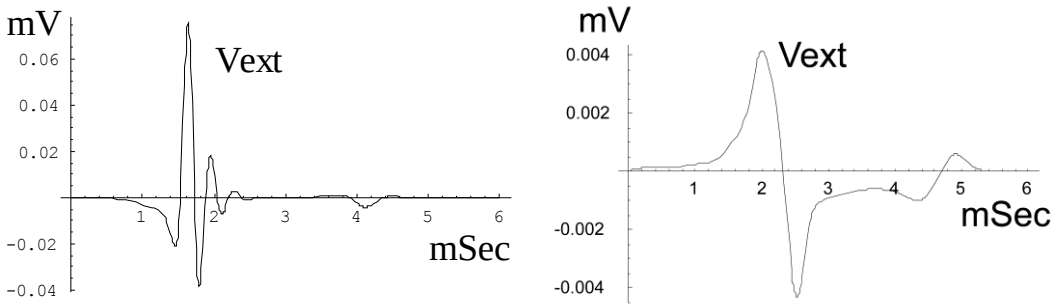

Figure 6-25: The Mathematica simulation. The extracellular potential of a propagated AP. The left resulted from the core-conductor method. The right was from the multi-compartment method.

6.10. Waveforms of extracellular field potential

The waveforms of action potential recorded by intracellular electrode are different with respect to cell types and the recording spot. Still these waveforms share some common features. They all started with a rising phase that is caused by the influx of Sodium ions. And then there is a falling phase due to the outflow of Potassium ions and the cease of Sodium ion current.

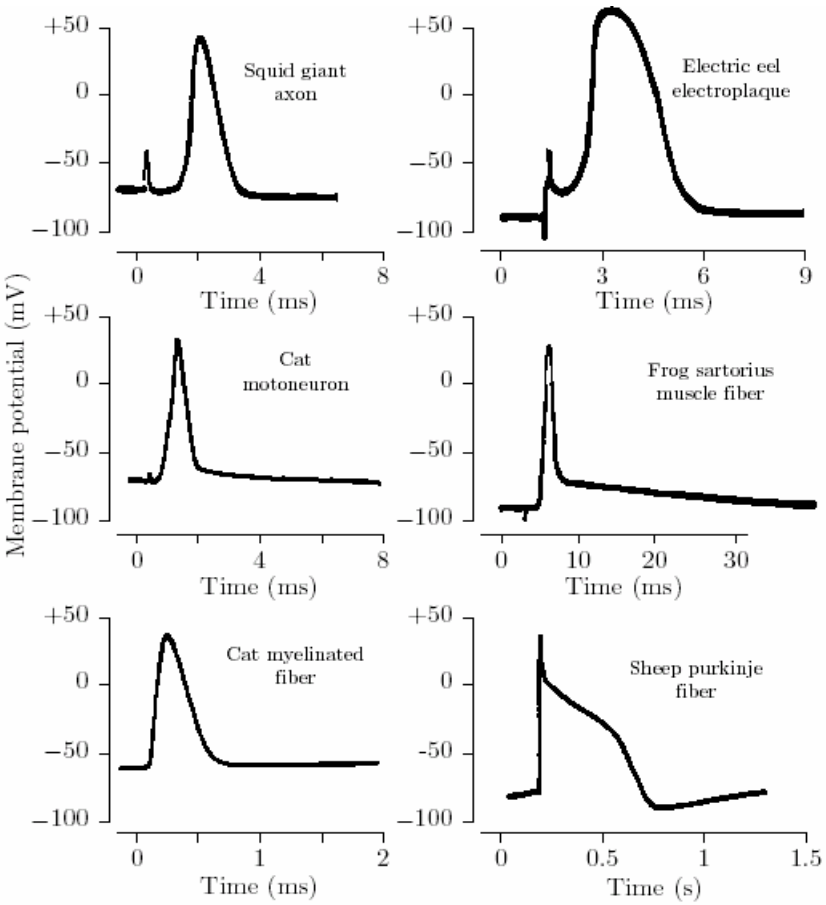

Figure-6-26: The action potential measured in different types of neuron. The diagram is adapted from [Keynes and Aidley, 1991, Fig 2.4].

In contrast, the waveforms of extracellular potential vary more in forms. As described in the beginning of this chapter, the extracellular field potential is closely related to the current sinks and sources. As derived in section 6.9, the current sinks and sources are caused by the asymmetric distribution of ion channels or the propagation of action potential. So the waveform of the extracellular potential is related to these two factors too. Besides, the neuron to microelectrode coupling effects the recording and so changes the waveforms of recorded signal. A series of simulations were performed to reveal how these three

factors affect the recorded waveforms of extracellular potential.

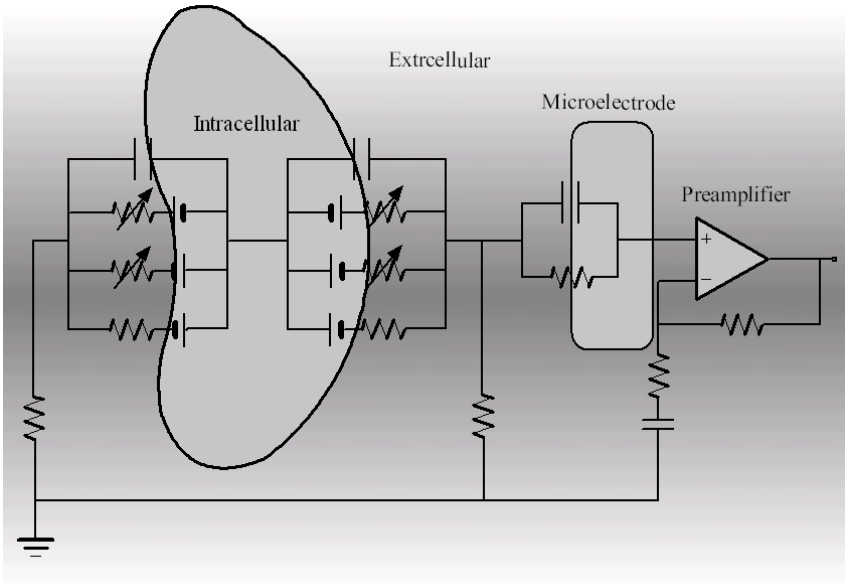

Figure-6-27: The circuit model of the neuron, its interface to microelectrode and the preamplifier.

The circuit models described in this chapter is built under electronics simulation software (PSPICE). The PSPICE alone cannot finish all the work. Mathematica is assigned to work out the variable resistance of the ion channels. The H-H circuit part is transformed into differential equations and numerically solved in Mathematica. The results obtained from solving these equations complement and verify the simulation by PSPICE. The results of these simulations quantitatively prove the qualitative conclusions made in the beginning of this chapter. In this section, different simulated waveforms of extracellular field potential under different setting of parameters are presented. At the end of this section (more in chapter 8), real signals recorded with extracellular MEA are shown. The simulations will help with the understanding on the waveforms of these real signals.

6.10.1. First derivative

The PSPICE simulation could render different waveforms according to different parameters, like different density of ion channels. The parameters in the simulations in this section are tuned to render extracellular waveform in similarity with the first derivative of the intracellular action potential.

The calculation is processed in spreadsheet software (Excel). Forward Difference Derivative Approximation is applied to the waveform of the intracellular potential.

$$f'(t) = (f(t+\Delta t)-f(t))/\Delta t \quad \text{Eq-11}$$

$$f''(t) = (f'(t+\Delta t)-f'(t))/\Delta t \quad \text{Eq-12}$$

$$f''(t) = (f(t+\Delta t)-2f(t)+ f(t-\Delta t))/\Delta t^2 \quad \text{Eq-13}$$

As shown in the following figure, the simulated extracellular field potential is similar to the first derivatives of the intracellular action potential. This feature has been mentioned in some documents. [Bierer, S.M. et.al. 1994]

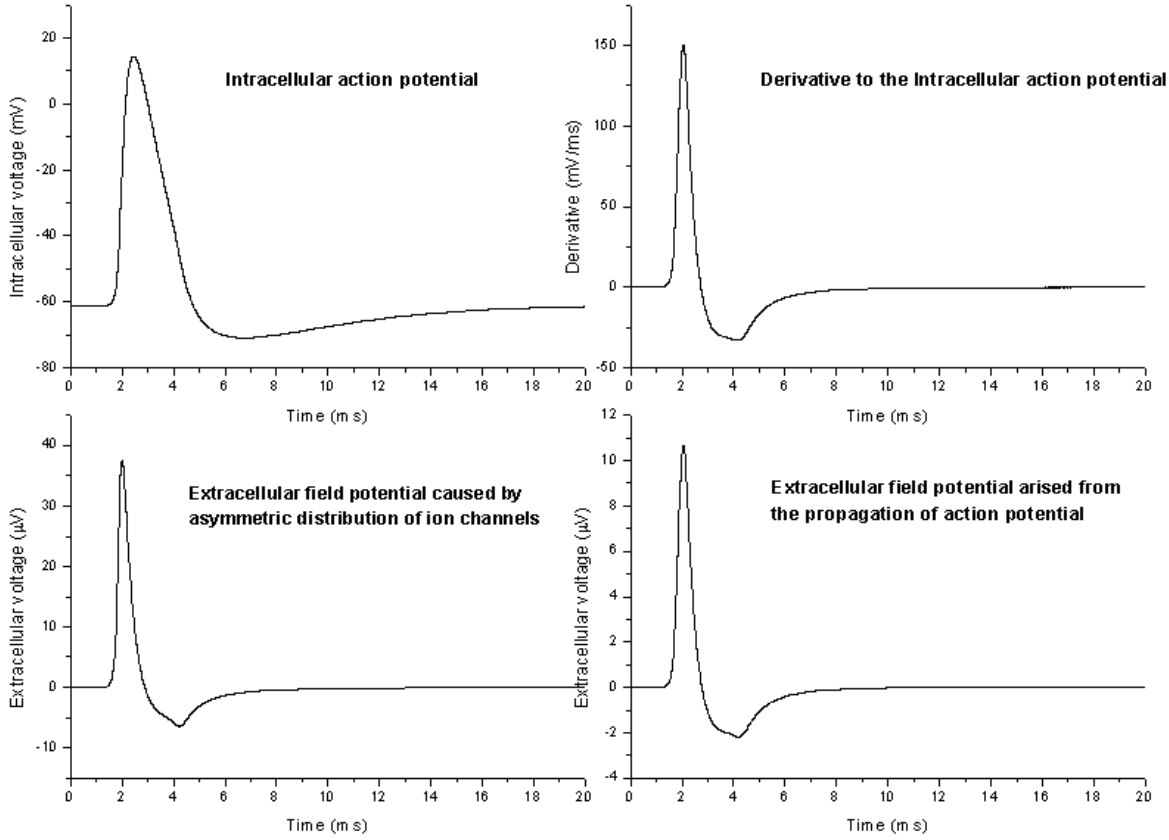

Figure-6-28: Intracellular action potential (from spreadsheet simulation of H-H model of giant axon of squid under current clamp), the first derivative of it (with spreadsheet), extracellular field potential caused by asymmetric distribution of ion channels (PSPICE simulation) and extracellular field potential arised from the propagation of action potential (PSPICE simulation).

6.10.2. Second derivative

There are also reports about the similarity between the extracellular action potential with the second derivative of the intracellular action potential. In this section, some references are listed. In the following sections, some of our simulation results showing the second derivative similarity will be described.

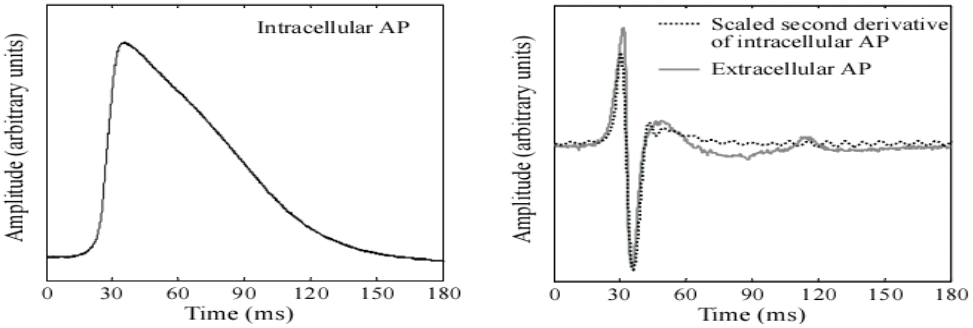

Figure-6-29: This diagram is from [K. H. Gilchrist, his thesis, 2003]. The diagram shows the action potential of an HL-1 cell. The extracellular action potential is similar in waveform with the second derivative of the intracellular action potential.

Many believes that the seal resistance controls the waveform of the extracellular action potential. With the increase of seal resistance, the extracellular action potential at the beginning is similar with the second derivative of the intracellular action potential, then the first derivative. If seal resistance is extremely high, it even resembles the intracellular action potential itself. [Grattarola and Martinoia, 1993] [David A. Borkholder, his thesis, 1998]

6.10.3. Distribution of ion channels

As stated earlier, the membrane area with denser Sodium ion channels or sparser Potassium ion channels acts like a current sink when these ion channels are switched on. While the other area with lower density of Sodium ion channels or higher density of Potassium ion channels act as current source. The current flows from source to sink through extracellular medium and so creates field potential.

The variation on the distribution of ion channels affects the current and the extracellular field potential. The detail of the effect is explored with a Hodgkin and Huxley model of two compartments. One compartment (A) simulates the membrane area that is in contact to the microelectrode and the other compartment (B) represents the membrane area that is emerged in the extracellular medium.

Parameters used in the model can be found in appendix section 6.15.

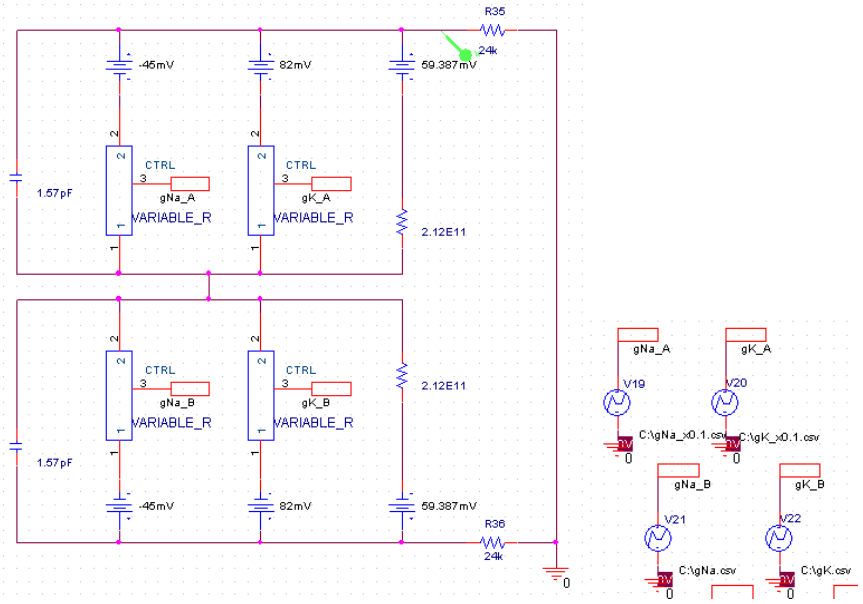

Figure-6-30: Equivalent circuit of HH model with two elements drawn in PSPICE.

The figure below shows the simulated waveforms of extracellular potential by varying the maximal conductance of ion channels in the model. The maximal conductance of ion channels is proportional to the density of ion channels. Therefore the distribution of ion channels is changed by varying these constants in the model.

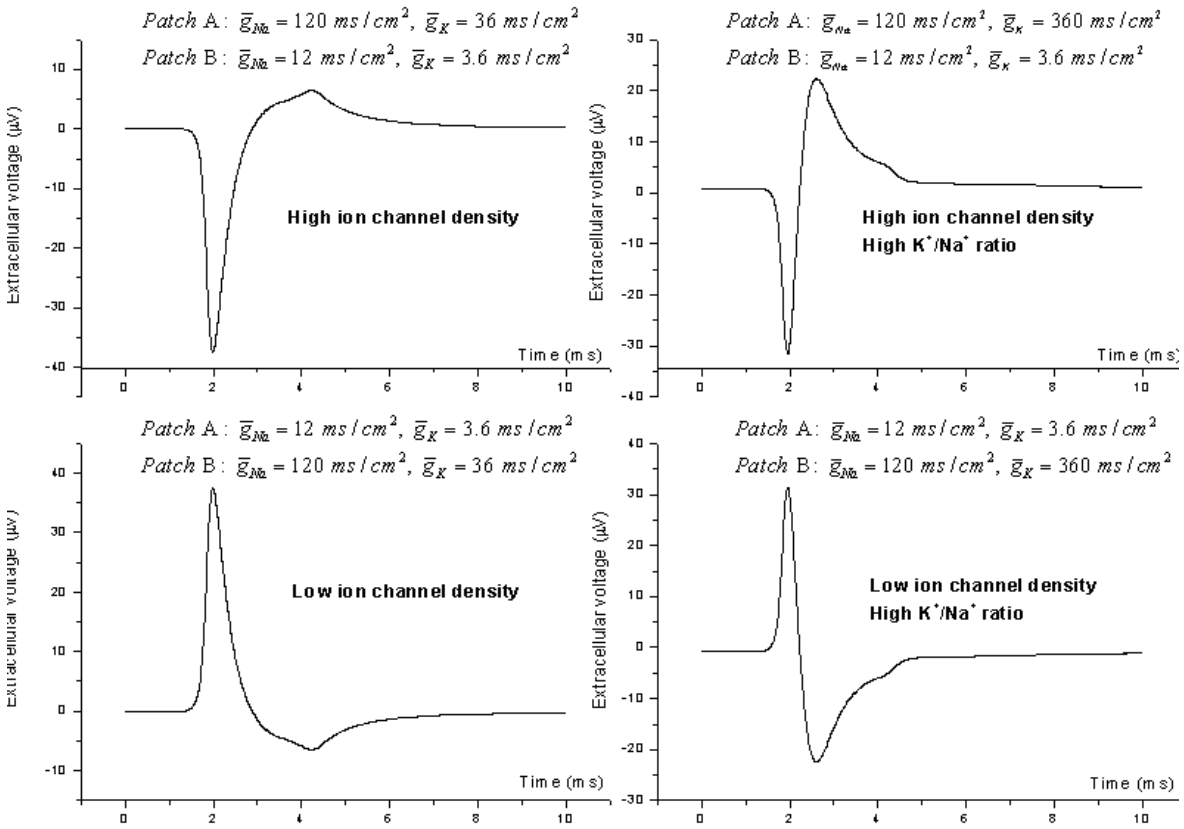

Figure-6-31: Extracellular field potential caused by asymmetric distribution of ion channels. The maximal conductance of membrane patch A to Sodium and Potassium ions differs from 0 S to 170 × 10^{-9} S. The maximal conductance of patch B is kept at 17 × 10^{-9} S. The waveforms in the figure

simulate the recorded extracellular voltage at patch A when its maximal conductance varies.

Current flows through extracellular medium between the compartments with different density of ion channels. The difference scales the magnitude of the current and the field potential. The waveform in these diagrams make people think of their similarity with the first derivative and second derivative of intracellular action potential. They also remind people the positive spikes recorded near dendrites and the negative spikes recorded near axons.

The waveform of an action potential is often comprised with a peak and a valley. The magnitude of the first wave peak or valley is related to the difference between the density of the Sodium ion channels. That of the second wave valley or peak is related to the difference between the densities of the Potassium ion channels. Hence, the ratio between the density of Sodium and Potassium ion channels changes the shape of the waveform.

The distribution of ion channels shapes the waveform. However, it is not the only factor contributed to the shaping.

6.10.4. Propagation of action potential

Propagated action potential gives rise to the formation of current sinks or sources along the neural membrane. The propagation of action potential causes the asynchronous switching of the ion channels. This asynchrony in effect is similar to the asymmetric distribution of the ion channels. The propagation also creates the membrane capacitance current flowing through extracellular medium.

The propagation is simulated with two methods here. One uses the multi-compartment model (**Figure-6-33**) and the other uses the core-conductor model (used by Hodgkin and Huxley, 1952). The multi-compartment model is built under both Mathematica and PSPICE. The core-conductor model runs by Mathematica only. In other words, the propagated action potential is simulated in three different ways. They offset the shortcomings and testify the results of each other.

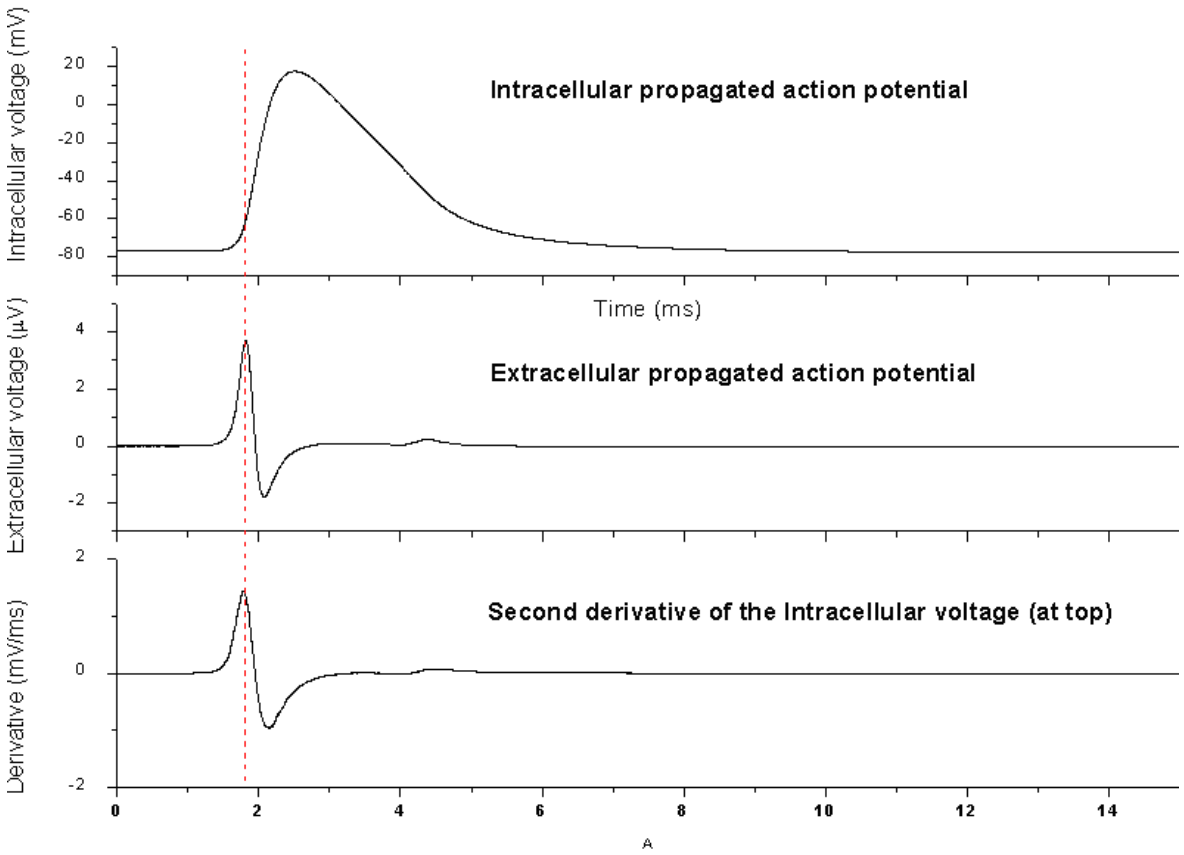

Figure-6-32: Extracellular field potential arise from the propagation of action potential. The action potential arrived later or early at membrane patch A than at membrane patch B. The time of delay or advance is 0.1 ms.

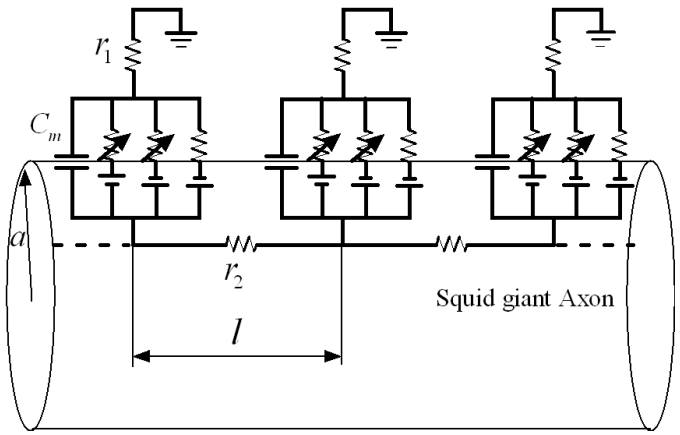

Figure-6-33: A multi-compartment model of a squid giant axon.

The multi-compartment model simulated the action potential propagating in squid giant axon at 18.5 ^{o}C (Hodgkin and Huxley, A quantitative description…, 1952). The known parameters in this model also come from the paper above.

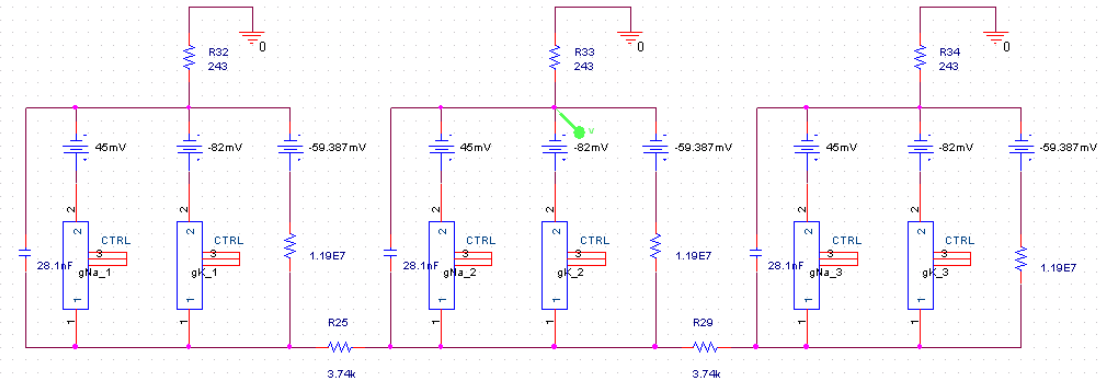

Figure-6-34: The equivalent circuit of the HH model with multiple elements in PSPICE. The propagation of action potential is simulated with this model.

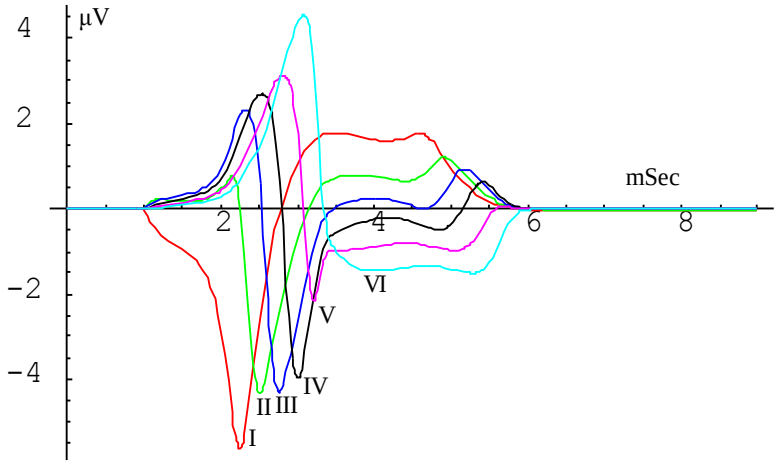

Figure-6-35: The extracellular potential waveforms outside six different compartments against time. The waveform changes at different locations along the axon. The shift of the peak and valley shows the propagation of action potential. It is simulated with multi-compartment model under Mathematica.

The action potential originates at the compartment A. The Sodium ion channels of this compartment open first when those of other compartment are closed still. This asynchronous action of ion channels gives rise to a current flowing from other compartments to the compartment A. A current sink is formed at compartment A extracellularly. After that, the asynchronous action of Potassium ion channels causes the formation of current source there. The waveform at compartment A is similar with those waveforms at compartment with low density of ion channels caused by the asymmetric distribution of ion channels.

Similar process repeated along the axon with the propagation of the action potential. These waveforms have a significant difference with the waveform at the compartment A. They all start with a rising phase. Those compartments work as current source before they generate their own action potential.

The comparison of intracellular and extracellular signal

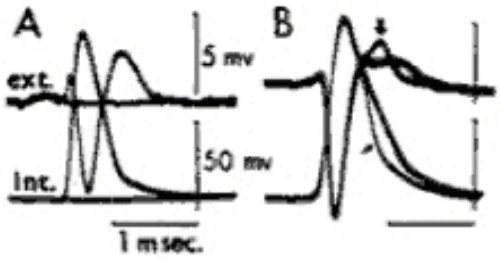

Figure-6-36: The intracellular and extracellular action potential recorded with a stereo-micropipette. Motoneurons of the lumbar spinal cord in response to single pulses applied to the ventral roots. Motor axon (A), initial segment (B). The diagram is from [Terzuolo and Araki, 1961].

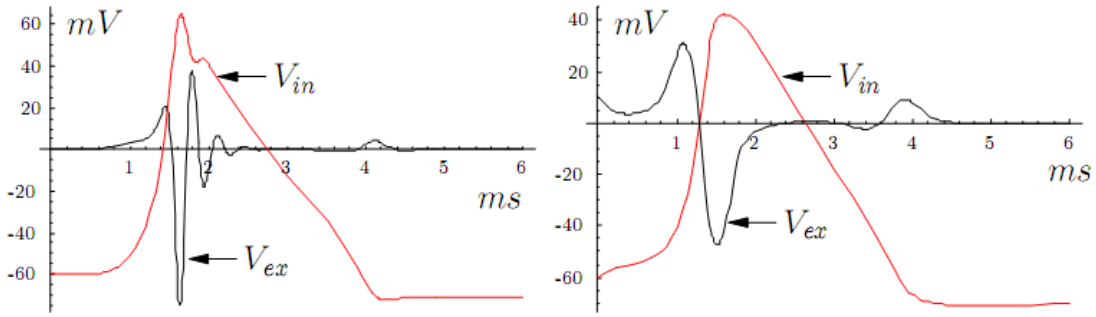

Figure-6-37: Mathematica simulation of the propagated action potential. The left one used the core-conductor method and the one at right hand side used the multiple elements method. The red lines are the intracellular action potential and the black lines are the extracellular action potential near membrane in medium without coupling to electrode. The extracellular potentials are magnified by 1000 times (left) and 3000 times (right) respectively.

The parameters of these two simulation are listed below.

The core-conductor method
radius of the axon: a_1 = *2.38 μm*;
specific resistance of axoplasm (intracellular): *R = 35.4 Ω cm*;
Medium conductivity: 13 ms cm^{-1}
Intracellular resistance per unit length: 1.99×10^5 *KΩ/cm*
Extracellular (radial) earth resistance unit length: 0.1 *KΩ*cm*
Extracellular axial resistance per unit length: 1.99×10^4 *KΩ/cm*
Action potential tansfer velocity: 0.188 *cm/ms*
The capacity per unit area of membrane: C_m = *1.0 μF/*cm^2*;*
The equilibrium potential of Sodium ions: E_{Na} = *45 mV;*
The equilibrium potential of Potassium ions: E_K = *-82 mV*;
The leakage potential: E_{Leak} = *-59.387 mV*
The maximum resistance of the Sodium ion channels: $\hat{g}_{Na}$ = *120 ms /* cm^2;
The maximum resistance of the Potassium ion channels: $\hat{g}_K$ = *36 ms /*cm^2;
The resistance of the leak current channels: g_{Leak} = *0.3 ms /* cm^2

The multiple compartment method
radius of the axon: a_1 = *2 μm*;
Length of each compartment: 400 *μm*;
specific resistance of axoplasm (intracellular): *R = 35.4 Ω cm*;
Medium conductivity: 13 ms cm^{-1}
Intracellular resistance of a compartment: 1.13×10^4 *KΩ*
Extracellular (radial) earth resistance of a compartment: 2.61 *KΩ*
Extracellular axial resistance of a compartment: 1.13×10^3 *KΩ*

The capacity per unit area of membrane: $C_m = 1.0\ \mu F/cm^2$;
The equilibrium potential of Sodium ions: $E_{Na} = 45\ mV$;
The equilibrium potential of Potassium ions: $E_K = -82\ mV$;
The leakage potential: $E_{Leak} = -59.387\ mV$
The maximum resistance of the Sodium ion channels: $\hat{g}_{Na} = 120\ ms / cm^2$;
The maximum resistance of the Potassium ion channels: $\hat{g}_K = 36\ ms / cm^2$;
The resistance of the leak current channels: $g_{Leak} = 0.3\ ms / cm^2$

6.10.5. The couple of neuron/microelectrode

An ideal recording system introduces minimal interference to the object system and obtains undistorted recording. The extracellular MEA system records neurons in a relatively less disturbing way comparing with most of the intracellular systems. However, the extracellular MEAs nowadays are still not ideal transducers and so the recorded signals are often distorted.

Most extracellular MEAs are made of metal or other conductors. Conductors immersed in the electrolyte gain charges and build up an electrical double layer around their surface. The electrode/electrolyte interface and the electrode/neuron coupling are based on this double layer. The MEA coupling to neurons are more or less capacitive due to the double layer structure.

To obtain an undistorted recording, resistive electrode/neuron coupling is ideal. The resistive coupling passes signal in all bandwidth. Capacitive or reactive coupling is like a filter and distort the signals in some certain frequency range. The distortion of signal happens when any part of the signal located in the stopband of the coupling.

Typical electrode/neuron coupling of MEA is capacitive and is virtually a highpass filter. Its passband varies depending on the strength of the coupling and the properties of the electrode including size, surface area and conductivity etc. The microelectrodes used in this project is made of golden thin film and is coated with platinum black. The diameter is around 20-25 μm. An equivalent circuit model of the electrode/electrolyte interface is built based on measurement (chapter 3). Combining this circuit model with the seal resistance which indicates the strength of coupling, an equivalent circuit model of electrode/neuron coupling is obtained. Preliminary simulation of this model in PSPICE gives its passband.

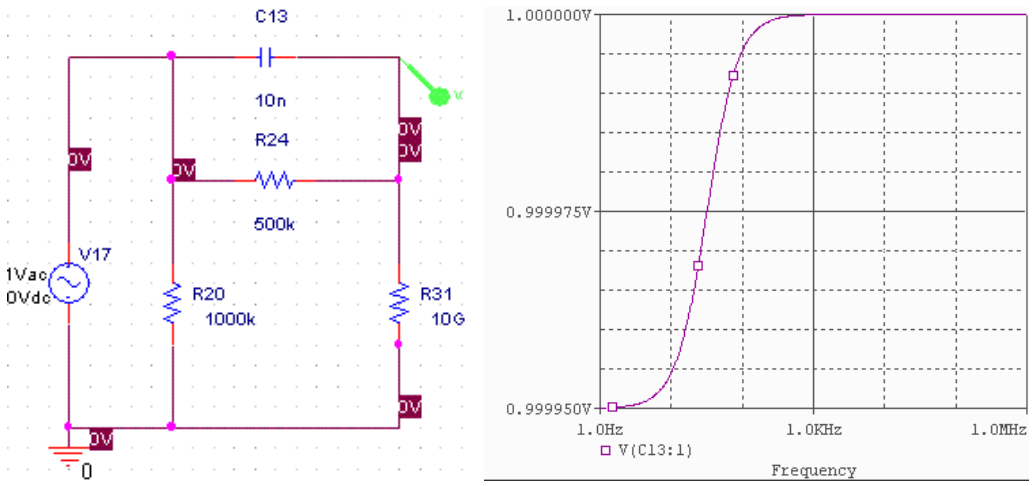

Figure-6-38: The equivalent circuit of the coupling of metal microelectrode with neuron. The diagram at right is the passband of this interface. The parameters are as following. Seal resistance: 1 MΩ; Interfacial capacitance: 10 nF; Charge transfer resistance: 500KΩ; input resistance of preamplifier: 10GΩ.

As shown above, the coupling interface with high input impedance of the preamplifier supports a wider passband. The electrode/electrolyte interface itself does not cause significant signal distortion or attenuation.

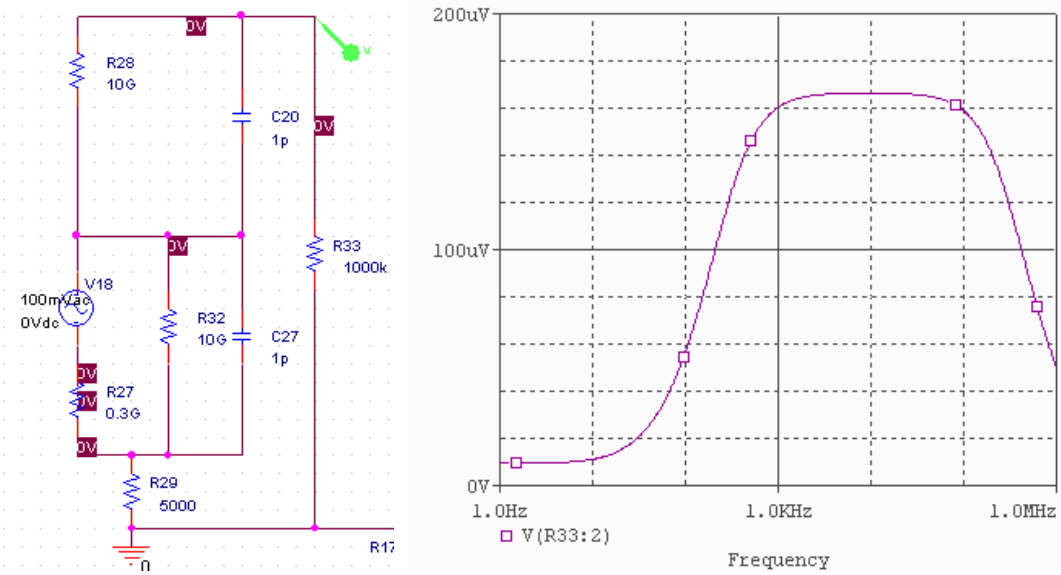

Figure-6-39: The equivalent circuit of the neural membrane and the seal resistance. The diagram at right is their passband. The parameters are as following. Seal resistance: 1MΩ; membrane capacitance: 1 pF; membrane resistance: 10 GΩ.

The capacitance of the neural membrane in series connection with seal resistance and forms a high pass filter. This causes the difference between the waveform of intracellular action potential and the extracellular field potential.

As shown above, typical electrode/neuron coupling does not causes significant

distortion to recording. Though there are different opinions. [M.Bove et al. 1995. Martinoia S, et al. 2004]

According to these documents, electrode/neuron coupling greatly affects the waveforms of the recorded extracellular signal.

Though not agreed with the opinion that electrode/neuron coupling has significant effect on waveform of the recorded extracellular signal, the simulation does show some distorted waveforms caused by certain electrode/neuron coupling, which is not likely to appear in typical extracellular MEA recording.

6.10.6. Waveforms of spikes from our experiments

This section provides a few pictures of the spikes from our recording using our own MEA systems. More details and discussions about the signal and experiments are in chapter 8.

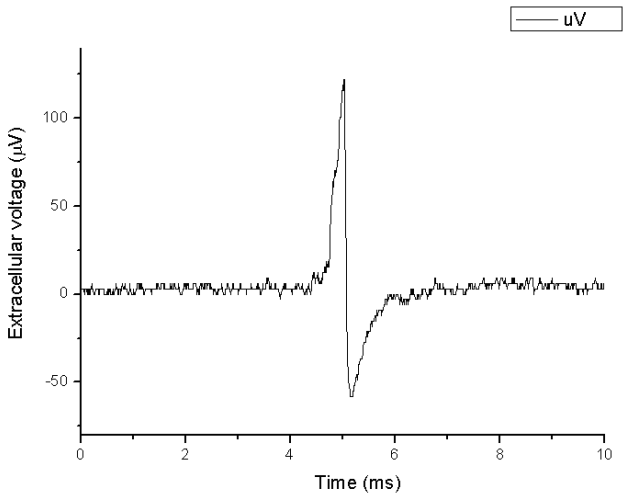

Figure-6-40: The extracellular action potential recorded with FlexMEA from spinal cell culture. The waveform is similar with the second derivative of the intracellular action potential.

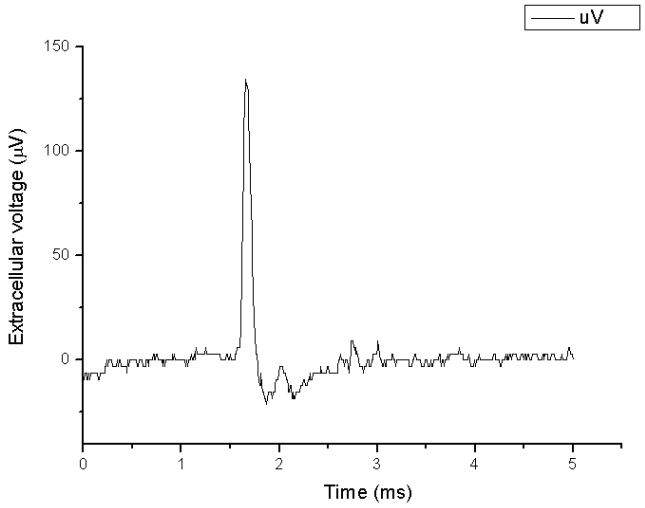

Figure-6-41: The extracellular action potential recorded with FlexMEA from spinal cell culture. The waveform is similar with the first derivative of the intracellular action potential.

6.11. Some results from the simulation of the propagated action potential

This equivalent circuit model of the nerve fibre is built combining the core-conductor theory with the HH model. The action potential propagation along the nerve fibre is simulated.

The parameters describing this model

The radius of the nerve fiber (a).
The resistivity of cytoplasm in nerve fiber (R_2, which is used by Hodgkin and Huxley, or R_{in} or ρ, which is used by Ichiji Tasaki). The membrane capacitance per unit area (C_m). The resistance per unit length of medium (R_{ex}). The maximum of the membrane resistance to sodium ions and potassium ions ($\hat{g}_{Na}$, $\hat{g}_K$). They reflect to the ion channel density.

Dependent variables

Intracellular voltage (V);
Extracellular potential (V_{ex}); membrane current density (I_m); The conduction velocity (θ); leakage current (g_{Leak})

Other variables

Temperature: Temperature is not included as a variable in this model. Its influence will be described later in this section.

This model is built and simulated under 'Mathematica'. Some of the conclusions of

the simulation are followed:

6.11.1. The extracellular voltage is proportional to the second derivative of the intracellular voltage

This conclusion is based on this particular cable model. It assumes nerve fibre suspended in the uniform medium and the action potential is propagated along the nerve fibres in an constant velocity. Such a relationship between the extracellular and the intracellular signal may not necessarily be followed under other more complicated conditions, like within a nerve tissue or the matrix of a neural culture.

There are many publishing on this second derivative relation. E.g. [Steven M. Bierer et al., 1994; Thesis of Kristin Hedgepath Gilchrist, 2001]

The membrane current is proportional to the second derivative of the intracellular voltage

According to core-conductor equation:

$$d^2V / dx^2 = (r_e + r_i)\, I_m \qquad \text{Eq-14}$$

Where,

V is the transmembrane voltage;
r_e is the resistivity of extracellular medium (ohm / length), r_i is the membrane resistivity (ohm / length); I_m is the membrane current density (current / area)

The membrane current density is proportional to the second partial derivative of the transmembrane voltage. The proportion scale is the summation of the extracellular and the intracellular membrane resistivity. The transmission velocity is assumed to be constant. Therefore the spatial derivative is proportional to the temporal derivative.

$$d^2V / dx^2 = d^2V / (\theta^2\, dt^2) \qquad \text{Eq-15}$$

So
$$d^2V / dt^2 = \theta^2 (r_e + r_i)\, I_m \qquad \text{Eq-16}$$

The membrane current is proportional to the extracellular voltage within a certain range.

The membrane current is not a local current. Its ‘river basin’ covers also other parts of the neural membrane. There is also local current that circulates only within the local membrane capacitance and the local ion channels. The local

current does not flow through the extracellular medium and therefore does not cause any vibration on the extracellular potential. It is the membrane current that generates the extracellular signal.

The value of the extracellular potential at a region is dependent on the current sink or the current source located at this region. The extracellular solution is uniform in this model. Therefore the amplitude of the potential is only determined by and proportional to the local current intensity.

However, this proportional relationship is only valid within a certain range. When the extracellular resistivity rises and is comparable to the intracellular resistivity, the relationship is no longer correct. This phenomenon is detailed at later.

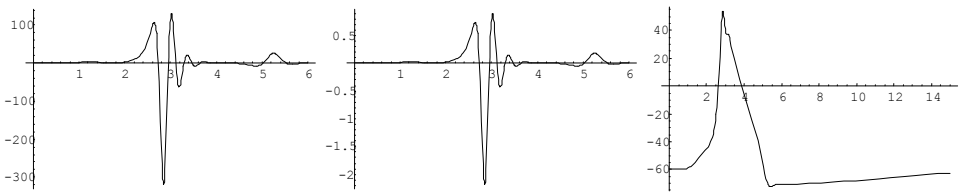

Figure-6-42: The membrane current (μA / cm^2), the extracellular potential (mV) and the intracellular potential (mV). The x axis is time (ms).

The radius of the neural fiber: $a = 1\ (\mu m)$;
The specific resistance of cytoplasm: $R_2 = 35.4 \times 10^{-3}\ (K\Omega\ cm)$; The resistivity of extracellular medium: $r_e = 13\ (m\Omega\ /\ cm)$; The transmission velocity: $\theta = 0.13\ (cm\ /\ ms)$;

From those relations above about membrane current, intracellular potential and extracellular potential, conclusion can be drawn that the extracellular potential is proportional to the second derivative of the intracellular potential in a certain range.

6.11.2. The second derivative of the intracellular potential is depend on some parameters

The intracellular potential does not change significantly with the changes of the characteristics of nerve fibre. But its second derivative is apparently affected much by those parameters. The examples are followed:

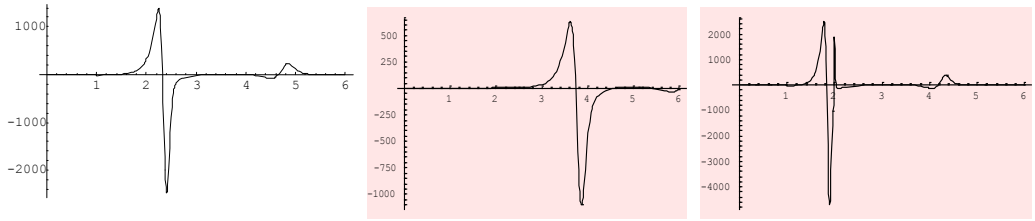

Figure-6-43: The second derivative of intracellular potential (V") when membrane capacitance (C_m) has different value. The membrane capacitance from left to right is respectively C_m = 1 (μF / cm^2), C_m = 2 (μF / cm^2) and C_m = 0.5 (μF / cm^2).

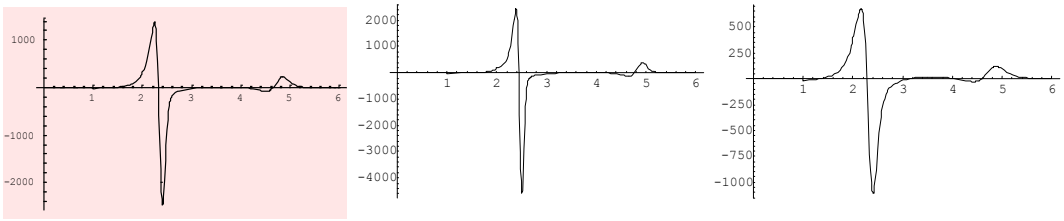

Figure-6-44: The second derivative of intracellular potential (V") when ion channel density is different. The maximum membrane resistance ($\hat{g}_{Na}$, $\hat{g}_K$) from left to right is respectively $\hat{g}_{Na}$ = 120 ms / cm^2 , $\hat{g}_K$ = 36 ms / cm^2 ; $\hat{g}_{Na}$ = 240 ms / cm^2 , $\hat{g}_K$ = 72 ms / cm^2 ; $\hat{g}_{Na}$ = 60 ms / cm^2 , $\hat{g}_K$ = 18 ms / cm^2 .They represent different ion channel density, whose proportion is 1 : 2 : 0.5

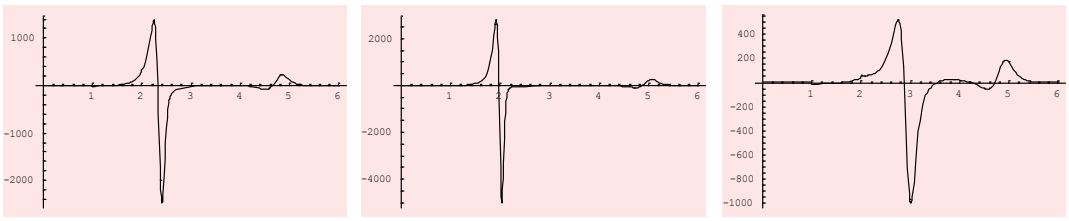

Figure-6-45: The second derivative of intracellular potential (V")when sodium ion channel density is different. The maximum membrane resistance to sodium from left to right is respectively $\hat{g}_{Na}$ = 120 ms / cm^2 , $\hat{g}_{Na}$ = 240 ms / cm^2 , $\hat{g}_{Na}$ = 60 ms / cm^2 .

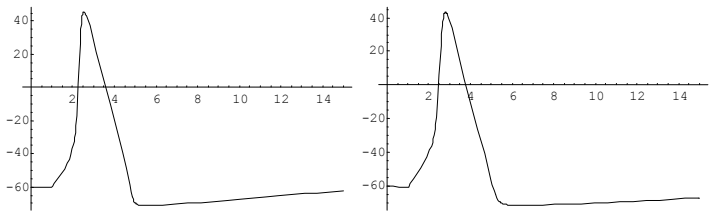

Figure-6-46: The intracellular potential (V) when sodium ion channel density is different. The density at the right diagram is half of the density at left diagram. As shown, the intracellular potential does not change significantly.

6.11.3. Extracellular resistance and fiber radius (a) has little effect on membrane current density (I_m)

The radius of the nerve fiber(*a = 238 (μm)*);
The resistivity of cytoplasm in nerve fiber ($R_2 = 35.4 \times 10^{-3}$ *(KΩ cm)*);
The extracellular resistance per unit length ($R_{ex} = 10^{-3} R_{in}$);
The transmission velocity (*θ = 1.88 (cm / ms)*)

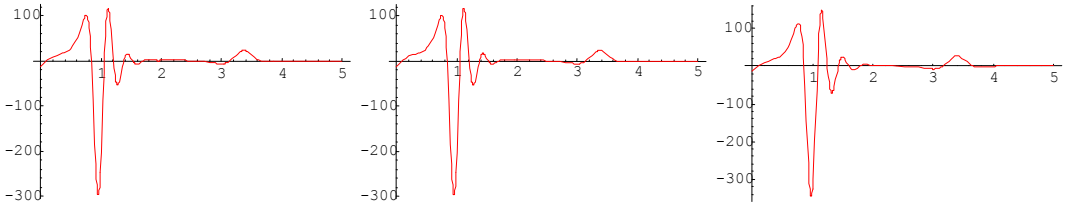

Figure-6-47: The membrane current density (I_m) when extracellular resistance (R_{ex}) changes. The extracellular resistance per unit length from left to right is: $R_{ex} = 10^{-6} R_{in}$, $R_{ex} = 10^{-3} R_{in}$, $R_{ex} = R_{in}$.

As shown in above diagrams, tremendous change of extracellular resistance does not change much of the membrane current density.

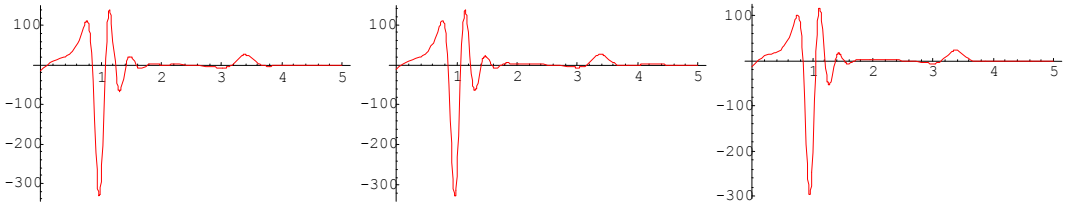

Figure-6-48: The membrane current density (I_m) when the fibre radius (a) changes. The fibre radius from left to right is: a = 238 (μm), a = 23.8 (μm) (the velocity decrease to θ = 0.6 cm / ms), a = 2.38 (μm) (the velocity decrease to θ = 0.2 cm / ms).

6.11.4. The membrane current density (I_m) is depend on some parameters

The radius of the nerve fibre(*a = 238 μm*);
The resistivity of cytoplasm in nerve fiber (*R_2 = 35.4 × 10^{-3} KΩ cm*);
The medium resistivity (*R_{medium} = 13 mΩ / cm*);
The transmission velocity (*θ ≈ 1.88 cm / ms*)

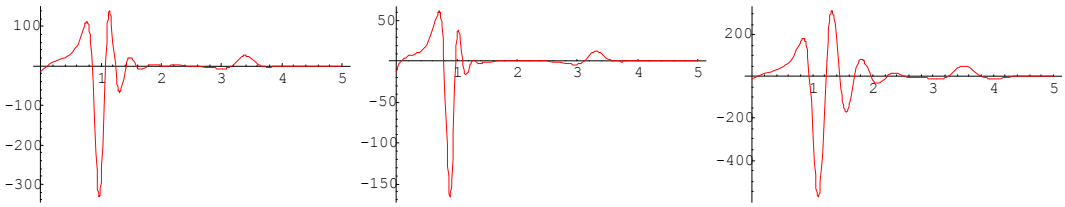

Figure-6-49: The membrane current density (I_m) when intracellular resistivity (R_2) changes. The intracellular resistivity from left to right is: $R_2 = 35.4 \times 10^{-3}$ KΩ cm, $R_2 = 70.8 \times 10^{-3}$ KΩ cm , $R_2 = 17.7 \times 10^{-3}$ KΩ cm.

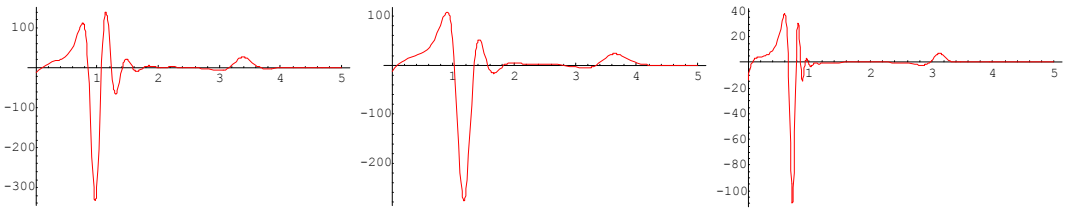

Figure-6-50: The membrane current density (I_m) when membrane capacitance (C_m) changes. The intracellular resistivity from left to right is: C_m = 1 μm / cm^2, C_m = 2 μm / cm^2, C_m = 0.5 μm / cm^2.

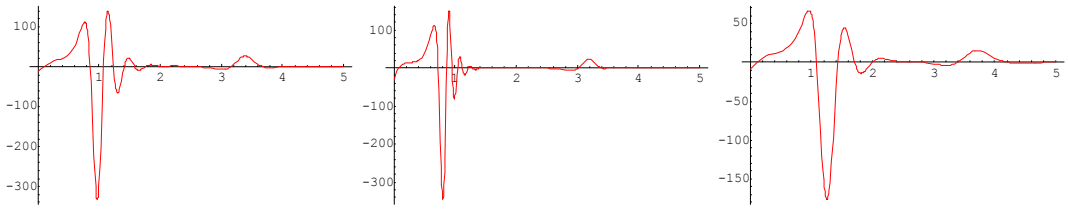

Figure-6-51: The membrane current density (I_m) when ion channels density changes. The density proportion from left to right is: 1 : 2 : 0.5. The transmission velocity is θ ≈ 1.8 cm / ms, θ ≈ 2.5 cm / ms , θ ≈ 1.7 cm / ms .

6.11.5. The extracellular potential depends on some parameters

The surface area of the axon is proportional to its radius. The extracellular resistance is inversely proportional to the logarithm of the radius. Therefore the extracellular potential decreases with the decreasing of the radius.

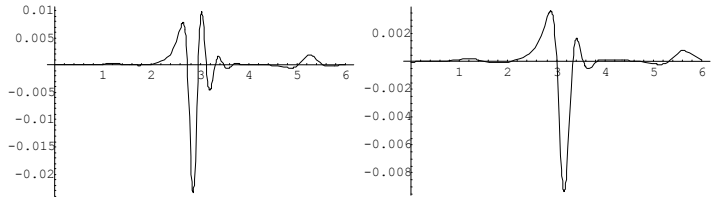

Figure-6-52: The extracellular potential when ion channel density changes. The density proportion from left to right is 2 : 1. The magnitude of extracellular potential reduces from 20 μV to 8 μV.

6.11.6. The extracellular potential increases with the decreasing of the conductivity of the extracellular medium

The extracellular potential increases with the decreasing of the conductivity of the extracellular medium. The upper limit of the extracellular potential is the value of the intracellular potential. In another words, the extracellular potential cannot be higher than the intracellular potential.

If the density of the membrane current is kept at the same value, lower conductivity of medium results in higher potential. In fact, sucrose was used to increase the extracellular potential.

The core-conductor model is not grounded. This bring trouble to the potential calculation with no reference as a zero point. The HH model avoids this problem by neglecting the resistance of the extracellular medium. Since there is no resistance, there is no extracellular potential difference. Therefore either core-conductor model or HH model cannot be used directly to carry out the simulation of extracellular potential.

Some modifications have been made to these two models in order to be able to simulate the extracellular potential. E.g. the extracellular resistor is added to the model. The extracellular potential is proportional to the density of local membrane current. the proportional coefficient is the extracellular resistivity. The simulation went wrong. The extracellular goes high up to hundreds of millivolts. This value exceeds the intracellular potential and it is obviously impossible.

The extracellular resistance in this model refers to the spreading resistance between neighbouring membrane area on the axon. This kind of volume resistance has no off-the-shelf formula to calculate. Specific programming or professional software is required for precise solution. The extracellular resistance is only estimated here. There is spreading resistance between membrane area and bulk medium. This resistance can be calculated easily. And it must be bigger than the extracellular resistance. Because the resistance of each resistor in parallel connection must be bigger than the total resistance. Based on this conclusion, a rough estimation of the extracellular resistance is made.

Without a precise function of extracellular resistance, the relation between the radius of axon and extracellular resistance is not clear too. The relation between the extracellular potential and the radius is not clear too. These flaws of this model are tolerated here, since the purpose of the simulation is only to help with our understanding.

After the failure of above models, the multi-elements model is tried. This is a model that separates the nerve fibre into many sections. Each section is a H-H element that contains its own membrane capacitor and ion channels. The model is expressed entirely in Kirchhoff circuit laws and the H-H functions in Mathematica. The difference between it and the core-conductor model is in fact the number of sections. Each section in core-conductor model is only differential length, which means infinitely short. The sections in multi-elements model are defined with definite length, e.g., one millimetre. The result of simulation shows that the membrane potential increases with the increasing of extracellular resistance. Both the amplitude and the waveform gradually approach the intracellular potential.

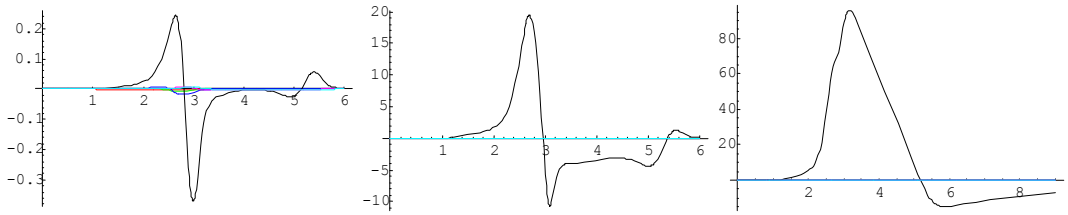

Figure-6-53: The simulation results of the multi-elements model. The waveforms are the extracellular potential signal corresponding to different medium resistance. The medium resistance of two elements is raised and one element shows significant rising of local extracellular potential. The units of the vertical axis is millivolts, the horizontal is milliseconds. The corresponding medium resistance of three figure is 7 Ω, 700Ω and 7 KΩ. The third figure approximates the intracellular potential in both the amplitude and waveform.

This model is comprised by six H-H components. The common parameters are as follows:

The length of each H-H element: 200 *μm*
The radius of the nerve fibre(a = *1 μm*);
The resistivity of cytoplasm in nerve fibre (R_2 = *35.4 × 10^{-3} KΩ cm*);
The extracellular resistance per unit length (R_{medium} = *13 mΩ / cm*);

6.11.7. The coupling of microelectrode to axon increases the local seal resistance and so increases the local extracellular potential

The extracellular potential measuring MEA couple with neural fibre and form seal resistance. Seal resistance obstructs the flow of membrane current. The local extracellular resistance is raised by the presence of microelectrode. The local extracellular potential rises too. Simulation shows that the extracellular potential increases slightly less than that of extracellular resistance.

The model assumes that the coupling increases the extracellular resistance, which is proportional to the coverage area. The model of coupled axon is similar with the original model, except defining the relationship between extracellular resistance and coverage area. Simulation shows that the increase of extracellular resistance raises the local extracellular potential and has small impact on the transmission velocity.

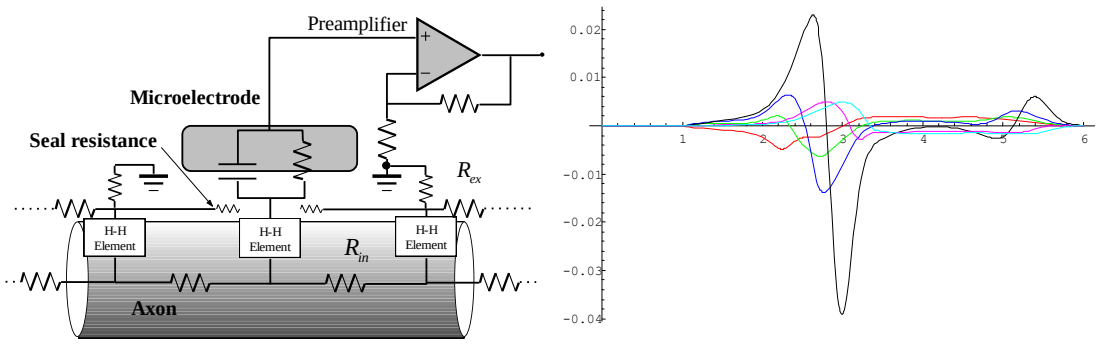

Figure-6-54: The simulation result of the affection of the microelectrode coupling on the

extracellular potential. Two of the six HH compartments raise their extracellular resistance by ten times. The extracellular potential of one compartment (black line) rises by about five times. Another (blue line) shows no significant change.

6.11.8. Electrode size does not affect the waveforms of recorded signal

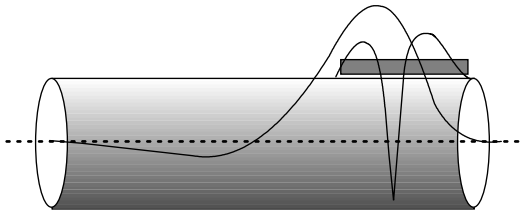

Figure-6-55: The intracellular potential and the extracellular potential along the fibre.

If the assumption is made that the propagation of action potential along the axon is in constant velocity, then the following equation can be derived.

$$dV / dt = i\, dV / dx$$

This equation states that the spatial and time distribution of the action potential is similar.

As drawn in the above figure, if the size of the microelectrode is in comparable with the length of the spatial distribution of the action potential, the signal acquisited is actually a mean value of the potential over the electrode. As known in theory of signal, taking the mean value is a algorithm of low-pass filter. Therefore the acquisited action potential will lose some part of its high frequency signal. This conclusion is established on the assumptions of a rather large size of the microelectrode. The following is to find out how large a microelectrode needs to be large enough to make any difference.

The un-myelinated nerve fibre of class C of human conducts signal at speed of about 2 m/sec. The myelinated fibre of class A is about (a deduced velocity) 8~140 m/sec. Take the lowest value (this will give the shortest estimation) of 2 m/sec for estimation. Assume the diameter of electrode is 10 microns. The signal needs about 5 microseconds to cross this length. The corresponding frequency is 200 kHz. Any signal that is higher than this frequency will be filtered. The frequency range of an action potential is below 10 kHz. Therefore microelectrodes can easily detect the action potential with no risk of high-frequency loss at all.

Although the size of microelectrode does not cause any trouble to loss any high frequency part of a signal. However, for other reasons, in many occasions, it is still necessary to keep the microelectrode tiny. First, a larger electrode is difficult to be completely covered by or coupled with the cell. Only a small part of the electrode in low resistance contact with medium will lead to a much lower seal resistance. Without seal resistance of enough height, the extracellular potential will not be detected. This phenomenon is described in detail later.

Second, when there are a number of signal source within the detection range of the microelectrode, interference or overlapping may occur. Smaller microelectrode reduces the detection range and the possibility of interference.

Third, the locating of the source of a signal is more difficult for a larger microelectrode. It is not only due to the bigger detecting range but also the lower spatial resolution. Sometimes, a array of electrodes is required to locate the coordinates by analyzing the differential amplitude of each acquired signal. The large-size electrode does not have the advantage of integrating many microelectrodes.

Fourth, the extracellular potential distributed at the different parts of a neuron are different in their waveform. For example, those along axon are often negative impulses. Those around dendrites are positive impulses. Smaller microelectrode has better spatial resolution to distinguish these waveforms.

6.12. Estimate the signal amplitude

6.12.1. Different signal amplitude from different distance

Table 6-4: The magnitude of the signal recorded at different distance to the brain. [Purves, 1981]

Distance	Signal magnitude	Recording method	Electrode type
2~10 mm	10~200 μV	Scalp recording, EEG	Metal electrode
1~3 mm	0.2~5 mV	Surface recording, EcoG	Glass micropipette
1~50 μm	0.4~20 mV	Extracellular recording	Glass micropipette
0.5~3 μm	1~100 mV	Intracellular recording	Glass micropipette

6.12.2. Extracellular recording

When an action potential is generated, the energy stored in the membrane releases. Ions flow through membrane into extracellular medium (vice versa) and build up a field potential along the direction they travelling. Can electrode in vicinity of the membrane detect the existing of such a field potential? It depends on the amplitude of the field potential and the noise level of the detector. The noise level of the recording device in this project is a few micro volts. Here we try to give a estimation of the signal level.

Extracellular field potential

Assumes this section of cylindrical nerve fibre is 10 *μm* long and the radius of its cross-section is 5 *μm*. In order to obtain the value of the field potential in vicinity of membrane, we must know the membrane current and the resistance of the bulk medium surrounding neuron. The estimation is start with these two parameters.

Estimate the membrane current by membrane capacitor

Making the calculation easier, membrane of neuron can be simplified here as a capacitor. In it the energy is stored in the form of electric field. Opposite charges accumulate in the medium side and the intracellular side of the membrane. It is the field potential distribution in the extracellular side that we are interested in. While neuron is at rest, there is 70 mV voltage across membrane. But there is no potential difference outside of membrane since medium is a conductor. Potential difference can not built up inside conductor in electrostatic situation. Hence no field potential signal can be detected during resting period.

The membrane capacitance of unit area is: $C_{mem} = 1\ \mu F / cm^2$ (Schatzthauer and Fromherz, 1998).

$$C_{mem} = 4\pi r^2 \times 1 = 3.14\ pF$$

The membrane capacitance of this spherical neuron is about 3.14 pF.

The change rate of the membrane voltage (the voltage across the membrane capacitor) can be estimated by the waveform of action potential recorded intracellularly.

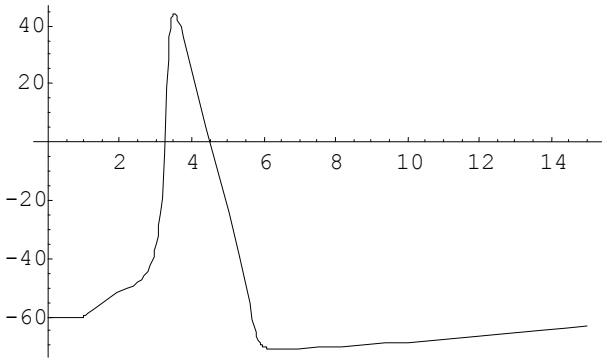

Figure 6-56: The Mathematica simulated intracellular action potential of neuron soaked in the medium(Y axis: mV; X axis: ms). All parameters are based on giant squid axon [H and H, 1952]. A stimulating current starts at the first second and raises slowly the membrane potential over the threshold. At about the third second, an impulse is generated. It takes about 0.5 miliseconds to reach the peak and takes another 2 milliseconds to return with a little overshoot. Then it spends longer time getting back to the resting potential.

In about one ms, membrane voltage increases by 100 mV approximately. The first derivative of the voltage function against time is:

$$dV_{mem} / dt \approx 100\ V/s$$

Now the membrane current can be obtained:

$$I = C_{mem}\, dV_{mem} / dt = 314\ pA$$

Here we take 314 *pA* as the estimation of the membrane current.

The neuronal membrane current changes during the whole action potential firing time. The above result is a rough estimation of membrane current during the rising term of the membrane potential. Another worth noting point is that the current here is the so-called membrane capacitance current. It is not the current flowing through the extracellular medium. The relationship between them is as following:

Extracellular current through medium = the displacement current through membrane capacitor + the ion currents through membrane

$$I_{mem} = (C_{mem}\, dV_{mem} / dt) + I_{Na} + I_K + I_{Leak}$$

I_{mem} is the current through extracellular medium. It is often called membrane current. It is the net current flowing through membrane. It flows through the medium and creates field potential. The extracellular potential detected by the MEAs is caused by this current. I_{Na} , I_K , I_{Leak} are different types of ion currents through the membrane.

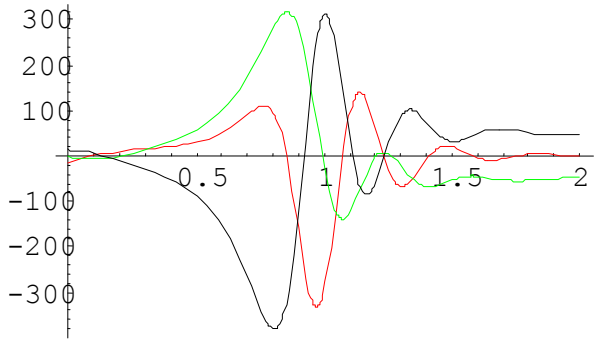

Figure 6-57: The Mathematica simulated action potential propagating along the squid giant axon. The diagram shows the membrane current at a point on the axon during an action potential. The red curve with a negative trough represents the membrane current. The green curve with a positive peak is the capacitive current (the displace current). The black curve with both peak and trough is ionic current. The units of the vertical axis is μA/cm^2. The unit of the horizontal axis is ms.

The above diagram shows that the magnitude of three currents are at the same order. The magnitude of the membrane current is similar with that of the capacitive current, which has been estimated to be *314 pA*.

Estimate with membrane current density

There is another method to estimate the membrane. According to Mathematica simulation of the action potential propagating in the giant squid axon, the membrane current density is relatively stable for each action potential. The membrane current density is: *300 μA / cm*^{2} (peak) , 100 *μA / cm*^{2} (average). This value is smaller than the value used by Lind, Connolly [1991]. They used 1000 *μA / cm*^{2}.

For the membrane area of our neuron. The membrane current is: I_{mem} = *900 pA (peak), 300 pA (average)*.

The resistance of the extracellular solution is required. After it, the magnitude of the extracellular potential can be calculated.

Spreading resistance

To simplify the calculation, assume the neuron is a sphere of radius *5 μm*. The spreading resistance of the bulk medium outside this sphere is:

$$R_s = \varepsilon \,/\, \sigma C = (r_2 - r_1) \,/\, (2\pi\, r_1\, r_2\, \sigma)$$

r_2 is the radius of outer sphere (r_2 = *1 cm*). The chosen of this value does not effect much of the result, as long as it is much bigger than the radius of neuron.

σ is the conductivity of extracellular medium, which is mainly DMEM ($\sigma = 1.3\ s/m$, from measurement under room temperature).

r_1 is the radius of the neuron sphere ($r_1 = 5\ \mu m$).

$$R_{spreading} = (r_2 - r_1) / (2\pi\ r_1\ r_2\ \sigma) = 24\ K\Omega$$

6.12.3. Extracellular potential without seal resistor

A direct current of *78pA* flow through this *24 KΩ* resistor. The voltage across this resistor can be obtained easily:

$$U = I\ R_{spreading} \approx 21\ \mu V$$

This value is about 12 times smaller than the value concluded by Lind, Connolly [1991]. It is because that the parameters used here are smaller than that used by them. The conductivity of medium (DMEM) here is $\sigma = 1.3\ s / m$. They used $\sigma = 0.33\ s / m$. The current density here is $300\ \mu A / cm^2$. They used 1000 $\mu A / cm^2$.

According to above, a electrode located close to membrane can only get a maximal potential reading of a few micro volts. This is much lower than the value from real recording, which is in range of tens of micro volts to hundred micro volts.

6.12.4. Extracellular potential with seal resistor

Real signal is much bigger than the estimation. This difference may arise from the influence of the electrode being very close to neuron membrane. The existence of electrode changes the geometrical shape of the bulk medium conductor. The former spherical shell model changes where the electrode is. The medium confined in the gap between the cell membrane and the electrode surface has resistance, which is called seal resistance. The resistance is related to the contact area, the distance of membrane to electrode and the conductivity of medium.

The calculation in the previous section does not take consideration of the coupling of electrode with cell membrane. The extracellular potential is simply caused by the membrane current flowing through the spreading resistance of extracellular medium. The real signal recorded in experiments can be much bigger than the estimated value. It is because of the coupling of electrode with cell. The so-called seal resistance is formed. The seal resistance of a good couple can be much bigger

than the spreading resistance. The seal resistance is from the medium sealed in the gap between the cell membrane and the electrode. It is related to the contact area, the contact distance and the conductivity of the medium. If the electrode and the cell are closely attached, the seal resistance could reach megohms. The membrane current obstructed by the seal resistance results in higher membrane potential. Therefore, the extracellular potential recorded with well coupled electrode is higher than that without seal resistance.

Considering 1MΩ seal resistance, which is in the range of the typical value for good coupling.

$$U = I\, R_{seal} = 78\ \mu V$$

This result is well agree with the value obtained from experiment, typically on the order of *10~500 μV*.

The high seal resistance will also increase the thermal noise voltage. For one megohm resistor, the thermal noise is about 13 *μV*. This is still much lower than the amplitude of the signal voltage. The signal amplitude is roughly proportional to the seal resistance. The thermal noise voltage is roughly proportional to the square root of the seal resistance. Therefore, seal resistance improves the signal to noise ratio.

Borkhold (2000) summarises in his thesis the research of many groups in a proportional realationship between the extracellular potential and the seal resistance as shown in the above diagram. The waveform also changes with different seal resistance. The waveform is similar to the second derivative of the intracellular signal when seal resistance is small. Then to the first derivative. In the end, to the intracellular signal itself when seal resistance is very high. Experiments by [Regehr, et al, 1989; and Breckenridge, et al., 1995] and simulation by [Grattarola and Martinoia, 1993].

Breckenridge (1995) proved with experiments the linear relationship described above. He used 10 *μm* diameter platinum black coated microelectrode. The neurons of snail are directly grown on the electrodes. The experiment data is shown in the above diagram. [Breckenridge, et al, 1995]

How big should the seal resistance be?

Buitenweg concludes that for the regular size of microelectrodes, the seal resistance in range of 1~5 MΩ is high enough. [Buitenweg et al., 1998 ~ 2002]. In the experiments by Breckenridge, the microelectrodes of 10 microns diameter can record signal when seal resistance is from 500 KΩ to 3 MΩ.

6.12.5. Summary

From the estimation above with simple electrical element model. It can be found that the seal resistance is critical in detection of extracellular field potential. A good neuron to electrode coupling need high seal resistance of MΩ range. This raises the amplitude of the potential signal greatly.

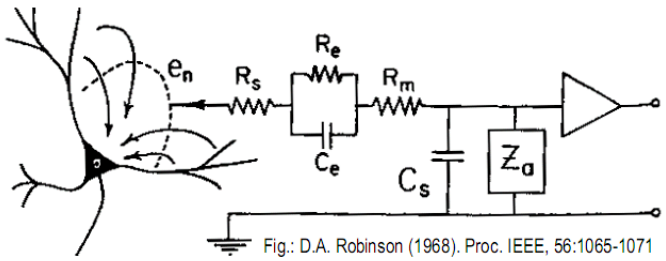

Figure 6-58: The equivalent circuit model of the extracellular recording by Robinson [1968] is almost the same with that in this thesis. He already know that the extracellular potential is established by the current flowing through the volume resistance of medium or the seal resistance. The current is from nerve fibres to the soma. This ideal is also the same with our.

6.12.6. Partly coupled electrode

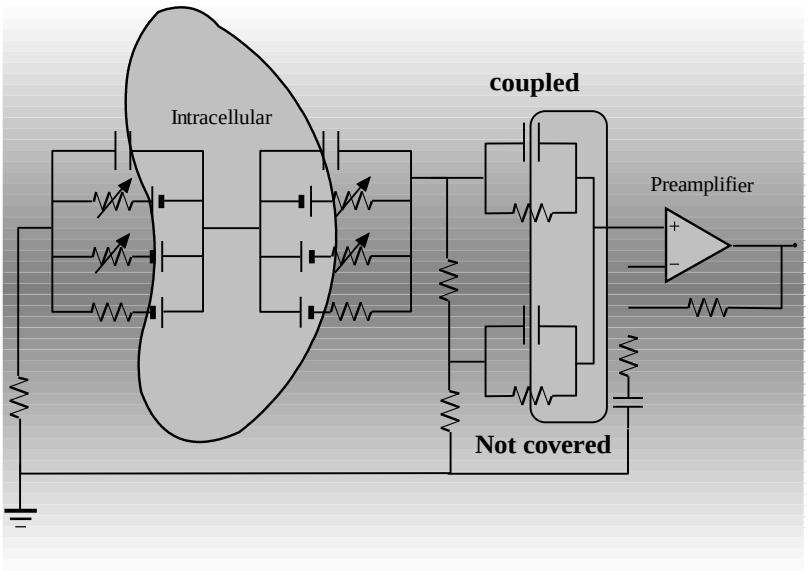

Figure 6-59: The equivalent circuit model of a neuron partly coupled to an electrode.

In the previous estimation, the coupling of electrode with neuron is assumed to be

good. In fact, the couple is not always good. For example, only part of the electrode area is covered and the rest of the area is exposed to the medium. This is a kind bad coupling, which is called ‘partly coupling’ here. The effect of this partly coupling to the magnitude of the extracellular potential is analysed in the following section.

From the circuit perspective, partly coupling has two impacts on the extracellular recording. First, the input resistance of the pre-amplifier is reduced. Second, the seal resistance is reduced. The original input resistance of the pre-amplifier is very high. However, the part of the electrode exposed in medium is in parallel to the input resistance of the pre-amplifier and that greatly reduces the input resistance.

Assume that the original seal resistance is one megohms. The average resistance of the microelectrode over frequency range 1~10 KHz is about 100 KΩ. Half area of the electrode is not coupled. The resistance of each half is 200 KΩ. With estimation, the magnitude of the extracellular voltage is reduced to 15% of the original value when the electrode is fully covered.

6.13. Can MEA do extracellular current measurement?

Few report was found on extracellular current recording using metal MEAs during my investigation session of writing this thesis. Loose patch recording uses glass micropipettes. Most extracellular recording with metal MEAs are on field potential and some others are on magnetic field. The reasons why this happens are beyond the scope of my thesis. Here estimation is made on the magnitude of the current. As a way to investigate the possibility of extracellular current recording using metal MEA.

A 100 KΩ electrode has thermal noise current of 40 pA in 10 KHz bandwidth. This is the noise level we would expect in a extracellular current recording if a platinised metal electrode is employed. The simulation of a 10 micron diameter neuron using the parameter of squid giant axon in previous sections tells that the peak membrane current is about 900 pA. But not all the current can be collected by the microelectrode. The microelectrode can only cover part of the membrane and part of the current will leak through the seal resistance. Coverage and seal resistance among many factors will affect the amount of current that can be collected by microelectrode. Therefore, the magnitude of the signal and noise are roughly in

the same order. The extracellular current recording could be difficult.

According to former investigation, good seal is required in extracellular field potential recording. Let us put seal resistance into consideration and see if it helps. The seal resistance in parallel with the membrane resistance. The increase of seal resistance will increase the resistance of the signal source. Assumes that seal resistance is one megohms. Then the resistance of signal source will be certainly less than 1 MΩ. Therefore, the minimum thermal noise current is:

$$I = \sqrt{(4k\ T\ B\ /R)} \approx 13\ pA$$

It is easily seen that the increase of seal resistance can reduce the thermal noise current of electrode.

For metal MEAs, the seal resistance of 1 MΩ is high. This reduces the noise to 13 pA. The glass micropipette can reach much higher seal resistance than that. It is one reason why glass micropipette is often used to record extracellular current rather than metal MEAs.

The input resistance of current pre-amplifier is very small. It is called virtual ground. If the seal resistivity increases, there will be more current flows through electrode into the virtual ground. Assuming seal resistance of 1 MΩ. It is in parallel with the 100 KΩ resistance of electrode. There will be 90% of the current flowing into the pre-amplifier. In other words, the majority of signal current is recorded.

The above estimation shows that the extracellular current recording with metal MEAs is possible. But a good coupling with high seal resistance is required. The reason why glass micropipettes can easily record current signal is that the glass wall can form very high seal resistance with the membrane.

6.13.1. On-cell recording and intracellular recording

Both on-cell recording and intracellular recording symbols with high ohm seal formation between membrane and electrode. Seal resistance of tens MΩ to hundreds MΩ is common. So called ‘loose seal patch’ keeps tens MΩ seal and patch clamp even reaches GΩ seal resistance easily.

Most of the intracellular recording and all on-cell recording employ micropipette electrodes as transducer. The glass wall of micropipette attaches to cell membrane

and form tight seal. It is very difficult for metal microelectrode, without this special structure, to form seal of more than ten MΩ to single neuron, unless neuron itself grown on the electrode.

Similar to the discussion made to extracellular recording, seal resistance helps to rise the amplitude of potential or current signal coupled into electronics. And especially in current recording, it also reduces thermal noise current.

In 1976 Neher and Sakmann first recorded single ion current, resulting in a patch-clamp (Patch Clamp) technology. The high resistance seal (10-100 GΩ) greatly reduced the noise levels recorded [Sigworth, 1980]. After further refine, the technology gets 1 pA current sensitivity, 1 μm spatial resolution and 10 μs time resolution.

6.14. Noise in the neural recording

There are four main sources of electric noise in the preamplifier for neural recording:

(1) the Johnson or thermal noise of the resistance of the microelectrode,

(2) the voltage noise of the head stage preamplifier,

(3) current noise of the preamplifier,

(4) “excess noise” in the microelectrode.

The Johnson noise is due to the thermal motion of electrons, and sets a lower limit to the total noise.

The voltage noise inherent in the preamplifier is the noise measured at the output when the input is grounded.

Microelectrodes display a noise component that is additional to their Johnson noise. This excess noise depends strongly on the voltage applied to the microelectrode, even though some excess noise is present in the absence of any applied voltage. The current noise is linearly dependent on the resistance of the electrode in contrast with the square root dependence exhibited by the Johnson noise.

6.14.1. Noise from metal microelectrode

Noise of electrode electrolyte interface comes from two main sources, thermal noise and shot noise.

Thermal noise

Thermal noise results from the Brownian motion of ionized molecules within the electrode electrolyte interface. It is a random sequence of short pulses as many ions travel between collisions. The magnitude of the thermal noise is linear with the real part of the impedance of the electrode.

Shot noise

There is often current flowing through the electrode–electrolyte interface (e.g. the bias current from the input of the preamplifier). The current flows across the double layer of electrode electrolyte interface in the way of relocations of ions. Each relocation of individual ion equals a little impulse of current. The shot noise rises from the sum of these impulses current. It can be imagined as the patter of rain on a roof.

6.14.2. Spectrum of shot noise

A noise made up of a random sequence of short impulses has a flat spectrum. This is the case for most thermal noise and shot noise appears in electronics where electron is the carrier of current. The travel time of electron between each collision (generates thermal noise) is very short, as well as the transit time of electron across a dense electrical field (generates shot noise). Therefore the small current in the above two situations can be simplified as a impulse. Single impulse has a flat spectrum and so does the sum of a random sequence of impulses.

In spite of electron, ionized molecular take the role of current carrier in the electrode-electrolyte interface. Here, ionized molecular across the electrode-electrolyte interface in the way of drift or diffusion. The velocity of ionized molecular is much slower than electron in the same level of momentum. As a result, the duration of impulses is elongated. Square function is a more appropriate interpretation than the impulse function in this occasion. Hence, shot noise and thermal noise in electrode-electrolyte interface, the sum of a random sequence of square functions has lower magnitude at high frequency part.

6.14.3. Estimation of noise level

Shot noise

$$I_s = \sqrt{(2e\ I_o\ B)} \qquad \text{Eq. 6-17}$$

Where,
e = electron charge, 1.60×10^{-19} coulombs;
I_o = dc current, 10 pA; The bias current of the preamplifier through electrode-electrolyte interface is in tens of Pico Amps range.
B = bandwidth, 10KHz.

$$I_s = \sqrt{(2e\ I_o\ B)} \approx 0.18\ pA$$

Shot noise is below Pico Amp range. This shot noise current can only generate sub-microvolts range noise voltage across a MΩ resistor. It is much smaller than the extracellular field potential signal and hence can be ignored.

Thermal noise

The thermal noise recorded by the MEA system is mainly from the resistance between two input terminals of the pre-amplifier. This resistance is an adding of all the resistances between the microelectrode and the reference electrode. The smallest possible value of this resistance is from the microelectrode itself when these two electrodes are immerged in the medium. Therefore the minimum thermal noise can be estimated by calculating the thermal noise from the microelectrode.

Action potential signal is in 1Hz~10 KHz frequency range. The real part of the impedance of the electrode in my project is around tens of ohms at this frequency range. Here we have 100kΩ resistor in the bandwidth of 10KHz. Its thermal noise current is:

$$I_t = \sqrt{(4k\ T\ B\ /\ R_e)} \qquad \text{Eq. 6-18}$$

Where,

k = Boltzmann's constant, $1.38 \times 10^{-23}\ J\ /\ K$;
T = absolute temperature, 310K (room temperature)
R_e = resistance of electrode, 100 KΩ;
B = bandwidth, 10 KHz

$$I_t = \sqrt{(4k\ T\ B\ /\ R_e)} \approx 41\ pA$$

Similarly thermal noise voltage can be obtained:

$$V_t = \sqrt{(4k\ T\ B\ R_e)} \approx 4\ \mu V$$

Thermal noise is in micro volts range. This result is close to the noise level found in the real recording. Thermal noise from the electrode electrolyte interface is the main noise source of electrode as a transducer. For simplicity, thermal noise is often mentioned in this thesis, whereas the shot noise and the noise from other sources i.e. electronics, biological etc. are left absent.

For an electrophysiology recording, noise may come from electrode, electronics itself or environmental EM interference. For the extracellular action potential recording device built in this project, noise from electronics and environment is minimized satisfactorily and can be ignored. Noise measurement approves that the thermal noise from the electrode-electrolyte interface dominants other noise. The noise level predicted by the above simple thermal noise model fit well with measurement, which is a few *μV*.

6.14.4. The niose of preamplifier

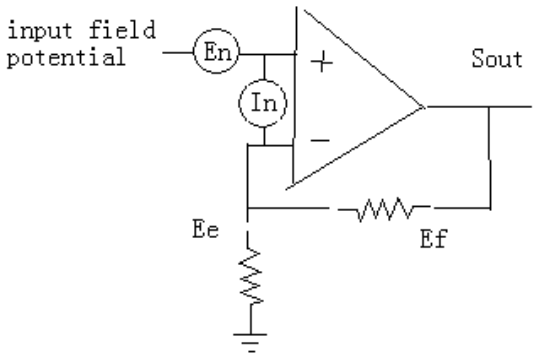

Figure 6-60: The noise voltage and noise current caused by pre-amplifier itself.

$$e_{out}^{\ 2}(f) = i_n^{\ 2} R_f^{\ 2} + e_n^{\ 2}((R_e + R_f)^2 / R_e^{\ 2}) + e_f^{\ 2} + e_e^{\ 2}(R_e + R_f)^2 / R_e^{\ 2} \qquad \text{Eq. 6-19}$$

The total output noise is composed of three independent parts. They are independent random variables. Therefore, the total noise is the root of the square of three parts. The elements in this equation are explained in the following.

$i_n^2\ R_f^2$: There are three type of current flowing through the feedback resistor (R_f). They are signal current, C_g current and i_n. The i_n current caused output voltage (PSD) is $i_n^2\ R_f^2$.
$e_n^2\ (R_e + R_f)^2 / R_e^2$: the e_n caused noise (PSD) at the output.
e_f^2: the feedback resistor caused noise (PSD) at the output.
$e_e^2\ (R_e + R_f)^2 / R_e^2$: the resistaor R_e caused noise (PSD) at the output.

The Eq. 6-19 can be transformed into the input noise voltage by multiplying $e_e^2\ (R_e$

+ $R_f)^2$ to both side of the equation.

$$e_{in}^{\ 2}(f) = i_n^{\ 2} R_f^{\ 2} R_e^{\ 2} / (R_e + R_f)^2 + e_n^{\ 2} + e_f^{\ 2} R_e^{\ 2} / (R_e + R_f)^2 + e_e^{\ 2} \qquad \text{Eq. 6-20}$$

Calculation of noise voltage

Note that the PSD is calculated here. Noise value needs integration over the frequency domain.

i_n shot noise: If current at the gate junction is 0.2 pA, the shot noise (rms) at 10 KHz frequency range is 0.025 pA. For example, the op amp LT1793 has input current noise 1 fA Hz^{--2}. The current noise at 10 KHz frequency range is 0.1 pA.
e_n: for common FET pre-amplifier, e_n is approximately 2 ~ 3 nV Hz^{-2}. Over the bandwidth of 10 KHz, it is 0.2 ~ 0.3 μV (rms). For example, op amp LT1793 has e_n = 6 ~ 8 nV Hz^{-2}. It is 0.6 ~ 0.8 μV (rms) at the bandwidth 10 KHz.
R_f = 250 KΩ (refer to chapter 2) ;
R_e = 500 Ω ;
e_f : The thermal noise of feedback resistor over bandwidth 10 KHz is 6.5 μV (rms).
e_e : The thermal noise of resistor R_e over bandwidth 10 KHz is 0.3 μV (rms).

The total input noise is:

$$\begin{aligned}
e_{in} &= \sqrt{i_n^{\ 2} R_f^{\ 2} R_e^{\ 2} / (R_e + R_f)^2 + e_n^{\ 2} + e_f^{\ 2} R_e^{\ 2} / (R_e + R_f)^2 + e_e^{\ 2}} \\
&= \sqrt{i_n^{\ 2} + e_n^{\ 2} + e_f^{\ 2} / 500^2 + e_e^{\ 2}} \\
&= \sqrt{0.1^2\, pV^2 + 0.6^2\, \mu V^2 + 6.5^2\, \mu V^2 / 500^2 + 0.3^2\, \mu V^2} \\
&\approx \sqrt{0.36 \mu V^2 + 0.09 \mu V^2} \\
&\approx 0.7 \mu V
\end{aligned}$$

As shown above, the noise component e_n and e_e dominate the total noise.

The total output noise is:

$$\begin{aligned}
e_{out} &= \sqrt{i_n^{\ 2} R_f^{\ 2} + e_n^{\ 2} ((R_e + R_f)^2 / R_e^{\ 2}) + e_f^{\ 2} + e_e^{\ 2} (R_e + R_f)^2 / R_e^{\ 2}} \\
&= \sqrt{(0.1pA \cdot 250K\Omega)^2 + (0.6\mu V \cdot 500)^2 + (6.5\mu V)^2 + (0.3\mu V \cdot 500)^2} \\
&= \sqrt{(25nV)^2 + (0.3mV)^2 + (6.5\mu V)^2 + (0.15mV)^2} \\
&\approx \sqrt{(0.3mV)^2 + (0.15mV)^2} \\
&\approx 0.34mV
\end{aligned}$$

6.15. Appendix

6.15.1. The old criterion of the voltage

The data of the voltages in this paper [Hodgkin and Huxley, 1952] took the intracellular potential as the reference potential. This is different with nowadays habits of using earth as the zero potential. Also the direction of current is negative to that we use today. The moving direction of the electrons was taken as the direction of current. So these data are converted by adding -70mV to reversed voltages (assume the intracellular potential is -70mV).

Table 6-1: The data of voltage used by Hodgkin and Huxley (1952).

The intracellular resting potential: V_{in} = *0 mV;*
The equilibrium potential of Sodium ions: E_{Na} = *-115 mV*;
The equilibrium potential of Potassium ions: E_K = *+ 12 mV*
The leakage potential: E_{Leak} = *-10.613 mV*

Table 6-2: The data of voltage used nowadays.

The intracellular resting potential: V_{in} = *-70 mV*
The equilibrium potential of Sodium ions: E_{Na} = *45 mV*
The equilibrium potential of Potassium ions: E_K = *-82 mV*
The leakage potential: E_{Leak} = *-59.387 mV*

6.15.2. Resolve the circuit model in Mathematica

The main equation of Hodgkin-Huxley model:

$$C_m \, dV_m / dt + \hat{g}_{Na} \, m^3 \, h \, (V_m - E_{Na}) + \hat{g}_K \, n^4 \, (V_m - E_K) + g_{Leak} \, (V_m - E_{Leak}) = I_m$$

(Eq-21)

Most parameters (C_m , $\hat{g}_{Na}$, $\hat{g}_K$, g_{Leak} , E_{Na} , E_K , E_{Leak}) are constants describing the characteristics of the modeled neural membrane and are given in advance of solving the equations. The gating parameters (m , h , n) are time (t) and membrane voltage (V_m) dependent. Their time dependencies are given by the following differential equations and their membrane voltage dependencies is exhibited in the rate constants:

$$dm / dt = \alpha_m (1 - m) - \beta_m m \quad \text{Eq-22}$$

$$dn / dt = \alpha_n (1 - n) - \beta_n n \quad \text{Eq-23}$$

$$dh / dt = \alpha_h (1 - h) - \beta_h h \quad \text{Eq-24}$$

The rate constants (a_m , β_m , a_n , β_n , a_h , β_h) are defined by functions of membrane voltage (V_m).

$$\alpha_n = 0.01 (V_m + 10) / (Exp (1 + 0.1 V_m) - 1) \quad \text{Eq-25}$$

$$\beta_n = 0.125 Exp (V_m / 80) \quad \text{Eq-26}$$

$$\alpha_m = 0.1 (V_m + 25) / (Exp (0.1 V_m + 2.5) - 1) \quad \text{Eq-27}$$

$$\beta_m = 4.0 Exp (V_m / 18.0) \quad \text{Eq-28}$$

$$\alpha_h = 0.07 Exp (V_m / 20.0) \quad \text{Eq-29}$$

$$\beta_h = 1.0 / (Exp (3.0 + 0.1 V_m) + 1) \quad \text{Eq-30}$$

As shown above, most equations except the main equation (Eq-21) are used to define the time (t) and membrane voltage (V_m) dependent resistors (g_{Na} , g_K).

$$g_{Na} = \hat{g}_{Na} m^3 h \quad \text{Eq-31}$$

$$g_K = \hat{g}_K n^4 \quad \text{Eq-32}$$

The main equation (Eq-21) of Hodgkin-Huxley model is based on the Kirchhoff's current law.

For a multi-compartment Hodgkin-Huxley model, more equations are obtained by implementing Kirchhoff's laws to the whole circuit.

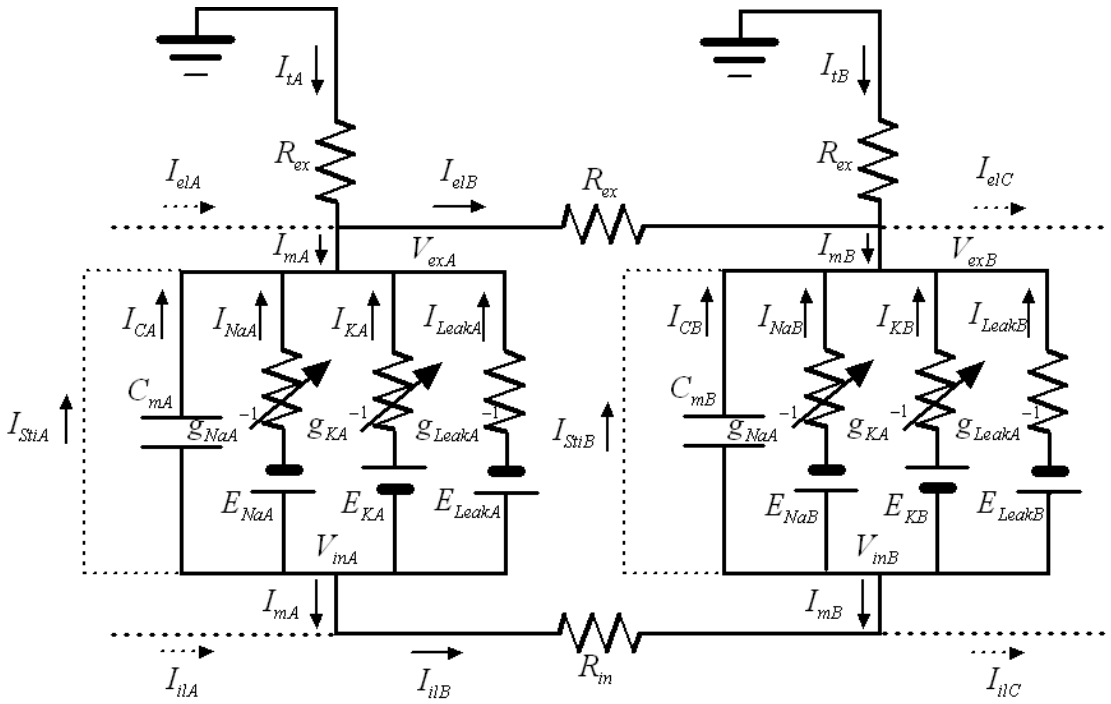

Figure-6-61: The circuit of the two compartmental Hodgkin-Huxley model. Currents flowing through each segments and the potentials at each joints are marked. The four dashed horizontal lines denote that the two compartments model could be extended to more compartments. The two dashed vertical lines show the path of stimulus current. The stimulus current is often injected with a electrode piercing through the neural membrane.

Take the two compartmental Hodgkin-Huxley model (**Figure-6-61**) as example. These equations based on Kirchhoff's laws are followed:

$$C_{mA}\, dV_{mA} / dt + I_{NaA} + I_{KA} + I_{LeakA} + I_{mA} = 0 \quad \text{Eq-33}$$

$$C_{mB}\, dV_{mB} / dt + I_{NaB} + I_{KB} + I_{LeakB} + I_{mB} = 0 \quad \text{Eq-34}$$

$$I_{mA} + I_{ilA} + I_{ilB} = 0 \quad \text{Eq-35}$$

$$I_{mB} + I_{ilB} + I_{ilA} = 0 \quad \text{Eq-36}$$

$$V_{inA} - V_{exA} = V_{mA} \quad \text{Eq-37}$$

$$V_{inB} - V_{exB} = V_{mB} \quad \text{Eq-38}$$

$$-V_{exA} = I_{tA}\, R_{ex} \quad \text{Eq-39}$$

$$-V_{exB} = I_{tB}\, R_{ex} \quad \text{Eq-40}$$

$$I_{elA} + I_{tA} - I_{mA} - I_{elB} = 0 \quad \text{Eq-41}$$

$$I_{elB} + I_{tB} - I_{mB} - I_{elA} = 0 \quad \text{Eq-42}$$

$$V_{inB} - V_{inA} = -I_{ilB}\, R_{in} \quad \text{Eq-43}$$

$$V_{exA} - V_{exB} = -I_{elB}\, R_{ex} \quad \text{Eq-44}$$

Together with the known elements of the circuit, the initial values of variables and the boundary conditions, these differential equations could be numerically solved in Mathematica.

6.15.3. Build time variable resistor in PSPICE

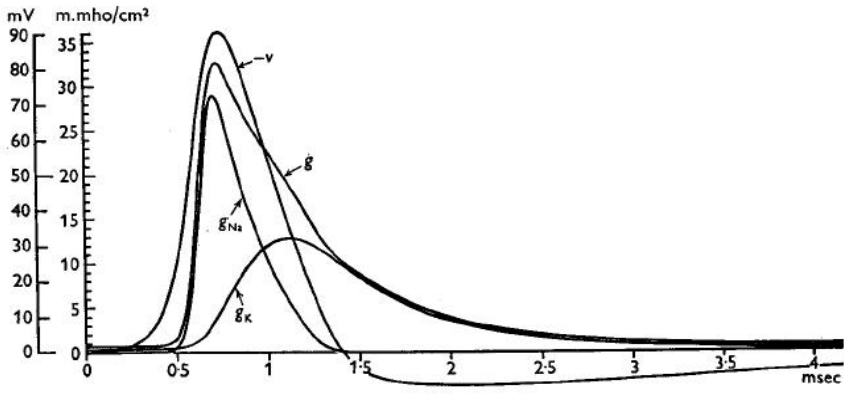

Figure-6-62: The g_{Na} , g_K calculated by Hodgkin, A.L. and Huxley, A.F. (1952).

The Hodgkin-Huxley model defines two variable resistors, i.e. g_{Na} , g_K , as a function of time. Other parameters in the circuit are constants, e.g., C_m , E_{Na} , E_K , g_{Leak} . Unfortunately, PSPICE does not contain any models of the time variable

resistor in its library. PSPICE does not accept in-line equations to describe a resistor too. A possible method to solve this problem is to use a substitute element, which accepts equations and works exactly like a resistor. A variable current source can be a substitute for the resistor in principle.

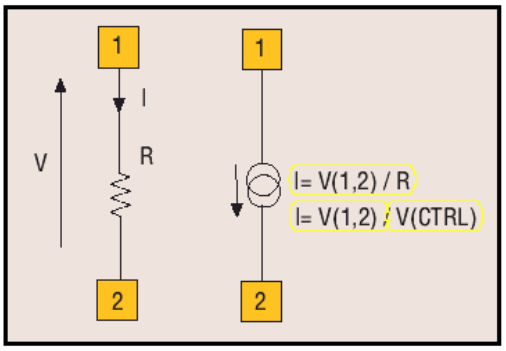

Figure-6-63: A resistor and its equivalent in PSPICE, a current source.

Based on Ohm's law: $I = U / R$, the current through a resistor is proportional to the voltage across the resistor. If the value of a current source is made to be proportional to the voltage across it, this current source is equivalent to a resistor in terms of Ohm's law. As shown in Figure-6-64, a current source plays the role of a resistor by keeping its own value equals to V(1,2)/R. The parameter R is namely the resistance of this virtual resistor. If we replace the parameter R with a function of time, the current source becomes an equivalent of a time variable resistor. Its virtual resistance $R = F(t)$.

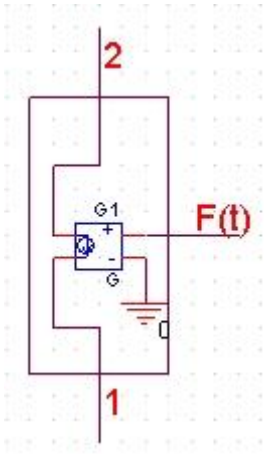

Figure-6-65: The virtual resistor is packed into a three pin element, which is called 'part' in PSPICE.

A Voltage Controlled Current Source (VCCS) is used to simulate the virtual resistor (a CCCS can be used too). The code describing the VCCS is follows:

```
.subckt Variable_R 1 2 F(t)
G1 1 2 Value = {V(1,2)*V(F(t)}
.ENDS
```

This subcircuit is packed into one part. It contains three pins, two as the terminals of the virtual resistor and the other as an input for control. This part can be used in PSPICE as one element, like other parts, e.g. capacitors, inductors etc.

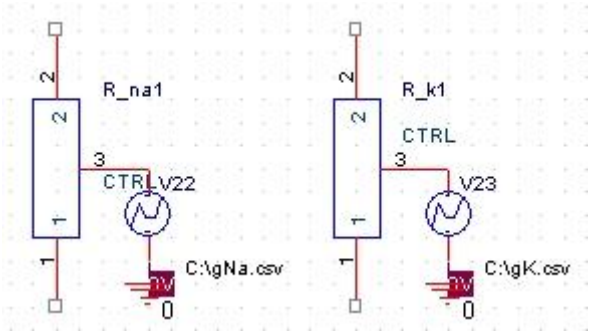

Figure 6-66: The model of the time variable resistors representing the conductance of Sodium and Potassium ion channels.

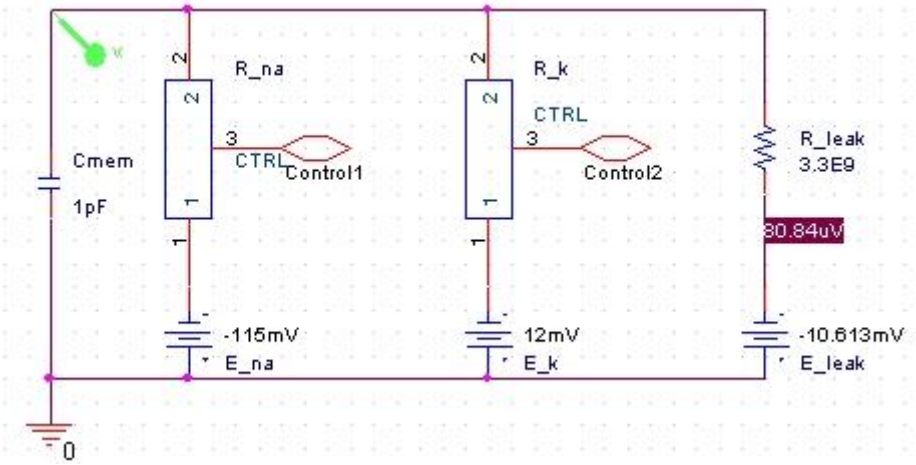

Figure-6-67: The Hodgkin-Huxley model built in PSPICE.

6.15.4. Calculate g_K, g_{Na} with spreadsheet

Mentioned above, the voltage clamp is not a natural situation for neuron. The current clamp is closer to the actual situation of neuron in real live. The current clamp device simply generates a stimulating current, and then measures passively the changes in membrane potential. The membrane conductance cannot be calculated with a simple function. They have to be solved by numerical method. Spreadsheet software 'Excel' (part of the Microsoft office pack) and Mathematica are used. A Mathematica built-in function is used to look for numerical solution. How does the function work is not clear. In comparison, the calculation procedure by spreadsheet software 'Excel' is very clear. Each step in the calculation is in list

and under control. The time is divided into finite pieces. Start from the initial time, the membrane conductance is calculated step by step. Each value at a time is calculated from the value of at last time. This process is repeated and the membrane conductance in the entire period of time is obtained in the end. The result is plotted in the following diagram.

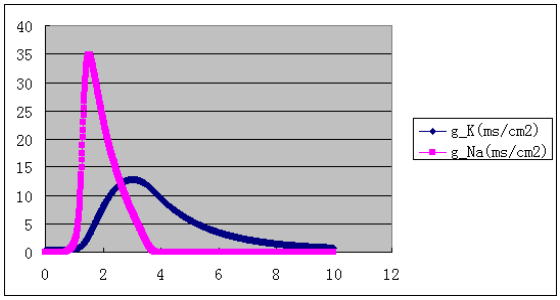

Figure-6-68: The membrane conductivity to sodium and potassium ions (mmho/cm^2). Parameters in two compartment model

The parameters are used in the simulation of different distribution of ion channels with the two compartments model (section 6.10.3).

Known parameters: (6.3 °C)

radius of the soma: $a_1 = 5\ \mu m$;
specific resistance of axoplasm (intracellular): $R = 35.4\ \Omega\ cm$;
capacity per unit area of membrane: $C_m = 1.0\ \mu F/cm^2$
The equilibrium potential of Sodium ions: $E_{Na} = 45\ mV$;
The equilibrium potential of Potassium ions: $E_K = -82\ mV$;
The leakage potential: $E_{Leak} = -59.387\ mV$;
maximum Sodium conductance:
Patch A: $\hat{g}_{Na}$ = 120 ms / cm^2 ; Patch B: $\hat{g}_{Na}$ = 12 ms / cm^2 ;
maximum Potassium conductance:
Patch A: $\hat{g}_K$ = 360 ms / cm^2 ; Patch B: $\hat{g}_K$ = 3.6 ms / cm^2 ;
The leak conductance:
Patch A: g_{Leak} = 0.3 ms / cm^2: Patch B: g_{Leak} = 0.03 ms / cm^2

Extracellular resistance (r_1):

It is assumed that the neuron is a sphere ($a_1 = 5\ \mu m$). The resistance of the bulk medium outside a sphere (r_1) is:

$$r_1 = \varepsilon\ /\ (\sigma\ C) = (a_2 - a_1)\ /\ (2\pi\ a_1\ a_2\ \sigma) \approx a_1\ /\ (2\pi\ a_1\ \sigma)$$

a_2 is the radius of outer sphere. It is much bigger than the radius of neuron and can be take out of the equation without much effect on the value of r_1.

σ is the conductivity of extracellular medium (DMEM, $\sigma = 1.3\ s\ /\ m$, measured under room temperature).

$$r_1 = a_1 / (2\pi a_1 \sigma) = 24\ K\Omega$$

Membrane capacitance (*c*):

Firstly assume the membrane area of each compartment is half of the total membrane area.

$$S = 2\pi a_1^2 = 1.57 \times 10^{-10}\ m^2$$

Then the membrane capacitance of this length of membrane is:

$$c = C_m S = 1.57\ pF$$

Resistance of ion channels ($\hat{g}_{Na}$, $\hat{g}_K$, R_{Leak}):

The minimum resistance of the Sodium ion channels:

$$\bar{R}_{Na} = \frac{1}{\bar{g}_{Na} \cdot S} = 1/120 \times 10^{-1} \times 1.57 \times 10^{-10} = 5.3 \times 10^8\ \Omega$$

;

The minimum resistance of the Potassium ion channels:

$$\bar{R}_K = \frac{1}{\bar{g}_K \cdot S} = 1/36 \times 10^{-1} \times 1.57 \times 10^{-10} = 1.77 \times 10^9\ \Omega$$

The resistance of the leak current channels:

$$R_{Leak} = 1 / (g_{Leak} S) = 2.12 \times 10^{11}\ \Omega$$

6.15.5. Parameters in multi-compartment model

These parameters are used in the simulation of the propagated AP with multi-compartment model. The known parameters come from this paper [Hodgkin and Huxley, A quantitative description…, 1952]. Other parameters come from the calculation followed.

Known parameters: (6.3 °C)

Conduction velocity: $\theta = 18.8\ m / s$;
The radius of axis cylinder: $a = 238\ \mu m$;
The specific resistance of axoplasma (intracellular): $R_2 = 35.4\ \Omega\ cm$;
The capacity per unit area of membrane: $C_m = 1.0\ \mu F/cm^2$;
The equilibrium potential of Sodium ions: $E_{Na} = 45\ mV$;
The equilibrium potential of Potassium ions: $E_K = -82\ mV$;
The leakage potential: $E_{Leak} = -59.387\ mV$

The maximum resistance of the Sodium ion channels: $\hat{g}_{Na} = 120\ ms\ /\ cm^2$;
The maximum resistance of the Potassium ion channels: $\hat{g}_K = 36\ ms\ /cm^2$;
The resistance of the leak current channels: $g_{Leak} = 0.3\ ms\ /\ cm^2$

Intracellular resistance (r_2):

$$r_2 = R_2\ l\ /\ A \qquad \text{Eq-45}$$

Where,

r_2 is the intracellular resistance between two membrane patches
l is the length between two membrane patches
A is the cross-sectional area of the axon

The length that the propagated action potential travels along the axon within 0.1 ms[3] is:

$l = \theta\ t = 1.88 \times 10^{-3}\ m$

The intracellular resistance of this length is:

$r_2 = R_2\ l\ /\ A = 3.74 \times 10^3\ \Omega$

Extracellular resistance (r_1):

r_1 is the extracellular resistance between two membrane patches

To simplify the calculation, assume the neural fiber is a cylinder. The spreading resistance of the bulk medium outside this cylinder is:

$$r_1 = \varepsilon\ /\ (\sigma\ C) = Log(a_2\ /\ a_1)\ /\ (2\pi\ \sigma\ l) \qquad \text{Eq-46}$$

Where,

a_2 is the radius of outer sphere of the cylinder ($a_2 = 1\ cm$). The chosen of this value does not effect much of the result, as long as it is much bigger than the inner radius of the cylinder.
σ is the conductivity of extracellular medium, which is mainly DMEM* ($\sigma = 1.3\ s\ /\ m$, from measurement under room temperature),
a_1 is the inner radius of the cylinder ($a_1 = 238\ \mu m$),
l is the length of the part of the cylinder: $l = 1.88 \times 10^{-3}\ m$

$r_1 = Log(r_2\ /\ r_1)\ /\ (2\pi\ \sigma\ l) = 243\ \Omega$

Membrane capacitance (c):

The membrane capacitance of this length of membrane is:

---

3 Other value of the compartment length can be defined according to requirement. Here is the distance the action potential travels in 0.1 ms.

$S = 2\pi\, a\, l = 2.81 \times 10^{-6}\ m^2$

$c = C_m\, S = 28.1\ nF$

Resistance of ion channels ($\hat{g}_{Na}$, $\hat{g}_K$, R_{Leak}):

The minimum resistance of the Sodium ion channels;

$$\bar{R}_{Na} = \frac{1}{\bar{g}_{Na} \cdot S} = 1/120 \times 10^{-1} \times 2.81 \times 10^{-6} = 2.96 \times 10^{4}\ \Omega$$

The minimum resistance of the Potassium ion channels;

$$\bar{R}_{K} = \frac{1}{\bar{g}_{K} \cdot S} = 1/36 \times 10^{-1} \times 2.81 \times 10^{-6} = 9.89 \times 10^{4}\ \Omega$$

The resistance of the leak current channels;

$$R_{Leak} = 1 / (g_{Leak}\, S) = 1.19 \times 10^{7}$$

Chapter 7. Recording experiments and preliminary signal analysis

7.1. Introduction

In this project many electrical signal from different cell cultures using different MEA systems were recorded. These experiments are described in this chapter. The characteristics of the signal are discussed. Both the success and failure of these experiments are evaluated. Possible improvements to the experiment in the future are presented at the end.

To acquire a signal from a 'neuronal bathtub' is an important goal of this project. This task is difficult. For clarity, a step-by-step approach is taken to discussing these experiments, starting from the easiest one and finishing with the most difficult one.

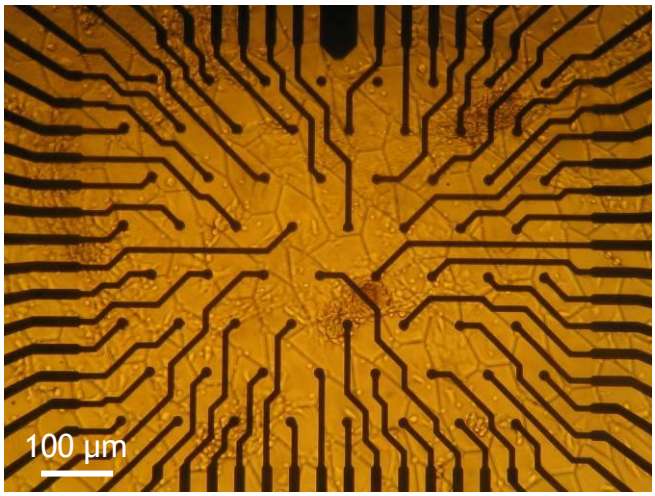

Figure 7-1: The Ti/Au pMEA and 'bathtub' under the optical microscope. The field of view is about 0.9 x 0.7 mm. The 'bathtub' and the cells cultured in it are faintly visible things behind the dark electrodes. The gray pattern is the Jude pattern embossed into the PDMS of the 'bathtub'. These nerve cells were densely cultured and were not supposed to form any predetermined network. Therefore the ‘bathtub’ was not aligned to the pMEA. In a one electrode to one neuron recording, the ‘bathtub’ needs to be aligned to the pMEA.

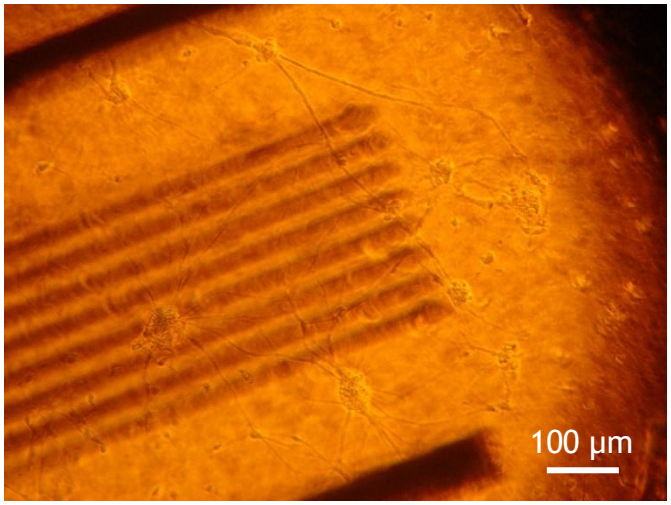

Figure 7-2: The FlexMEA and rat spinal cord cells under the optical microscope. The cells were in focus and clearly visible. The fussy dark lines are eight microelectrodes and two reference electrodes.

7.2. Rat cardiomyocytes in a Petri dish, recorded with a Flexible MEA

Initial work was done with rat cardiomyocytes as cardiomyocytes have intensive electrical activity, and even better, beating (or contraction) is associated with the electric activity. The active cells can be easily identified and located under the microscope. The cardiomyocytes were cultured in a Petri dish first as it provides a biocompatible substrate The FlexMEA system is easy to manoeuvre, so by locating the beating cell under a microscope, and operating a micromanipulator to approach the cell, large number of extracellular potentials can be recorded from one sample.

Table 7-1: The experiment setup.

Recording system: FlexMEA
Preamplifier: FET OP LT1793, mono (non-differential)
Amplification: ≈ 50× (1 µF , 4 KΩ , 200 KΩ)
Cell type: dense culture of rat cardiomyocytes on petri dish
Temperature: petri dish on *40 °C* hot stage
Culture medium: DMEM with FBS etc. (refer to chapter 2)

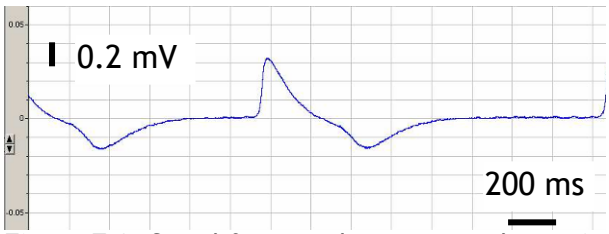

Figure 7-3: Signal from cardiomyocytes cluster A. Each impulse lasts about 800 ms. Voltage of

peak-valley is about 1 mV.

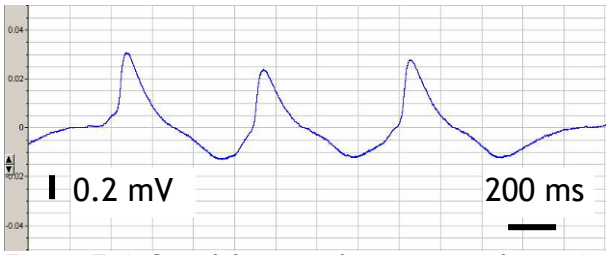

Figure 7-4: Signal from cardiomyocytes cluster B. Each impulse lasts about 800 ms. Voltage of peak-valley is about 0.8 mV.

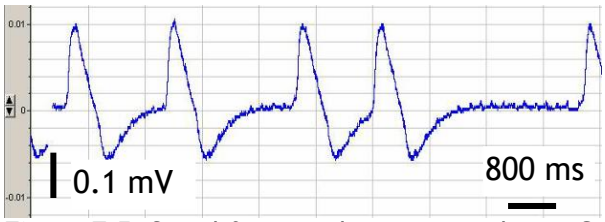

Figure 7-5: Signal from cardiomyocytes cluster C. Each impulse lasts about 800 ms. Voltage of peak-valley is about 0.3 mV.

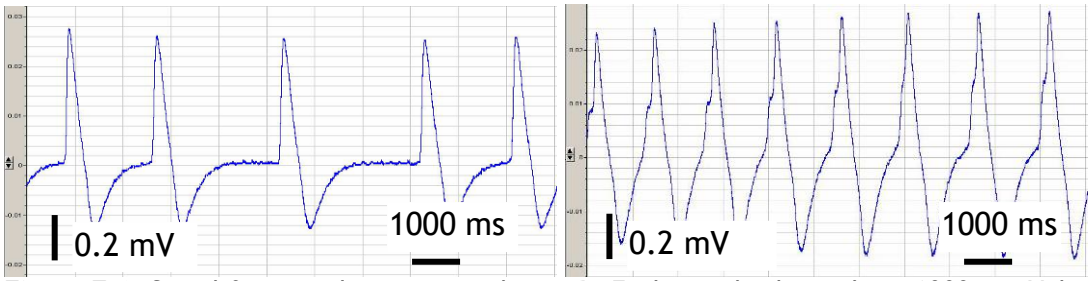

Figure 7-6: Signal from cardiomyocytes cluster D. Each impulse lasts about 1000 ms. Voltage of peak-valley is about 0.8 mV.

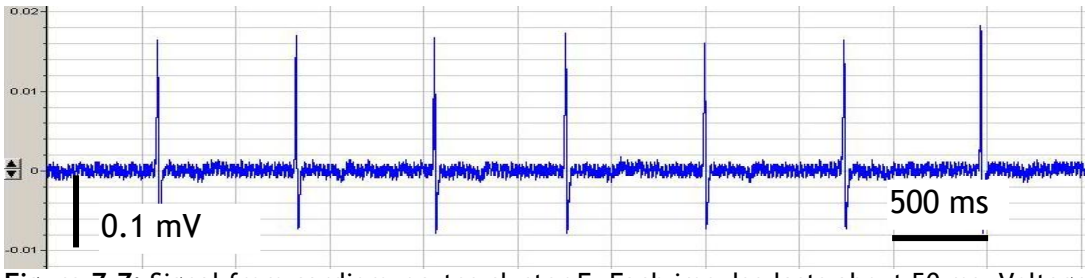

Figure 7-7: Signal from cardiomyocytes cluster E. Each impulse lasts about 50 ms. Voltage of peak-valley is about 0.3 mV.

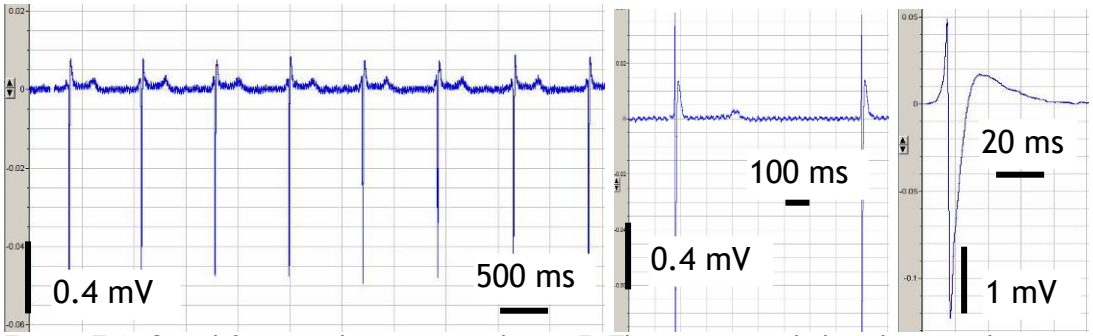

Figure 7-8: Signal from cardiomyocytes cluster F. They are recorded at the same location, but with different pressure by tiny adjustment to manipulator. The impulse at three diagram all last about 50 ms. The signal magnitude at three diagrams are different. The peak-valley voltage is about 1 mV at the first diagram, 2 mV at the second one and 4 mV at the last one.

Those images display the signals recorded from six different clusters of cardiomyocytes. The waveforms are different. Even the signals from the same cluster are different. For example, cluster E and F. Some waveforms have two-phase, some have three-phase. The difference may be related to the coupling of cells to the electrode, or may be associated with the nature of those cells.

The peak voltage recorded ranges from 0.3 mV to 4 mV. The duration of the pulses is from 50 ms to 1000 ms. Those signals can be classified into two types by their duration time. The slow pulses last about 1000 ms, such as cluster A, B, C, D. The fast pulses last about 50 milliseconds, such as cells E, F.

The background noise is mainly from the thermal noise of the resistance between the microelectrode and the reference electrode, which is the seal resistance in parallel with the internal resistance (section 6.5). When an electrode couples with a patch of cell membrane, seal resistance occurs in parallel with the membrane resistance. The seal resistance in range of 500 KΩ to 3 MΩ (Breckenridge, 1995) or 1 to 5 MΩ [Buitenweg et al., 1998 ~ 2002] is suitable for recording. The membrane resistance can be estimated by using the data of the squid giant axon: 1000 Ω cm2 (resting), 25 Ω cm2 (excited). The resistance of a membrane patch of 7×10-6 cm2 (cover 30 μm diameter electrode) is about 140 MΩ (resting) or 3.5 MΩ (excited). This value could be higher for a mammalian neuron (table 7.1). The seal resistance changes with the level of coupling of electrode/neuron. The membrane resistance remains relatively stable and much higher than the seal resistance at the time of resting. Therefore the resistance between the microelectrode and the reference electrode is mainly determined by the seal resistance.

The background noise is mainly from the thermal noise of the internal resistance of the signal source, which is determined by the seal resistance. Therefore, the background noise reflects the magnitude of the seal resistance and the level of the electrode/cell coupling. The background noise of those slow pulses (about 10-20 μV) is smaller than that of the spikes (about 20-40 μV). The slow pulses may come from the synchronous activity of many cells. The overlap of many spikes smooths the signal. The fast pulse may come from fewer cells and contains fewer components. Another possible reason is that the slow pulses and the sharp pulses are from different types of ion currents. Action potential of Calcium ions has slow pulses.

7.3. Rat cardiomyocytes cultured on pMEA

The next step in the experiments was to use a pMEA system to acquire the signals. The cardiomyocytes are cultured directly on the surface of pMEA. This experiment is more difficult than last one as at least one active cell cluster must be located in the vicinity of an electrode. In order to promote the probability of this happening, the cells are cultured in high density and large number of pMEAs were used. It took the use of 20 pieces of pMEAs, to obtain a successful recording.

Table 7-2: The experiment setup.

Recording system: Ti/Au pMEA
Preamplifier: FET OP LT1793, mono (non-differential)
Amplification: *≈ 100*×
Cell type: dense culture of rat cardiomyocytes on pMEA
Temperature: *45 °C* hot air circulating
Culture medium: DMEM with FBS etc. (refer to chapter 2)

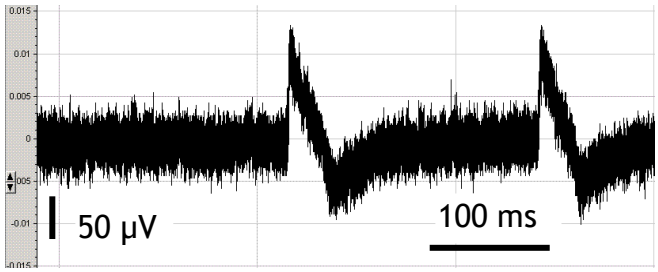

Figure 7-9: The pulse from a cell cluster. The cluster is located just on the recording microelectrode. Each pulse lasts for about 100 ms. The peak-valley voltage of the pulse is about 200 µV. Background noise is about 50-75 µV.

As the picture shows, the noise is relatively big. The average value is about 50 microvolts. The noise is mainly from the thermal noise of the resistance between the input terminals of the pre-amplifier (section 6.14). This resistance is mainly from the electrode/electrolyte interface when cells are not obstructing between the microelectrode and the reference electrode. Seal resistance occurs when cells adhere to microelectrode. The resistance between the inputs increases with the seal resistance which may be greatly raised by culturing the cells directly on the microelectrode. Therefore the seal resistance raises the noise level in the recording. It is possible to estimate the seal resistance from the thermal noise level [P J Johnson, 1986]. The pulse is relatively small, about 200 microvolts, almost drowned in the noise background. Probably the active cells are not well coupled with the electrode. The active cell cluster is just located on top of the electrode from the microscopic observation. The cells may not cover the electrode

completely or there is something between them. Both will reduce the signal to noise ratio.

7.4. Rat cardiomyocytes cultured in ‘neural bathtub’, recorded by pMEA

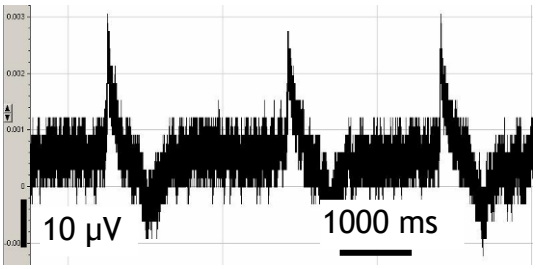

Figure 7-10: Signal from a cardiomyocytes cluster in ‘bathtub’ by pMEA. The microelectrode is in loose couple with cells, which means just touchs cells. Each impulse lasts about 1000 ms. Voltage of peak-valley is about 40 µV. Noise is about 10-15 µV.

This signal is weak. The amplitude is only about 40 microvolts. It is only just not be drowned by the noise. This may caused by the loose coupling of electrode to cell.

As shown in the picture, the noise is much lower than that in the previous experiment. The average value is only about 10 μV. The band-pass filter in the pre-amplifier surely did its job, but the main reason may come from the structure of the 'bathtub'. Cells are not grown directly on the electrode but on the bottom of the ‘bathtub’. The pillars surrounding the ‘bathtub’ support and separate the cells from the surface of pMEA. Some cell clusters were seen squeezed and touching the pMEA under the microscope during the recording. Most area of cells did not touch the pMEA. The electrodes may be in loose contact with the cells at this recording. This could explain the lower thermal noise in this recording. To estimate by the difference of the thermal noise (10-15 µV in this section and 50-75 µV in section 7.4), the seal resistance at this interface of electrode/cell is about 25 times lower than that with cells grown directly on the electrode.

7.5. Rat spinal cells in the 'bathtub', recorded with FlexMEA system

The previous experiments with cardiomyocytes showed that the whole system is working well. The next experiment was concerned with recording from neurons.

Table 7-3: The experiment setup.

Recording system: Ti/Au pMEA Preamplifier: FET OP LT1793, mono (non-differential), Amplification: ≈ *100*× channel 1, 2, 3 (*1 μF, 400 Ω, 50 KΩ*), Channel 4 (*1 μF, 5 KΩ, 560 KΩ*). Cell type: 80000 cells/area, dense culture of E14 rat embryonic, spinal cells in 'bathtub' Temperature: 'bathtub' in Petri dish on 40 °C hot stage Culture medium: DMEM with FBS etc. (refer to chapter 2)

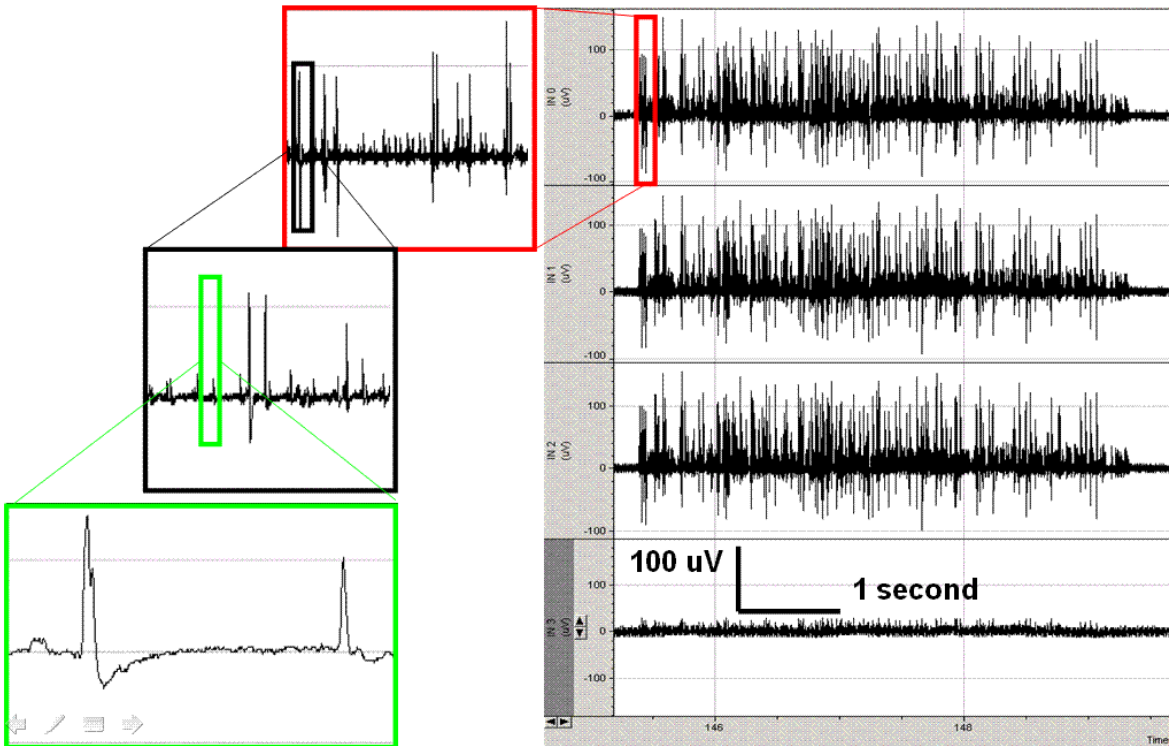

Figure 7-11: This diagram is from data file '05n21004.abf'. This is four channel recording of a spontaneous pulse sequence from the spinal cord cells of rat. Lasted about six seconds. Noise is about 10μV. The largest pulse is over 100μV.

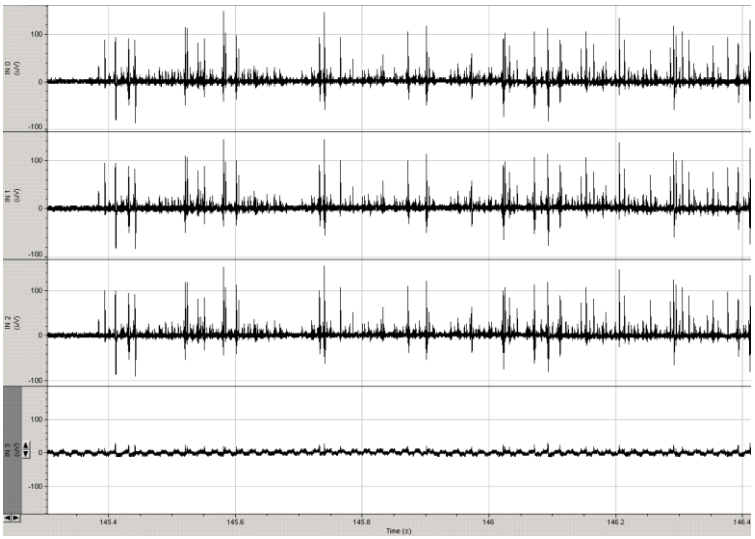

Figure 7-12: From data file '05n21004.abf'. A closer view to the spikes.

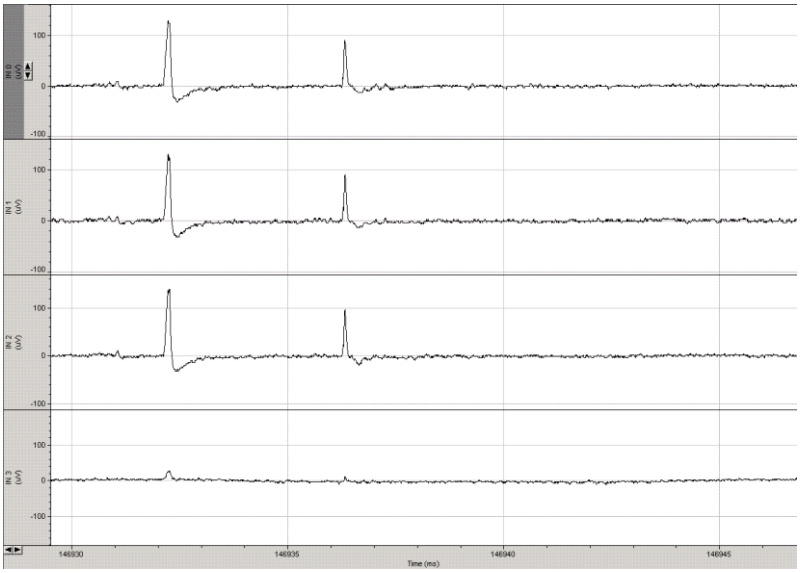

Figure 7-13: From data file ’05n21004.abf’. An even closer look. Single spikes are clearly visible. The waveforms are similar with the first derivative of the intracellular action potential. (section 6.10.1)

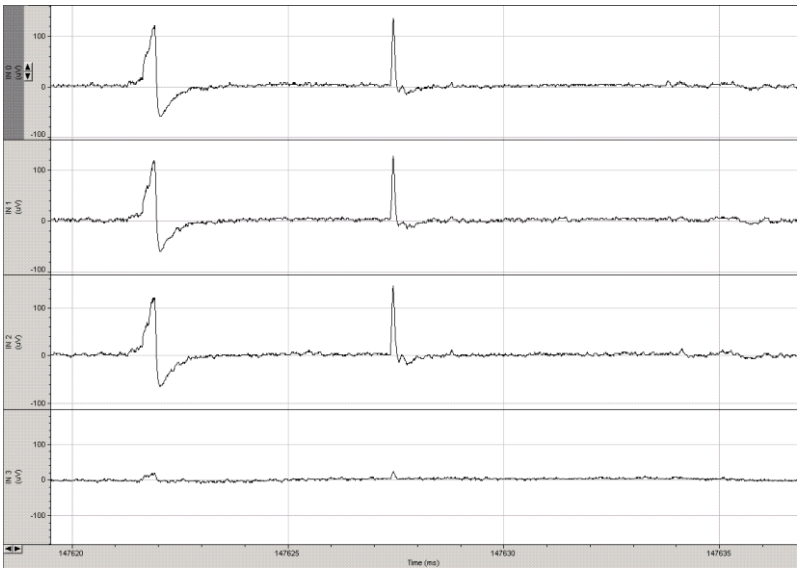

Figure 7-14: From data file ’05n21004.abf’. The waveform of the single spikes at left is similar with the simulation of propagated action potential of extracellular. (section 6.10.4)

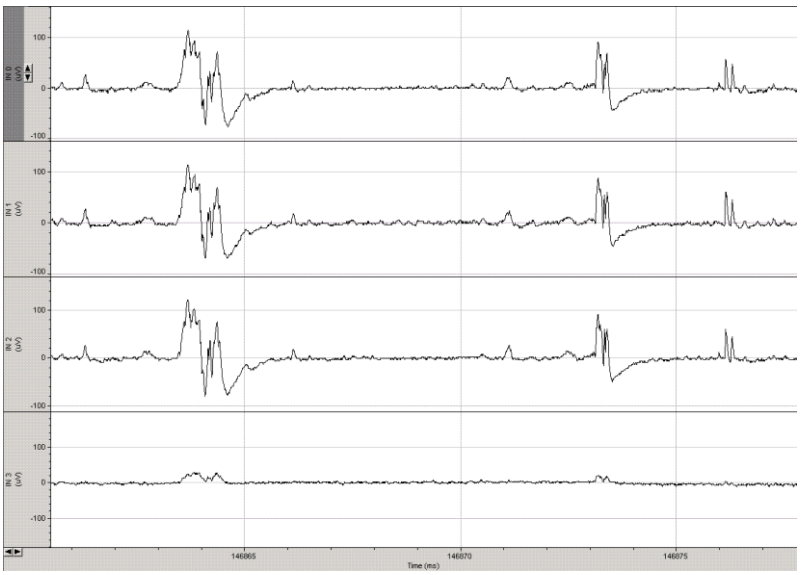

Figure 7-15: From data file ’05n21004.abf’. Many spikes are overlapping with each other.

To judge by the noise level, the electrodes are coupled with cells closely. The amplitude of pulses is also high and shows good coupling.

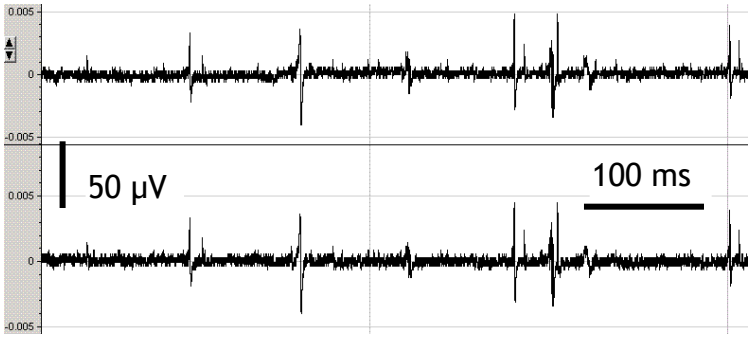

Figure 7-16: From data file ’05n15019.abf’. This is from another recording experiment. Noise is about 10 microvolt. The largest pulse is not higher than 100µV. channel 1,2 (1µF, 400Ω, 40KΩ)

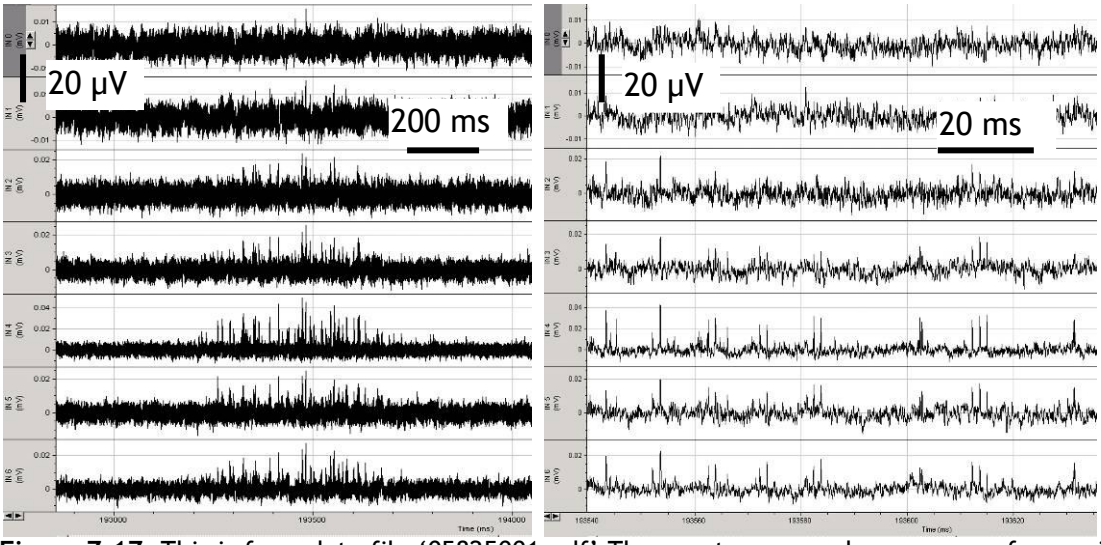

Figure 7-17: This is from data file ‘05825001.adf’.The spontaneous pulse sequence from spinal cells. 1000× magnification. It lasts about 500 ms. Noise is over 10µV. The largest pulse is over 50 µV.

Although high seal resistance is very important, but it does not guarantee a successful recording. As this recording shown above, the noise level suggests a high seal resistance. But the recorded signal is very weak. Old electrode or electrode of poor quality also causes high noise. As measured in chapter 4, the resistance of FlexMEA itself rises after being used in recording. Besides a bad coupling, many other reasons may cause bad recording, such as a poor electrode, an unreliable earth, a wrong cell, a right but unhappy cell or simply bad luck.

7.6. Rat spinal cells cultured in the 'bathtub', recorded with pMEA

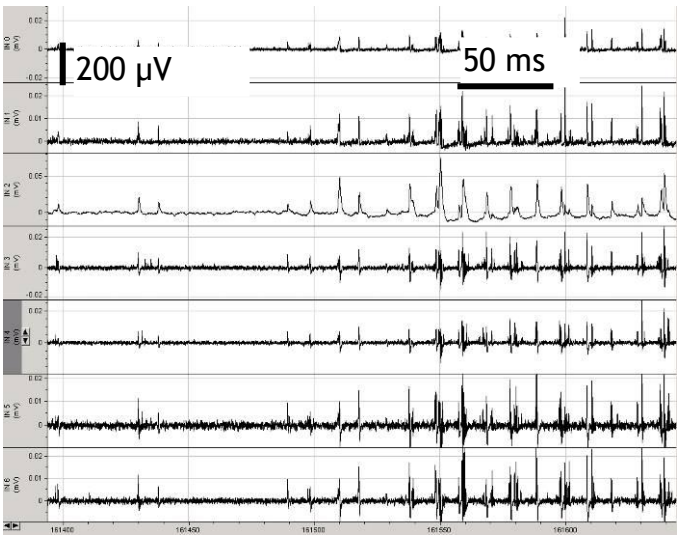

Figure 7-18: This is from data file '05805003.adf'. The spontaneous pulse sequence from spinal cells. 100× magnification. It lasts about 200 ms. Noise is about 20 µV. The largest pulse is over 200 µV.

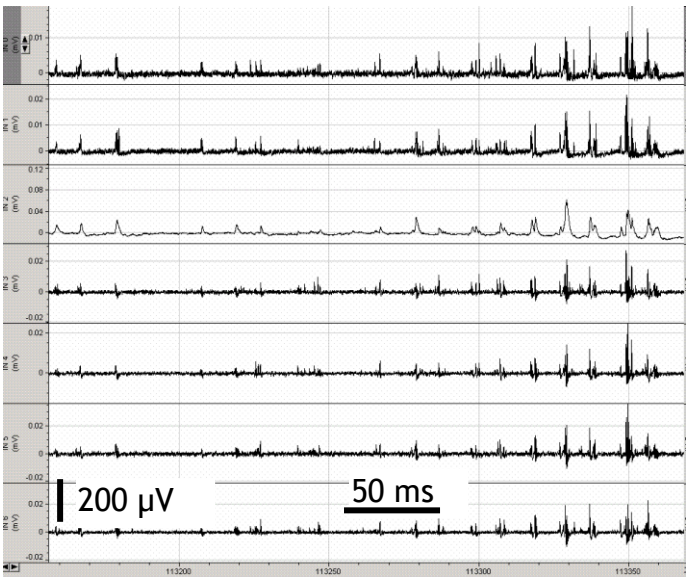

Figure 7-19: This is from data file '05805007.adf'. This is a spontaneous pulse sequence from spinal cells. 100× magnification. It lasts about 200 ms. Noise is over 15 µV. The largest pulse is over 200 µV.

This is a 7 channel recording. Up to 16 channels is possible. The pMEA has 64 electrodes. The number of working electrodes is only limited by the number of the preamplifiers in our system, which is 16 channels. The first two channels, the third channel and the remaining four channels have different circuit structure. Their pre-amps have different magnification and different bandwidth. The first two channels inhibit negative part of the signal. This may caused by a mistake of using polarized capacitor. Significant reverse current can flow through a polar capacitor.

The capacitor will not be the same capacitor anymore when inverse current is applied. The negative part of the signal is attenuated comparing with that of other channels.

The high cut-off frequency of the third channel is about 1 KHz. The high frequency part of the signal is lost, which can be seen from the waveform. The other four channels are proved to be good. Their bandwidth is from about 1 Hz to 5 KHz. The magnification is 100 times.

For the first look, the signal in each channel seems to be simply the same. The neurons or glial cells appear to be excited simultaneously. However there are some distinctions in detail between those signals. This suggests that the excitation and inhibition states of neurons are different too.

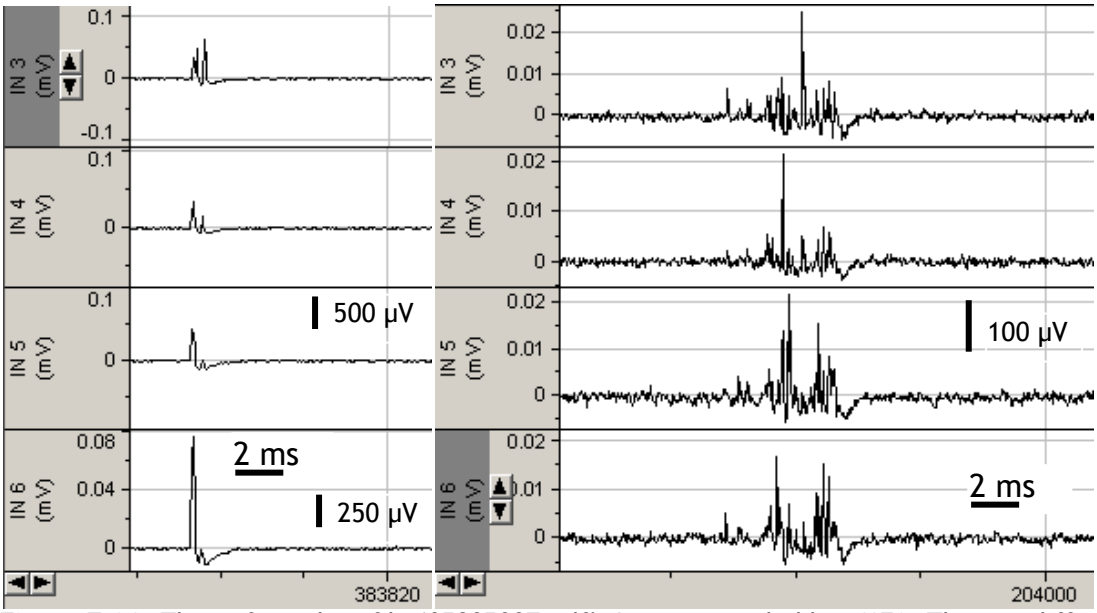

Figure 7-20: This is from data file '05805007.adf'. It was recorded by pMEA. There is difference between each channels.

The figure recorded a number of pulses happened closely together within a millisecond. Each channel at its location recorded its version of the signal. In the first channel, only one pulse is recorded. While other channels recorded more. The fourth channel even recorded three pulses. The amplitude of the pulses in different channels is also different. In the fourth and fifth channel, the final pulses are the highest one. But in the other channels, the final pulses are smaller, or even not there.

The electrodes on FlexMEA are closer to each other than those on pMEA. The neighbouring electrodes on FlexMEA are only about 50 *µm* apart. The entire region

where the electrodes inhibited is about 360 *μm* in width. The electrodes on pMEA are further divided and the distance to each other is about 100 *μm*. Those electrodes in the above seven channels stretch about 500 *μm*. The whole area of electrodes expands about 1 mm square. The signal differences between each channels of the pMEA are more significant than that of the FlexMEA. This probably has something to do with the density of the electrodes.

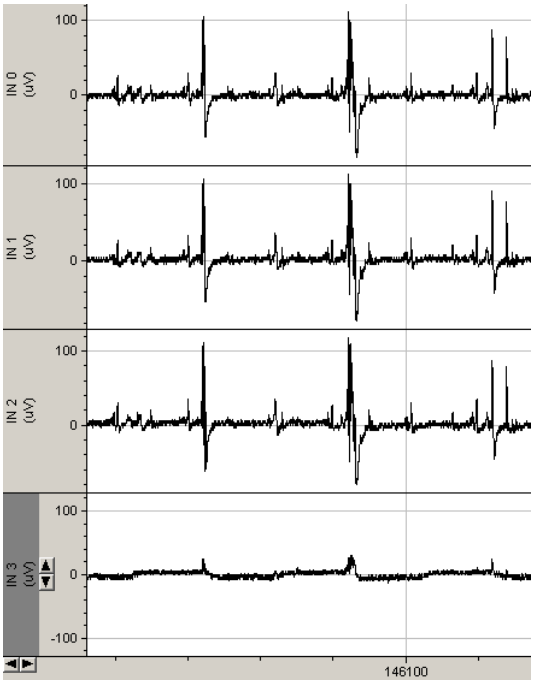

Figure 7-21: This is from data file '05n21004.abf'. It is recorded by FlexMEA. The signal in each channel appears to be the same.

7.7. Statistics of noise and signal

The noise level varies at different situations of recording. The noise levels are listed here. The list provides a preliminary overview. However, the noise levels are not precisely measured. Those methods like root mean square, etc. are not used to evaluate the noise. The noise values listed here are only estimated from the screen captured pictures.

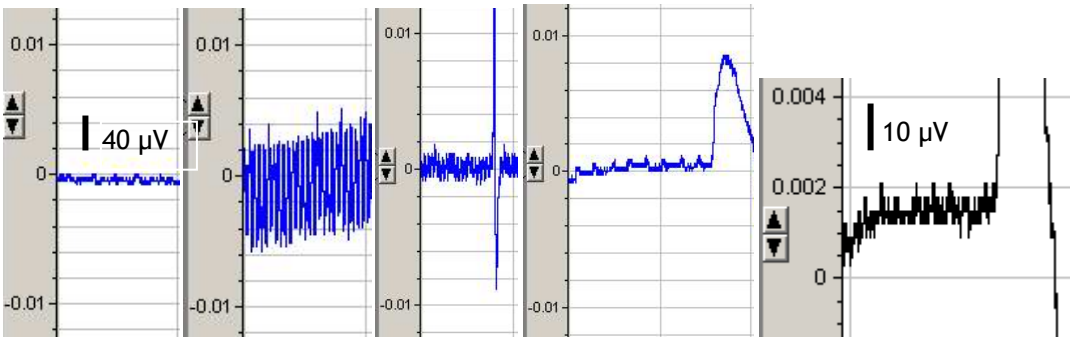

Figure 7-22: From left to right these figures show the noise level of different setups. FlexMEA and reference electrode suspend in medium without contact with cells (50×, Noise: 10-15 µV). FlexMEA and reference electrode suspend in air (50×, Noise: 120-150 µV). FlexMEA from heart cell in petri dish, sharp waveform (50×, Noise: 30-40 µV). FlexMEA from heart cell in petri dish, blunt waveform(50×, Noise: 15-20 µV). FlexMEA from heart cell in petri dish, blunt waveform (50×, Noise: 20 µV, 04n22000.abf).

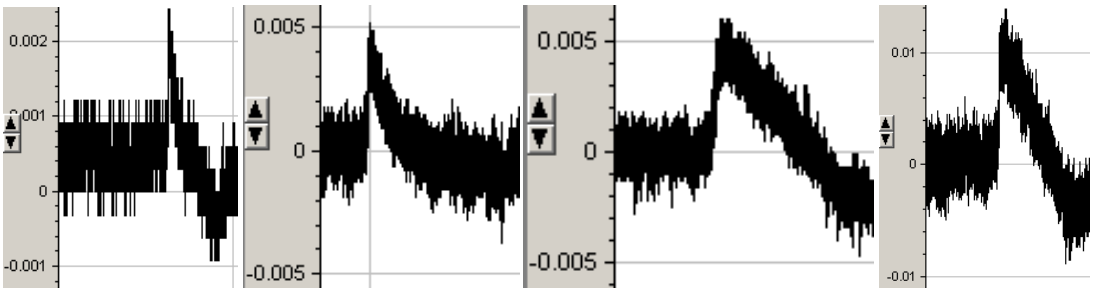

Figure 7-23: From left to right these figures show the noise level of different setups. PMEA from heart cell in bathtub (1-1KHz, 100×, Noise: 10-15 µV 05802004.abf). Heart cell on pMEA (5-1KHz, 100×, Noise: 30-40 µV, 05601000.abf). Heart cell on pMEA (1-1KHz, 100×, Noise: 40 µV, 05601001.abf). Heart cell on pMEA (1-50KHz, 100×, Noise: 80 µV, 05601004.abf).

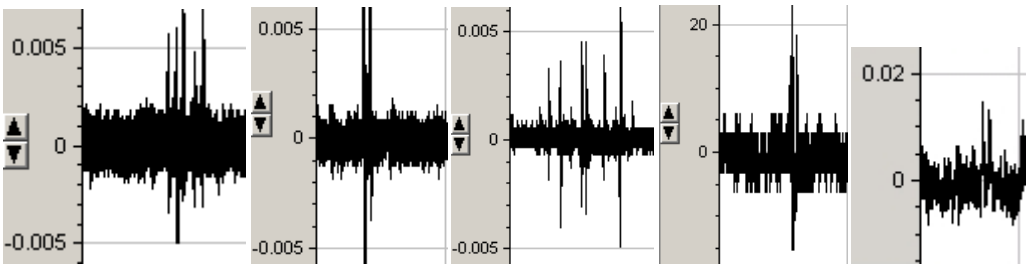

Figure 7-24: From left to right these figures show the noise level of different setups. PMEA from neuron in bathtub (1-5KHz, 100×, Noise: 30-40 µV, 05805003.abf). pMEA from neuron in bathtub (1-5KHz, 100×, Noise: 20-30 µV, 05805007.abf). FlexMEA from neuron in bathtub (1-5KHz, 100×, Noise: 15 µV, 05n15019.abf). FlexMEA from neuron in bathtub (1-5KHz, 100×, Noise: 10 µV, 05n21004.abf). FlexMEA from neuron in bathtub (1-5KHz, 1000×, Noise: 15 µV, 05825001.abf).

Table 7-4: The background noise level at recordings with different setup.

Recording setup	Passband	Noise level	Spike size and duration
FlexMEA and reference electrode in medium no touching cells.	1Hz~1KHz	10-15 *µV*	0
FlexMEA and reference electrode suspend in air.	1Hz~1KHz	120-150 *µV*	0
FlexMEA in contact with heart cells in petri dish (sharp waveform)	1Hz~1KHz	30-40 *µV*	0.25-4 mV, 50 ms
FlexMEA in contact with heart cells in petri dish (blunt waveform)	1Hz~1KHz	15-20 *µV*	0.3 -1 mV, 800-1000 ms

PMEA touch heart cells in bathtub	1Hz~1KHz	10~15 *μV*	40 *μV, 1000 ms*
PMEA with heart cells grow on it	1Hz~1KHz	30~40 *μV*	*200 μV, 100 ms*
PMEA with heart cells grow on it	1Hz~50KHz	80 *μV*	*200 μV, 100 ms*
PMEA from neurons in bathtub	1Hz~5KHz	20-40 *μV*	20-200 *μV, 0.3-2 ms*
FlexMEA from neurons in bathtub	1Hz~5KHz	10-15 *μV*	20-100 *μV, 1-5 ms*

7.8. Summary

The extracellular action potentials recorded from the spinal cells in this chapter are show two types of waveform. Both types start with a positive peak. One type ends with a negative peak. The other type is only a positive spike with a little or without the negative ending.

An actively propagated action potential, e.g. along an axon or between neurons, can give the first type waveform extracellularly (Fig 6.31). The positive peak comes from the capacitive current flows to other part of the membrane that is in action. The negative peak rises when the local membrane itself is in action and the ion currents flows through it into the cell.

An passively propagated action potential, e.g. along an dendrite or inhibited neurons, generates the second type of waveform in the medium. As there is no ion channel in action, all that matters is the capacitive current which gives the positive peak.

In a situation when the propagation can be neglected, the distribution of ion channels will play the important role to effect the waveform. This situation could happen when the local neurons near the microelectrode all generate action potential at the same time. A low ion channel density will give positive peak. A high K^+/Na^+ ratio will give the negative ending to the spike. (Fig 6.28)

7.8.1. The successful aspects of these experiments

One success: Signal of multi-channels have been recorded from the 'bathtub chip' using the pMEA and FlexMEA systems.

Success two: the nerve cells in the 'bathtub chip' form a predetermined network connections. The signal from them is valuable for the study of neural networks.

7.8.2. Why the experiment is not fully successful

First: the amount of the signal is insufficient. The signals are quite many by the

total, but they come from different samples. The signal from one same neural network is not enough. The signals are normally several spontaneous pulse sequences with long time interval. The probability to see a spontaneous firing is low. Usually it takes many 'bathtub chip' and to wait for long time (from a few minutes to hours) to record a pulse sequence. The lack of signal makes the neural network research very difficult.

Second: The network formed by nerve cells is not ideal. There are often many cells occupying one node or some nodes without any cell occupying. However, from large area, a part with satisfactory network connection can be found still.

Third: The coupling of electrodes with the nodes of the neural network is not ideal. The coupling of single mammalian neuron with one extracellular electrode has always been a difficult task. The micron-sized neuron must cover the microelectrode of tens of microns to create a high seal resistance. This is a work that needs precision. It is even more difficult when many neurons need to be coupled with their own electrode at the same time. This is why more experiments are on intensive neural culture or individual neuron, and fewer experiments are on sparse neural culture.

7.9. Future improvements

The stimulation function needs to be integrated into the system. The nerve cells can be stimulated to fire, instead of waiting for the spontaneous impulses. This may increase the chance of recording. The function of stimulation is also necessary for the neural network research. It can be investigated that how the neural network responses to, processes or remember the stimulation.

The further minimization of the microelectrodes is necessary. Smaller electrodes may be easier to couple with neuron. The diameter of the electrode is about 25 to 30 μm at present. It is roughly in comparable with the size of a neuron. It is very difficult for one neuron to fully cover an electrode.

The resistivity of the medium can be raised by adding in sucrose to the medium. In theory and from the result of simulation, the signal amplitude of the extracellular potential can be increased by raising the resistivity of the medium. However, this approach has not been practiced in this project. It is worth trying. Since the coupling of the MEA with the neural network is so difficult, any method to reduce

the difficulty is valuable.

The topographic guidance is not as good as protein guidance and so the final step is to record from a neural bathtub that has been patterned with protein. So far this recording from patterned neural network has not been successful.

List of References

Becker, F. F., Wang, X. B., Huang, Y., Pethig, R., Vykoukal, J., & Gascoyne, P. R. (1994). The Removal of Human Leukaemia Cells from Blood Using Interdigitated Microelectrodes. *J. Phys. D: Appl. Phys. , 27*, 2659-2662.

Becker, F. F., Wang, X. B., Huang, Y., Vykoukal, J., Gascoyne, P. R., & Pethig, R. (1995). Separation of Human Breast Cancer Cells from Blood by Differential Dielectric Affinity. *Proc. Nat. Acad. Sci. (USA) , 92*, 860-864.

Bergveld, P. (1972). Development, operation, and application of the ion-sensitive field-effect transistor as a tool for electrophysiology. *IEEE Transactions on Biomedical Engineering* , 19 (5), 342-351.

Bierer, S. M., & Sheppard, N. F. (1994). Extracellular electrode model applied to the pancreatic beta cell. *Engineering Advances: New Opportunities for Biomedical Engineers. Proceedings of the 16th Annual International Conference of the IEEE* , 2, 802-803.

Bierer, S. M., & Sheppard, N. F. (1994). Extracellular electrode model applied to the pancreatic beta cell. *Engineering Advances: New Opportunities for Biomedical Engineers. Proceedings of the 16th Annual International Conference of the IEEE , 2*, 802-803.

BLAU, A., ZIEGLER, C., HEYER, M., ENDRES, F., SCHWITZGEBEL, G., MATTHIES, T., et al. (November 1997). Characterization and optimization of microelectrode arrays for in vivo nerve signal recording and stimulation. *Biosensors and Bioelectronics* , 12(9), 883-892(10).

Bockris, J. O., Reddy, A. K., & Gamboa-Aldeco, M. (1970). *Modern Electrochemistry* (Vol. 2). New York: Plenum.

Borroni, A., Chen, F. M., LeCursi, N., Grover, L. M., & Teyler, T. J. (1991). An integrated multielectrode electrophysiology system. *J Neurosci. Method , 36*, 177-184.

Bove, M., Grattarola, M., Martinoia, S., & Verreschi, G. (October 1995). Interfacing cultured neurons to planar substrate microelectrodes: characterization of the neuron-to-microelectrode junction. *Bioelectrochemistry and Bioenergetics , 38* (2), 255-265.

Breckenridge, L. J., Wilson, R. J., Connolly, P., Curtis, A. S., Dow, J. A., Blackshaw, S. E., et al. (1995). Advantages of using microfabricated extracellular electrodes for In Vitro neuronal recording. *Journal of Neuroscience Research , 42*, 266-276.

Brewer, G. J., & Cotman, C. W. (Aug 1989). Survival and growth of hippocampal neurons in defined medium at low density: advantages of a sandwich culture technique or low oxygen. *Brain-Res. , 494* (1), 65-74.

Claverol-Tinturé, E., Ghirardi, M., Fiumara, F., Rosell, X., & Cabestany, J. (June 2005). Multielectrode arrays with elastomeric microstructured overlays for extracellular recordings from patterned neurons. *J. Neural Eng.* (2), L1-L7.

Craib, W. H. (1927). A study of the electrical field surrounding active heart muscle. *In heart , 14*, 71-109.

Craib, W. H. (September 1928). A study of the electrical field surrounding skeletal muscle. *J Physiol. , 66* (1), 49–73.

CRANK, J. (1975). *The Mathematics of Diffusion.* Oxford University Press.

Crotty, P. (2006). Metabolic Energy Cost of Action Potential Velocity. *J Neurophysiol , 96*, 1237–1246.

Curtis, A., Breckenridge, L., Connolly, P., Dow, J., Wilkinson, C., & Wilson, R. (1992). Making real neural nets: design criteria. *Medical and Biological Engineering and Computing* , 30(4), CE33-CE36.

Dittmann, L., Sensenbrenner, M., Hertz, L., & Mandeli, P. (1973). Respiration by cultivated astrocytes and neurons from the cerebral hemispheres. *Journal of Neurochemistry , 21*, 191-198.

Edes, R. E. (1892). On the transmission of the impulse of medullated fibres. *Journal of physiology , 13*, 428-444.

Feeney, R., & Kounaves, S. P. (October 1999). Determination of heterogeneous electron transfer rate constants at microfabricated iridium electrodes. *Electrochemistry Communications , 1* (10), 453-458.

Finn, W. E., & LoPresti, P. G. (2003). *Handbook of Neuroprosthetic Methods.* CRC Press.

Finn, W. E., & LoPresti, P. G. (2003). *Handbook of Neuroprosthetic Methods.* CRC Press.

Fromherz, P., Offenhäusser, A., Vetter, T., & Weis, J. (1991). A Neuron-Silicon Junction: A Retzius-Cell of the Leech on an Insulated-Gate Field-Effect Transistor. *Science , 252*, 1290-1293.

Furshpan, E. J., & Furukawa, T. (1962). Intracellular and extracellular responses of the several regions of the mauthner cell of the golfish. *J. neurophysiol. , 25*, 732-771.

Ganong, W. F. (2003). *Review of Medical Physiology* (21th Edition ed.). McGraw-Hill.

Gascoyne, P. R., Burt, J. P., Becker, F. F., & Pethig, R. (1993). Membrane changes accompanying the induced differentiation of Friend erythroleukemia cells studied by dielectrophoresis. *Biochim.Biophys.Acta , 1149*, 119-126.

Ge, W.-P., Yang, X.-J., Zhang, Z., Wang, H.-K., Shen, W., Deng, Q.-D., et al. (2006). Long-Term Potentiation of Neuron-Glia Synapses Mediated by Ca2+-Permeable AMPA Receptors. *Science , 312*, 1533-1537.

Goldman, D. E. (1943). Potential, impedance, and rectification in membranes. *J. Gen. Physiol. , 27*, 37-60.

GRAHAM, J., & GERARD, R. W. (1946). Membrane potentials and excitation of impaled single muscle fibers. *Journal of Cellular and Comparative Physiology , 28*, 99-118.

Gross, G. W. (1979). Simultaneous single unit recording in vitro with a photoetched laser deinsulated gold multimicroelectrode surface. *IEEE Trans. Biomed. Eng. , 26* (5), 273-279.

Gross, G. W., & Schwalm, F. U. (1994). A closed flow chamber for long-term multichannel recordmg and optical monitoring. *J. Neurosci. Methods, 52: 73-85 , 52*, 73-85.

Gross, G. W., Wen, W., & Lin, J. (1985). Transparent indium tin oxide electrode patterns for extracellular, multisite recording in neuronal cultures. *J. Neurosci. Meth. , 15*, 243-252.

Gross, G. W., Williams, A. N., & Lucas, J. H. (1982). Recording of spontaneous activity with photoetched microelectrode surface from mouse spinal neurons in culture. *J. Neurosci. Meth. , 5*, 13-22.

Hanna, G. R., & Johnson, R. N. (Sep 1968). A rapid and simple method for the fabrication of arrays of recording electrodes. *Electroencephalogr Clin Neurophysiol. , 25* (3), 284-286.

Hodgkin, A. L., & Huxley, A. F. (1952). A quantitative description of membrane current and its application to conduction and excitation in nerve. *Journal of Physiology , 117* (4), 500-544.

Hodgkin, A. L., & Huxley, A. F. (1952). Currents carried by sodium and potassium ions through the membrane of the giant axon of Loligo. *Journal of Physiology , 116*, 449-472.

Hodgkin, A. L., & Huxley, A. F. (1952). The components of membrane conductance in the giant axon of Loligo. *Journal of Physiology , 116*, 473-496.

Hodgkin, A. L., & Huxley, A. F. (1952). The dual effect of membrane potential on sodium conductance in the giant axon of Loligo. *Journal of Physiology , 1952*, 497-506.

Hodgkin, A. L., Huxley, A. F., & Katz, B. (1952). Hodgkin, A.L. and Huxley, A.F., and Katz, B (1952) Measurement of current-voltage relations in the membrane of the giant axon of Loligo. *Journal of Physiology , 116*, 424-448.

James, C. D. (JANUARY 2000). Aligned Microcontact Printing of Micrometer-Scale Poly-L-Lysine Structures for Controlled Growth of Cultured Neurons on Planar Microelectrode Arrays. *IEEE TRANSACTIONS ON BIOMEDICAL ENGINEERING , 47 (1)* .

James, C. D., Spence, A. J., Dowell-Mesfin, N. M., Hussain, R. J., Smith, K. L., Craighead, H. G., et al. (Sept. 2004). Extracellular recordings from patterned neuronal networks using planar microelectrode arrays. *Biomedical Engineering, IEEE Transactions on , 51* (9), 1640-1648.

Janossy, V., Toth, A., Bodocs, L., Imrik, I., Madarasz, E., & Gyevai, A. (1990). Multielectrode culture chamber: a device for long-term recording of bioelectric activities in vitro. *Acta Biol. Hung , 41*, 309-320.

Jimbo, Y., Robinson, H. R., & Kawana, A. (1993). simultaneous measurement of intracellular calcium and electrical activity from patterned neural networks in culture. *IEEE Trans on Biomed. Eng. , 40*, 804-810.

Johnson, P. J. (1986). The determination of electrical conductivity by thermal noise measurement. *J. Phys. D: Appl. Phys. , 19*, 835-840.

Kandel, E., Schwartz, J., & Jessel, T. (2000). *Principles of Neural Science* (4th Edition ed.). New York: McGraw–Hill.

Kandel, E., Schwartz, J., & Jessell, T. (Eds.). (2000). *Principles of Neural Science*. New York: McGraw-Hill.

Kovacs, G. T. (1994). *Introduction to the theory, design, and modeling of thin-film microelectrodes for neural interfaces in Enabling technology for cultured neural networks*. London: Academic Press.

Kraus, J. D. (1953). *Electromagnetics* (First Edition ed.). New York: Mcgraw-hill.

KRNJEVIC, K., & MILEDI, R. (1958). Acetylcholine in Mammalian NeuromuscularTransmission. *Nature , 182* (4638), 805-806.

KRNJEVIC, K., & MILEDI, R. (Mar 1958). Failure of neuromuscular propagation in rats. *J Physiol. , 140* (3), 440-461.

Krnjevic, K., & Miledi, R. (1958). Motor units in the rat diaphragm. *J. physiol. , 140*, 427-439.

Lee, I.-S., Whang, C.-N., Choi, K., Choo, M.-S., & Lee, Y.-H. (June 2002). Characterization of iridium film as a stimulating neural electrode. *Biomaterials , 23* (11), 2375-2380.

LING, G., & GERARD, R. W. (Dec 1949). The normal membrane potential of frog sartorius fibers. *J Cell Physiol. , 34* (3), 383-396.

Liu, J., Cai, B., Zhu, J., Ding, G., Zhao, X., Yang, C., et al. (2004). Process research of high aspect ratio microstructure using SU-8 resist. *Microsystem Technologies , 10* (4), 265-268.

Mailley, S. C., Hyland, M., Mailley, P., McLaughlin, J. M., & McAdams, E. T. (September 2002). Electrochemical and structural characterizations of electrodeposited iridium oxide thin-film electrodes applied to neurostimulating electrical signal. *Materials Science and Engineering: C , 21* (1-2), 167-175.

Mark, J. E. (1999). *POLYMER DATA HANDBOOK* (2nd Edition ed.). New York: Oxford University Press.

Markx, G. H., & Pethig, R. (1995). Dielectrophoretic Separation of Cells: Continuous Separation. *Biotechnol. Bioeng , 45*, 337-343.

Markx, G. H., Huang, Y., Zhou, X. F., & Pethig, R. (1994). Dielectrophoretic characterization and separation of micro-organisms. *Microbiology , 140*, 585-591.

Markx, G. H., Talary, M. S., & Pethig, R. (1994). Separation of viable and non-viable yeast using dielectrophoresis. *J. Biotechnology , 32*, 29-37.

Marrese, C. A. (1987). Preparation on strong adherent platinum black coatings. *Analytical Chemistry , 59(1)*, 217-218.

Martinoia, S., Bove, M., Carlini, G., Ciccarelli, C., Grattarola, M., Storment, C., et al. (1993). A general-purpose system for long-term recording from a microelectrode array coupled to excitable cells. *J Neurosci Methods , 48* (1-2), 115-21.

Martinoia, S., Massobrio, P., Bove, M., & Massobrio, G. (2004). Cultured neurons coupled to microelectrode arrays: circuit models, simulations and experimental data. *IEEE Trans Biomed Eng. , 51* (5), 859-64.

Mathieson, K. (June 2003). Fabricating high-density microarrays for retinal recording. *Microelectronic Engineering , 67-68*, 520-527.

McAdarns, E. T. (1995). The linear and non-linear electrical properties of the electrode-electrolyte interface. *Biosensors & Bioelectronics* .

Morin, F. O., Takamuraa, Y., & Tamiya, E. (August 2005). Investigating neuronal activity with planar microelectrode arrays:achievements and new perspectives. *Journal of Bioscience and Bioengineering , 100* (2), 131-143.

Morin, F., Nishimuraa, N., Griscomb, L., LePioufleb, B., Fujitac, H., Takamuraa, Y., et al. (January 2006). Constraining the connectivity of neuronal networks cultured on microelectrode arrays with microfluidic techniques: A step towards neuron-based functional chips. *Biosensors and Bioelectronics , 21* (7), 1093-1100.

Morrison, R. (1967). *Grounding and shielding techniques in instrumentation.* New York: John Wiley & Sons.

Nakamura, Y., Suzuki, Y., & Watanabe, Y. (1996). Effect of Oxygen Plasma Etching on a Adhesion between Polyimide Films and Metal. *Thin Solid Films* , 367-369.

Nernst, W. H. (1888). Zur Kinetik der in Losung befindlichen Korper: Theorie der Diffusion. *Z. Phys. Chem. , 3*, 613-37.

Newman, E. A., & Zahs, K. R. (February 1997). Calcium Waves in Retinal Glial Cells. *Science , 275 (5301)*, 844-847.

Novak, J. L., & Wheeler, B. C. (1986). Recording from the Aplysia abdominal ganglion with a planar microelectrode array. *IEEE Trans Biomed Eng , 33* (2), 196-202.

Pethig, R. (1991). Application of A.C. electrical fields to the manipulation and characterization of cells. In I. Karube (Ed.), *Automation in Biotechnology* (pp. 159-185). Elsevier.

Pethig, R., & Markx, G. H. (1997). Applications of dielectrophoresis in biotechnology. *Trends Biotechnol , 15* (10), 426-432.

Pickard, R. S. (1979). Printed circuit microelectrodes. *Trends in Neurosci , 2*, 259-261.

Pine, J. (1980). Recording action potentials from cultured neuron with extracellular microcircuit electrodes. *J. Neurosci. Meth. , 2*, 19-31.

Pohl, H. A. (1978). *Dielectrophoresis.* Cambridge: Cambridge University Press.

Pohl, H. A. (1958). Some Effects of Nonuniform Fields on Dielectrics. *J. Appl. Phys. , 29*, 1182-1188.

Purves, D., Augustine, G. J., Fitzpatrick, D., Hall, W. C., Lamantia, A.-S., McNamara, J. O., et al. (Eds.). (2004). *Neuroscience* (3rd Edition ed.). Sinauer Associates.

R, L. D. (2003). *CRC Handbook of Chemistry and Physics.* CRC press.

Regehr, W. G., Pine, J., & Rutledge, D. B. (1988). A long term in vitro silicon-based microelectrode-neuron connection. *IEEE Trans. Biomed. , 35* (12), 1023-1031.

Renshaw, B. (May 1946). CENTRAL EFFECTS OF CENTRIPETAL IMPULSES IN AXONS OF SPINAL VENTRAL ROOTS. *J Neurophysiol. , 9* (3), 191-204.

Rieke, F. (1997). *Spikes: Exploring the Neural Code.* MIT Press.

Sadiku, M. N. (1995). *Elements of electromagnetics.* New York: Oxford University Press.

Sandison, M. (2001). Fabrication of Flexible Microelectrodes for Neural Recording. *not being published* .

Sandison, M., Curtis, A. S., & Wilkinson, C. D. (2002). Effective extracellular recording from vertebrate neurons in culture using a new type of microelectrode array. *Journal of Neuroscience Methods , 114*, 63-71.

Schuettler, M., & Stieglitz, T. (2002). Corrosion of Thin-Film Electrodes In Vitro: Comparison of Disk and Lily Pad Design, , 25.-29.06.200. *Proceedings of the 7th Annual Conference of the International Functional Electrical Stimulation Society in Ljubljana (Slovenia) , 25*, 228-230.

Stoppini, L., Duport, S., & Correges, P. (1997). A new extracellular multirecording system for electrophysiological studies:application to hippocampal organotypic cuhures. *J Neurosci. Methods , 72*, 23-33.

Talary, M. S., Mills, K. I., Hoy, T., Burnett, A. K., & Pethig, R. (1995). Dielectrophoretic Separation and Enrichment of CD34 Cell Subpopulation from Bone Marrow and Peripheral Blood Stem Cells. *Med. & Biol. Eng. & Comp. , 33*, 235-237.

Tank, D. W., Cohan, C. S., & Kater, S. B. (1986). Cell body capping of array electrodes tmproves measurements of extracellular voltages in macro-cultures of invertebrate neurons. *IEEE Conference on Synthetic Mlcrostructures* .

Tasaki, I. (2006). A note on the local current associated with the rising phase of a propagating impulse in nonmyelinated nerve fibers. *Bulletin of Mathematical Biology , 68*, 483-490.

Tasaki, I., Watanabe, A., Sandlin, R., & Carnay, L. (1968). Changes in fluorescence, turbidity, and birefringence associated with nerve excitation. *PNAS , 61*, 883-888.

Thomas, C. A., Loeb, G. E., Berwald-Netter, Y., & Okun, L. M. (1972). A miniature microelectrode array to monitor the bioelectric activity of cultured cells. *Exp Cell Res. , 74* (1), 61-66.

Various. (n.d.). the exchange current density. *http://www.corrosion-doctors.org/Kinetics/Exchange.htm* .

VERZEANO, M. (August 1956). Activity of Cerebral Neurons in the Transition from Wakefulness to Sleep. *Science , 124* (3217), 366-367.

Wang, X.-B., Huang, Y., Burt, J. P., Markx, G. H., & Pethig, R. (1993). Selective Dielectrophoretic Confinement of Bioparticles in Potential Energy Wells. *J.Phys.D: Appl.Phys. , 26*, 1278-1285.

Weiss, T. F. (1994). *Cellular biophysics, electrical properties.* Massachussets: MIT Press.

Wilkinson, C. D. (1993). Research on information processing by neural networks cultured on subsrates. *Jpn. J. Appl. Phys. , 32*, 6210-6212.

Windhorst, U., & Johansson, H. (1999). *Modern Techniques in Neuroscience Research.* Springer.

Windhorst, W., & Johansson, H. (1999). *Modern Techniques in Neuroscience Research.* Springer.

Wise, K. D., & Angell, J. B. (1975). A low-capacitance multielectrode probe for use in extracellular neurophysiology. *IEEE Trans. on Biomed. Eng. , 22* (3), 212-9.

Wise, K. D., Angell, J. B., & Starr, A. (1970). An Integrated-Circuit Approach to Extracellular Microelectrodes. *Biomedical Engineering, IEEE Transactions on , 17* (3), 238-247.

Xing, W.-L., & Jing, C. (2006). *Frontiers in Biochip Technology.* Springer.

Yu, Z., Xiang, G., Pan, L., Huang, L., Yu, Z., & Yao, W. (2004). Negative Dielectrophoretic Force Assisted Construction of Ordered Neuronal networks on Cell Positioning Bioelectronic Chips. *Biomedical Microdevices , 6* (4), 311-324.